



Universitat Autònoma de Barcelona

ADVERTIMENT. L'accés als continguts d'aquesta tesi queda condicionat a l'acceptació de les condicions d'ús establertes per la següent llicència Creative Commons:  http://cat.creativecommons.org/?page_id=184

ADVERTENCIA. El acceso a los contenidos de esta tesis queda condicionado a la aceptación de las condiciones de uso establecidas por la siguiente licencia Creative Commons:  <http://es.creativecommons.org/blog/licencias/>

WARNING. The access to the contents of this doctoral thesis it is limited to the acceptance of the use conditions set by the following Creative Commons license:  <https://creativecommons.org/licenses/?lang=en>

Preparation and processing of molecular materials with optoelectronic properties

Wenjie Qian

Director

Prof. Núria Aliaga-Alcalde

Tutor

Dr. Jordi Hernando Campos

Material Science PhD thesis

2018

Institut de Ciència de Materials de Barcelona (ICMAB-CSIC)



Memoria presentada para acceder al Grado de Doctor por:

Wenjie Qian

Director

Prof. Núria Aliaga-Alcalde

ICREA Research Professor

CSIC-ICMAB

Tutor

Dr. Jordi Hernando Campos

Departamento de química

Universitat Autònoma de Barcelona

Bellaterra, Mayo de 2018

Table of contents

Table of contents	I
Acknowledgements	V
Abstract	VII
Resumen	IX
Abbreviations	XI
Chapter I. General Introduction	1
1.1 Organic functional materials used in organic solar cell and single molecular electronic	2
1.1.1 Small molecules solution-processed bulk heterojunction organic solar cells	2
1.1.2 Studies of single-molecule electronic performance via mechanically controllable break junction (MCBJ) technique	5
1.1.3 Relevant small molecules toward BHJ OSC and MCBJ studies	6
1.2 Porphyrin	7
1.3 Curcuminoids	9
References:	12
Chapter II. Boosting self-assembly diversity of chiral/achiral acetate-based Zn(II) porphyrins	17
2.1 Introduction	18
2.2 Objectives	21
2.3 Synthesis of acetate-based Zn(II) porphyrins bearing chiral/achiral centres....	21
2.3.1 Synthesis of chiral/non-chiral aldehyde (R)-G1 and G2	22
2.3.2 Formation of the free-based porphyrin H ₂ (4R-PPP) and H ₂ PPP	23
2.3.3 Metalation of the free-base porphyrins with zinc(II) ion.....	24
2.3.4 Self-assembly of Zn(II) porphyrins by crystallization	24
2.4 Structural descriptions of chiral/achiral acetate-based Zn(II) porphyrins	26
2.4.1 Study the aggregates obtained for Zn(4R-PPP) using single X-ray diffraction	26
2.4.1.1 Crystal structure of 1a	26
2.4.1.2 Crystal structure of 1b	29
2.4.1.3 Study regarding the origin of the molecule of H ₂ O in 1a absent in 1b....	30
2.4.2 Study the aggregates obtained for Zn(PPP) using single X-ray diffraction.....	32
2.4.2.1 Crystal structure of 2a	32
2.4.2.2 Crystal structure of 2b	33
2.4.2.3 Crystal structure of 2c	34
2.4.3 Discussion of the Zn(4R-PPP) and Zn(PPP) self-assembly by crystallography....	35
2.5 Studies performed in solution: NMR, UV-Vis absorption and CD spectra	36
2.6 Study of the self-assembly of Zn(II) porphyrins in the solid state	38
2.6.1 Study the stability of 1a and 1b by ESI-Mass.....	38
2.6.2 Study the aggregates by ATR-FTIR	38
2.6.3 Study the aggregates by solid-state ¹³ C NMR	39
2.6.4 Study the aggregates by solid UV-Vis absorption spectroscopy	40

2.6.5 Study the aggregates by solid-state circular dichroism spectroscopy	41
2.6.6 Study the aggregates by solid-state vibrational circular dichroism spectroscopy	44
2.7 Morphological studies of Zn(II) porphyrins on surfaces	45
2.7.1 Studies of Zn(4R-PPP), from CH ₂ Cl ₂ /CH ₃ OH solutions	45
2.7.2 Studies of Zn(PPP), from CH ₂ Cl ₂ /CH ₃ OH solutions	46
2.7.3 Studies of Zn(4R-PPP), from CH ₂ Cl ₂ /n-hexane solutions	47
2.7.4 Studies of Zn(PPP), from CH ₂ Cl ₂ /n-hexane solution	48
2.8 Solution-processed BHJ OSCs based on porphyrin Zn(4R-PPP)	48
2.8.1 Optical absorption spectra, electrochemical and thermal properties	48
2.8.2 Morphological characterization and optical properties of the blends of Zn(4R-PPP) with P3HT and PCBM	50
2.8.3 Photovoltaic characteristics	52
2.9 Conclusions	53
Experimental Section:	54
References.....	57

Chapter III. Extended research on solution processable small molecules based on porphyrins for BHJ OSCs

3.1 Introduction	60
3.2 Objectives.....	61
3.3 Synthesis and crystallographic studies of TEP and Zn(TEP)	61
3.3.1 Synthesis of TEP (involving short ester substituents).....	61
3.3.2 Crystallographic studies of TEP and Zn(TEP)	62
3.4 Solution-processed BHJ OSCs based on porphyrin TEP	63
3.5 Conclusions	65
Experimental Section	66
References.....	67

Chapter IV. Porphyrin-based binary self-assembling systems.....

4.1 Introduction	70
4.2 Objectives.....	72
4.3 Intermolecular self-assembly of porphyrins bearing carbonyl and pyridine groups	73
4.3.1 Synthesis of Zn(4R-CPP)	73
4.3.2 Self-assembly studies of Zn(4R-CPP)	74
4.3.2.1 Crystals of Zn(4R-CPP).....	74
4.3.2.2 Self-assembly studies by UV-Vis absorption and circular dichroism	75
4.3.3 Supramolecular organization of porphyrin-Py compounds.....	78
4.3.3.1 Titration studies of Zn(4R-CPP) with pyridine.....	78
4.3.3.2 Self-assembly studies in solution of Zn(4R-CPP) and TPYP	79
4.3.3.3 Self-assembly morphological studies of Zn(4R-CPP) and TPYP	81
4.3.4 Self-assembly studies of TCPP and TPYP: titration experiments	82
4.4 Ionic self-assembly of water soluble porphyrins	83
4.4.1 Synthesis of Zn(4R-CPP) ^{m-}	83
4.4.2 Synthesis of H _n TPyP ⁿ⁺	84
4.4.3 Ionic self-assembly studies using Zn(4R-CPP) ^{m-} and H _n TPyP ⁿ⁺	86

4.5 Conclusions	88
Experimental Section	88
References	89
Chapter V.Exploratory study of new curcuminoids	91
5.1 Introduction	92
5.2 Objectives	93
5.3 Synthesis and characterization	94
5.3.1 Synthesis of CCMoids bearing chiral centres and ester groups	95
5.3.1.1 Synthesis and crystal structure of (R, R) (MeO) ₂ C	95
5.3.1.2 Synthesis and crystal structure of (R, R) (MeO) ₂ C-BF ₂	97
5.3.1.3 Synthesis and crystal structure of (R, R) (MeO) ₂ C-Zn	99
5.3.2 Synthesis of carboxylic CCMoids compounds bearing chiral centres	102
5.3.2.1 Synthesis of (R, R) (HO) ₂ C	103
5.3.2.2 Synthesis of (R, R) (HO) ₂ C-M compounds (M = metallic centre)	104
5.3.2.3 Synthesis of (R, R) (HO) ₂ C-BF ₂	107
5.3.2.4 Advanced synthesis using (R, R) (HO) ₂ C-BF ₂	109
5.3.2.5 Crystallization of (R, R) (HO) ₂ C and (R, R) (HO) ₂ C-BF ₂	109
5.3.3 Synthesis and structures of CCMoid ligands bearing achiral groups	110
5.3.3.1 Synthesis and crystallization of CCMoids bearing achiral groups	110
5.3.3.2 Crystal structure of (MeO) ₂ C	111
5.3.3.3 Crystal structure of (MeO) ₂ C-BF ₂	112
5.3.3.4 Crystal structure of (HO) ₂ C	113
5.3.4 Summary of the CCMoid structures of this chapter	115
5.4 Photophysical properties studies	116
5.5 Conclusions	117
Experimental Section	118
References	121
Chapter VI.Py-CCMoid-coordination polymers	123
6.1 Introduction	124
6.2 Objectives	126
6.3 Synthesis and characterization of CPs based on Py-CCMoid	127
6.3.1 Synthesis and structure of 3Py-CCM ligand	127
6.3.2 Synthesis and characterization of Py-CCMoid CPs	128
6.3.2.1 General methods to obtain the CPs based on 3Py-CCM	128
6.3.2.2 Crystal structures of PyC-Zn1 and PyC-Zn2	128
6.3.2.3 Stability of PyC-Zn1, PyC-Zn2 and PyC-Zn3	130
6.4 Top-down exfoliation of crystalline PyC-Zn2 towards the study of nanoscale aggregates	132
6.4.1 The effect of washing with DMA	132
6.4.2 Exfoliation studies using EtOH, CH ₃ OH and acetone	137
6.4.3 Exfoliation studies in H ₂ O, chlorobenzene and hexane	141
6.5 Conclusions	142
Experimental Section	143
References	143

Chapter VII. Studies of porphyrin derivatives and curcuminoids for single molecular electronics experiments	145
7.1 Introduction	146
7.2 Objectives.....	146
7.3 Synthesis	148
7.3.1 Synthesis of porphyrin $\text{th}_2(\text{}^t\text{Buph})_2\text{P}$	148
7.3.2 Synthesis of $(\text{MeS})_2(\text{}^t\text{Buph})_2\text{P}$	151
7.3.3 Characterization of SR-CCMoids.....	152
7.4 MCBJ experiments with $\text{th}_2(\text{}^t\text{Buph})_2\text{P}$	154
7.4.1 Redox properties of $\text{th}_2(\text{}^t\text{Buph})_2\text{P}$	154
7.4.2 Single-molecule break-junction experiments of $\text{th}_2(\text{}^t\text{Buph})_2\text{P}$	155
7.5 Electron transport studies with CCMoids	158
7.5.1 Single-molecule measurement MCBJ experiments on CCMoids	158
7.5.2 Stability of boron compounds	160
7.5.3 Solid state UV-Vis absorption studies of CCMoids	161
7.5.4 CV and DPV measurements of CCMoids	163
7.6 Conclusions	164
Experimental Section:	165
References.....	168
Appendix	171
Chapter II.....	172
Chapter III.....	191
Chapter IV	193
Chapter V	194
Chapter VI	205
Chapter VII	207
References.....	211

Acknowledgements

The journey of pursuing my dream of getting my Ph.D. title is getting closer to the end and now it is time to show my most sincere appreciation to all the people who have contributed in this process.

First of all, I would like to dedicate this thesis with my deepest gratitude and love to my family members: my parents, parents-in-law and husband, Dr. Changyong Lu. Thank you so much for your constant understanding, encouragement and support during all these years. I am proud to be the first female in our family to receive the Ph.D. title, especially abroad. Without your good family education and love, I wouldn't find the strength to persist in my efforts until today. (感谢求学这些年爸爸妈妈们的理解,支持和鼓励,正因为您们多年来正确的养育观,我很开心在 30 岁的时候,成为了自己想成为的 30 岁的样子,我爱你们。)

Regarding my work and life here, firstly, I would like to express my deepest gratitude to my supervisor Prof. Núria Aliaga-Alcalde for her guidance and concern not only in science but also in life during these four years. I am really happy to be your first Ph.D. student at the ICMAB, even though the process was tough and we faced severe difficulties, thanks to your professionalism, confidence and intelligence, finally we could do it and I learned a lot from you. To Prof. David Amabilino, who gave me the opportunity to come at the ICMAB in 2013 and guided me during my year, I would like to show him my deepest respect and gratitude. With their help, I could perform the research projects of this thesis with the financial support of the Spanish Government, the Generalitat de Catalunya and the European Union: MINECO (ID: MAT2013-47869-C4-2-P), CSIC (ID: 201660E014), CSIC, I-COOP+2016 (ID: COOPA20162), European Research Council (ID: Tmol4TRANS). Thanks for the support and special thanks must be given to the Generalitat de Catalunya for my FI-DGR 2014 grant.

This work would not have been finished without the collaboration with other research groups and experts in various fields. Therefore, I would like to give my deepest gratitude:

To the research staffs in ICMAB, especially to Dr. Mariano Campoy, Dr. Bernhard Döring and Laura Corcoles, for their collaboration in the subject of organic solar cells; Drs. C. Ocal, E. Barrera and A. Pérez, for the AFM measurements and Dr. José Giner, for his guidance in the synthesis of coordination polymers (CPs).

To the members in the group of Prof. Daniel Maspoch in ICN2, for the single crystal X-ray diffraction measurements and analyses, and also their help regarding laboratory work; to Prof. Klaus Wurst (Universität Innsbruck) and Dr. E. Carolina Sañudo (UB), for their crystallographic measurements and analyses; to Prof. E. Ruiz (UB), for the theoretical calculations; to Alvaro Etcheverry-Berriós and Joseline Iribarra Araya, members of the group of Prof. Monica Soler from Universidad de Chile, for their work with curcuminoid molecules. To Prof. Herre S. J. van der Zant (TU Delf) and Dr. Diana Dulić (Universidad de Chile), for their MCBJ measurements.

Also, I am very grateful to all the people and friends who have helped me during the years: Drs. Josep Puigmarti Luis, Alessandro Sorrenti, Roman Rodriguez, Cristina Oliveras and Marta Riba: thanks for the help at the beginning of my research work. To all the colleagues in my group (*Funnanosurf*), especially to Dr. Arántzazu González-Campo, Raúl Díaz, Sandra Giraldo, Ezhil Amithalingam, Laura Rodriguez and my TFG students Xavier Domingo and Carles Ràfols, I

appreciate the help in the daily lab work and accompany in life during this period. I would like also mention the scientific and technique services and administrative staff of the ICMA B: thanks for your help with the research work and the public affairs. To my roommates and all my friends who have encouraged and helped me during my most difficult time, and friends who taught me how to grow up, I take this opportunity to express my sincere thanks.

Finally, thanks to the good environment and weather in Barcelona, I can gain the Ph.D. title together with a healthy body, and I enjoy the life a lot here.

Abstract

Organic small molecules materials with optoelectronic properties are particularly attractive in the fields of organic solar cells and molecular electronics. Porphyrins and curcuminoids (CCMoids) are prospective candidates in these fields due to their modifiable chemical structures and outstanding properties. In this thesis, the design and preparation of these two families of molecules, together with their self-assembly abilities and potential applications have been studied.

In Chapter II, two metalloporphyrins (**Zn(4R-PPP)** and **Zn(PPP)**) containing long chiral or achiral moieties with carbonyl substituents in the four *meso*-positions of their porphyrin cores have been synthesized. Then, a complete study related to non-covalent multiporphyrin assemblies has been performed, and initial solution-processed bulk heterojunction organic solar cell experiments were presented.

To extend the above study, in Chapter III, new porphyrins (**TEP** and **Zn(TEP)**) with shorter carbonyl substituents have been investigated and the effect of the length of the ligands in intermolecular interactions was studied, searching how this factor affects as well the OSCs performance.

With the same chiral centres in the *meso*-positions, a porphyrin **Zn(4R-CPP)** involving carboxylic groups was obtained in Chapter IV. And the binary self-assembling systems based on its derivations were achieved through non-covalent interaction or ionic self-assembly towards their potential application as active components in nanomaterials.

In Chapter V, CCMoids containing chiral groups, in a similar manner as chapter II, were synthesized. In addition, research towards the achievement of terminal acid groups from the hydrolyzation of the ester groups (as Chapter IV shows) allowed the investigation of the possible creation of systems with different dimensionalities. Then in Chapter VI, the synthesis of CPs/networks was explored by the use of a CCMoid containing pyridine moieties at its endings (**3Py-CCM**).

The last chapter is devoted to the design of new porphyrin derivatives containing sulphur-based anchoring groups for their application in single molecular electronics together with the study of their electronic properties in solution and solid state. In addition, a family of CCMoids has also been analysed in a similar manner as the porphyrin derivatives, with the aim of gathering information to improve their molecular design for electronic applications.

Resumen

Materiales orgánicos basados en moléculas pequeñas con propiedades optoelectrónicas son particularmente atractivos en los campos de celdas solares orgánicas y en el campo de la electrónica molecular. Porphirinas y curcuminoides (CCMoids) son moléculas que suscitan interés, siendo buenas candidatas en los campos mencionados, debido a que presentan estructuras químicas modificables y excelentes propiedades electrónicas. En esta tesis, se han estudiado la preparación y diseño de moléculas pertenecientes a las dos familias aquí indicadas, la capacidad de autoensamblaje de dichas moléculas conjuntamente con sus posibles aplicaciones.

En el Capítulo II, se han sintetizado dos metaloporphirinas (**Zn(4R-PPP)** y **Zn(PPP)**) ligandos largos que contienen centros quirales o aquirales conjuntamente con grupos carbonilos en las cuatro posiciones *meso* de sus respectivos núcleos de porfirina. Posteriormente, se ha sintetizado un estudio completo relacionado con las interacciones intermoleculares no covalentes de dichas multiporphirinas y experimentos iniciales con la creación de celdas solares orgánicas de hetero-unión (BHJ-OSCs) donde este tipo de porfirinas han sido procesadas en solución para el estudio de su comportamiento como sistemas donadores en dichas celdas.

Dicho estudio se extendió en el Capítulo III a dos nuevas porfirinas (**TEP** y **Zn (TEP)**) con sustituyentes carbonilos pero más cortos donde se investigó el efecto de las dimensiones de los ligandos en las interacciones intermoleculares finales, y cómo esto afecta el rendimiento de OSCs.

En el Capítulo IV se explica como con los mismos centros quirales en las posiciones *meso*, se obtuvo una nueva porfirina, **Zn(4R-CPP)**, que contiene grupos carboxílicos. También se muestran los estudios con dicho sistema y porfirinas adicionales con la formación de sistemas de autoensamblaje binarios basados en interacciones no covalentes o de autoensamblaje iónico para su posible aplicación como nanomateriales.

En el Capítulo V, se sintetizaron CCMoids que contienen grupos quirales, de forma similar al capítulo II, así como el estudio del efecto de la quiralidad de dichos materiales. Además, la investigación hace énfasis en el logro de grupos ácidos terminales a partir de la hidrolización de los grupos ésteres (como se muestra en el Capítulo IV) que permitió investigar la posible creación de sistemas con diferentes dimensionalidades. Después, en el Capítulo VI, se exploró la síntesis de CPs/redes mediante el uso de CCMoids que contienen grupos piridínicos en sus terminaciones (**3Py-CCM**).

El último capítulo está dedicado al diseño de nuevos derivados de porfirina que contienen grupos de anclaje basados en azufre para su aplicación en electrónica molecular conjuntamente con el estudio de sus propiedades electrónicas en solución y en estado sólido. Además, una familia de CCMoids también se ha analizado de manera similar a los derivados de porfirina, con el objetivo de recopilar información para mejorar su diseño molecular para aplicaciones electrónicas.

Abbreviations

δ	Chemical shift (delta)
AcOEt	Ethyl acetate
AFM	Atomic force microscopy
ATR-FTIR spectroscopy	Attenuated total reflection Fourier-transform infrared
BHJ OSCs	Bulk heterojunction organic solar cells
CD	Circular Dichroism
CE	Cotton effect
CT	Charge-transfer state
CPs	Coordination polymers
CCM	Curcumin
CCMoid	Curcuminoid
CV	Cyclic Voltammetry
D-A	donor - acceptor
DDQ	2,3-Dichloro-5,6-dicyano-p-benzoquinone
DIAD	Diisopropyl azodicarboxylate
DMA	Dimethylacetamide
DMF	Dimethylformamide
DMSO	Dimethyl sulfoxide
DPV	Differential Pulse Voltammetry
EtOH	Ethanol
ESI-MASS	Electrospray Ionisation Mass Spectrometry
Fc/Fc ⁺	Ferrocene/ferrocenium
FF	Fill factor
HMBC	¹ H detected heteronuclear multiple bond correlation
HOPG	High oriented pyrolytic graphite
HOMO	Highest Occupied Molecular Orbital
HSQC	Heteronuclear Single Quantum Coherence

HT	Hight tension
ITO	Indium tin oxide
IR	Infra-red spectroscopy
J _{sc}	Short-circuit current
LUMO	Lowest Unoccupied Molecular Orbital
MALDI-Tof	Matrix-assisted laser desorption ionization-time of flight
MCBJ	Mechanically controlled break junction
MCH	Methylcyclohexane
Me	Methyl
NMR	Nuclear magnetic resonance
OPVs	Organic photovoltaics
ORTEP	Oak Ridge Thermal Ellipsoid Program
P3HT	Poly(3-hexylthiophène-2,5-diyl)
PCBM	[6,6]-phenyl-C61-butyric acid methyl ester
PCE	Power conversion efficiency
PEDOT:PSS	Poly(3,4-ethylenedioxythiophene) polystyrene sulfonate
Ph	Phenyl
Py	Pyridine
SEM	Scanning electron microscopy
TFA	Trifluoroacetic acid
THF	Tetrahydrofuran
UV-Visible	Ultraviolet-visible absorption spectroscopy
VCD	Vibrational circular dichroism
V _{oc}	Open circuit voltage

Chapter I

General Introduction

1.1 Organic functional materials used in organic solar cell and single molecular electronics

1.1.1 Small molecules solution-processed bulk heterojunction organic solar cells

The use of the sun as a source of energy and therefore the creation of devices capable of converting solar energy in electricity (solar cells) have been studied for the scientific community in different ways, being the molecular approach one of the most relevant from an engineering standpoint.¹⁻³

In the field of organic photovoltaics (OPVs), the fabrication of bulk heterojunction (BHJ) organic solar cells (OSCs) consists in the creation of a binary molecular-based phase, where p-type conjugated polymers, such as poly(3-hexylthiophene-2,5-diyl) (P3HT, acting as a donor, D) and phenyl-C₆₁-butyric acid methyl ester (PCBM, fullerene derivative, as an acceptor) mix to produce an active region that can promote electronic transport (efficient charge separation) supported by additional layers.⁴ This type of system (Figure 1) is indeed constant in most of the literature related to OPVs since the first breakthrough reported in 1995 by G.Yu *et al.*⁵ The use of the two components mentioned above (P3HT/PCMB) has been so far the most successful blend found in BHJs (with power conversion efficiencies (PCEs) over 9 %),⁶ however it has been postulated that small molecules would be improved donor materials presenting several advantages: (i) defined morphologies, with synthetic paths that can be reproduced at high purity and (ii) their absorption spectra, and therefore HOMO-LUMO energy levels can be easily modified by introducing additional groups in the molecular design.^{4,7-9}

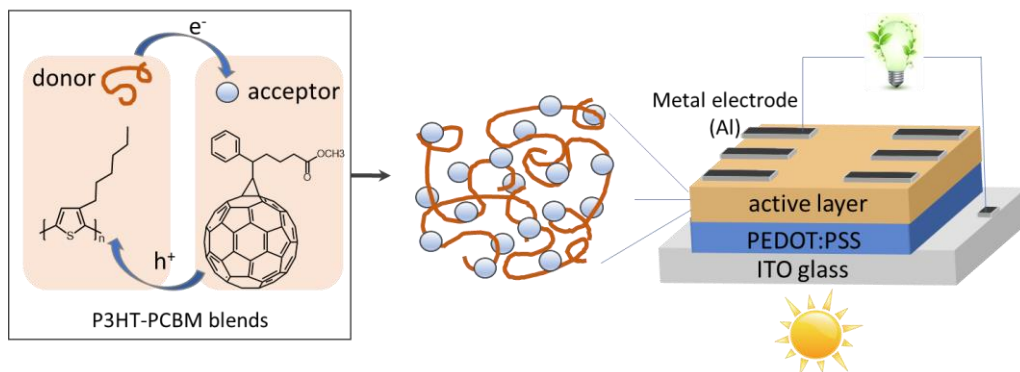


Figure 1. (Left) Schematic diagram of the photoinduced charge transfer process in P3HT-PCBM (D-A) blends. (Right) Sketch of the general structure of the photovoltaic cell fabricated with bulk heterojunction material.

One of the most appealing aspects, in BHJ OSCs, is that the blends which form the final devices can be deposited from solution like inks, enabling large-scale production at low process costs by the use of roll-to-roll coating.¹⁰

In the following paragraphs, the most important features of solution-processed small molecule based BHJ-OSCs are described, together with general traits of the architecture required for the creation of the organic solar cells and the most commonly materials used toward such goal. In a second step, the principles for the assembly of molecules (to create active blends) and the morphology influence on the OSCs efficiency are also depicted.

BHJ Organic solar cells are formed by sandwiching the blending of the two (D and A) organic materials between a transparent electrode (typically indium-tin oxide, ITO) and a reflective metal electrode (Ag or Al) as shown in Figure 1. The fabrication of the final device requires hole-transporting materials such as PEDOT: PSS (added as buffer layer). In the heterojunction configuration (organic blend), the main light-absorbing material is the electron donor, which has higher electron affinity and ionization energy, whereas the other one acts as the acceptor part. Overall, there is a 4-step efficiency model, as shown in Figure 2a, from light absorption to the extraction of charge carriers at the electrodes.⁹ These key points are: (i) illumination process and absorption of photons, where the efficiency of this process depend on the absorption wavelength; (ii) photoexcitation, caused by the initial step and followed by diffusion into a heterointerface, having lifetimes from ps to ns;¹¹ (iii) dissociation of the exciton, with the corresponding formation of a charge-transfer state (CT) at the donor-acceptor interface, where the energy level offsets between the two materials provide a driving force to separate the electron-hole pair; (iv) separation of the charge carriers and transport to their respective electrodes.

The power conversion efficiency (PCE, also depicted as η_p) defined as the ratio of available maximum power (P_{out}) to the incident solar powder (P_{in}) is one of the most important figures towards the comparison of the performance among solar cells (Figure 2b), where the P_{out} is proportional to the product of the short-circuit current (J_{sc}), the open circuit voltage (V_{oc}) and the fill factor (FF).

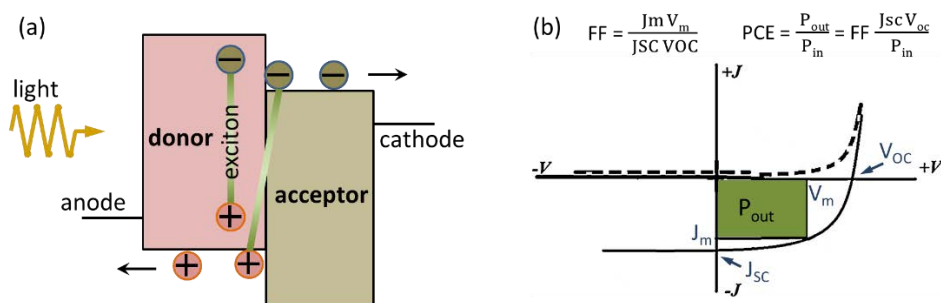


Figure 2. (a) 4-step model of a BHJ OSC performance in terms of light absorption, photoexcitation, exciton dissociation and charge extraction. (b) Typical current–voltage characteristics for dark and light current in a solar cell.

During the last decades, a large number of small molecules with suitable absorption bands, energy levels and gaps have been synthesized.^{4,8,9} Among these, C_{60} and derivatives have shown outstanding electrical properties, therefore big efforts have focused on the finding of suitable

electron donating small molecules such as merocyanines (MCs),¹² phthalocyanines (Pcs),¹³ borondipyrrromethene (BODIPY) dyes,¹⁴ diindenoperylene (DIP)¹⁵ and oligothiophenes¹⁶. As a result, OSCs based on small molecules processed from solution have reached efficiencies over 10 %.^{16,17}

From a chemical point of view, the most challenging part is to control the self-assembly of the nanostructures which exist in the organic active layer of the OSC (Figure 3): that is, the spontaneous compilation of molecules into structured, stable, noncovalently joined aggregates under equilibrium conditions through specific interactions among them.¹⁸ Reaching stable and optimal blending (effective layer) in the final assembly requires the combination of a variety of non-covalent interactions involved in the formation of the self-assembled aggregates, including van der Waals force, hydrogen bonding, π - π interactions and metal coordination. Moreover, such interactions between the donor/acceptor molecules must be more energetically favoured than additional competing interactions, as those provided by the solvent, to overcome degeneration of the ordered new aggregate into disordered or dissociated states (phase separation). However, this type of molecular interactions are significantly weaker than metallic or ionic forces, leading to the formation of localized states on two molecular phases rather than delocalized states, as it could be observed in inorganic semiconductors.¹⁹ In addition, the order in organic materials at the molecular level is limited by a number of factors: symmetry, rigidity, molecular size; the regularity in the monomer orientations; and the functional groups added to their backbones. Such factors, combined with the relatively weak forces between molecules, affect the final packing in the organic blend and as a consequence have severe repercussions on the mechanical, optical and electrical properties of the final organic solar cells.²⁰

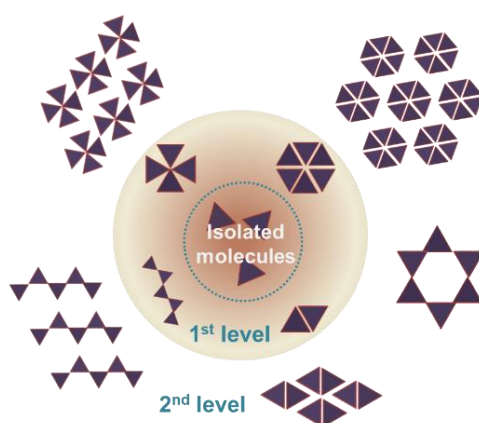


Figure 3. Schematic representation of self-assembly processes in small molecules.

Besides the molecular design and the blend preparation method, it is clear that a thorough characterization of the active materials morphology and properties is necessary to understand its impact on the OSCs performance. Therefore, it is crucial the proper use of techniques which are capable of clarifying the specific relationship between the molecular structure, the active layer morphology and their processing conditions, for improving OSC performance.

1.1.2 Studies of single-molecule electronic performance via mechanically controllable break junction (MCBJ) technique

In 1974, Aviram and Ratner proposed the idea of building an electronic device, a rectifier, by using a single organic molecule as the active component.²¹ Conceptually, this idea was totally different from conventional solid-state semiconductor electronics.

In the creation of molecular nanodevices, from a chemical point of view, organic systems present several advantages: they can be synthesized in large scales at low cost, present small sizes, are chemically designed and therefore suitable for flexible modifications,^{22,23} and capable of introducing additional properties including self-assembly.²⁴ Thus, for the last two decades advanced techniques used to characterize the charge transport across metal-molecule-metal junctions have been developed together with advanced materials to correlate the structures of molecules with their electron transport properties. These studies include crucial points such as the effect of molecular anchoring groups,²⁵ the molecular length dependency with the electronic measurement, and quantum interference effects.²⁶ The sum of these factors is a key step towards the development and future implementation of single-molecule electronic devices.

Regarding the nanodevices, the mechanically controllable break junction (MCBJ) technique is an excellent tool to probe electronic transport through metal-molecule-metal junctions. Figure 4 shows a schematic illustration of a MCBJ set-up and how molecules may contact in the junctions.^{25,27} This technique offers a continuously tuneable gap size between two tip-shaped electrodes by pushing rod to bend/release the substrate. With the vertical movement of the push rod, the metal wire fixed on the substrate starts to elongate and finally completely fractures, resulting in two clean facing nanoelectrodes and the creation of a nanogap.²⁸ To perform the measurements of single molecule conductance, target molecules can be assembled on the electrodes in advance: In our case, we dissolve the molecules in low boiling point solvents and then add them to the nanodevice by drop-casting. After integrating the molecules into the nanogap, they may bridge the two fresh formed electrodes, enabling direct observation of charge transport through the molecules (by the study of I-V curves; current vs. voltage measurements). While repeatedly breaking and fusing two electrodes, the conductance is monitored as a function of the electrode displacement.

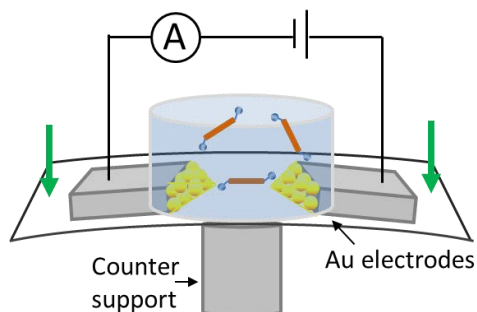


Figure 4. Schematic illustration of the mechanically controllable break junction (MCBJ) device.

The molecular unit can be divided into two parts: the molecular kernel, involving the internal electronic structure, and the anchoring groups, that will link to the metallic contacts (electrodes), which determine the overall performance of the single-molecule electronic device.²⁹ Thus, chemical design and the synthesis of new molecules are crucial for the improvement of the performance of the nanodevice. Electron transport through molecules in nanoscale junctions is sensitive to very small changes related to the atomic configuration. Structural differences in molecular wires, including their anchoring groups, length, conformation and alignment with the Fermi level of the electrodes, as well as the variations in the type of electrode material, different molecular geometries and conformations heavily influence the final electronic properties measured within the metal-molecule-metal junction.^{25,28-35}

1.1.3 Relevant small molecules toward BHJ OSC and MCBJ studies

There are several publications on the potential use of porphyrin derivatives and curcumin derivatives (also called curcuminoids) in organic solar cells^{36,37} and molecular electronics.^{38,39} The main purpose of the present work is the study of both families, by the synthesis of novel molecules, toward their application as active components in BHJ OCs and/or MCBJ experiments.

The most outstanding work regarding solution-processed BHJ OSCs based on small molecules is from the group of X. Peng, using porphyrin derivatives. Since 2012, they have developed a number of effective molecules with porphyrinic cores summarized in Figure 5.⁴⁰⁻⁵⁴ To improve the PCEs of their devices, a series of conjugated donor-acceptor (D-A) groups have been attached to the porphyrin units. In this way, their comparative study between *meso*-alkyl chains and *meso*-phenyl substituents has shown the improvement of the intermolecular charge transport by the increase of intermolecular π - π stacking and porphyrin self-assembly. In a similar way, Emilio Palomares *et al.*^{55,56} designed A- π -D- π -A molecular structures using conjugated donor backbones connected to electron withdrawing terminal groups. Another approach to cover the most of the UV-Vis spectrum is to enhance the absorption characteristics by designing π -extended porphyrin systems with boron-dipyrromethane groups.⁵⁷ In the case of curcuminoid, BHJ OSCs have been built following the same D-A-D design, where the curcuminoid skeleton ends contain triphenylamine groups and have the final molecule coordinated to a boron centre.⁵⁸ The latest work focuses exclusively on the molecular design and intramolecular charge transfer, where the intermolecular self-assembly is not emphasized.

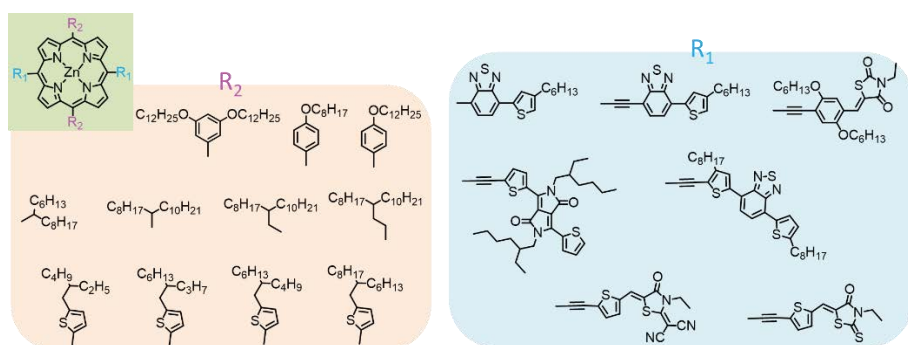


Figure 5. Chemical structures of a family of porphyrins used in BHJ OSCs by the group of X. Peng.

In addition, relatively small and stable aromatic systems are particularly attractive in the field of molecular electronics because their structures are promising for the electronic transport through such molecules in the electrode-molecule-electrode junctions and in several cases their HOMO-LUMO energy gaps are in tune with the Fermi level of the electrodes. In this case, porphyrin and curcumin derivatives are aromatic dyes capable of performing as the active molecular components in electronic devices.^{39,59} Most of the studies with such molecules relate to the effect of anchoring groups for single molecular electronic applications,⁵⁹ and a number of anchoring groups have been investigated using porphyrin derivatives and curcuminoids systems, including amino (-NH₂),^{60,61} cyanide (-CN),⁶² thiophene,^{63,64} pyridyl (-PY),^{59,65} thiol (-SH),⁶⁶⁻⁶⁸ isothiocyanide (-SCN),⁶⁹ methyl sulphide (-SMe),⁷⁰ hydroxyl (-OH),⁷¹ carbodithiolate,⁷² and thiochroman-based moieties.^{71,73}

1.2 Porphyrin

Nature uses chlorophylls in plants to harvest light for the conversion of solar energy.¹ Artificial chlorophylls, therefore porphyrin derivatives, have intrigued chemists for more than one century now for a number of reasons.^{2,3} Porphyrins, as it is shown in Figure 6, are heterocyclic macrocycle organic systems, composed of four modified pyrrole subunits interconnected through their α carbon atoms via methine bridges (=CH-). This core is called porphine (Figure 6 left), and substituted porphines are named porphyrins. Different families of β and *meso*-substituted porphyrins have been studied together with metalloporphyrins.⁷⁴

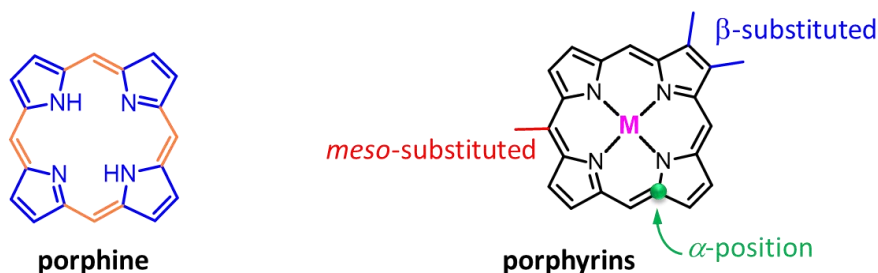


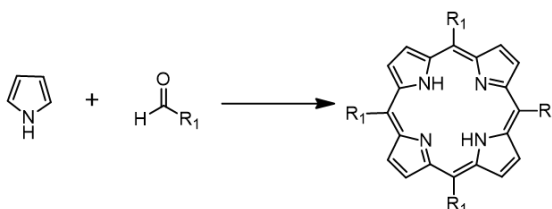
Figure 6. Chemical structures of porphine and general description of the constituent parts in porphyrins.

Because of their structure, and electronic and redox properties, porphyrins are studied towards their use in molecular electronics and photonics. The absorption bands in porphyrin display an intense Soret band at 400-450 nm and moderate Q bands at 500-700 nm. UV-Vis absorption spectrometry is an excellent technique to determine porphyrinic nature as well as to identify coordination of the final porphyrins and the effects of substituents by the relative changes in energy of those transitions. The physical properties of porphyrins can be appropriately tuned by synthetically modifying the substituents of the macrocyclic ring and/or the coordination to a metal ion in the central cavity.

There are two common routes to achieve porphyrin derivatives with substituents at different positions:

(1) "4+4" method. Condensation method involving pyrrole and aldehyde groups.

The classic methods to achieve porphyrins are Adler-Longo method^{75,76} and Lindsey method^{77,78} (Scheme 1). The former is developed from the Rothmund reaction,⁷⁹⁻⁸¹ allowing pyrrole and aldehyde molecules to react for few hours in refluxing propionic acid. The latter, Lindsey method, is an acid-catalysed condensation of pyrrole with aldehyde at room temperature to obtain chlorin core first, followed by an oxidation process, with an electron-deficient quinone such as p-chloranil and 2,3-Dichloro-5,6-dicyano-1,4-benzoquinone (DDQ).



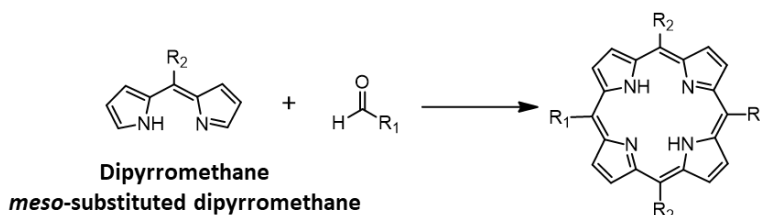
Alder-Longo method: refluxing propionic acid (141 °C)

Lindsey method: (i)BF₃·OEt₂, CH₂Cl₂, r.t.; (ii)DDQ

Scheme 1. "4+4" porphyrin synthesis by Adler-Longo and Lindsey method.

(2) "2+2" method. Condensation method involving dipyrromethane and aldehyde groups.

Direct approaches to *trans*-substituted porphyrins are provided by the condensation of dipyrromethanes with aldehyde molecules (Scheme 2). Asymmetrically substituted porphyrins are synthesized employing a variety of dipyrromethene units. As in the "4+4" method, the "2+2" synthesis could be carried out under heating⁸² or at room temperature.⁸³⁻⁸⁵



Scheme 2. General scheme of the "2+2" methodology.

There are additional methods to carry out the synthesis of porphyrins, such as those involving the use of tripyrrolic intermediates, specially employed in the synthesis of porphyrin analogues with one or two furan or thiophene sub-units.⁸⁶ Also, β -substituted porphyrins could

be obtained by the methods described above, by changing the start materials, pyrrole and dipyrromethene, for β -substituted derivatives.

Metalloporphyrins are synthesized through the reaction of the porphyrin system with a metallic salt under heating.⁸⁷ The solvent should provide reasonable solubility for both, the porphyrin and metal ion, "free" forms under the reaction conditions, being the most commonly used methanol (CH₃OH), ethanol (EtOH), propanol (PrOH), tetrahydrofuran (THF), or high boiling point solvents such as dimethyl sulfoxide (DMSO) and N, N'-dimethylformamide (DMF).

Due to the functional groups at the periphery of the macrocycles and the coordination of metal ions in the core, porphyrins present a strong ability for self-assembly, where highly ordered aggregations could be constructed in solution or crystalline solid phases on surfaces, which are widely used in molecular materials.^{88,89}

Regarding this section, this thesis focuses on the design and synthesis of functional porphyrins for the potential applications in OSCs and molecular electronics, with emphasis on the self-assembly ability of the designed molecules by the study of their crystal structures and deposition on surfaces.

1.3 Curcuminoids

Curcumin (CCM) is a bright yellow natural occurring molecule produced by the plant *Curcuma longa*, being the principal curcuminoid constituent (up to ~9%) of turmeric acid. Since Vogel and Pierre Joseph Pelletier firstly isolated this "yellow colouring-matter" and named it curcumin in 1815, the extraction and purification of CCM from turmeric has been widely studied.⁹⁰ Even though Lamper *et al.*⁹¹ elucidated the molecular structure in 1910, it was not until 1964 that H. J. J. Pabon⁹² optimized the reaction factors to achieve pure curcumin in high yields, which was the foundation of most of the curcuminoids synthesized nowadays.

Curcumin (1,7-bis-(4-hydroxy-3-methoxyphenyl)-1,6-heptadiene-3,5-dione) can be described as two aromatic groups connected through a conjugated alkyl chain that contains a diketone central moiety (Figure 7). Curcumin could present tautomeric equilibrium between the enol- and keto- forms as Figure 7 illustrates. The phenolic groups at the ends provide the molecule with additional reactivity points.



Figure 7. Chemical structures of curcumin and its enol-keto tautomerism.

In Asian countries, turmeric is well-known as herbal supplement to treat various illnesses such as rheumatism, skin diseases, diarrhoea, intermittent fevers and colic.⁹³⁻⁹⁵ Also,

pharmacological activities of CCM as anti-oxidant, anti-inflammatory,⁹³ anti-virus and anti-tumoral agent have been demonstrated.^{94,95} Nevertheless, successful clinical trials of CCM are still in progress.⁹⁶ Nowadays, research about CCM and curcuminoids (CCMoids) focus on the improvement of their properties for biological purposes and exploring their application in different fields. CCMoids can demonstrate relevant structural changes of the basic curcumin system, with a number of variations present in the so-called head, body, arms and leg, respectively, as Figure 8 shows.

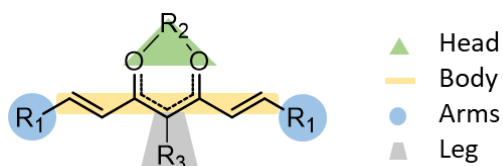
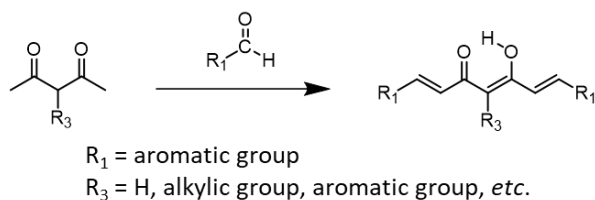


Figure 8. Description of the parts of a curcuminoid molecule.

The number of possible modifications that the CCMoids molecules can present in their four different parts opens new opportunities to create curcuminoids-based multifunctional systems. In this way, the body can be shortening (having acac derivatives) or elongated (containing 11 C atoms instead of 7 in the chain),⁹⁷ displaying changes in their electronic absorption and oxidation potentials.⁹⁸ Aromatic substituents, such as phenyl, anthracene,⁹⁹ thiophenyl⁶³ and pyridyl groups, among others, have been used in the arm positions. Introduction of functional legs expands the properties of curcuminoids, such as biological activities with pharmaceutical applications;¹⁰⁰ moreover, a leg can be seen as a new reactive point providing the opportunity of reacting with other organic molecules to create more complex structures¹⁰¹ or to be attached on surfaces or nanoparticles (e.g.: silicon wafers and nanoparticles) applied in the field of optoelectronics. Additional variations can be attempted by reacting the β -diketone moiety (e.g.: curcuminoxime, curcuminsemi-carbazone and curcumin-thiosemicarbazone). The β -diketone can also be modified using electron-rich groups as pyrazole or isoxazole aromatic species.¹⁰² Furthermore, a series of metal/metalloid compounds, containing Cu(II), Zn(II) and B(III) ions have been successfully synthesized by the coordination of the former with diketone¹⁰³ and diketimine¹⁰⁴ moieties, demonstrating the extending possibilities of modification of the curcuminoids.

Most symmetric curcuminoids could be synthesized from β -diketone acac derivatives (Scheme 3) employing the already mentioned Pabon's method.⁹² In a first step, an acetylacetonate-boron compound is formed to prevent Knoevenagel condensation on the methylene group, activating this way the methyl positions of 2,4-pentanedione by the aldol condensation with aromatic aldehyde molecules. The release of the free ligand from the boron centre is performed by the addition of a dilute acid aqueous solution,¹⁰⁵ or in some cases, by the addition of pure water.⁹⁹ straightforward synthesis and the average low cost of this methodology make it promising with regards to organic molecules synthesis.



Scheme 3. General steps for the synthesis of symmetric curcumin analogues.

Coordination compounds containing CCM or CCMoids as ligands have been achieved with most of the elements from the periodic table within the past 20 years.¹⁰⁶ Among the main elements, boron derivatives is by far the most investigated,¹⁰⁷ followed by copper, zinc, nickel, iron centres. Metallo-CCMoids normally involves deprotonation of the free CCMoid by a suitable base such as potassium hydroxide,¹⁰⁸ sodium hydroxide,¹⁰⁹ or triethylamine.¹¹⁰ Then, the addition of the corresponding metal or metalloid salt, in the appropriate molar ratios, give rise to the final coordination compound leading to homoleptic or heteroleptic structures (Figure 9). Most of the metallo-CCMoids described so far are the homoleptic type. The heteroleptic compounds only contain one CCMoid per metal atom combined with other co-ligands (“spectator ligands”) mainly bi- and tridentate N-donor ligands (e.g.: 2,2'-bipyridine, phenanthroline and terpyridine and derivatives).¹¹¹⁻¹¹⁴

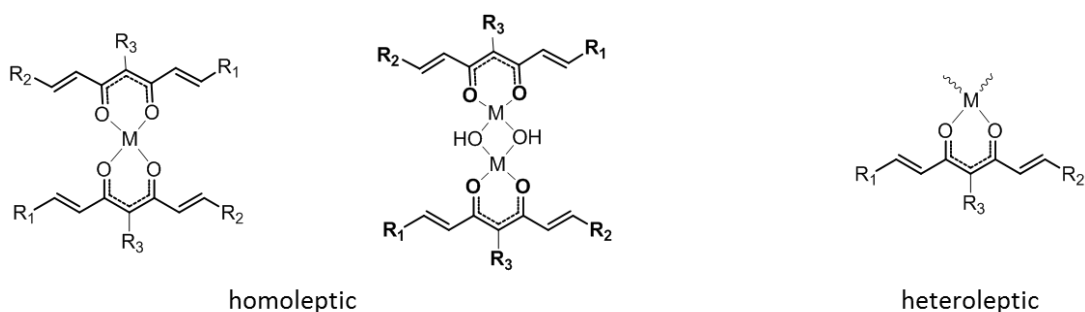


Figure 9. Schematic drawing of the metallo-CCMoids.

CCMoids modifications have been achieved by the organic conventional synthesis or by Pabon's.⁹² However, owing to the simplicity, high rates and environment friendly, the use of microwave in organic synthesis has become very popular,¹¹⁵ and numerous cyclic analogues of curcumin have been achieved by microwave-assisted synthesis under solvent-free conditions in excellent yields.¹¹⁶ For the creation of metallo-CCMoids, microwave reaction is also noteworthy. For example, a variety of anthracene-based curcuminoids compounds have been obtained with metals such as Mg(II) and Co(II),^{117,118} and crystals could be directly isolated from the final solutions.

Taking into account that the versatile chemistry described for CCMoids and metallo-CCMoids, the creation of functional CCMoid materials is a developing research. From

applications except the biological subject, the oldest known is the use of CCMoids as sensors of boron.¹¹⁹ In addition, they have been postulated as molecular-based logic gates¹²⁰ and the fluorescent single-molecule magnets have been achieved.¹¹⁸ In the recent years, CCM has been used towards the creation of MOFs.¹²¹ In the molecular electronics field, after depositing curcuminoids molecules onto few-layer graphene electrodes¹²² or gold electrodes⁶³ the conductance properties of the single molecules have been established, which is the central task for developing reliable molecular electronic devices. Finally, boron difluoride compounds included in BHJ OSCs have shown a power conversion efficiency of 4.14%.¹²³

In this sense, this thesis also emphasises on the design, synthesis and characterization of functional curcuminoids for their applications in the field of molecular electronics and MOFs.

References:

- (1) Otsuki, J. *Journal of Materials Chemistry A* **2018**.
- (2) Panda, M. K.; Ladomenou, K.; Coutsolelos, A. G. *Coordination Chemistry Reviews* **2012**, 256, 2601.
- (3) Frischmann, P. D.; Mahata, K.; Würthner, F. *Chemical Society Reviews* **2013**, 42, 1847.
- (4) Walker, B.; Kim, C.; Nguyen, T.-Q. *Chemistry of Materials* **2010**, 23, 470.
- (5) Yu, G.; Gao, J.; Hummelen, J. C.; Wu, F.; Heeger, A. J. *Science* **1995**, 270, 1789.
- (6) Li, G.; Zhu, R.; Yang, Y. *Nature photonics* **2012**, 6, 153.
- (7) Li, Y.; Guo, Q.; Li, Z.; Pei, J.; Tian, W. *Energy & Environmental Science* **2010**, 3, 1427.
- (8) Mishra, A.; Bäuerle, P. *Angewandte Chemie International Edition* **2012**, 51, 2020.
- (9) Moench, T.; Koerner, C.; Murawski, C.; Murawski, J.; Nikolis, V. C.; Vandewal, K.; Leo, K. In *Molecular Devices for Solar Energy Conversion and Storage*; Springer: 2018, p 1.
- (10) Brabec, C. J.; Durrant, J. R. *Mrs Bulletin* **2008**, 33, 670.
- (11) Lin, J. D.; Mikhnenko, O. V.; Chen, J.; Masri, Z.; Ruseckas, A.; Mikhailovsky, A.; Raab, R. P.; Liu, J.; Blom, P. W.; Loi, M. A. *Materials Horizons* **2014**, 1, 280.
- (12) Kronenberg, N. M.; Deppisch, M.; Würthner, F.; Lademann, H. W.; Deing, K.; Meerholz, K. *Chemical Communications* **2008**, 6489.
- (13) Terao, Y.; Sasabe, H.; Adachi, C. *Applied Physics Letters* **2007**, 90, 103515.
- (14) Rousseau, T.; Cravino, A.; Bura, T.; Ulrich, G.; Ziessel, R.; Roncali, J. *Chemical Communications* **2009**, 1673.
- (15) Gruber, M.; Rawolle, M.; Wagner, J.; Magerl, D.; Hörmann, U.; Perlich, J.; Roth, S.; Opitz, A.; Schreiber, F.; Müller-Buschbaum, P. *Advanced energy materials* **2013**, 3, 1075.
- (16) Kan, B.; Li, M.; Zhang, Q.; Liu, F.; Wan, X.; Wang, Y.; Ni, W.; Long, G.; Yang, X.; Feng, H. *Journal of the American Chemical Society* **2015**, 137, 3886.

- (17) Liu, Y.; Chen, C.-C.; Hong, Z.; Gao, J.; Yang, Y. M.; Zhou, H.; Dou, L.; Li, G.; Yang, Y. *Scientific reports* **2013**, *3*, 3356.
- (18) Whitesides, G. M.; Mathias, J. P.; Seto, C. T. *Science* **1991**, *254*, 1312.
- (19) Brédas, J.-L.; Calbert, J. P.; da Silva Filho, D.; Cornil, J. *Proceedings of the National Academy of Sciences* **2002**, *99*, 5804.
- (20) Noriega-Manez, R. J., Stanford University, 2012.
- (21) Aviram, A.; Ratner, M. A. *Chemical Physics Letters* **1974**, *29*, 277.
- (22) Ernzerhof, M.; Zhuang, M.; Rocheleau, P. *The Journal of chemical physics* **2005**, *123*, 134704.
- (23) Otsubo, T.; Aso, Y.; Takimiya, K. *Journal of Materials Chemistry* **2002**, *12*, 2565.
- (24) Joachim, G.; Gimzewski, J.; Aviram, A. *Nature* **2000**, *408*, 541.
- (25) Kaliginedi, V.; Rudnev, A. V.; Moreno-García, P.; Baghernejad, M.; Huang, C.; Hong, W.; Wandlowski, T. *Physical Chemistry Chemical Physics* **2014**, *16*, 23529.
- (26) Tomfohr, J. K.; Sankey, O. F. *Physical Review B* **2002**, *65*, 245105.
- (27) Perrin, M. L.; Verzijl, C. J.; Martin, C. A.; Shaikh, A. J.; Eelkema, R.; Van Esch, J. H.; Van Ruitenbeek, J. M.; Thijssen, J. M.; Van Der Zant, H. S.; Dulić, D. *Nature nanotechnology* **2013**, *8*, 282.
- (28) Xiang, D.; Jeong, H.; Lee, T.; Mayer, D. *Advanced Materials* **2013**, *25*, 4845.
- (29) Sun, L.; Diaz-Fernandez, Y. A.; Gschneidner, T. A.; Westerlund, F.; Lara-Avila, S.; Moth-Poulsen, K. *Chemical Society Reviews* **2014**, *43*, 7378.
- (30) Song, H.; Reed, M. A.; Lee, T. *Advanced Materials* **2011**, *23*, 1583.
- (31) Huang, C.; Rudnev, A. V.; Hong, W.; Wandlowski, T. *Chemical Society Reviews* **2015**, *44*, 889.
- (32) Wang, L.; Wang, L.; Zhang, L.; Xiang, D. *Topics in Current Chemistry* **2017**, *375*, 61.
- (33) Su, T. A.; Neupane, M.; Steigerwald, M. L.; Venkataraman, L.; Nuckolls, C. *Nature Reviews Materials* **2016**, *1*, 16002.
- (34) Zhang, J. L.; Zhong, J. Q.; Lin, J. D.; Hu, W. P.; Wu, K.; Xu, G. Q.; Wee, A. T.; Chen, W. *Chemical Society Reviews* **2015**, *44*, 2998.
- (35) Xiang, D.; Wang, X.; Jia, C.; Lee, T.; Guo, X. *Chem. Rev* **2016**, *116*, 4318.
- (36) Walter, M. G.; Rudine, A. B.; Wamser, C. C. *Journal of Porphyrins and Phthalocyanines* **2010**, *14*, 759.
- (37) Kesters, J.; Verstappen, P.; Kelchtermans, M.; Lutsen, L.; Vanderzande, D.; Maes, W. *Advanced Energy Materials* **2015**, *5*.
- (38) Burrell, A. K.; Wasielewski, M. R. *Journal of Porphyrins and Phthalocyanines* **2000**, *4*, 401.
- (39) Jurow, M.; Schuckman, A. E.; Batteas, J. D.; Drain, C. M. *Coordination chemistry reviews* **2010**, *254*, 2297.
- (40) Huang, Y.; Li, L.; Peng, X.; Peng, J.; Cao, Y. *Journal of Materials Chemistry* **2012**, *22*, 21841.
- (41) Li, L.; Huang, Y.; Peng, J.; Cao, Y.; Peng, X. *Journal of Materials Chemistry A* **2013**, *1*, 2144.
- (42) Li, L.; Huang, Y.; Peng, J.; Cao, Y.; Peng, X. *Organic Electronics* **2013**, *14*, 3430.
- (43) Qin, H.; Li, L.; Guo, F.; Su, S.; Peng, J.; Cao, Y.; Peng, X. *Energy & Environmental Science* **2014**, *7*, 1397.
- (44) Chen, S.; Xiao, L.; Zhu, X.; Peng, X.; Wong, W.-K.; Wong, W.-Y. *Chemical Communications* **2015**, *51*, 14439.
- (45) Gao, K.; Li, L.; Lai, T.; Xiao, L.; Huang, Y.; Huang, F.; Peng, J.; Cao, Y.; Liu, F.; Russell, T. P. *Journal of the American Chemical Society* **2015**, *137*, 7282.
- (46) Li, L.; Xiao, L.; Qin, H.; Gao, K.; Peng, J.; Cao, Y.; Liu, F.; Russell, T. P.; Peng, X. *ACS applied materials & interfaces* **2015**, *7*, 21495.

- (47) Gao, K.; Miao, J.; Xiao, L.; Deng, W.; Kan, Y.; Liang, T.; Wang, C.; Huang, F.; Peng, J.; Cao, Y. *Advanced Materials* **2016**, *28*, 4727.
- (48) Gao, K.; Xiao, L.; Kan, Y.; Yang, B.; Peng, J.; Cao, Y.; Liu, F.; Russell, T. P.; Peng, X. *Journal of Materials Chemistry C* **2016**, *4*, 3843.
- (49) Liang, T.; Xiao, L.; Liu, C.; Gao, K.; Qin, H.; Cao, Y.; Peng, X. *Organic Electronics* **2016**, *29*, 127.
- (50) Nian, L.; Gao, K.; Liu, F.; Kan, Y.; Jiang, X.; Liu, L.; Xie, Z.; Peng, X.; Russell, T. P.; Ma, Y. *Advanced Materials* **2016**, *28*, 8184.
- (51) Wang, H.; Xiao, L.; Yan, L.; Chen, S.; Zhu, X.; Peng, X.; Wang, X.; Wong, W.-K.; Wong, W.-Y. *Chemical Science* **2016**, *7*, 4301.
- (52) Xiao, L.; Chen, S.; Gao, K.; Peng, X.; Liu, F.; Cao, Y.; Wong, W.-Y.; Wong, W.-K.; Zhu, X. *ACS applied materials & interfaces* **2016**, *8*, 30176.
- (53) Li, M.; Gao, K.; Wan, X.; Zhang, Q.; Kan, B.; Xia, R.; Liu, F.; Yang, X.; Feng, H.; Ni, W. *Nature Photonics* **2017**, *11*, 85.
- (54) Liang, T.; Xiao, L.; Gao, K.; Xu, W.; Peng, X.; Cao, Y. *ACS applied materials & interfaces* **2017**, *9*, 7131.
- (55) Kumar, C. V.; Cabau, L.; Koukaras, E. N.; Sharma, A.; Sharma, G. D.; Palomares, E. *Journal of Materials Chemistry A* **2015**, *3*, 16287.
- (56) Kumar, C. V.; Cabau, L.; Koukaras, E. N.; Sharma, G. D.; Palomares, E. *Nanoscale* **2015**, *7*, 179.
- (57) Sharma, G. D.; Siddiqui, S.; Nikiforou, A.; Zervaki, G. E.; Georgakaki, I.; Ladomenou, K.; Coutsolelos, A. G. *Journal of Materials Chemistry C* **2015**, *3*, 6209.
- (58) Archet, F.; Yao, D.; Chambon, S.; Abbas, M.; D'aléo, A.; Canard, G.; Ponce-Vargas, M.; Zaborova, E.; Le Guennic, B.; Wantz, G. *ACS Energy Letters* **2017**, *2*, 1303.
- (59) Li, Z.; Smeu, M.; Ratner, M. A.; Borguet, E. *The Journal of Physical Chemistry C* **2013**, *117*, 14890.
- (60) Hybertsen, M. S.; Venkataraman, L.; Klare, J. E.; Whalley, A. C.; Steigerwald, M. L.; Nuckolls, C. *Journal of Physics: Condensed Matter* **2008**, *20*, 374115.
- (61) Sivanesan, A.; John, S. A. *Langmuir* **2008**, *24*, 2186.
- (62) Mishchenko, A.; Zotti, L. A.; Vonlanthen, D.; Bürkle, M.; Pauly, F.; Cuevas, J. C.; Mayor, M.; Wandlowski, T. *Journal of the American Chemical Society* **2010**, *133*, 184.
- (63) Etcheverry-Berríos, A.; Olavarría, I.; Perrin, M. L.; Díaz-Torres, R.; Jullian, D.; Ponce, I.; Zagal, J. H.; Pavez, J.; Vásquez, S. O.; van der Zant, H. S. *Chemistry-A European Journal* **2016**, *22*, 12808.
- (64) Takahashi, H.; Kanehara, M.; Teranishi, T. *Journal of Photopolymer Science and Technology* **2007**, *20*, 133.
- (65) Sedghi, G.; Esdaile, L. J.; Anderson, H. L.; Martin, S.; Bethell, D.; Higgins, S. J.; Nichols, R. J. *Advanced Materials* **2012**, *24*, 653.
- (66) Perrin, M. L.; Prins, F.; Martin, C. A.; Shaikh, A. J.; Eelkema, R.; van Esch, J. H.; Briza, T.; Kaplanek, R.; Kral, V.; van Ruitenbeek, J. M. *Angewandte Chemie International Edition* **2011**, *50*, 11223.
- (67) Perrin, M. L.; Martin, C. A.; Prins, F.; Shaikh, A. J.; Eelkema, R.; van Esch, J. H.; van Ruitenbeek, J. M.; van der Zant, H. S.; Dulić, D. *Beilstein journal of nanotechnology* **2011**, *2*, 714.
- (68) Al-Galiby, Q. H.; Sadeghi, H.; Algharagholi, L. A.; Grace, I.; Lambert, C. *Nanoscale* **2016**, *8*, 2428.
- (69) Han, W.; Li, S.; Lindsay, S.; Gust, D.; Moore, T. A.; Moore, A. L. *Langmuir* **1996**, *12*, 5742.
- (70) Imahori, H.; Ozawa, S.; Ushida, K.; Takahashi, M.; Azuma, T.; Ajavakom, A.; Akiyama, T.; Hasegawa, M.; Taniguchi, S.; Okada, T. *Bulletin of the Chemical Society of Japan* **1999**, *72*, 485.
- (71) Tanaka, Y.; Kiguchi, M.; Akita, M. *Chemistry-A European Journal* **2017**, *23*, 4741.

- (72) Li, Z.; Smeu, M.; Park, T.-H.; Rawson, J.; Xing, Y.; Therien, M. J.; Ratner, M. A.; Borguet, E. *Nano letters* **2014**, *14*, 5493.
- (73) Liu, Z.-F.; Wei, S.; Yoon, H.; Adak, O.; Ponce, I.; Jiang, Y.; Jang, W.-D.; Campos, L. M.; Venkataraman, L.; Neaton, J. B. *Nano letters* **2014**, *14*, 5365.
- (74) Smith, K. M. *Porphyryns and metalloporphyryns*; Elsevier Amsterdam, 1975; Vol. 9.
- (75) Adler, A. D.; Longo, F. R.; Shergalis, W. *Journal of the American Chemical Society* **1964**, *86*, 3145.
- (76) Adler, A. D.; Longo, F. R.; Finarelli, J. D.; Goldmacher, J.; Assour, J.; Korsakoff, L. *The Journal of Organic Chemistry* **1967**, *32*, 476.
- (77) Lindsey, J. S.; Schreiman, I. C.; Hsu, H. C.; Kearney, P. C.; Marguerettaz, A. M. *The Journal of Organic Chemistry* **1987**, *52*, 827.
- (78) Lindsey, J. S.; Wagner, R. W. *The Journal of Organic Chemistry* **1989**, *54*, 828.
- (79) Rothmund, P. *Journal of the American Chemical Society* **1935**, *57*, 2010.
- (80) Rothmund, P. *Journal of the American Chemical Society* **1936**, *58*, 625.
- (81) Rothmund, P. *Journal of the American Chemical Society* **1939**, *61*, 2912.
- (82) Arsenault, G.; Bullock, E.; MacDonald, S. *Journal of the American Chemical Society* **1960**, *82*, 4384.
- (83) Lee, C.-H.; Lindsey, J. S. *Tetrahedron* **1994**, *50*, 11427.
- (84) Young, R.; Chang, C. K. *Journal of the American Chemical Society* **1985**, *107*, 898.
- (85) Lindsey, J. S. *Accounts of chemical research* **2009**, *43*, 300.
- (86) Lash, T. D. *Chemistry—A European Journal* **1996**, *2*, 1197.
- (87) Adler, A. D.; Longo, F. R.; Kampas, F.; Kim, J. *Journal of Inorganic and Nuclear Chemistry* **1970**, *32*, 2443.
- (88) He, Y.; Ye, T.; Borguet, E. *Journal of the American Chemical Society* **2002**, *124*, 11964.
- (89) Wang, Z.; Li, Z.; Medforth, C. J.; Shelnutt, J. A. *Journal of the American Chemical Society* **2007**, *129*, 2440.
- (90) Jackson, C. L.; Menke, A. In *Proceedings of the American Academy of Arts and Sciences*; JSTOR: 1881; Vol. 17, p 110.
- (91) Lampe, V.; Milobedzka, J.; Kostaneski, V. *Ber Deutsch Chem Ges* **1910**, *43*, 2163.
- (92) Pabon, H. *Recueil des Travaux Chimiques des Pays-Bas* **1964**, *83*, 379.
- (93) Menon, V. P.; Sudheer, A. R. In *The molecular targets and therapeutic uses of curcumin in health and disease*; Springer: 2007, p 105.
- (94) Pari, L.; Tewas, D.; Eckel, J. *Archives of physiology and biochemistry* **2008**, *114*, 127.
- (95) Kocaadam, B.; Şanlıer, N. *Critical reviews in food science and nutrition* **2017**, *57*, 2889.
- (96) Nelson, K. M.; Dahlin, J. L.; Bisson, J.; Graham, J.; Pauli, G. F.; Walters, M. A. *Journal of medicinal chemistry* **2017**, *60*, 1620.
- (97) Burzurí, E.; Island, J. O.; Díaz-Torres, R.; Fursina, A.; González-Campo, A. n.; Roubeau, O.; Teat, S. J.; Aliaga-Alcalde, N. r.; Ruiz, E.; van der Zant, H. S. *ACS nano* **2016**, *10*, 2521.
- (98) Gao, P.; Tsao, H. N.; Yi, C.; Grätzel, M.; Nazeeruddin, M. K. *Advanced Energy Materials* **2014**, *4*.
- (99) Aliaga-Alcalde, N.; Marqués-Gallego, P.; Kraaijkamp, M.; Herranz-Lancho, C.; den Dulk, H.; Görner, H.; Roubeau, O.; Teat, S. J.; Weyhermüller, T.; Reedijk, J. *Inorganic chemistry* **2010**, *49*, 9655.
- (100) Lin, L.; Shi, Q.; Su, C.-Y.; Shih, C. C.-Y.; Lee, K.-H. *Bioorganic & medicinal chemistry* **2006**, *14*, 2527.
- (101) Ayyagari, N.; Jose, D.; Mobin, S. M.; Namboothiri, I. N. *Tetrahedron letters* **2011**, *52*, 258.
- (102) Amolins, M. W.; Peterson, L. B.; Blagg, B. S. *Bioorganic & medicinal chemistry* **2009**, *17*, 360.

- (103) Ran, C.; Xu, X.; Raymond, S. B.; Ferrara, B. J.; Neal, K.; Bacskai, B. J.; Medarova, Z.; Moore, A. *Journal of the American Chemical Society* **2009**, *131*, 15257.
- (104) Annaraj, J.; Srinivasan, S.; Ponvel, K.; Athappan, P. *Journal of inorganic biochemistry* **2005**, *99*, 669.
- (105) Ferrari, E.; Pignedoli, F.; Imbriano, C.; Marverti, G.; Basile, V.; Venturi, E.; Saladini, M. *Journal of medicinal chemistry* **2011**, *54*, 8066.
- (106) Wanninger, S.; Lorenz, V.; Subhan, A.; Edelmann, F. T. *Chemical Society Reviews* **2015**, *44*, 4986.
- (107) Sui, Z.; Salto, R.; Li, J.; Craik, C.; de Montellano, P. R. O. *Bioorganic & medicinal chemistry* **1993**, *1*, 415.
- (108) Aliaga-Alcalde, N. r.; Rodríguez, L.; Ferbinteanu, M.; Höfer, P.; Weyhermüller, T. *Inorganic chemistry* **2011**, *51*, 864.
- (109) Zhou, S.-S.; Xue, X.; Wei, D.; Jiang, B.; Wang, J.-F.; Lu, C.-H. *Chemical Research in Chinese Universities* **2012**, *28*, 647.
- (110) Pucci, D.; Crispini, A.; Mendiguchía, B. S.; Pirillo, S.; Ghedini, M.; Morelli, S.; De Bartolo, L. *Dalton Transactions* **2013**, *42*, 9679.
- (111) Mendiguchia, B. S.; Aiello, I.; Crispini, A. *Dalton Transactions* **2015**, *44*, 9321.
- (112) Pucci, D.; Bellini, T.; Crispini, A.; D'Agnano, I.; Liguori, P. F.; Garcia-Orduna, P.; Pirillo, S.; Valentini, A.; Zanchetta, G. *MedChemComm* **2012**, *3*, 462.
- (113) Shahabadi, N.; Falsafi, M.; Moghadam, N. H. *Journal of Photochemistry and Photobiology B: Biology* **2013**, *122*, 45.
- (114) Hussain, A.; Somyajit, K.; Banik, B.; Banerjee, S.; Nagaraju, G.; Chakravarty, A. R. *Dalton Transactions* **2013**, *42*, 182.
- (115) de la Hoz, A.; Diaz-Ortiz, A.; Moreno, A. *Chemical Society Reviews* **2005**, *34*, 164.
- (116) Nichols, C. E.; Youssef, D.; Harris, R. G.; Jha, A. *Arkivoc* **2006**, *13*, 64.
- (117) Menelaou, M.; Weyhermüller, T.; Soler, M.; Aliaga-Alcalde, N. *Polyhedron* **2013**, *52*, 398.
- (118) Díaz-Torres, R.; Menelaou, M.; Roubeau, O.; Sorrenti, A.; Brandariz-de-Pedro, G.; Sañudo, E. C.; Teat, S. J.; Fraxedas, J.; Ruiz, E.; Aliaga-Alcalde, N. *Chemical Science* **2016**, *7*, 2793.
- (119) Aznarez, J.; Bonilla, A.; Vidal, J. *Analyst* **1983**, *108*, 368.
- (120) Kim, S.-H.; Gwon, S.-Y.; Burkinshaw, S.; Son, Y.-A. *Spectrochimica Acta Part A: Molecular and Biomolecular Spectroscopy* **2010**, *76*, 384.
- (121) Su, H.; Sun, F.; Jia, J.; He, H.; Wang, A.; Zhu, G. *Chemical Communications* **2015**, *51*, 5774.
- (122) Prins, F.; Barreiro, A.; Ruitenber, J. W.; Seldenthuis, J. S.; Aliaga-Alcalde, N.; Vandersypen, L. M.; van der Zant, H. S. *Nano letters* **2011**, *11*, 4607.
- (123) Archet, F.; Yao, D.; Chambon, S.; Abbas, M.; D'Aléo, A.; Canard, G.; Ponce-Vargas, M.; Zaborova, E.; Le Guennic, B.; Wantz, G. *ACS Energy Letters* **2017**, *2*, 1303.

Chapter II

Boosting self-assembly diversity of
chiral/achiral acetate-based Zn(II)
porphyrins

2.1 Introduction

In the fields of solution-processed bulk heterojunction (BHJ) organic solar cells (OSCs), small organic molecules (SMs) used as components of the active layer materials have drawn a great deal of attention due to their potential advantages: high purity, defined structure and easily reproduced synthesis and modifications. It's known that the performances of BHJ-OSCs often depend on the processing conditions, which mainly affect the non-covalent intermolecular interactions of the active materials and the overall morphology of the film. Comparing to polymers which have extended π -conjugated system, it is still a challenge for small molecules to create ordered films with high hole mobilities; in part, this is because of the formation of amorphous or disordered morphologies during the solution processing.

In an ideal BHJ, donor and acceptor domains should display in order, which size closely related to the diffusion length of the excitons.¹ In the case of small molecules, the control rely on the modulation of the molecular structure, optimization of the device architecture and material processing conditions. The first strategy is important as it affects not only processing but also self-assembly toward the achievement of ordered domains. Besides, it leads the fundamental material properties of organic electronic systems such as light absorption, molecular energy level, conjugation length and process-ability. On the other hand, the structural diversity and functionally intriguing supramolecular self-assembly observed in nature have inspired the search and design of molecular based materials.^{2,3} For example, bacteriochlorophyll c, a porphyrin derivative, is the key component in the light-harvesting organelles of green photosynthetic bacteria.⁴

Ruling the self-assembly process, by controlling non-covalent intermolecular interactions (H-bonding, π - π stacking and weak coordination bonding)⁵⁻⁷ to achieve proposed functional products are challenging works due to the diversity of the arrangements and the lack of reversibility. In this regard, porphyrins are excellent molecular candidates for organic photovoltaic devices due to their conjugated structures and supramolecular assembly capabilities.⁸ We can ensure porphyrin based self-assembly, because of the sum of its manifold features: (i) conjugated core, that has given copious studies with plenty of data regarding the formation of H/J aggregates;⁹ (ii) coordination to metallic centres, that provide additional interactive sites in the final metalloporphyrin¹⁰ and (iii) the addition of organic groups in the *meso*-positions of the tetrapyrrolic units, that afford extra interactions depending on their number and nature.^{2,11} A typical example for the organization of porphyrins is shown in Figure 1, where ferrocene-bridged Zn trisporphyrins form dimer rings that could be transformed into linear porphyrin units by the coordination of pyridine molecules from the solvent, and a series of porphyrin macrocycles appear from trimer to decamer when ethanol is used instead.¹¹

respectively (Figure 3), presenting chiral and achiral moieties on the final molecules. Based on the previous experiences with related systems,^{16,20-23} and foreseen the rich molecular recognition capacity and tendency to organize in solution of these metalloporphyrins, a complete study related to non-covalent multiporphyrin assemblies has been performed.

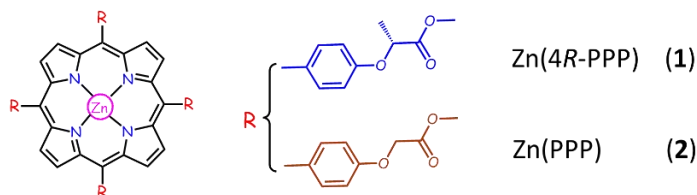


Figure 3. General scheme of the disposition of the arms in the *meso*-porphyrins involving phenoxy propanoate (**1**) and methyl 2-phenoxy acetate groups (**2**) respectively.

To explore the self-assembly structures of our molecules caused by the solution process, we restricted the recrystallization methods for the chiral/achiral Zn-porphyrin systems; this allowed new findings in the solid state primarily by the use of single crystal X-ray diffraction. Slow liquid-liquid diffusion method for crystal growth represented in Figure 4, and the solvent effect for the porphyrin organization study could be done by varying the mixture system: CH₂Cl₂/CH₃OH, CH₂Cl₂/n-hexane and THF/n-hexane. With regards to the porphyrin moiety, phenoxy propanoate and methyl 2-phenoxy acetate groups, as directing substituents at the *meso*-positions, are the active sites in the supramolecular rearrangements, displaying weak intermolecular forces or via coordinative bonding with the Zn(II) centres.

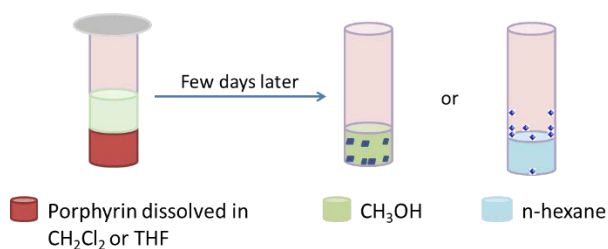


Figure 4. General description of the methodology followed to re-crystallize **1** and **2**.

This work describes the self-assembling ability of these zinc porphyrins and highlight the polyvalent coordination of the Zn(II) ions. In addition, our study integrates the application of solid-state techniques to describe the final self-assembled architectures. Here, the dynamics of the supramolecular arrangements are not focused but on the outcomes, portraying how small changes in solution process can make a great difference in the organization of the porphyrin entities. The controllable activities of these functional materials indicate the potential application in BHJ OSCs based on porphyrin small molecules.

2.2 Objectives

This project involves the design, preparation and processing of the novel zinc porphyrins and the study of their properties. The main objectives are the preparation of chiral/achiral molecules capable of electron transport via self-assembly and the finding of procedures to optimize their process ability. The ultimate goal is the incorporation of such materials into optoelectronic devices.

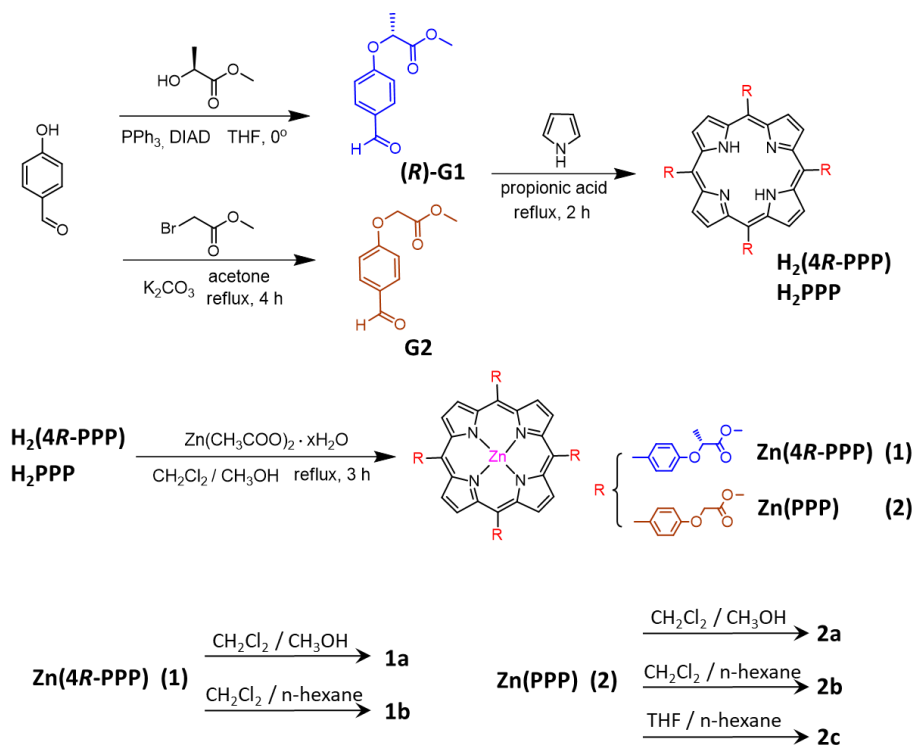
To achieve our initial goals, **Zn(4R-PPP)** and **Zn(PPP)** (**1** and **2** in Figure 3) were designed and synthesized. The four *meso*-positions were occupied by the same functional moieties, resulting the symmetric molecules, which simplify the porphyrin synthesis process. Functionalized by carbonyl groups which contain electronegative oxygen atoms, the periphery of the tetrapyrrolic macrocycle exhibits a high tendency to interact with the Zn(II) ions in the macrocycle centres of other porphyrin molecules, resulting in expected coordination networks. In addition, chirality effect on supramolecular aggregates could be explored. The introduction of chiral and achiral substituents towards the variation of the steric configurations of the porphyrins, therefore the final aggregates of these compounds could reveal the effects of chirality on their supramolecular structures and provide a hint on the properties such as their optical activity.

In this work, NMR technic was used to identify the free porphyrin ligands and the coordination systems based on them, and the molecular organization of the porphyrin derivatives was revealed by single crystal X-ray diffraction. As the crystal structure is a powerful proof to illustrate the self-assembly, we concentrated our efforts on the solid-state properties of the crystals, and investigated them by optical techniques, ¹³C NMR, solid state circular dichroism and vibrational circular dichroism (VCD). Moreover, the topographies of porphyrin aggregations deposited onto highly oriented pyrolytic graphite (HOPG) and mica were studied by atomic force microscopy (AFM) and scanning electron microscopy (SEM).

A preliminary study of porphyrin small molecule used in BHJ OSCs, as active compound, was performed by the fabrication of the devices and investigation of the properties such as power conversion efficiency (PCE). The energy gap and redox behaviours of porphyrin were decided by UV-Vis spectra on film and electrochemical characterization in solution.

2.3 Synthesis of acetate-based Zn(II) porphyrins bearing chiral/achiral centres

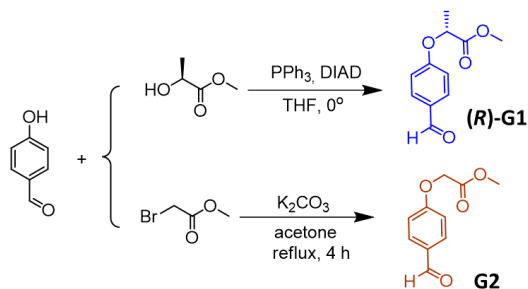
The symmetric *meso*-substituted Zn(II) porphyrins, ending in ester groups and contain chiral or achiral moieties, have been synthesized following the synthetic route shown in Scheme 1, and the self-assembling porphyrin single crystals were obtained in different mixed solvent systems.



Scheme 1. Synthesis and crystallization of metalloporphyrin **Zn(4R-PPP)** and **Zn(PPP)** (**1** and **2**).

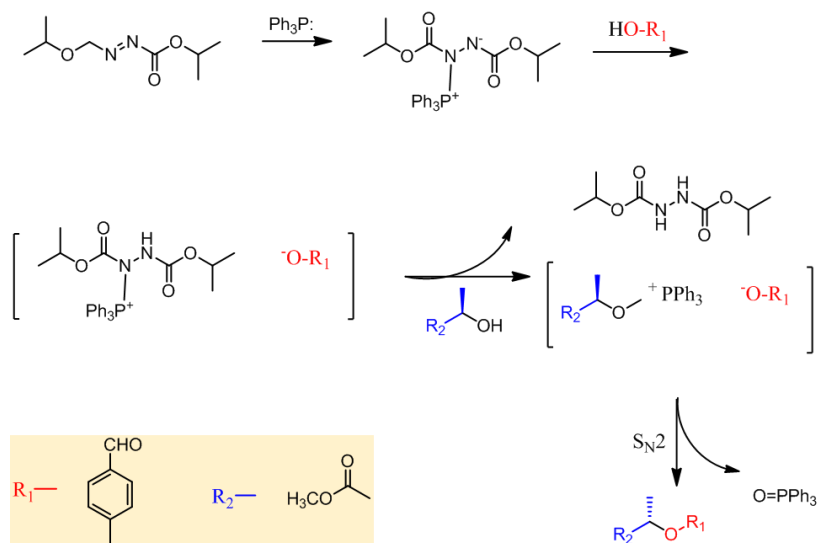
2.3.1 Synthesis of chiral/non-chiral aldehyde (R)-G1 and G2

The first step toward the synthesis of the porphyrin macrocycle was the preparation of aldehyde. The route, shown in Scheme 2, was used for producing the chiral and achiral aldehydes by one step. The chiral aldehyde derivative (R)-G1 was achieved by the Mitsunobu reaction²⁴ where 4-hydroxybenzaldehyde and (S)-(-)-Methyl lactate were reacted under mild conditions, using a combination of the oxidizing azo reagent diisopropyl azodicarboxylate (DIAD) and the reducing phosphine reagent triphenylphosphine (PPh₃). Reaction between 4-hydroxybenzaldehyde and methyl bromoacetate furnished G2 with almost percentile yield in the refluxing potassium carbonate acetone solution.^{25,26}



Scheme 2. Synthesis of chiral aldehyde (R)-G1 and achiral aldehyde G2.

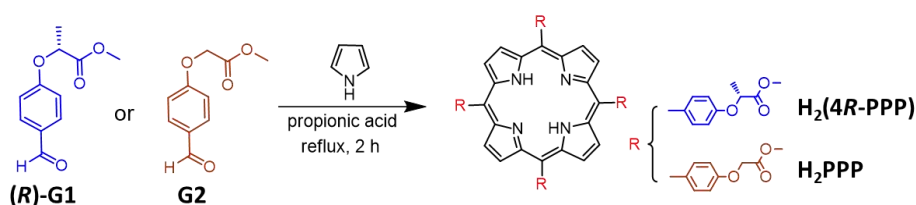
It is important to mention that in the previous Mitsunobo reaction, to obtain **(R)-G1**, an inversion of the stereochemistry of the methyl lactate took place. Scheme 3 shows a putative mechanism of the process, where triphenylphosphine oxide (PPh₃O) is formed as a by-product. For efficient purification of the aldehyde by column chromatography (yield: 73%), a crucial step was the isolation of the PPh₃O from the crude compound, which could be performed though separation using a AcOEt/n-hexane (1:9) solvent mixture overnight.



Scheme 3. Reaction mechanism of **(R)-G1**.

2.3.2 Formation of the free-based porphyrin H₂(4R-PPP) and H₂PPP

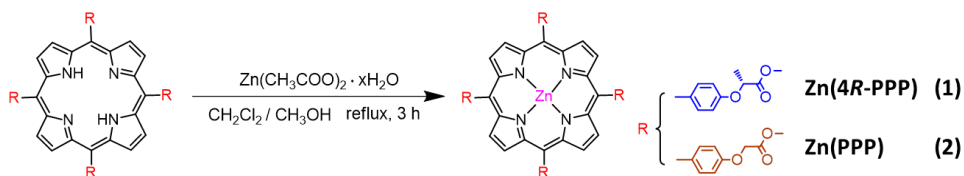
Following our synthetic strategy by Adler-Longo reaction²⁷ shown in Scheme 4, the condensation of the aldehyde **(R)-G1** and **G2** respectively with pyrrole in a 1:1 ratio in the refluxing propionic acid afforded the *meso*-substituted free-base porphyrin. The purple compounds were isolated in an approximate 30 % yield in both cases. Here, the reaction did not present additional difficulties but the creation of the macrocycle was accompanied by some by-products (non-cycled systems); the initial crude was dark and viscous and further purification processes were carried out via column chromatography, providing the pure system.



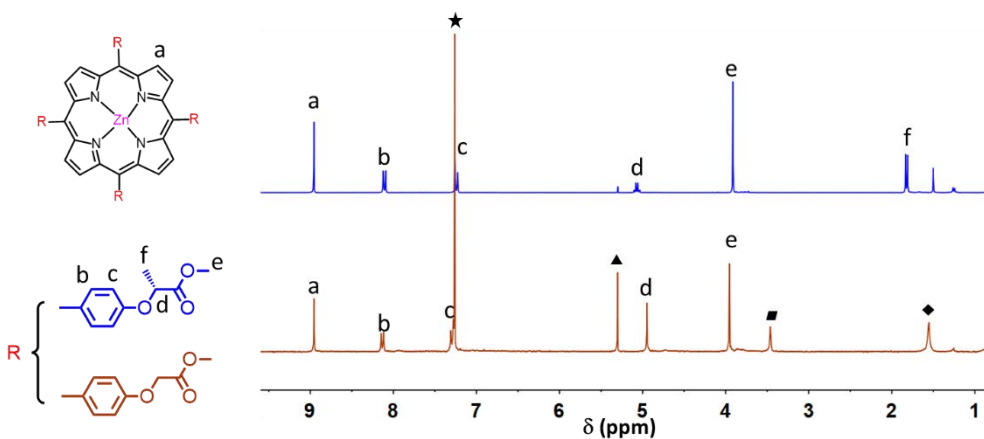
Scheme 4. Synthesis of free-based porphyrin **H₂(4R-PPP)** and **H₂PPP** by Adler-Longo reaction.

2.3.3 Metalation of the free-base porphyrins with zinc(II) ion

The final step was the coordination of the porphyrin macrocycle with Zn(II) ions, following the procedure depicted in Scheme 5.²³ An excess of the $\text{Zn}(\text{CH}_3\text{COO})_2 \cdot 2\text{H}_2\text{O}$ was used to achieved porphyrin **1** and **2** (**Zn(4R-PPP)** and **Zn(PPP)**, respectively). The yield was relatively high (86 %), where a purple solid was isolated by organic extraction.



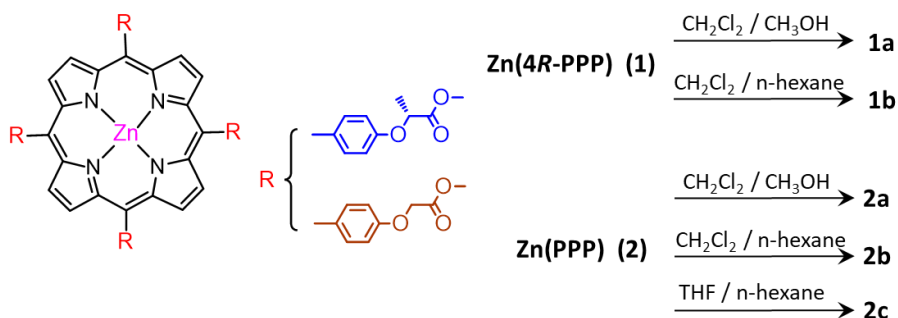
The ^1H NMR spectra of **1** and **2** are shown in Figure 5. The chiral centre of the porphyrin substituent was composed by the phenoxy-, ester, methyl groups and one proton atom. The main difference between both species resides in the achiral centre that in the case of **2** presents a single peak, where before **1** showed a shift of high multiplicity (d and f in Figure 5 top). Protons far away from the chiral centre were not affected presenting similar shifts in both spectra.



2.3.4 Self-assembly of Zn(II) porphyrins by crystallization

Compound **1** and **2** (**Zn(4R-PPP)**, **Zn(PPP)**) are the precursors of the following systems, and by the use of different solvent mixtures presented in Scheme 6, crystals suitable for X-ray crystallography were grown by slow diffusion of CH_3OH or *n*-hexane into a concentrated solutions of Zn(II) porphyrins. In this way, **1a** and **1b** were obtained by the use of the

CH₂Cl₂/CH₃OH mixture, while **2a** and **2b** were isolated from the CH₂Cl₂/n-hexane system. The crystals of **1a** and **1b** presented flake shapes, **1b** displayed octahedron forms and **2b** showed cubes (Figure 6). Due to the absence of methyl groups in **2**, the solubility of this achiral system in CH₂Cl₂ was poor, and it was difficult to crystallize in high quantities, especially in the CH₂Cl₂/n-hexane, where few crystals were obtained which were resolved by single crystal X-ray diffraction. Additional studies were not carried out due to the low quantity of crystals. In a further attempt to study the effect of solvents within the chiral/achiral porphyrins, tetrahydrofuran THF, was used. As a result, the porphyrin **1** with chiral centres did not form crystals, meanwhile the achiral one provided good yields, sized and quality crystal, better than with CH₂Cl₂ (Figure 6), indicating the intense participation of the solvent in the organization of well-ordered structures in **2c**.



Scheme 6. Preparation of metalloporphyrin crystals.

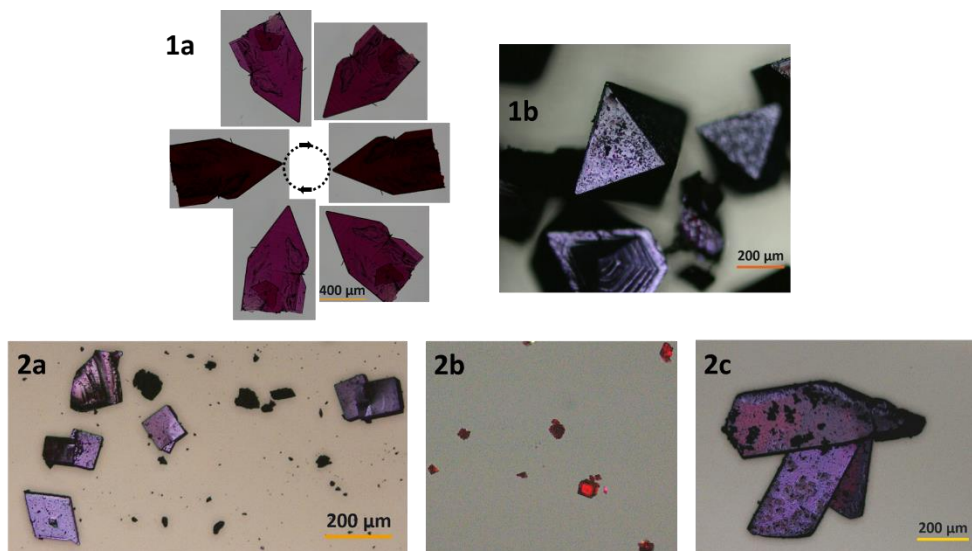


Figure 6. Microscope images of Zn(II) porphyrins crystals.

2.4 Structural descriptions of chiral/achiral acetate-based Zn(II) porphyrins

All the single crystals with X-ray quality were obtained by the methodology mentioned above. The crystallographic details of the five Zn(II)-porphyrin species (**1a-b**, **2a-c**) are summarized in the appendix Table A2.1. Their molecular structures in the solid state and selected bond lengths and angles for each system are listed in the Tables A2.2 to A2.6 respectively, as well as additional Figures A2.1-2.5 display different projections.

As a general feature, all the structures present a Zn(II) porphyrin core, where the macrocycle is tetra-substituted occupying the *meso*-positions, with chiral (**1a**, **1b**) or achiral (**2a-c**) groups respectively. In each structure, the zinc atom is located at the centre of the porphyrin ring with four Zn-N_{pyrrole} bonds. Depending on the supramolecular arrangements, the Zn(II) ions can extra coordinate to oxygen atoms, from solvents or neighbours. The major differences between the species and the basic molecular descriptions concentrating on the supramolecular arrangements of all the systems were discussed in the following content.

2.4.1 Study the aggregates obtained for Zn(4*R*-PPP) using single X-ray diffraction

2.4.1.1 Crystal structure of **1a**

1a crystallizes in the orthorhombic space group $P2_1/c$, and four independent Zn(OH₂)(4*R*-PPP) molecules are included in the unit cell. The mononuclear species contain one penta-coordinated Zn(II) centre bonded to four N atoms from the porphyrin core and one O atom from H₂O (Figure 7a). The Zn(II) site is above the porphyrin plan (by 0.204 Å) toward the axially bonded H₂O. Such binding is nearly perpendicular to the plane of the Zn-porphyrin core (O-Zn-N angles between 89.85 - 101.43 °) with a Zn-O bond length of 2.247 Å. (Figure 7b) The molecular plane of the core exhibits a deck chair shaped distortion, one of the *meso*-groups is upwards and the other three are downwards (Figure 7c). This *meso*-Zn(II)-porphyrin displays four identical substituents containing chiral ester groups (C45, C49, C53, C57 in Figure 7), all of them with an absolute *R* configuration. These peripheral moieties, from the 4*R*-PPP²⁻ system, spread in different orientations from the porphyrin plane with a variety of dihedral angles (-122.04, -109.56, 77.88 and -62.42 °).

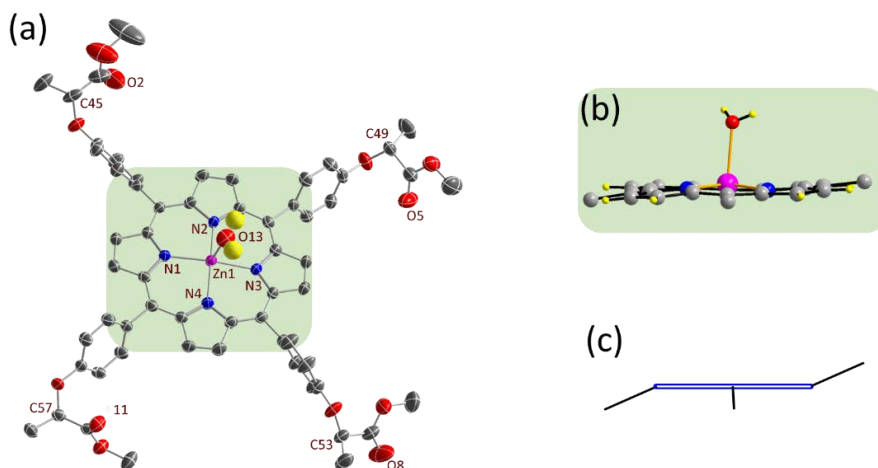


Figure 7. (a) POV-Ray view of **1a** with thermal ellipsoids fixed at 50 %. Protons are omitted for the sake of simplification. Colour legend: Zn in purple, O in red, N in blue and C in grey. (b) The macrocycle core of **1a**. (c) Deck chair shaped conformation of **1a** unit.

The supramolecular arrangement of **1a** molecules consists on linear arrays of the porphyrin species, which held together by O \cdots H-O hydrogen bonds (Figure 8, O \cdots O 2.9009 Å) between the carbonyl group of one neighbouring porphyrin and an oxygen atom of the H₂O which coordinated to the Zn(II) centre. Thus, every porphyrin is hydrogen bonded to one adjacent moiety, constructing a gear-like belt with the perpendicular height is 3.917 Å. The Zn-porphyrin molecules in the chain are facing opposite to each other in an alternating fashion, where the hydrogen bonding makes the porphyrin moieties displaced. The chains are aligned with closes vertical distances (2.465 Å) to another chain, leading to the 2D organization. (Figure A2.6)

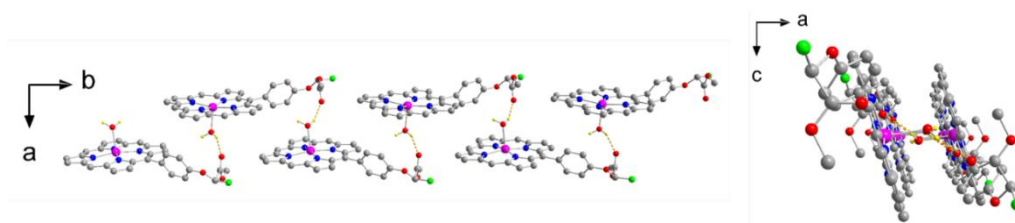


Figure 8. 1D supramolecular organization of **1a**. Branches in the *meso*-positions which are not involved in H-bonding are omitted for the sake of simplification. Colour legend: Zn in purple, O in red, N in blue, C in grey (C of -CH₃ connected to chiral centres in green) and H-bonding in yellow dash line.

The large size of the crystals obtained for **1a** allowed positioning them on the stage of an AFM equipment. This work was in collaboration with Drs. C. Ocal and E. Barrena from the ICMAB. The surface of this particular 3D crystal was measured by AFM (Figure 9). It consists of large and atomically flat terraces (several micrometres long and hundreds of nm wide in average)

separated by well-defined steps. As it can be extracted from the line profile in Figure 9(b), the steps heights are ≈ 1.8 nm, which fully agrees with the distance of the two Zn atoms indicated in the crystal packing (Figure 10), and that is equal to the thickness of the 2D wall.

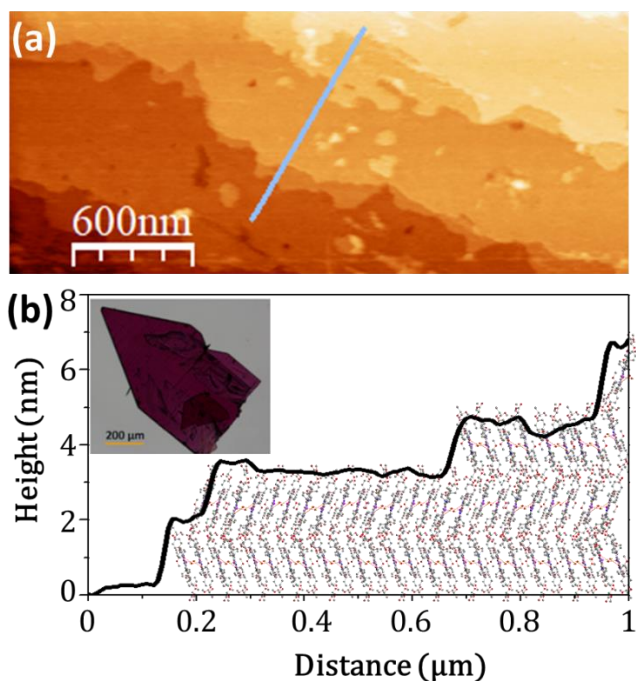


Figure 9. (a) Topographic AFM image of the surface of the crystal of **1a**. (b) Line profile corresponding to the segment signalled in (a).

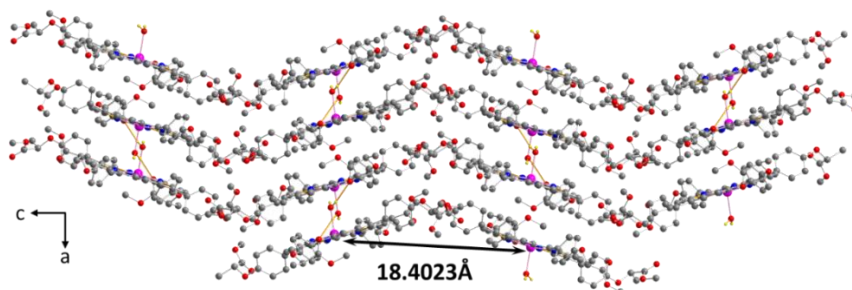


Figure 10. Crystal packing of **1a**. Colour legend: Zn in purple, O in red, N in blue, C in grey and H-bonding in yellow dash line.

2.4.1.2 Crystal structure of **1b**

1b crystallizes in the orthorhombic space group $P2_12_12_1$. **1b** is a coordination polymer $Zn(4R-PPP)_n$ made by the self-assembly of the same porphyrin molecule described in **1a** (same porphyrin ring and chiral branches, Scheme 6). The difference now resides in the fact that the Zn centre of each porphyrin unit is not coordinated to a molecule of H_2O but to the C=O group of an ester branch from an adjacent molecule. Such coordinative bond, provides the final polymeric structure depicted in Figure 11.

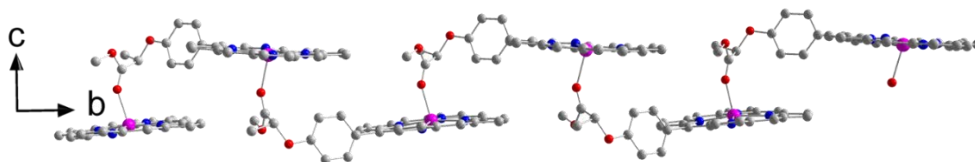


Figure 11. Arrangement of the coordination polymer (1D system). Branches in the *meso*-positions not involved in coordination are omitted for the sake of simplification. Colour legend: Zn in purple, O in red, N in blue and C in grey.

In **1b**, each monomeric unit (Figure 12a) shows a penta-coordinated Zn(II) centre, with the metal slightly shifted up from the plane of the porphyrinic core (by 0.188 Å). The Zn-O bond length distance is now 2.210 Å, shorter than the Zn-O distance shown in **1a** (Zn-OH₂), with a noticeable deviation from previous perpendicular disposition (O-Zn-N angles between 86.50 - 104.21 °). Here, the organic moiety, 4*R*-PPP²⁻, presents sprains, where two moieties at the opposite *meso*-positions bended in the same direction, up or down, resulting in a saddle-distortion (Figure 12b) of the monomeric units. As it happened in **1a**, only one C=O from a chiral ester group interacts with the neighbour molecule, leaving the other three free.

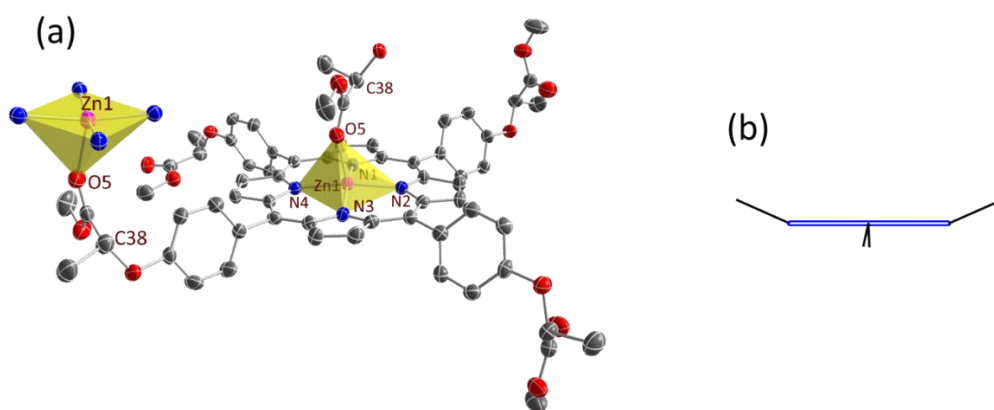


Figure 12. (a) POV-Ray view of **1b**. (b) Saddle-conformation of the **1b** monomeric unit. Colour legend: Zn in purple, O in red, N in blue and C in grey.

The final arrangement of a single 1D zigzag chain coordination structures is shown in Figure 13. The shifted distance of the adjacent porphyrin cores is 4.023 Å, displaying vertical distances of 3.875 Å. To the best of our knowledge, system **1b** is the first coordination polymer of porphyrin that is formed by the coordination of one branch of the porphyrin system and one metal of the nearby molecule as well as the first one displaying chiral properties. Other two coordination polymers have been described in the literature where the metalloporphyrin units are connected by means of coordinative bonding of the metallic centre and one of the pyridyl moieties from the neighbour, providing also 1D systems.^{12,13} However, the ones described in the previous reports, always presented the coordination of two branches of the same monomeric porphyrin unit with two others.^{28,29}

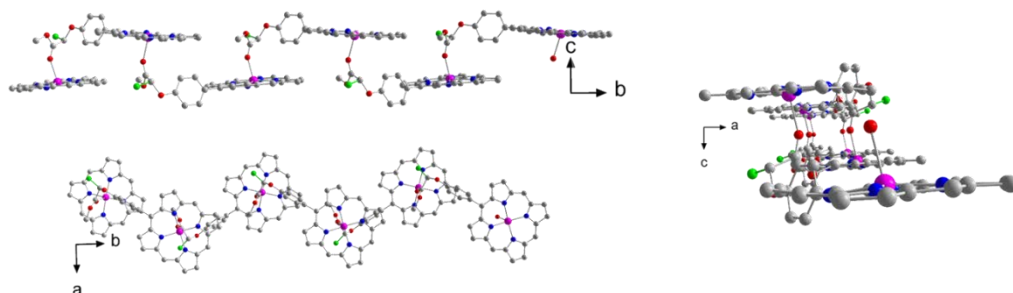


Figure 13. Different crystallographic projections of 1D supramolecular organization of **1b**. Branches in the *meso*-positions not involved in coordination are omitted for the sake of simplification. Colour legend: Zn in purple, O in red, N in blue and C in grey (C of -CH₃ connected to chiral centres in green).

Further interactions of **1b** zigzag chain molecules give rise to the 3D structure shown in the Appendix (Figure A2.7), where each polymer organizes first in parallel arrays, with distances of 16.860 Å, forming 2D plains and then stack layer by layer with the height of 8.955 Å giving the final 3D arrangement.

2.4.1.3 Study regarding the origin of the molecule of H₂O in **1a** absent in **1b**

As explained above, the Zn(II) ion in **1a** is penta-coordinated with H₂O in the apical position; **1a** crystallized from a CH₂Cl₂/CH₃OH mixture; however, there is not H₂O molecule in the structure of **1b**, from a CH₂Cl₂/*n*-hexane mixture. In order to establish the origin of the coordinated H₂O in the case of **1a**, absented in the second case, we performed a series of experiments varying the source of Zn(II) and summarized in Table 1. The results of all the studies were analysed by X-ray powder diffraction and then compared with the simulated graph of **1a** and **1b**.

The first modification was performed by the use of dehydrated Zn(CH₃COO)₂ with the same crystallographic procedure and materials as for **1a** (CH₂Cl₂(HPLC)/CH₃OH), the resulting sample was named **C1**. The X-ray powder diffraction pattern of **C1** (Figure 14) matches well with **1a**. Therefore, our analysis shows that **C1** may also contain the Zn-OH₂ coordination, demonstrating that the H₂O, in **1a**, is not from the Zn(CH₃COO)₂·2H₂O source.

In a second test, dehydrated $\text{Zn}(\text{CH}_3\text{COO})_2$ was used, but 3 mL of H_2O was added in the recrystallization process. This step hampered the achievement of good crystals (Figure 14). After the full evaporation of the organic solvent, we studied the films floating on the remaining water (here called **C2**). This strategy was taken because methanol is water rich, but in this case, a large amount of H_2O went against the crystallization process.

Finally, $\text{Zn}(\text{CH}_3\text{COO})_2 \cdot 2\text{H}_2\text{O}$ was used as the source of metal following the recrystallization method of **1b**, $\text{CH}_2\text{Cl}_2(\text{HPLC})/n\text{-hexane}$. In addition, after the metallization reaction, half of the crude compound was precipitate from CH_3OH , the other part was purified by column chromatograph (SiO_2 , $\text{CH}_2\text{Cl}_2/\text{CH}_3\text{OH}$ 200:1), then both of them crystallized from the mixture solvent $\text{CH}_2\text{Cl}_2(\text{HPLC})/n\text{-hexane}$. The results of both match well with **1b**, displaying a porphyrin polymeric arrangement (Figure 14, right).

Table 1. Conditions of the experiments.

Compound	Zn ^{II} used in reaction	Solvent for crystallization
1a	$\text{Zn}(\text{CH}_3\text{COO})_2 \cdot 2\text{H}_2\text{O}$	$\text{CH}_2\text{Cl}_2(\text{HPLC})\text{-CH}_3\text{OH}$
1b	$\text{Zn}(\text{CH}_3\text{COO})_2$	$\text{CH}_2\text{Cl}_2(\text{HPLC})\text{-hexane}$
C1	$\text{Zn}(\text{CH}_3\text{COO})_2$	$\text{CH}_2\text{Cl}_2(\text{HPLC})\text{-CH}_3\text{OH}$
C2	$\text{Zn}(\text{CH}_3\text{COO})_2$	$\text{CH}_2\text{Cl}_2(\text{HPLC})\text{-CH}_3\text{OH}\text{-H}_2\text{O}(3\text{ mL})$
C3	$\text{Zn}(\text{CH}_3\text{COO})_2 \cdot 2\text{H}_2\text{O}$	$\text{CH}_2\text{Cl}_2(\text{HPLC})\text{-hexane}$

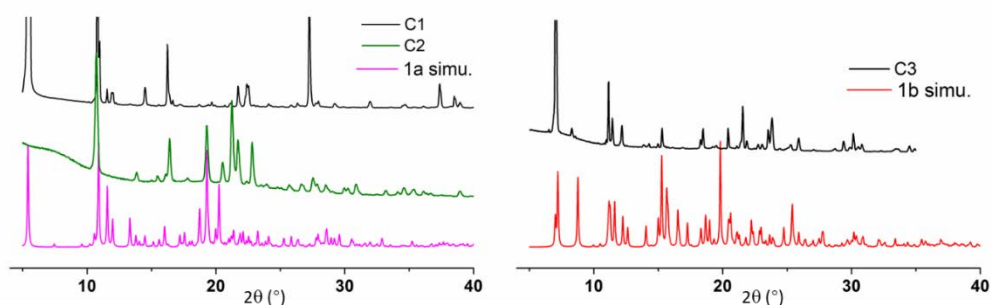


Figure 14. (Left) XRD of **C1** and **C2** comparing with **1a**. (Right) XRD of **C3** comparing with **1b**.

Regarding our experiments we concluded that the crystal structures, and the water content, were controlled by the conditions of the crystallization procedure. The supramolecular organization of Zn(II) porphyrin **Zn(4R-PPP)** and the different structures obtained are strongly dependent on the solvent conditions.

2.4.2 Study the aggregates obtained for Zn(PPP) using single X-ray diffraction

2.4.2.1 Crystal structure of **2a**

Compound **2a** crystallizes in the $C2/c$ monoclinic space group and the asymmetric unit consists exclusively in one molecule of the Zn(II)-porphyrin moiety. Here, the Zn(II) centre is tetra-coordinated and adopts a square planar geometry, forming a perfect plane with the four porphyrin nitrogen atoms of the core. The planarity of the PPP^{2-} ligand does not present any deformation, in contrast with what it happens in the units of **1b**. As Figure 15 shows, the structure has resemblance to that described in **1a**, due to the similarities of the peripheral groups, but now the replacement of the $-CH_3$ groups by protons leads to achiral molecules.

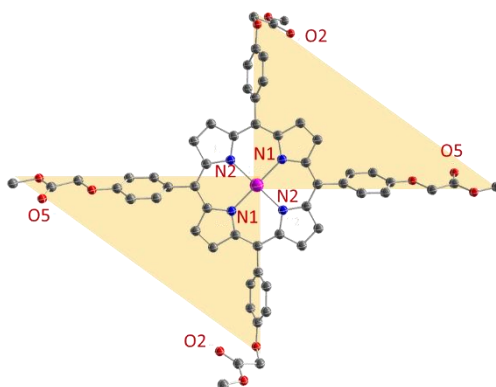


Figure 15. POV-Ray view of **2a** with thermal ellipsoids fixed at 50 %.

Advanced supramolecular organization of **2a** is giving in the Appendix (Figure A2.8-2.9). Although the compact packing of the molecules shows proximity among neighbours, the Zn(II) centre in **2a** is further away from the C=O moiety (3.333 and 3.908 Å) and no molecules of solvent or H_2O appear in the final supramolecular architecture (Figure 16).

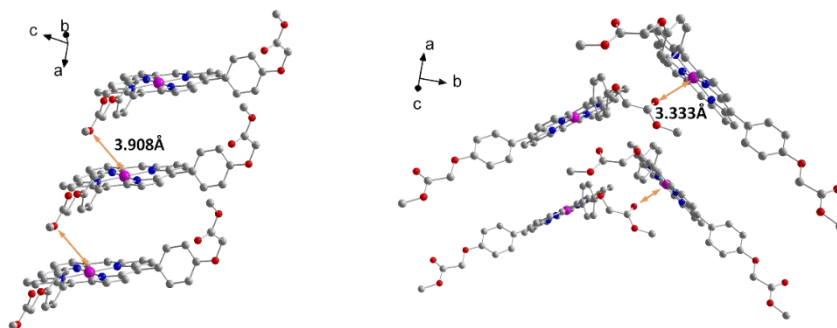


Figure 16. Side views of the disposition of **2a** molecules and intermolecular interactions among them. Some of the side branches not involved in the interactions and protons are omitted for the sake of simplification.

2.4.2.2 Crystal structure of 2b

The second of this family of compounds is **2b**, Zn(PPP)_n , that crystallizes, as the previous, in the monoclinic space group C2/c. The asymmetric unit is described by a molecule of " Zn(PPP)O_2 " where the oxygen atoms relate to the C=O groups of two neighbouring molecules (Figure 17).

The Zn(II) is therefore hexa-coordinated, with a pseudo-octahedral symmetry due to its coordination to four nitrogen atoms from the PPP^{2-} organic moiety and the two oxygen atoms already mentioned. As it happens in **2a**, the Zn(II) centre forms a perfect plane within the chromophore core. In the rearrangement, the oxygen atoms are tilted from 90° (84.27° , 85.64° and reciprocal). Each Zn(PPP) is attached to four other units creating 2D networks, where the Zn(II)-porphyrin molecules present alternating orientations and one single Zn...Zn distance of 13.663 \AA (Figure 18). The structure grows layer by layer, where the adjacent 2D networks are parallel to each other with small interactions between them through the branches that are not involved in coordination (Figure A2.10-2.11).

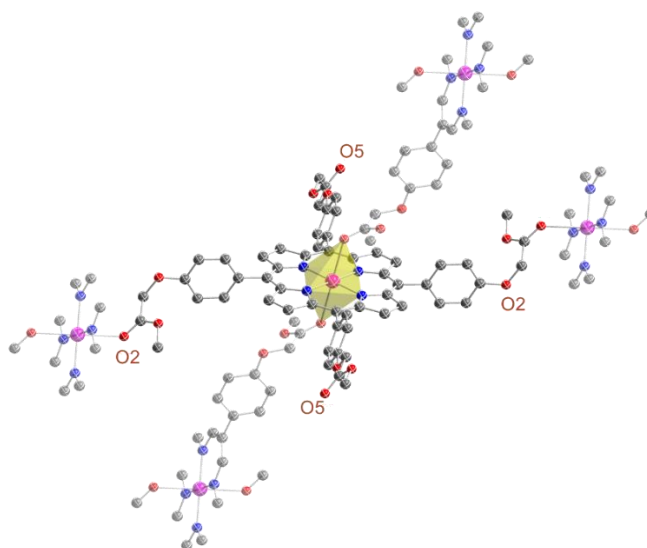


Figure 17. POV-Ray view of **2b** with thermal ellipsoids fixed at 50 %. Colour legend: Zn in purple, O in red, N in blue and C in grey.

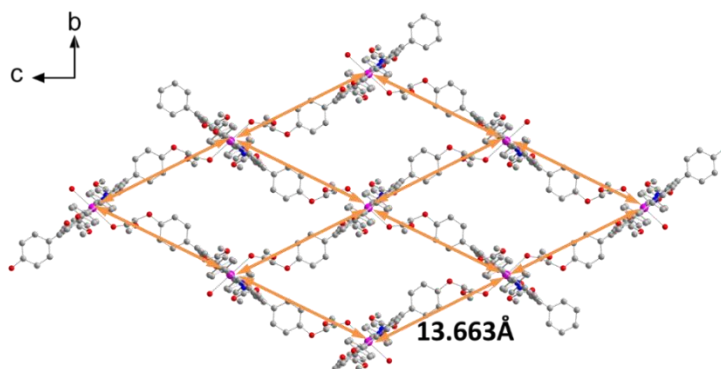


Figure 18. The 2D ladder-shaped grid of complex **2b** stretching in the bc plan. Zn(II)⋯Zn(II) distances are in all cases 13.663 Å.

2.4.2.3 Crystal structure of **2c**

2c crystallizes in the triclinic space group P_1 , where two independent Zn(THF)(PPP) molecules are included in the unit cell. Besides, there are two THF solvent molecules (Figure A2.12). The mononuclear species contain one penta-coordinated Zn(II) centre bonded to four N atoms from the porphyrin core and one O atom from a THF molecule. The structure analysis shows there is a slight displacement of Zn ion from the N4 plane, and the Zn-O binding is nearly perpendicular to the plane with a length of 2.161 Å (Figure 19). In the structure of **2c**, THF solvent only provides the oxygen atoms for the coordination to the porphyrin cores like the H₂O in **1a**, but there is not hydrogen bonding assistance to form 1D chains as in the former. The **2c** monomers combine to create a densely packed supramolecular 2D and 3D structures shown in the Appendix Figure A2.13-2.14.

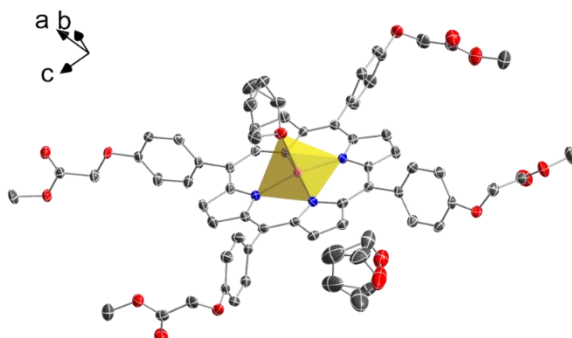


Figure 19. POV-Ray view of **2c** with thermal ellipsoids fixed at 50 %. Colour legend: Zn in purple, O in red, N in blue and C in grey.

2.4.3 Discussion of the Zn(4R-PPP) and Zn(PPP) self-assembly by crystallography

We found a Zn-porphyrin setup with great ability towards crystallization, and confined the combination of solvents for such task ($\text{CH}_2\text{Cl}_2/\text{CH}_3\text{OH}$, $\text{CH}_2\text{Cl}_2/\text{n-hexane}$ and $\text{THF}/\text{n-hexane}$) to investigate chirality and polarity. By doing so, we created a map with a rich variety of supramolecular arrangements.

Having a Zn centre and four terminal benzylic ester moieties at the *meso*-positions, both electron-acceptor and donor parts in that order, we expected the Zn porphyrin to self-assemble (coordinative binding) with terminal moieties from neighbouring molecules, which is the fact that we saw in two of the systems under study (**1b** and **2b**). However, the final picture is more complex, where the coordination number of the Zn(II) varies from four to six, depending on the solvent conditions. Single X-ray diffraction shows us that in the case of the chiral systems, **1a** and **1b**, the Zn is always penta-coordinated, choosing as the fifth ligand a molecule of H_2O or the terminal benzylic branch of one neighbouring species, respectively. The same methodology applied to the achiral versions provides tetra- and hexacoordinated Zn centres, **2a** and **2b**, respectively, and the penta-coordinated could be achieved by inducing solvent molecules of THF which has affinity for the Zn centres in **2c**. A feature that seems general it is the achievement of mononuclear structures when the recrystallization solvents are polar (CH_3OH , THF); instead, the use of apolar solvents (e.g.: n-hexane) encourage aggregation (providing 1D or 2D coordinative systems).

In all cases, the size and geometry of the crystals for all the four samples differ. We could argue that the changes in solubility regarding the existence of a $-\text{CH}_3$ vs. a $-\text{H}$ (**1** vs. **2**) in the branches of the porphyrins make the rigorous comparison unfeasible, but the two methodologies used work in a similar manner in the four systems, having crystals in all the cases after few days. Therefore, chirality may be involved in the results; where the $-\text{CH}_3$ of the coordinated branches are always outside, improving the disposition of the $\text{C}=\text{O}$ group toward the Zn (Figures 20).

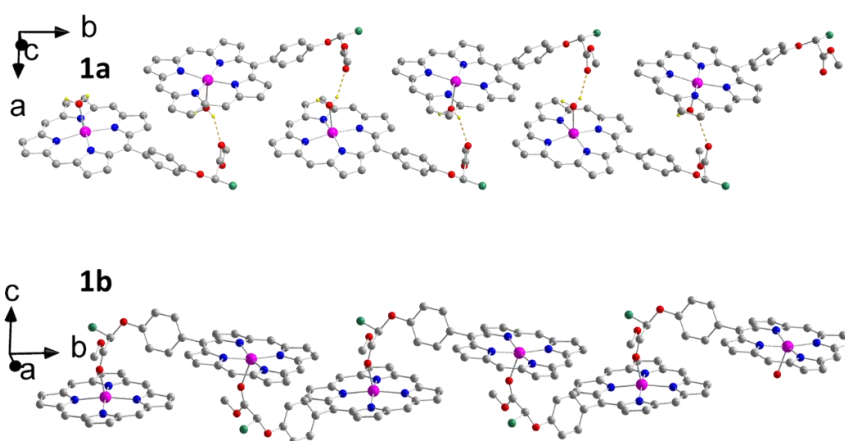


Figure 20. Comparison between **1a** and **1b**. Colour legend: Zn in purple, O in red, N in blue, C in grey and $-\text{CH}_3$ of the coordinated branch in green.

2.5 Studies performed in solution: NMR, UV-Vis absorption and CD spectra

This section shows the efforts made toward the analysis of the different systems (**1a-1b**, **2a-2c**) in solution. Initial studies were performed using ^1H NMR spectroscopy. To study the stability of the different systems in solution, and therefore the stability of the aggregation formed, crystals of **1a** and **1b** were used. Both systems contain the same unit, **Zn(4R-PPP)**, but as shown in previous sections, **1a** displays a supramolecular 1D system and **1b** a coordination bond between neighbouring molecules presenting 1D coordination polymers. ^1H NMR spectroscopy in CDCl_3 was performed with crystals from both species; the idea was to vary the concentration of the units "**Zn(4R-PPP)**" to observe the formation in solution of different aggregates and to identify them depending on which system, **1a** or **1b**, were used. Studies from lower concentration to higher, from 0.25 mM up to 20 mM were performed in both cases. Figure 21 shows, as example, the results found out for **1a** (the results for **1b** are in the Figure A2.15.). As the spectra show, the variation of the concentration did not have any effect on the signals. The number and shape were kept in both cases, and more importantly, they were identical. Such results indicate that in solution the units were identical, with no recognition or memory of the supramolecular information on the crystals. Hence, the aggregates formed were not kept after re-dissolving the crystals. Studies using UV-Vis absorption spectroscopy at the same concentrations were impossible for the comparative study between **1a** and **1b** due to the saturation.

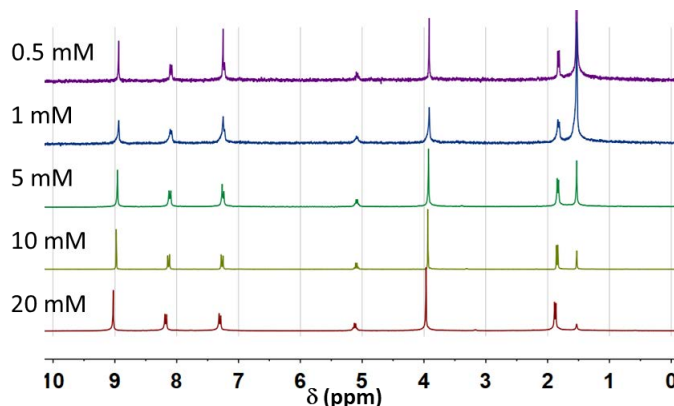


Figure 21. ^1H NMR of **1a** in different concentration in CDCl_3 .

In an attempt to further characterize the systems by NMR we performed HSQC experiments (^1H - ^{13}C heteronuclear single-quantum correlations) and HMBC (heteronuclear multiple bond correlations) directly on the uncrystallised metalloporphyrin **1**. Such techniques provide powerful NMR information regarding structural studies of porphyrins.³⁰ The former provides correlations between the carbon atoms and attached protons and the latest detects ^{13}C - ^1H long range couplings by using an inverse detection. In this way, it was possible to identify all the proton and carbon resonances (Figures 22 and 23). However, again the supramolecular actions were not observed in solution, supported by the presence of one kind of carbon signal.

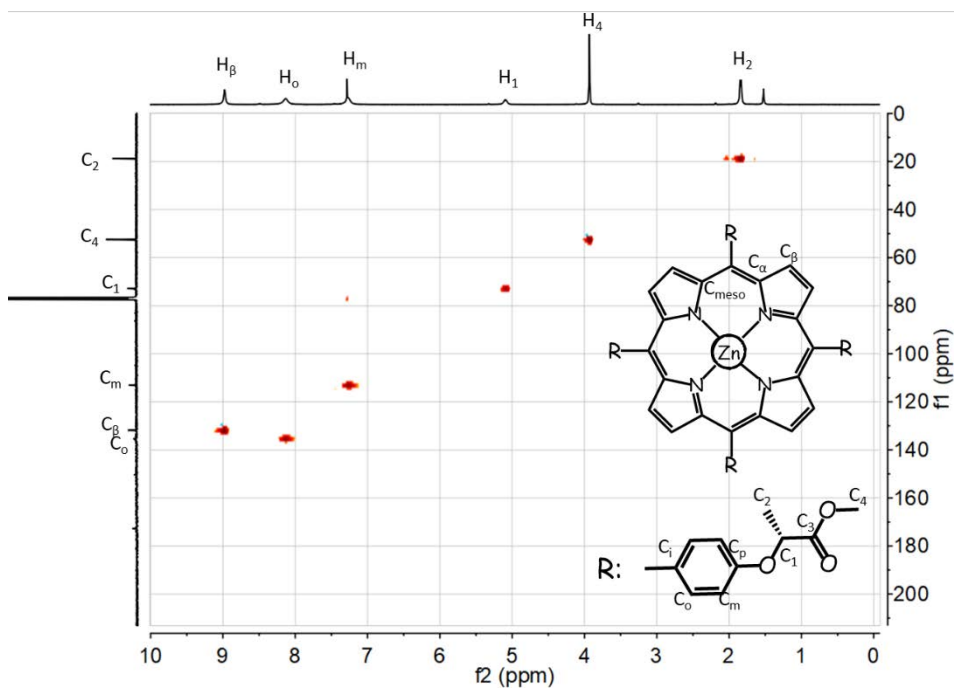


Figure 22. ^1H - ^{13}C NMR HSQC spectrum of **1** (**Zn(4R-PPP)**) in CDCl_3 .

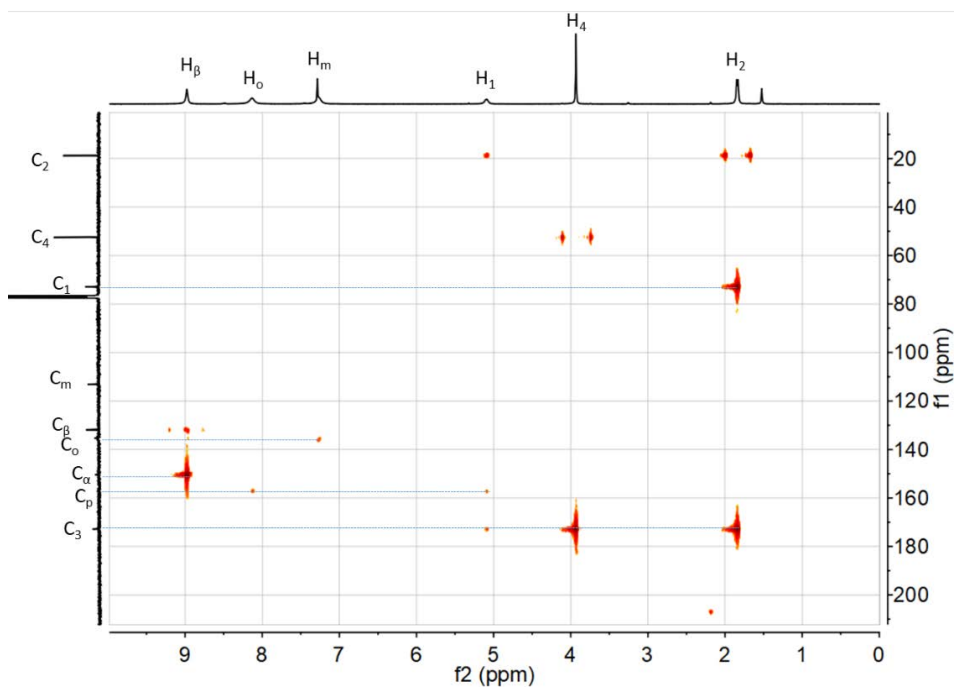


Figure 23. ^1H - ^{13}C NMR HMBC spectrum of **1** (**Zn(4R-PPP)**) in CDCl_3 .

Circular dichroism in CH₂Cl₂ was performed toward a further analysis of the systems with the aim of analysis and identification of **1a** and **1b**. The crystal structures indicated the self-assembly of **Zn(4R-PPP)** in both case (**1a** and **1b**) is mainly connected by Zn(II) centre and the carbonyl group, so we used the free-base porphyrin **4R-H₂PPP** as a reference. Taking into account the problems observed at high concentrations in the UV-Vis absorption experiments, the new CD studies were performed by fixing the absorbance value of each sample to 1 and the molar absorptivity ϵ from the corresponding UV-Vis spectra calculated (details in Appendix and Figure A2.16). In case of broad absorption, different band widths of the incident circularly polarized light were set to record CD spectra. Nevertheless, in all the cases, **Zn(4R-PPP)** and free-based **4R-H₂PPP**, there is an absence of CD signals (Figure A2.17); this may due to the distance between the chromophore cores and the chiral centres and the freedom of rotation of the latest.³¹

In summary, all the spectra are a mean of the molecular conformations adopted in a given solvent and the stereogenic centres influence slightly the chiral self-assembly of porphyrin molecules in CH₂Cl₂ under the given concentration in solution.

2.6 Study of the self-assembly of Zn(II) porphyrins in the solid state

2.6.1 Study the stability of **1a** and **1b** by ESI-Mass

Despite of the lack of information regarding aggregation in solution, a number of techniques were helpful corroborating the crystallographic data in the solid state. In this way, the use of ESI-Mass spectrometry shows that the experimental spectra of **1a** and **1b** agree well with the theoretical isotopic distribution of each sample (Figure A2.18-19). In the case of **1a**, the coordinated H₂O was not identified due to the lability of the coordination. As a result, the supramolecular chain could not be identified and instead there is a clear peak, corresponding to the isotopic distribution of the porphyrin **Zn(4R-PPP)** with a value of m/z 1085.29 [M+H]⁺ (Figure A2.18). In the case of **1b**, the polymer chain did not contain H₂O but the coordinative bonding was observed because the chain cracks into different Zn(4R-PPP) units, and it was possible to identify the m/z 1085.29 [M+H]⁺ signal followed by others that indicate the existence of dimers and divalent cations trimers at 2169.57 [2M+H]⁺ and 1630.43 [3M+2H]²⁺, respectively (Figure A2.19). For the system of **2**, we did not perform this measurement, because **2a** and **2c** are the mononuclear structures, and the coordinated THF in **2c** may not be identified like the H₂O in **1a**.

2.6.2 Study the aggregates by ATR-FTIR

Analyses based on crystalline samples of **1a-b** and **2a** compounds (**2b** was not studied because of the low yield of crystalline materials as explained above) provided clear evidences of the changes shown in their respective crystal structures. In the case of the chiral systems, **1a** and **1b**, the two molecules present almost identical ATR-FTIR spectra but differing in two areas between 3450-3470 cm⁻¹ and 1720-1760 cm⁻¹ respectively (Figure 24). The former area shows the appearance of a broad peak in the case of **1a** missing in **1b** that corresponds to the inserted H₂O molecule as the structure shows. On the other hand, the latter area relates to the C=O

stretching vibrational modes from the terminal ester groups of the four branches. In the case of **1a**, appear two peaks at 1732 and 1750 cm^{-1} while **1b** shows three peaks, at 1719, 1739 and 1757 cm^{-1} , agreeing well with the fact of having one ester group coordinated, different from **1a**. Regarding the same area, compound **2a** displays a single peak with a shoulder at 1752 cm^{-1} (Figure A2.20).

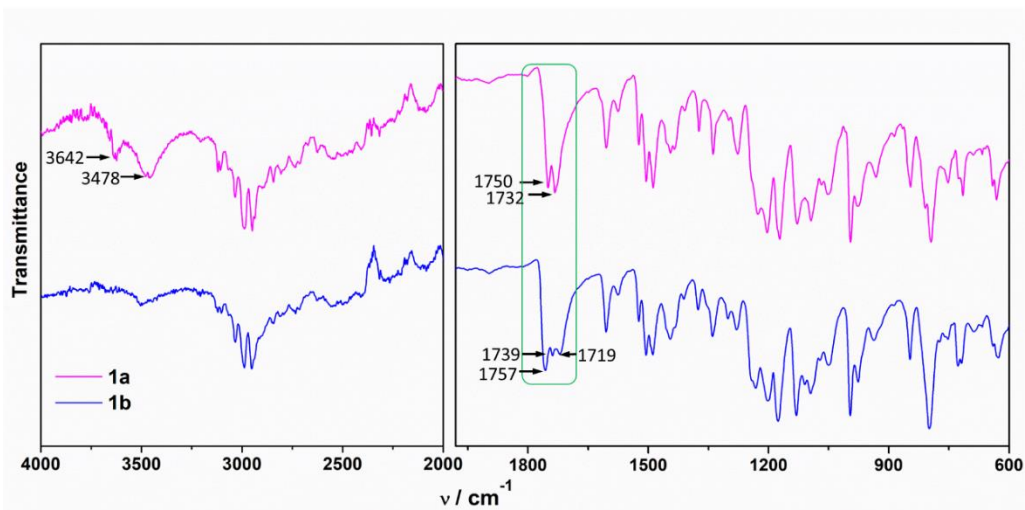


Figure 24. FT-IR of **1a** and **1b**.

2.6.3 Study the aggregates by solid-state ^{13}C NMR

Solid-state NMR can be a structurally informative technique for materials, such as coordination networks.³² High resolution solid-state ^{13}C NMR spectra with narrow peaks of crystals from samples **1a**, **1b**, **2a** and **4R-H₂PPP** are shown in Figure 25. The general assignments of the chemical shifts were made by comparison of the free chiral porphyrins, the coordination compounds (**1a-b** and **2a**) and the reported literature.³³ The similarities of our porphyrins to the 5,10,15,20-tetraphenyl porphyrin Zn(II) compound, used to be studied by Grant *et al.*³⁴, allowed us to describe the nature of the chemical shifts by their range of appearance (180 to 0 ppm). The previous study of 2D NMR in solution demonstrate the order of the carbon signal although specifics about individual shift assignments were not clear to elucidate because of the complicated interaction in solid state. The shifts could be grouped in four areas: signals appearing between 180-165 ppm (A), 165-125 ppm (B), 125-100 ppm (C) and from 80-20/0 (D), from down fields to high ones (Figure 25). The low field region "A" encloses C_3 related to the $\text{C}=\text{O}$ part of the macrocycle *meso*-substituent. "B" and "C" represent the conjugated system, where "B" is the sum of C_{para} , C_α , C_i , C_{ortho} and probably part of the $\text{C}_{\beta\text{B}}$ shifts, and "C" include $\text{C}_{\beta\text{B}}$, C_{meso} and C_{meta} . Finally, the high field region of "D" relies to the non-conjugated part of the molecule (branches) which are C_1 , C_4 and C_2 . The absence of C_2 in **2a** (Figure 25) corresponds to the achiral substituent. Comparing to the free-base porphyrin **4R-H₂PPP**, the peaks of complex **1a** and **1b** split, indicates the coordination and different arrangements in the molecule and within the neighbours.

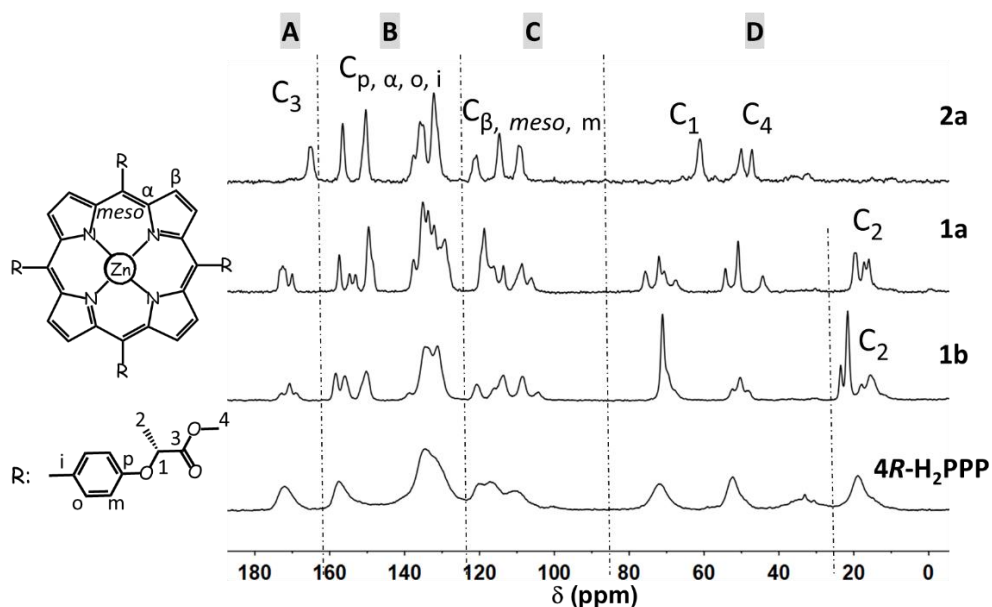


Figure 25. Comparison between the solid-state ^{13}C NMR spectra of **4R-H₂PPP**, **1a**, **1b** and **2a** between 180 - 0 ppm.

The variation in the number and shift of the chemical signals differ from one sample to another in a complex manner. It is already established that such variations relate to the overlap of the signals, the small structural differences inside the molecules (e.g. bending provide different number and shifts for C_1 , C_4 , etc.) and the proximity to neighbouring molecules (e.g.: electron cloud of the core) which provide different environments to most of the groups.³⁵ Comparing **1a** and **1b**, the multiple chemical shifts corresponding to the C_3 of **1b** suffers (at least one over four per molecule), such alterations in a stronger manner than the others. The final shape of these signals is different from both. In the case of **2a**, this shift appears at higher fields in 165.02 ppm compared to **1a** and **1b** (172.53 ppm (**1a**) and 170.70 ppm (**1b**)). Overall, this may relate to the coordination (**1b**) or proximity (**1a**) of the $\text{C}=\text{O}$ to a more electropositive system (Zn(II) ion). The shift to low fields of C_1 in **1a** and **1b** compared to **2a**, shows the dramatic spatial effect on the chiral/achiral carbons. When the -H was substituted by $-\text{CH}_3$, the δ value increased.

2.6.4 Study the aggregates by solid UV-Vis absorption spectroscopy

Freshly translucent pellets were prepared by the mixing of 0.1 mg of each crystalline sample within 100 mg of KBr respectively. Solid-state UV-Vis spectra were recorded of samples of **1a**, **1b** and **2a** (Figure 26). The three spectra display a Soret band between 430-435 nm with an obvious higher energy shoulder and two Q-bands around 560 and 602 nm. The UV-Vis absorption spectroscopy of Zn-porphyrins (**1** and **2**, respectively) in CH_2Cl_2 are almost identical (Table 2 down), nevertheless, the Soret band of **1a** and **1b** have a slight difference comparing to **2a** (435

nm) in solid state. The two Q-bands are almost similar in the three crystals, but the intensity ratios (Table 2 top) between the two Q-bands of **1a** and **1b** were a bit lower than to the value of **2a**, which is indicative of the ligand binding to the zinc centres.¹⁵ Furthermore, the monomeric molecules arranged in one dimension by the H-bonding or coordination bonding with the formation of J-type aggregates (side-by-side) in **1a** and **1b** (Figure 20), resulting in bathochromic shifts of the Soret and Q bands compared with the monomer band.³⁶ In **1b**, the distance of the adjacent porphyrin systems is shorter than in **1a**, producing a slight red shift of the bands. Overall, the spectra of all the final systems (chiral and achiral) remind very similar without further information of the different supramolecular formations.

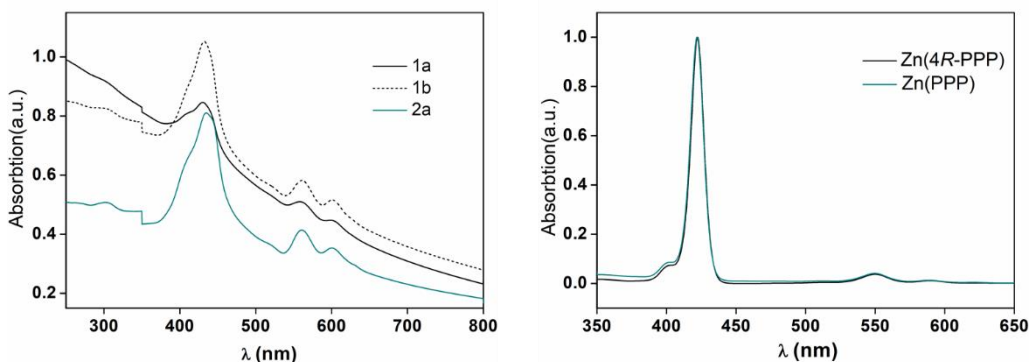


Figure 26. (Left) The solid-state UV-Vis of **1a**, **1b** and **2a**. (Right) UV-Vis absorption spectroscopy of **1** and **2** (**Zn(4R-PPP)** and **Zn(PPP)**) in CH_2Cl_2 .

Table 2. Maxima absorption of the solid-state UV-Vis spectra of crystals and UV-Vis absorption spectroscopic values of **1** and **2** in CH_2Cl_2 .

	Compound	Soret [nm] (I_{rel})	Q _{vib} [nm] (I_{rel})	Q (I_{rel})
	1a	430.0 (1.000)	558.4 (0.603)	598.6 (0.529)
Solid-state	1b	432.2 (1.000)	560.6 (0.554)	600.8 (0.491)
	2a	435.0 (1.000)	560.8 (0.511)	600.2 (0.436)
In CH_2Cl_2	Zn(4R-PPP)	422.2	550	589.4
	Zn(PPP)	422.0	549.2	589.8

2.6.5 Study the aggregates by solid-state circular dichroism spectroscopy

Since the spectra of the compounds in solution are related to the conformations adopted in a given solvent and do not reflect the solid-state condition, in order to correlate the structural differences of our Zn porphyrins, solid circular dichroism studies of **1a** and **1b** using a KBr matrix were performed. The key aspects for finding optimum conditions in the achievement of the spectra were described elsewhere.^{37,38} Here, both samples were grinded using an agate pestle during 5 min, 0.1 mg of the compounds (**1a-b**, **2a**) were added to 100 mg of KBr and the discs

were made under pressure for 5 min to obtain necessary thinness without disc fragility. Additionally, in the case of compounds with broad Cotton effects (CE), the band widths of the incident circularly polarized light under study were 1, 2, 5 and 10 nm respectively (see Figure A2.21-23) during the recording of the spectra. This experimental condition does not affect the spectra of the compounds reported here, since the Cotton effect of **1a** and **1b** are relatively broad while **2a** did not have clearly Cotton effect.

Taking into account isolated molecules, there are extensive literatures correlating the experimental Cotton effects (in solution and solid state) with the conformational stereoisomerism of chiral molecules.³⁹⁻⁴¹ But in supramolecular systems and condensed phases, the Cotton effects of chiral materials could be the consequence of the construction from chiral or achiral constituents.^{42,43} Our objective here was to establish the relationship between the CD spectra of the compounds and their supramolecular conformations via taking advantage of the existence of crystallographic data for all the systems under study. Figure 27 shows the comparison between the two species (**1a-b**) under such conditions (band width of 5 nm). In the solid state, compound **1a** displays two intense and proximate CD bands of opposite sign (positive-negative; positive chirality)⁴² between 375 and 500 nm (black solid line) centred at 431 and 444 nm respectively. In the case of **1b** (dotted line), CE are observed in the same range, although three CD signals appear (positive-negative-positive) and the one in the middle is the most intense in nature.

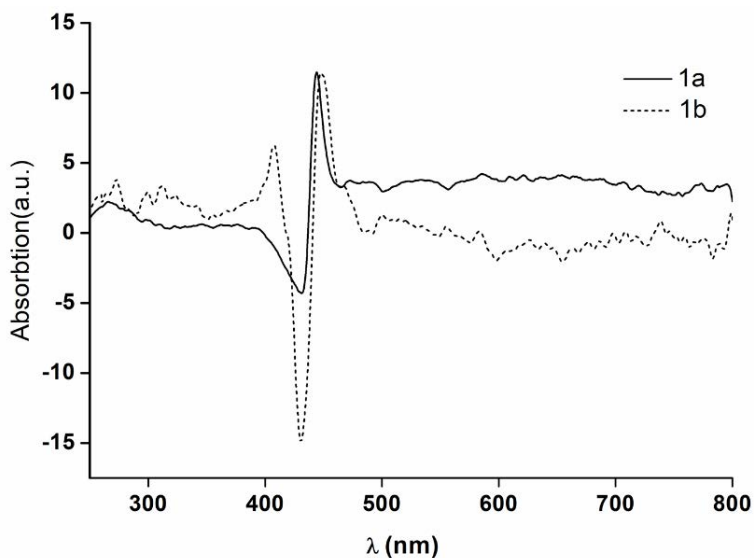


Figure 27. Solid state CD spectra of **1a** and **1b**.

Taking advantages of the collected X-ray diffraction data, the structural differences between the molecules are matched with changes in the CD spectra. In this way, the ligand which contained *R*-nature chirality was linked to an adjacent Zn porphyrin by H-bonding or coordination bonding, leading to a helical pattern in the crystal lattice (Figure 28 and 29).

In **1a**, the molecules are linked through H-bonding forming a 1D left-handed helical chain along b axis. The same system shows a bisignated signal with a negative Cotton effect at the lowest wavelength and a positive Cotton effect of similar intensity at higher wavelengths. This matches well with the position of the Soret absorption band of the porphyrin chromophore in solid and solution (Figure A2.24), where the presence of bisignate CD may also relate to the orientation of the adjacent porphyrin cores in a sliding face-to-face position, creating a 1D supramolecular structure through the H₂O interactions (Figure 28).

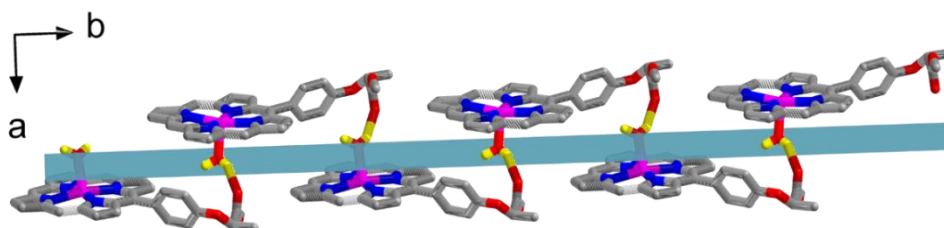


Figure 28. The adjacent chains of **1a** connected by left-handed helical H-bonding. Branches in the *meso*-positions not involved in H-bonding are omitted for the sake of simplification.

The above features are present in the CD spectrum of **1b** too, as the one-dimension porphyrin chain is helically twisted by the chirality of the peripheral groups, however, this right-hand helical (Figure 29) system differs from the previous by displaying a third positive CD signal, absent in **1a**, headed by the already mentioned strong positive-negative bisignate CD sign. The negative Cotton effect here is more pronounced than for **1a**. Such results could be associated to the expanded 1D network of **1b** by the coordination of the Zn(II) centres with CH₃CO₂⁻ moieties (instead of molecules of H₂O (**1a**)), and differences in the tridimensional packing between the two systems.⁴³ The first positive CD signals (highest wavelengths) for the two systems, **1a** and **1b**, with maxima at 444 nm and 448 nm respectively, following similar trends and intensity, indicate the close relation to the Soret band and therefore intrinsic structure of the other identical porphyrin units.

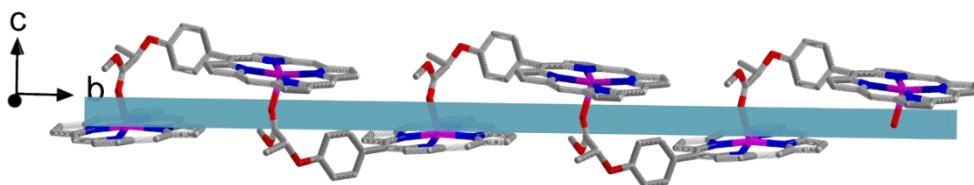


Figure 29. The adjacent chains of **1b** connected by right-handed helical coordination bonding. Branches in the *meso*-positions not involved in coordination are omitted for the sake of simplification.

2.6.6 Study the aggregates by solid-state vibrational circular dichroism spectroscopy

Solid-state VCD has great advantages toward the detailed analysis of molecular conformations because of the number of molecular vibrations in the IR region, and the sensitivity of the technique are larger than the electronic transitions in the UV-Vis region.⁴⁴ Nevertheless, working on the solid state one must be extremely careful to minimizing the spectral artefacts. The noise in each experiment and the signals found in the achiral system **2a** (Figure A2.25) were taken into account, as well as the theoretical calculations on system **1a** performed by collaborating with Prof. E. Ruiz from the University of Barcelona (UB) (Figure A2.26).

Experimentally, purple pellets were achieved by mixing/milling 2 mg of the samples and 150 mg of dry KBr. An 1800 cm^{-1} cut-off filter was used with two, 1700 and 1300 cm^{-1} , in both cases providing similar spectra. A set of spectra (five each time) were collected for **1a** and **1b** respectively, where each disk was rotated at intervals of 45°. Figure 30 shows the comparison between the IR and the VCD spectra of both systems. As expected, each absorbance band in the IR spectrum has a correspondence with a VCD band. DFT calculations, taking into account the single molecule **1a** (the length of the chain of **1b** hampers the study), display a number of motifs in the window under study in a similar manner although few shifted from the experimental values display opposite signal. Albeit contradiction, such results point out that the chiral response of the system involves the surroundings, where the supramolecular network is the responsible for the phenomenon.⁴⁵

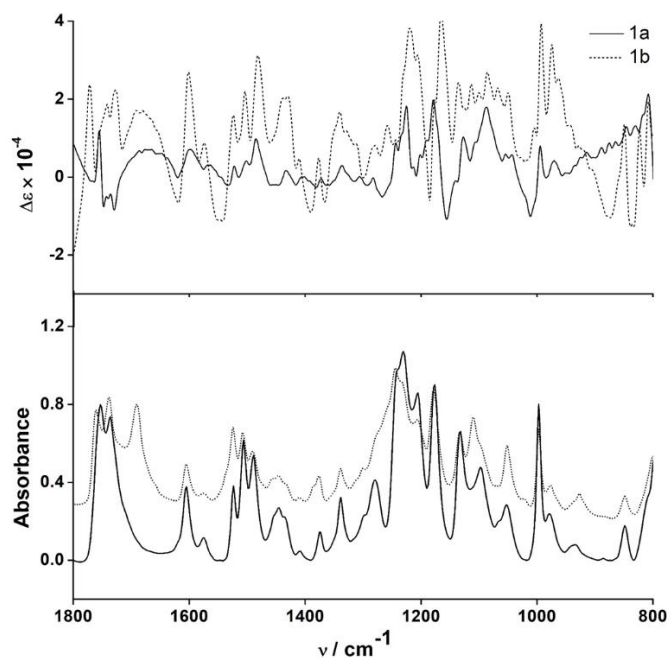


Figure 30. Solid state VCD spectra (top) and solid-state absorbance IR spectra (bottom) of **1a** and **1b**.

The measured and calculated VCD spectra of each system match well with those found in the IR experiment corresponding to 4*R*-systems (intensities are not comparable). The bands described in the range of 1800 to 1600 cm⁻¹ varies between the two species as anticipated due to the difference upon coordination of the Zn(II) centres of the porphyrin moieties with H₂O (**1a**) or some C=O groups (**1b**). In this region, the number of VCD bands found for **1b** is higher than **1a**, with some of them shifted to lower energies which probably due to the difference between the C=O groups bounded with respect to the non-bounded ones and additional intermolecular interactions in the tridimensional map of each system.

2.7 Morphological studies of Zn(II) porphyrins on surfaces

In a final attempt to study the factors that are involved in the formation of supramolecular structures, the reproducibility of crystals or aggregates on different surfaces were studied. Eight samples were prepared by drop casting solutions (10⁻³ M) of the chiral (**Zn(4*R*-PPP)**, **1**) and achiral (**Zn(PPP)**, **2**) porphyrins onto mica or highly oriented pyrolytic graphite (HOPG) substrates, in the same solvents mixture used to achieve **1a-b** and **2a-b** types: CH₂Cl₂/CH₃OH (1:1) or CH₂Cl₂/*n*-hexane (1:1) respectively. The porphyrins **1** and **2**, were completely dissolved and the aggregates were observed on the substrates by scanning electron microscopy (SEM). Once the aggregates formed, they were stable and maintain their shape for more than 2-3 weeks. There were no differences between the measurements carried out immediately after the preparation of the thin films and after several days, even without the metal coating which is normally used in SEM tests.

Here, the effects of solvents and surfaces were studied by the comparison with the morphologies found in the single X-ray diffraction experiments. This variety of **Zn(4*R*-PPP)** and **Zn(PPP)** nanoarchitectures were obtained by evaporation-driven self-assembly processes. The chiral and achiral porphyrins generated reproducible micro-vesicles, microrods flower-shaped aggregates and microplates bundles shapes, depending on the used conditions (Figures 31-35).

2.7.1 Studies of Zn(4*R*-PPP), from CH₂Cl₂/CH₃OH solutions

On mica and graphite, hollow vesicles appeared from the mixing and deposition of **Zn(4*R*-PPP)** in CH₂Cl₂/CH₃OH (Figure 31). On mica, the size and shapes of the aggregates were the most irregular, and sometime present cross-sectioned part of the vesicles, while on graphite, the micro-balls presented an average size of 600 nm with the pore diameter of ~300 nm. Overall, the vesicles in the latter were distinguishable and presented homogenous shapes, where some of them connected to others through small cords. In CH₂Cl₂/CH₃OH, hollow vesicles made of Zn-porphyrin systems have related to the π - π stacking of the porphyrin rings and the formation of J-type aggregates.⁴⁶ According to the crystallographic data of **1a**, our porphyrin micro-vesicles formation could be related to the ligand-assisted long-distance J-type formation.⁴⁷ In our case, the supramolecular 1D structure of **1a**, with up-down distributions of the porphyrins cores (Figures 28), differs from the regular staircase situation described in previous works.⁴⁸ The

general explanation for the holes formation, about the encapsulation of the volatile solvents inside the vesicles and later evaporation, is also applicable here.

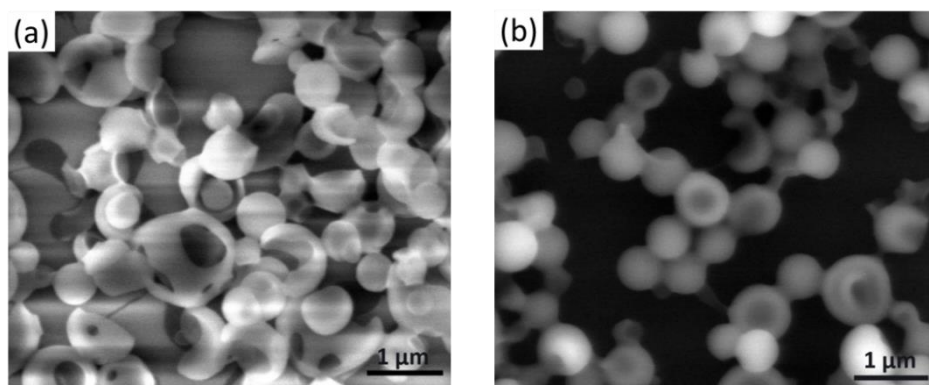


Figure 31. SEM images of **Zn(4R-PPP)** (10^{-3} M) prepared in $\text{CH}_2\text{Cl}_2/\text{CH}_3\text{OH}$ (1: 1) on substrates of (a) mica (b) HOPG.

2.7.2 Studies of **Zn(PPP)**, from $\text{CH}_2\text{Cl}_2/\text{CH}_3\text{OH}$ solutions

Repeating the exact same experiment but using **Zn(PPP)**, the architectures found on mica and graphene were totally different from before. Well-shaped microcrystals of different sizes presented parallelogram and prismatic geometries on mica (Figures 32(a)). The porphyrin was well crystallized without any more nanoballs left on the mica, and these crystalline cubes insert one by one along the same direction like a pine tree. On graphite, four-pointed star shapes were the most common morphology although bigger and amorphous aggregates were seen too (Figures 32(b)); all shapes intuitively relate to the layer-by-layer aggregation present in the structure of **2a** (Figure 16) and to the formation of short-distance J-type aggregates (staircase disposition).

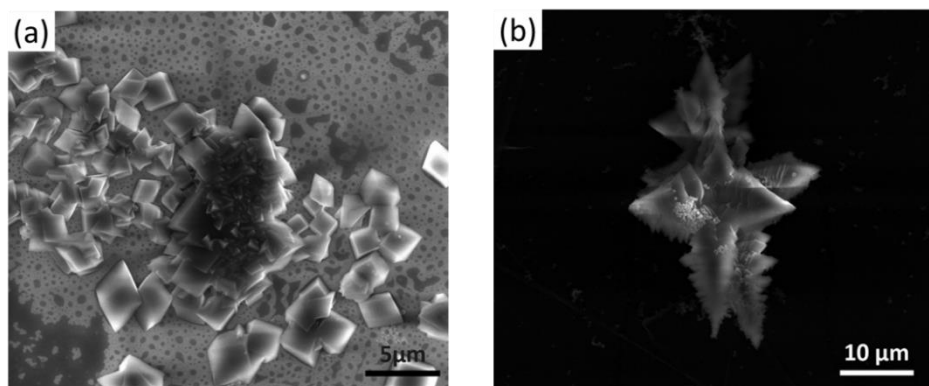


Figure 32. SEM images of **Zn(PPP)** (10^{-3} M) prepared in $\text{CH}_2\text{Cl}_2/\text{CH}_3\text{OH}$ (1: 1) on substrates of (a) mica (b) HOPG.

2.7.3 Studies of Zn(4R-PPP), from CH₂Cl₂/n-hexane solutions

On mica, when CH₂Cl₂/n-hexane was used with **1**, micro-balls together with slide micro-vesicles were observed again (Figure 33). The difference from the previous residues is that most of the micro-ball edges are smear and connecting each other, probably because of solvent flow and the longer sintering state during the evaporation process.

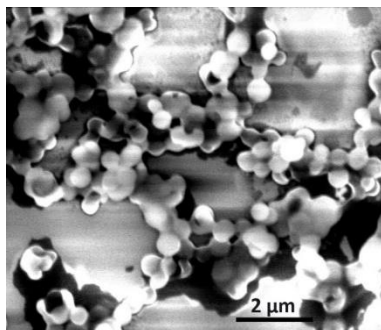


Figure 33. SEM images of Zn(4R-PPP) (10^{-3} M) prepared in CH₂Cl₂/n-hexane (1: 1) on mica.

On graphite, two distinctive morphologies were observed depending on the area of analysis. In this way, some of the parts presented micro-vesicles with sizes between 300-400 nm (Figures 34(a)). The topographic information in such cases was very similar to that found in CH₂Cl₂/CH₃OH; however, trigonal prisms were observed mostly in the edges of graphite (Figure 34(b)). They presented homogeneous size with a length of 8 μm and spherical defects in some of the prismatic faces (Figure 34(b1)). They were in the areas where the solvent gathered and the evaporation process was slower, providing more time for the ensemble and organization of the matter. The molecules flowed with the solvents and aggregated along one face of the initial prism, as the one edge decrease, leading to octahedron trending and 3D nanostructures were formed, which morphology match well with the crystal **1b** growth in the same condition in the solution. Such prismatic microcrystals show similarities with those at the macroscopic scale used for the X-ray diffraction analysis (Figure 6). This was established by the fact that exists of few cracked microcrystals suggest the aggregation of micro-vesicles like expanded polystyrene balls (Figure 34(b2)).

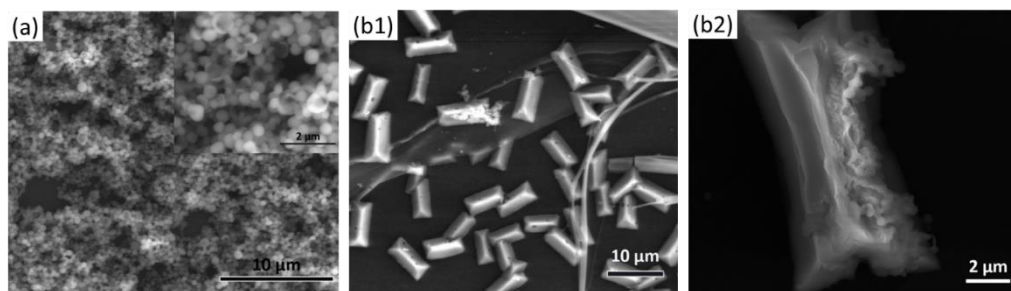


Figure 34. SEM images of Zn(4R-PPP) (10^{-3} M) prepared in CH₂Cl₂/n-hexane (1: 1) on surface of HOPG in different zone (a) quickly evaporate of solvent, (b1, b2) in the middle of solution drop.

2.7.4 Studies of Zn(PPP), from CH₂Cl₂/n-hexane solution

Finally, the same mixture using **2** on mica showed microplates, with diverse shapes and sizes, having flower-shaped topologies (Figure 35(a)). In former works, the formation of the latest relates usually to H₂O.⁴⁹ Here this association cannot be discriminated but neither defended. However, in both cases, microplates and micro-petals, it is clear that the existence of an extended face versus the others, connecting with the 2D layers observed in the **2b** system which is typical in other layered materials as well.⁵⁰

Regarding the experiment in graphite, multiple micro-blocks were presented again with a variety of size and prismatic shapes (Figure 35(b)). Generally speaking, the aggregates have an affinity to stick together under the preparation of the substrate with the formation of large blocks. In this case, the aggregates displayed smooth surfaces and sharp edges, and the size depends on the deposition and evaporation processes,⁵¹ in which the concentration of the material relies on the different terraces of the graphite surface. Either way, this result is different from the macroscopic scale in solution, where the crystals were scarce and difficult to achieve, pointing out the tendency of graphite to provide crystalline material under these conditions.

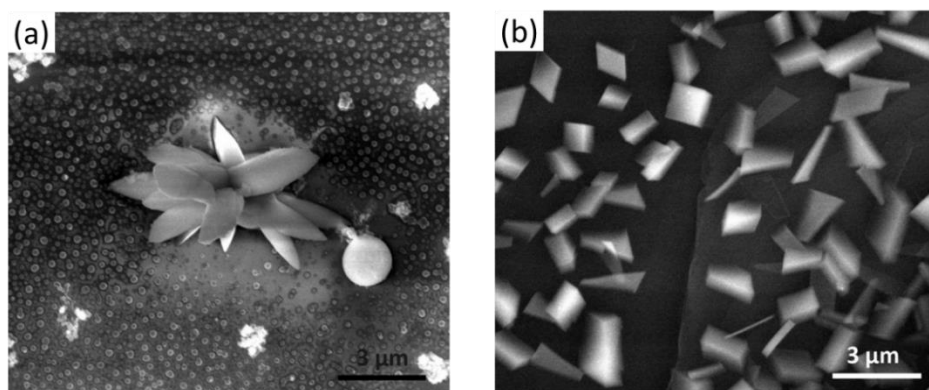


Figure 35. SEM images of Zn(PPP) (10^{-3} M) prepared in CH₂Cl₂/n-hexane (1: 1) on substrates of (a) mica (b) HOPG.

2.8 Solution-processed BHJ OSCs based on porphyrin Zn(4R-PPP)

2.8.1 Optical absorption spectra, electrochemical and thermal properties

As shown in Figure 36, the absorption spectra of Zn(4R-PPP) in solution and in film give partial spectral coverage in the UV and visible regions, which were commonly observed in other porphyrin systems. Notably, the absorption of Zn(4R-PPP) film shows a broader Soret band and a new shoulder peak at 624 nm, which is attributed to the formation of a vibronic crystalline

structure similar to previous reported porphyrins.⁵² Compared with the molecules in solution, the bathochromic shift of the absorption peaks on film also implies the improved crystallinity, probably due to lower density of conformational chain defects which would lead to longer π -conjugation systems and therefore lower bandlike energies.⁵³ The increased intermolecular interactions could be beneficial to a higher hole mobility and photovoltaic performance for OPVs,^{52,54} and the optical band gap of **Zn(4R-PPP)** is estimated to be 1.93 eV from the onset of the absorption spectrum in the film.

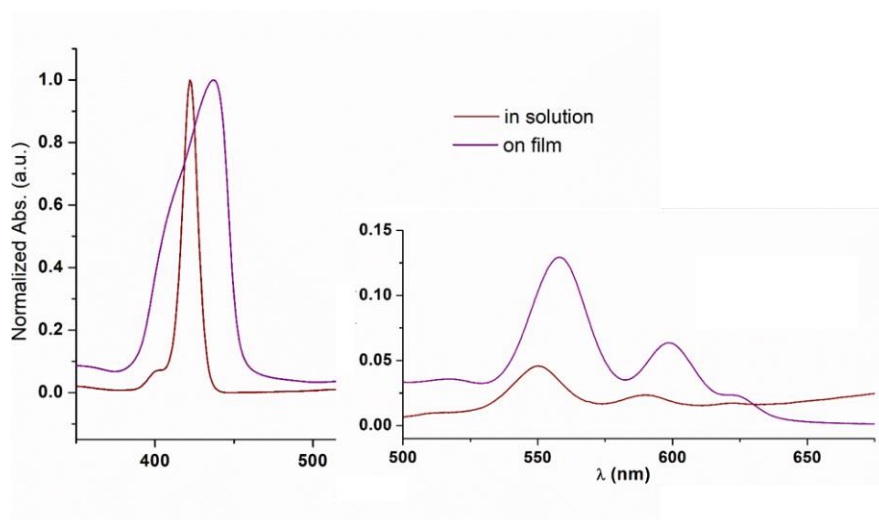


Figure 36. UV-Vis absorption spectra of **Zn(4R-PPP)** in CH_2Cl_2 solution and in film.

The HOMO and LUMO levels of **Zn(4R-PPP)** were measured by electrochemical cyclic voltammetry (CV) and differential pulse voltammetry (DPV). As shown in Figure 37(a), both the oxidation and reduction processes of this molecule are reversible. The onset points of the n- and p-doping processes are 0.10 and -1.87 V, and the HOMO and LUMO levels of **Zn(4R-PPP)** were calculated to be -4.90 and -2.93 eV, respectively (method described in Appendix). The LUMO energy level is positioned at 1.01 eV above the LUMO level of phenyl-C61-butyric acid methyl ester (PCBM) (-3.94 eV), and that would ensure an efficient photo-induced electron transfer. Compared with poly(3-hexylthiophene) (P3HT), which is normally used as a donor material in OSC, the energy levels of **Zn(4R-PPP)** are a bit higher. The energy level diagrams of the compounds⁵⁵ are illustrated in Figure 37(b).

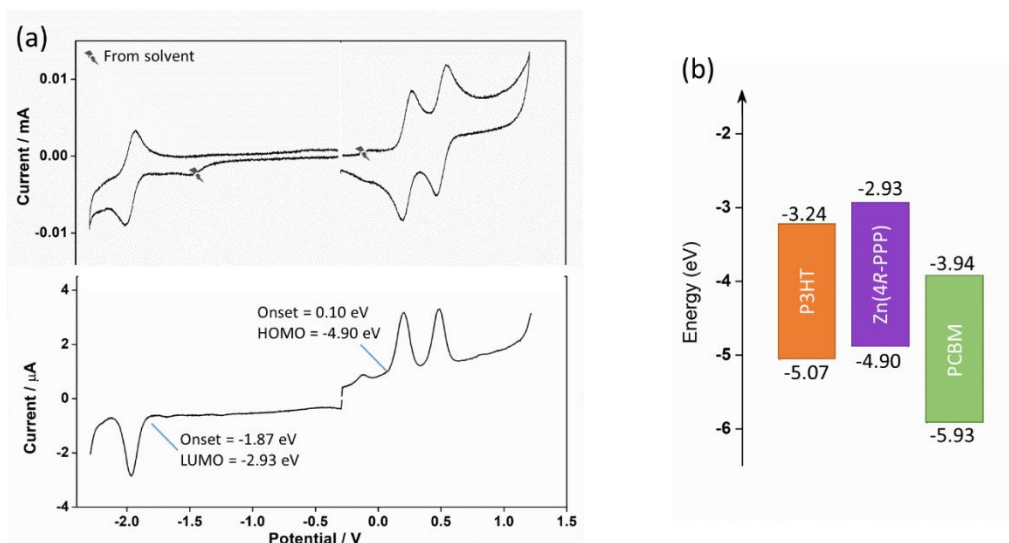


Figure 37. (a) Cyclic voltammograms (top) and differential pulse voltammograms (bottom) of **Zn(4R-PPP)** (0.5 mM) in 0.1 M TBAPF₆ CH₂Cl₂ solution. Potentials vs. Fc/Fc⁺. (b) Energy levels diagrams of **Zn(4R-PPP)**, P3HT and PCBM used in the OPV devices.

Thermogravimetric analysis shows that **Zn(4R-PPP)** exhibits good stability below 350 °C without the protection of an inert atmosphere (Figure A2.27), indicating that the thermal stability of the molecule is good enough for its application in optoelectronic devices.

2.8.2 Morphological characterization and optical properties of the blends of **Zn(4R-PPP)** with P3HT and PCBM

As the donor material, **Zn(4R-PPP)** exhibits good solubility in common organic solvents, such as CH₂Cl₂, CHCl₃, chlorobenzene (CB) and toluene. In our previous study, this metalloporphyrin demonstrated 1D structure by supramolecular (**1a**) or coordination (**1b**) from the CH₂Cl₂ contained mixture solvent. We tried to form compounds films by spin-coating from CH₂Cl₂ solution and use P3HT and PCBM as references, nevertheless, P3HT was not soluble in CH₂Cl₂ and the PCBM film was rather rough with big phase aggregations (Figure A2.28). Chlorobenzene is a considerable solvent due to the high boiling point (132 °C) and less relative polarity (0.05) which may benefit the polymeric assembly of **Zn(4R-PPP)**, since the molecules have more time to undergo the self-organization process before complete solidification. According to the study from Vanlaeke *et al.*⁵⁶, the active layer made from the solvent having a higher boiling point has higher crystallinity, resulting in higher device performance. Figure 38 presents the morphologies of the three compounds and their mixture (1:1 w/w) on the glass substrates from chlorobenzene solutions (20 mg/mL) and the preparation progress is described in the Appendix. The self-assembly ability from the chlorobenzene solvent allows the formation of thin-film morphologies for the **Zn(4R-PPP)** porphyrin without excess of aggregates. The surface of the blend films processed with the P3HT and PCBM are more or less the same smooth, suggesting that the molecule has good compatibility with the references compounds. The morphological features

may benefit for efficient exciton dissociation and charge transporting, leading to an expected efficiency for a corresponding solar cell.

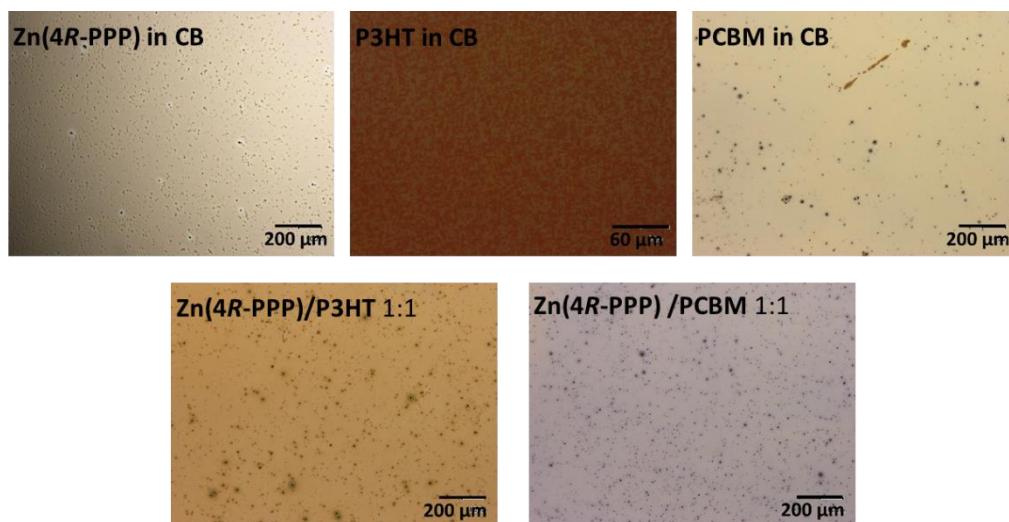


Figure 38. Microscope images of films formed by spin-coating chlorobenzene solution of **Zn(4R-PPP)**, P3HT, PCBM and the blends (1:1 w/w).

The normalized UV-Vis absorption spectra of the blends films processed with P3HT and PCBM were also measured to extract more information from the BHJ layers. As shown in Figure 39, the films of blends display the absorption of the combined contribution of porphyrin and P3HT or PCBM, which is at 514 and 335 nm respectively. By the four-orbital model of porphyrin,⁵⁷ that is the intensity changes and energy shifts of spectra are related to the properties of two top filled and two lowest empty π orbitals (HOMO and LUMO), the slight shift of the Soret band in the blends comparing to **Zn(4R-PPP)** indicates the effective interaction of the mixture.

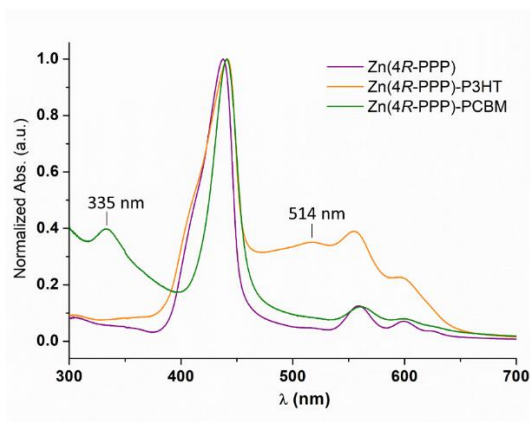


Figure 39. UV-Vis absorption spectra of the blend films (1: 1, w/w).

2.8.3 Photovoltaic characteristics

The fabrication of the BHJ OSCs devices was thanks to the in-house collaboration with the group of Dr. M. Campoy, at the ICMA. The devices were fabricated with a general structure of ITO/PEDOT:PSS/active materials/Al (Figure 40a) with a gradient film thickness and were measured under AM 1.5 solar simulator at $100 \text{ mW}\cdot\text{cm}^{-2}$. The remarkable blade-coating technique developed by our collaborator enable to brush a gradient thickness of the active layer from 400 nm to 50 nm in one device (Figure 40b), which was realized by varying the speed of the blade. In further, the back electrodes Aluminium were deposited at equidistant positions on the top, by which the efficiency of device with different thickness of active layer from one chip can be measured. This methodology simplified the study of fabricating devices and realized the material-saving.

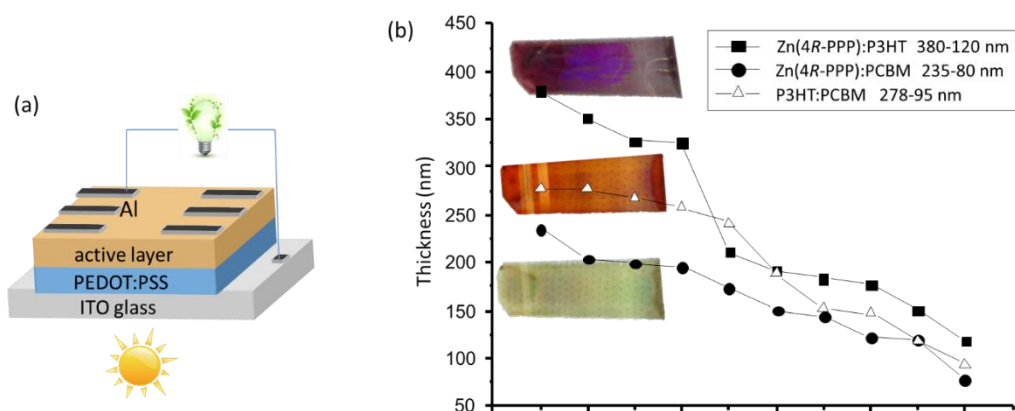


Figure 40. (a) Schematic of the ITO/PEDOT: PSS/active materials/Al device. (b) The thickness of active layer composed by blends of **Zn(4R-PPP)** with P3HT and PCBM.

To confirm the performance of the solar cell based on solution processed zinc porphyrins, here a reference (blank) using a P3HT-PCBM blend was prepared, which are commonly used as donor and acceptor materials in OSCs. Figure 41 presents the results of powder conversion efficiency (PCE) corresponding to gradient thickness of each chip, demonstrating the OPV performance changed with the thickness of the active layer. Due to unexpected problems with the PEDOT:PSS mixture used in the devices, the blank displays values lower than the expected for a P3HT-PCBM blend; nevertheless, these numbers were used to compare with the effect of porphyrin molecule **Zn(4R-PPP)**, indicating the latter worked better as a donor (in agreement with the HOMO-LUMO values obtained from electrochemistry). Together with PCBM, the final set up displayed a highest PCE of 0.01 %.

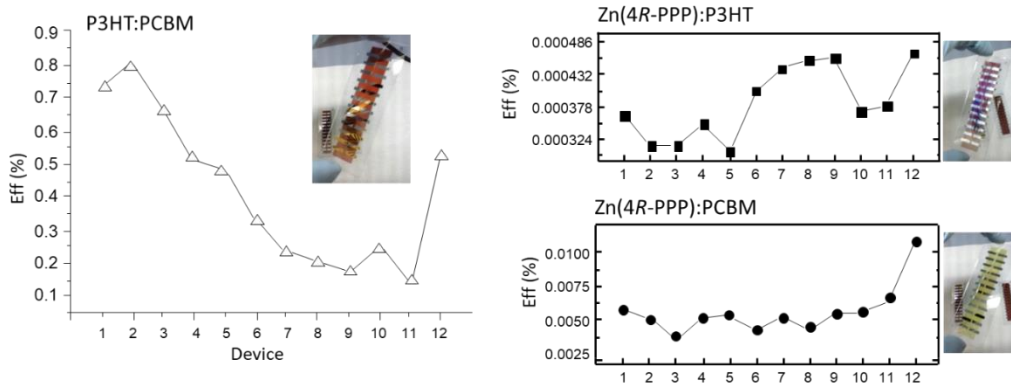


Figure 41. PCE (%) values of the devices at equidistant positions.

2.9 Conclusions

Using Zn-porphyrin derivatives as unit models, the construction of well-defined nanostructure based on a unique molecular unit was described. The addition of a metal centre increases the range of diversity in the coordinative way meanwhile blocks strong π - π stacking interactions among the porphyrin cores giving priority to the nature of the arms, which are key parts in the creation of the supramolecular arrays. The four arms are flexible enough and the carbonyl moieties, from the ester groups at the edges, present the freedom to attach the Zn(II) centres in different manners where the final coordination number of the metallic centre can vary from four to six, depending on the overall conditions.

The comparison between **Zn(4R-PPP)** and **Zn(PPP)** which bearing chiral and non-chiral moieties respectively (repeating exact conditions) provides different crystallographic species, pointing out the complexity of adding chirality among the other factors already mentioned (coordination and solubility). **1a** and **1b** show a quite distinctive 1D supramolecular structure, and **Zn(PPP)** could form porphyrin monomer without guest molecular (**2a**) and penta-coordinated centre (**2c**), or 2D grid polymer with Zn(II) hexa-coordinated (**2b**).

The tuning of solvent conditions directly affected the self-assembly process, and therefore the morphologies of aggregates. Even though not too much information of Zn porphyrins self-assembly in solution studies was obtained, the outcome crystals indicate that the nature of the precipitant solvents can change the stabilization of mononuclear entities. For **Zn(4R-PPP)**, the system of $\text{CH}_2\text{Cl}_2/\text{CH}_3\text{OH}$ and $\text{CH}_2\text{Cl}_2/n\text{-hexane}$ both work well, but in the case of **Zn(PPP)**, which has less methyl groups, the solubility decreased from polar (CH_3OH) to apolar ($n\text{-hexane}$) resulting in low crystallization yields. The use of THF (instead of CH_2Cl_2) changes the supramolecular architecture. In the case of **Zn(PPP)**, THF improves its solubility, favouring the formation of crystals in good yields. Our results emphasize on the relevance of porphyrin crystallization toward their future applications such as in solution-processed organic solar cells which face the present challenges, due to the lack of anticipation of the final architectures.

Successful results of porphyrin self-assembly have been achieved in the solid-state studies, and the type of supramolecular assembling in the crystal can be controlled by molecular design and organization conditions. ^{13}C NMR showed highly sensitivity to identify small but critical changes in the final conformations. On the topic of chirality, CD and VCD solid-state experiments presented differences between **1a** and **1b**, stressing their sensitivity as well, although the variations in the former were not intuitive and it would be difficult to understand without the assistance of the crystallographic data. In the second case, it presented relevant changes in the area related to the C=O stretching, which in agreement with the coordination to Zn atoms. Yet, it is worth to emphasize that the proper analysis of the structures by the exclusive use of such techniques requires the creation of extended libraries and corroboration from theoretical calculations. In addition, the studies of our systems on two different substrates HOPG and mica show the enormous effect of the surfaces on the final structures, providing a variety of vesicles, flower-shapes and well defined geometrical architectures, and enhancing the capacity of achieving microcrystals (e.g. **2b** in graphite).

Finally, an initial solution-processed BHJ OSCs experiments displayed power conversion efficiencies of 0.01 %, which could be improved by the quality of auxiliary constituents on the device in the future.

Experimental Section:

Synthesis Methods.

1. (R)-G1

Triphenylphosphine (12.9 g, 49.13 mmol), 4-hydroxybenzaldehyde (5 g, 40.94 mmol) and (-)-Methyl L-lactate (4.97 mL, 52.04 mmol) were dissolved in 150 mL dry THF. The catalyst, diisopropyl azodicarboxylate (DIAD) (9.95 mL, 52.04 mmol), was diluted in 50 mL of dry THF, then added into the mixture drop by drop. After stirring in an ice bath under N_2 overnight, the reaction was quenched with water. Evaporation to dryness of the solvent provided a crude compound. After adding n-hexane/AcOEt (20 mL, 1:1) to the solid and shake, white crystal came out, and the crude liquid compound became yellowish. The liquid was transfer to a column chromatograph (SiO_2 , n-hexane/AcOEt 80:20) and purified, affording the desired product as a yellow oil (6.24 g, 73 %). ^1H NMR (300MHz, CDCl_3 , 25 °C) δ : 9.89 (s, CHO), 7.83 (d, 2H, ArH), 6.96 (d, 2H, ArH), 4.87 (q, 1H, OCHCH₃COO), 3.77 (s, 3H, OCH₃), 1.66 (d, 3H, OCHCH₃COO). ATR-FTIR date (cm^{-1}): 2956 (br, CHO), 1738 (s, COO), 1685 (s, COH), 1598 (s, phenyl), 1508 (s, phenyl), 1131 (s, OCH₃), 831 (s, phenyl H).

2. 4-((1-methylacetate)oxy)-benzaldehyde (G2)

To a dry solution of 4-hydroxybenzaldehyde (5 g, 41 mmol) in acetone (120 mL), anhydrous potassium carbonate (8.5 g, 61.5 mmol, 1.5 eq) was added and the mixture was stirred vigorously at 20 °C. After portion-wise addition of methylbromoacetate (5 mL, 53 mmol, 1.3 eq), the mixture was stirred for another 30 minutes at 20 °C, and then was heated to reflux for 4 h and cooled down.

The mixture was concentrated in vacuo, dissolved in EtOAc, followed by addition of water. The aqueous phase, which presumably contained potassium hydrogen carbonate was removed, and the organic phase was washed with additional water, dried (Mg_2SO_4), filtered and concentrated under reduced pressure yielding the product as a yellow oil. After addition of a bit hexane and leave it in the ice bath, white crystal came out over time (6.77 g, 85 %). 1H NMR (400 MHz, $CDCl_3$) δ 9.90 (s, 1H, HCO), 7.85 (d, 2H, phenyl H), 7.01 (d, 2H, phenyl H), 4.73 (s, 2H, CH₂), 3.82 (s, 3H, CH₃).

3. 5,10,15,20-Tetra[(4-*R,R,R,R*)-methyl-2-phenoxy-propanoate]-porphyrin, (4R-H₂PPP)

Freshly distilled pyrrole (810 μ L, 11.53 mmol) was mixed with 4-formylphenoxy propanoate (2.4 g, 11.53 mmol) and refluxed during 2 h using propionic acid as solvent (42 mL). After the vacuum distillation of propionic acid, the remaining dark viscous solid was washed with a saturated sodium carbonate solution to remove residual acid. The free-base porphyrin was then isolated as a purple solid after purification by column chromatography (SiO_2 , CH_2Cl_2/CH_3OH 100:0.5)²¹. Yield: 790 mg (27 %). Anal. calcd for $C_{60}H_{54}N_4O_{12}$ (1023.09 $g \cdot mol^{-1}$): C 70.44; H 5.32; N 5.48. Found: C 70.57; H 5.27; N 5.39. 1H NMR (300 MHz, $CDCl_3$, 25 °C): δ 8.84 (s, 8H), 8.10 (d, J = 8.7 Hz, 8H), 7.24 (d, J = 8.7 Hz, 8H), 5.23 – 4.95 (m, 4H), 3.93 (s, 12H), 1.83 (d, J = 6.8 Hz, 12H), -2.80 (s, 2H). ATR-FTIR date (cm^{-1}): 3319(w), 2925(w), 1755(s), 1739(s), 1605(m), 1504(m), 1133(s), 967(m), 736(w). Maldi-TOF/MS m/z (%): 1022.68 ([4R-H₂PPP]⁺).

4. H₂(PPP)

Freshly distilled pyrrole (800 μ L, 11.53 mmol) was mixed with methyl (4-formylphenoxy) acetate (G2) (2.239 g, 11.53 mmol) in refluxing propionic acid (42 mL). After 2 hours, propionic acid was removed by vacuum distillation. The dark viscous material that remained was washed with saturated sodium carbonate solution. The free-base porphyrin (H₂PPP) was isolated as a purple solid (723mg, 26%) after purification by column chromatography (SiO_2 , CH_2Cl_2/CH_3OH 100:0.5). Anal. calcd for $C_{56}H_{46}N_4O_{12}$ (966.98 $g \cdot mol^{-1}$): C 69.56; H 4.79; N 5.79. Found: C 69.45; H 4.67; N 5.64. 1H NMR (300 MHz, $CDCl_3$, 25 °C): δ 8.85 (s, 8H), 8.13 (d, J = 8.5 Hz, 8H), 7.29 (d, J = 8.5 Hz, 8H), 4.94 (s, 8H), 3.95 (s, 12H), -2.79 (s, 2H). ATR-FTIR date (cm^{-1}): 3650(w), 2954(m), 1753(s), 1604(m), 1507(m), 1219(s), 1170(s), 1084(m), 997(w), 966(w), 802(m) Maldi-TOF/MS m/z (%): 966.22 ([H₂PPP]⁺).

5. Zn(4R-PPP), 1a and 1b

4R-H₂PPP (300 mg, 293 μmol) was dissolved and refluxed in 40 mL of CH_2Cl_2 under N_2 atmosphere. A solution of $\text{Zn}(\text{CH}_3\text{COO})_2 \cdot 2\text{H}_2\text{O}$ (220 mg, 1 mmol) in a mixture of $\text{CH}_3\text{OH}/\text{CH}_2\text{Cl}_2$ (10 ml:10 ml) was added drop wise. The reaction was monitored by absorption UV-Vis spectroscopy (~ 3 h). Afterward, the final solution was washed with NaHCO_3 saturated aqueous solution, brine and distilled water. The organic phase was extracted using CH_2Cl_2 . The removal of the solvent gave the desired product as a shining purple solid. Yield: 278 mg (86 %).

Synthesis of $[\text{Zn}(\text{OH}_2)(4\text{R-PPP})]$ (**1a**). Suitable crystals for X-ray diffraction analyses of **1a** were achieved after few days by dissolving the solid in a 1:1 mixture of CH_2Cl_2 and CH_3OH , leaving the final solution open to air. Anal. calcd for $\text{C}_{60}\text{H}_{52}\text{N}_4\text{O}_{12}\text{Zn} \cdot 1.45\text{H}_2\text{O}$: C 64.77; H 4.97; N 5.04. Found: C 64.64; H 4.80; N 4.94. ATR-FTIR date (cm^{-1}): 3642(w), 3478(w), 2989(w), 1751(s), 1733(s), 1605(m), 1505(s), 1488(s), 1445(m), 1338(m), 1277(m), 1203(s), 1172(s), 1129(s), 995(s), 846(m), 795(s). Maldi-TOF/MS m/z (%): 1084.62 ($[\text{Zn}(4\text{R-PPP})]^+$).

Synthesis of $[\text{Zn}(4\text{R-PPP})]_n$ (**1b**). **1b** was achieved by following previous procedure but using dehydrated $\text{Zn}(\text{CH}_3\text{COO})_2$. Yield: 277 mg (86 %). Crystals of **1b** were achieved by dissolving the final solid in CH_2Cl_2 and layering the solution with C_6H_{14} (Fig. 3 and 4). Anal. calcd for $\text{C}_{60}\text{H}_{52}\text{ZnN}_4\text{O}_{12}$ ($1086.45 \text{ g} \cdot \text{mol}^{-1}$): C 66.33; H 4.82; N 5.16. Found: C 66.61; H 5.07; N 5.02. ATR-FTIR date (cm^{-1}): 2988(w), 1757(s), 1739(s), 1721(s), 1605(m), 1506(s), 1445(m), 1340(m), 1201(s), 1176(s), 1131(s), 996(s), 799(s). Maldi-TOF/MS m/z (%): 1084.63 ($[\text{Zn}(4\text{R-PPP})]^+$).

6. Zn(PPP), 2a, 2b and 2c

To synthesis of $\text{Zn}(\text{PPP})$, the procedure was identical to that described in $\text{Zn}(4\text{R-PPP})$ but using H_2PPP .

Synthesis of $[\text{Zn}(\text{PPP})]$ (**2a**). Crystals of **2a** were achieved as for **1a**. Yield: 249 mg (78 %). Anal. calcd for $\text{C}_{56}\text{H}_{44}\text{N}_4\text{O}_{12}\text{Zn} \cdot 1.85\text{H}_2\text{O}$: C 63.23; H 4.52; N 5.27. Found: C 63.01; H 4.29; N 5.07. ATR-FTIR date (cm^{-1}): 3347(w), 2851(w), 1752(s), 1606(m), 1509(s), 1434(m), 1284(w), 1217(s), 1204(s), 1171(s), 1084(s), 997(s), 799(s), 717(m). Maldi-TOF/MS m/z (%): 1028.15 ($[\text{Zn}(\text{PPP})]^+$).

Synthesis of $[\text{Zn}(\text{PPP})]_n$ (**2b**). Crystals of **2b** were achieved by following the procedure described in **1b**. Crystallographic data was pursued and shown in the thesis. Further analyses were unfeasible due to the scarce amount of the crystalline samples.

Synthesis of $[\text{Zn}(\text{THF})(\text{PPP})]$ (**2c**). Crystals of **2c** were acquired in quantify from THF / n-hexane solution of $\text{Zn}(\text{PPP})$. Dissolved 10 mg of $\text{Zn}(\text{PPP})$ in 10 mL THF respectively, then add 10 mL hexane on the top of the solution for diffusion.

References:

- (1) Beaujuge, P. M.; Fréchet, J. M. *Journal of the American Chemical Society* **2011**, *133*, 20009.
- (2) Fujita, M. *Chemical Society Reviews* **1998**, *27*, 417.
- (3) Raymond, J. E.; Bhaskar, A.; Goodson III, T.; Makiuchi, N.; Ogawa, K.; Kobuke, Y. *Journal of the American Chemical Society* **2008**, *130*, 17212.
- (4) Balaban, T. S.; Goddard, R.; Linke-Schaetzl, M.; Lehn, J.-M. *Journal of the American Chemical Society* **2003**, *125*, 4233.
- (5) Huang, Z.; Kang, S.-K.; Banno, M.; Yamaguchi, T.; Lee, D.; Seok, C.; Yashima, E.; Lee, M. *Science* **2012**, *337*, 1521.
- (6) Martín, T.; Obst, U.; Rebek, J. *Science* **1998**, *281*, 1842.
- (7) Terazono, Y.; Kodis, G.; Chachisvilis, M.; Cherry, B. R.; Fournier, M.; Moore, A.; Moore, T. A.; Gust, D. *Journal of the American Chemical Society* **2014**, *137*, 245.
- (8) Sun, D.; Tham, F. S.; Reed, C. A.; Chaker, L.; Boyd, P. D. *Journal of the American Chemical Society* **2002**, *124*, 6604.
- (9) Hoeben, F. J.; Wolfs, M.; Zhang, J.; De Feyter, S.; Leclère, P.; Schenning, A. P.; Meijer, E. *Journal of the American Chemical Society* **2007**, *129*, 9819.
- (10) Rousseaux, S. A.; Gong, J. Q.; Haver, R. e.; Odell, B.; Claridge, T. D.; Herz, L. M.; Anderson, H. L. *Journal of the American Chemical Society* **2015**, *137*, 12713.
- (11) Shoji, O.; Okada, S.; Satake, A.; Kobuke, Y. *Journal of the American Chemical Society* **2005**, *127*, 2201.
- (12) Rui, X.; Zha, Q.-Z.; Wei, T.-T.; Xie, Y.-S. *Inorganic Chemistry Communications* **2014**, *48*, 111.
- (13) Fleischer, E. B.; Shachter, A. M. *Inorganic Chemistry* **1991**, *30*, 3763.
- (14) Yang, J.-W.; Zhang, J.; Yan, Y.; Huang, X.-C.; Tong, S.-L. *Solid State Sciences* **2010**, *12*, 1242.
- (15) Suijkerbuijk, B. M.; Tooke, D. M.; Spek, A. L.; van Koten, G.; Klein Gebbink, R. J. *Chemistry—An Asian Journal* **2007**, *2*, 889.
- (16) Oliveras-González, C.; Di Meo, F.; González-Campo, A. n.; Beljonne, D.; Norman, P.; Simón-Sorbed, M.; Linares, M.; Amabilino, D. B. *J. Am. Chem. Soc* **2015**, *137*, 15795.
- (17) Iavicoli, P.; Xu, H.; Feldborg, L. N.; Linares, M.; Paradinas, M.; Stafström, S.; Ocal, C.; Nieto-Ortega, B.; Casado, J.; Lopez Navarrete, J. T. *Journal of the American Chemical Society* **2010**, *132*, 9350.
- (18) Helmich, F.; Lee, C. C.; Schenning, A. P.; Meijer, E. *Journal of the American Chemical Society* **2010**, *132*, 16753.
- (19) Bellacchio, E.; Lauceri, R.; Gurrieri, S.; Scolaro, L. M.; Romeo, A.; Purrello, R. *Journal of the American Chemical Society* **1998**, *120*, 12353.
- (20) Minguet, M.; Amabilino, D. B.; Vidal-Gancedo, J.; Wurst, K.; Veciana, J. *Journal of Materials Chemistry* **2002**, *12*, 570.
- (21) Linares, M.; Iavicoli, P.; Psychogiopoulou, K.; Beljonne, D.; De Feyter, S.; Amabilino, D. B.; Lazzaroni, R. *Langmuir* **2008**, *24*, 9566.
- (22) Iavicoli, P.; Linares, M.; del Pino, A. P.; Lazzaroni, R.; Amabilino, D. B. *Superlattices and Microstructures* **2008**, *44*, 556.
- (23) Feldborg, L. N.; Saletta, W. J.; Iavicoli, P.; Amabilino, D. B. *Journal of Porphyrins and Phthalocyanines* **2011**, *15*, 995.
- (24) But, T. Y. S.; Toy, P. H. *Chemistry—An Asian Journal* **2007**, *2*, 1340.
- (25) Hoogendoorn, S.; Blom, A. E.; Willems, L. I.; van der Marel, G. A.; Overkleeft, H. S. *Organic letters* **2011**, *13*, 5656.
- (26) Karlsson, S.; Sörensen, J. H. *Organic Process Research & Development* **2012**, *16*, 586.

- (27) Adler, A. D.; Longo, F. R.; Shergalis, W. *Journal of the American Chemical Society* **1964**, *86*, 3145.
- (28) Huijser, A.; Suijkerbuijk, B. M.; Klein Gebbink, R. J.; Savenije, T. J.; Siebbeles, L. D. *Journal of the American Chemical Society* **2008**, *130*, 2485.
- (29) Teo, T.-L.; Vetrichelvan, M.; Lai, Y.-H. *Organic letters* **2003**, *5*, 4207.
- (30) Brotherhood, P. R.; Luck, I. J.; Crossley, M. J. *Magnetic Resonance in Chemistry* **2009**, *47*, 257.
- (31) Zsila, F.; Bikádi, Z.; Fitos, I.; Simonyi, M. *Current drug discovery technologies* **2004**, *1*, 133.
- (32) Habib, H. A.; Hoffmann, A.; Höpfe, H. A.; Janiak, C. *Dalton Transactions* **2009**, 1742.
- (33) Dugar, S.; Fu, R.; Dalal, N. S. *The Journal of Physical Chemistry B* **2012**, *116*, 9215.
- (34) Strohmeier, M.; Orendt, A. M.; Facelli, J. C.; Solum, M. S.; Pugmire, R. J.; Parry, R. W.; Grant, D. M. *Journal of the American Chemical Society* **1997**, *119*, 7114.
- (35) Bampos, N.; Prinsep, M. R.; He, H.; Vidal-Ferran, A.; Bashall, A.; McPartlin, M.; Powell, H.; Sanders, J. K. *Journal of the Chemical Society, Perkin Transactions 2* **1998**, 715.
- (36) Giovannetti, R. In *Macro to nano spectroscopy*; InTech: 2012.
- (37) Minguet, M.; Amabilino, D. B.; Wurst, K.; Veciana, J. *Journal of the Chemical Society, Perkin Transactions 2* **2001**, 670.
- (38) Castiglioni, E.; Biscarini, P.; Abbate, S. *Chirality* **2009**, *21*.
- (39) Avula, S. K.; Hussain, H.; Csuk, R.; Sommerwerk, S.; Liebing, P.; Górecki, M.; Pescitelli, G.; Al-Rawahi, A.; Rehman, N. U.; Green, I. R. *Tetrahedron: Asymmetry* **2016**, *27*, 829.
- (40) Górecki, M. *Chirality* **2015**, *27*, 441.
- (41) Kocourková, L.; Novotná, P.; Šťovíčková-Habartová, L.; Čujová, S.; Čeřovský, V.; Urbanová, M.; Setnička, V. *Monatshefte für Chemie-Chemical Monthly* **2016**, *147*, 1439.
- (42) Hembury, G. A.; Borovkov, V. V.; Inoue, Y. *Chemical reviews* **2008**, *108*, 1.
- (43) Zheng, C.-Y.; Li, H. *Inorganic Chemistry Communications* **2013**, *34*, 30.
- (44) Frelek, J.; Górecki, M.; Łaszcz, M.; Suszczyńska, A.; Vass, E.; Szczepek, W. J. *Chemical Communications* **2012**, *48*, 5295.
- (45) Jiang, N.; Tan, R. X.; Ma, J. *The Journal of Physical Chemistry B* **2011**, *115*, 2801.
- (46) Huang, C.; Li, Y.; Yang, J. e.; Cheng, N.; Liu, H.; Li, Y. *Chemical Communications* **2010**, *46*, 3161.
- (47) Morisue, M.; Morita, T.; Kuroda, Y. *Organic & biomolecular chemistry* **2010**, *8*, 3457.
- (48) Tamaru, S.-i.; Nakamura, M.; Takeuchi, M.; Shinkai, S. *Organic letters* **2001**, *3*, 3631.
- (49) Wang, T.; Chen, S.; Jin, F.; Cai, J.; Cui, L.; Zheng, Y.; Wang, J.; Song, Y.; Jiang, L. *Chemical Communications* **2015**, *51*, 1367.
- (50) Lu, J.; Zhang, D.; Wang, H.; Jiang, J.; Zhang, X. *Inorganic Chemistry Communications* **2010**, *13*, 1144.
- (51) Udaltsov, A.; Kazarin, L.; Sweshnikov, A. *Journal of Molecular Structure* **2001**, *562*, 227.
- (52) Li, L.; Huang, Y.; Peng, J.; Cao, Y.; Peng, X. *Journal of Materials Chemistry A* **2013**, *1*, 2144.
- (53) Chen, F.-C.; Tseng, H.-C.; Ko, C.-J. *Applied Physics Letters* **2008**, *92*, 96.
- (54) Kang, I.; Yun, H.-J.; Chung, D. S.; Kwon, S.-K.; Kim, Y.-H. *Journal of the American Chemical Society* **2013**, *135*, 14896.
- (55) Yu, C.-Y.; Chen, C.-P.; Chan, S.-H.; Hwang, G.-W.; Ting, C. *Chemistry of Materials* **2009**, *21*, 3262.
- (56) Vanlaeke, P.; Vanhoyland, G.; Aernouts, T.; Cheyns, D.; Deibel, C.; Manca, J.; Heremans, P.; Poortmans, J. *Thin solid films* **2006**, *511*, 358.
- (57) Gouterman, M. *Journal of Molecular Spectroscopy* **1961**, *6*, 138.

Chapter III

Extended research on solution processable
small molecules based on porphyrins for
BHJ OSCs

3.1 Introduction

In recent years, significant improvements have been achieved in the development of BHJ solar cells based on the combination of molecular design, morphological control and advanced techniques.^{1,2} For the solution processed small molecules BHJ OSCs, their performance has been increased and close to those shown by polymers in related solar cells. For example, small molecules containing 3,3'-di-2-ethylhexylsilylene³ or benzo[1,2-*b*:4,5-*b'*]-dithiophene (BDT)⁴ units as central building blocks could present PCE values up to 7.0 % when blended with fullerene derivatives.

Solution processable small molecules based on porphyrins for BHJ OSCs are very attractive due to the advantage of their photoelectrical properties and defined molecular structures. Connecting with the subject, the group of X. Peng has reported a series of porphyrins with conjugated donor-acceptor structures, that present power conversion efficiency values close to 7.23 % when used 4-octyloxy-phenyl groups in place of 3,5-di(dodecyloxy)-phenyl groups (longer chains than the former) at the *meso*-positions of porphyrinic cores. It is mentioned that this fact may enhance the intermolecular π - π stacking and therefore photovoltaic performance.^{5,6} Also, the same group has developed effective π -conjugation of porphyrin systems with the introduction of ethynylene linkages.⁷ Besides, the linear bidentate ligand 4,4'-bipyridyl were applied to mediate supramolecular assemblies of metalloporphyrin polymers to form well-organized complexes and increase the π -conjugation for amplifying the optical nonlinearity in their work.⁸

According to our previous studies, which demonstrate the self-assembly abilities of porphyrins with carbonyl groups locating in the peripheral positions, a new porphyrin system (**TEP**) containing exclusively carbonyl groups in the *meso*-positions (Figure 1) was developed. The design of the molecule may block some of the possible interactions observed in the long chain analogous systems. The **TEP** molecule has a much simpler structure where the π - π stacking may play a more prominent role in the molecule self-organization. This work was inspired by a related work published by Ma *et al.*⁹, where they studied the effect of the coordination of different metals in devices performance of triphenylamine-substituted metalloporphyrins. In this case, the central metal may effectively modify the HOMO and LUMO levels of porphyrins. In addition, the supramolecular interactions of the metal-porphyrin will affect the structure thus assisting the overall charge transport abilities. Here, the coordination with some metallic centres such as Zn(II) and Co(II) has been tried. Finally, crystallographic data was achieved for the systems containing Zn(II) ions, providing a coordination compound described as **Zn(TEP)**.

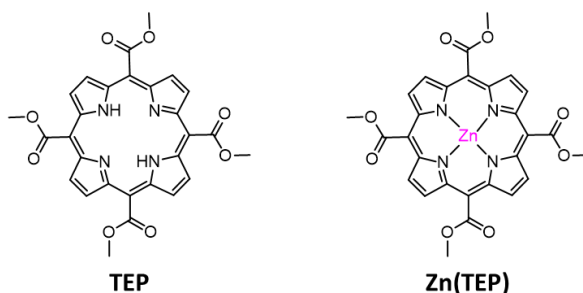


Figure 1. General scheme of the new *meso*-porphyrins containing methyl 2-oxoacetate groups.

3.2 Objectives

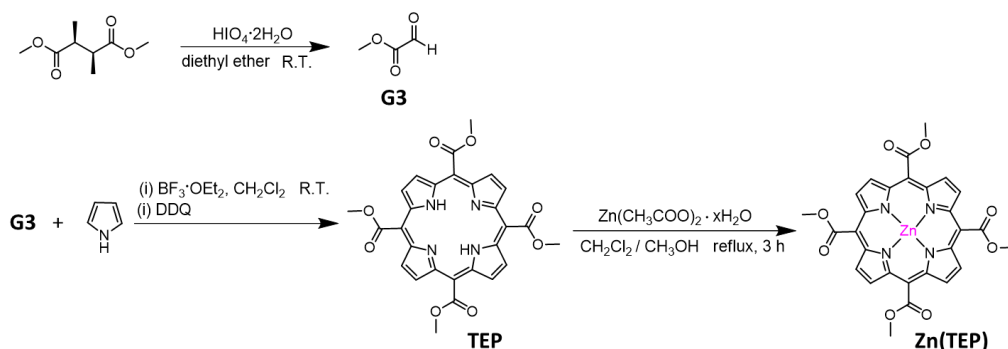
Similar to the previous chapter, this project involves the design, synthesis and device characterization of new porphyrins but with shorter carbonyl substituents. The aim is to investigate the effect of the short ligands (based on our previous knowledge with longer chains) in the intermolecular interactions among porphyrin molecules, and how this affects the OSCs performance.

The chapter encloses the following goals:

- (1) Synthesize of the new free-based porphyrin containing methyl 2-oxoacetate groups (**TEP**) and characterization of the sample in solid state by single X-ray diffraction.
- (2) Coordination of **TEP** with different metals, and self-assembly studies on the final coordination compounds.
- (3) Fabrication of organic solar cell devices with the new porphyrin derivatives as active layers and further investigation on their power conversion efficiency.

3.3 Synthesis and crystallographic studies of TEP and Zn(TEP)

3.3.1 Synthesis of TEP (involving short ester substituents)



Scheme 1. Synthesis of **TEP** and metalloporphyrin **Zn(TEP)**.

The synthesis of the symmetrical tetra-*meso*-porphyrin **TEP** has been previously reported by M. P. Trova *et al.*¹⁰ following Lindsey's method.¹¹ As it is shown in Scheme 1, the methyl 2-oxoacetate was prepared by the oxidative cleavage of the (+)-Dimethyl L-tartrate with periodic acid dehydrate. The resulting aldehyde was immediately transfer to a flask containing $\text{BF}_3 \cdot \text{OEt}_2$ which catalyses the condensation with the pyrrole units in dry CH_2Cl_2 . The following step involves an oxidation reaction with 2,3-Dichloro-5,6-dicyano-*p*-benzoquinone (DDQ) that provides **TEP**

with a 14 % yield. **Zn(TEP)** was achieved by the coordination of **TEP** with a Zn(II) source via the same method described in chapter II for **Zn(4R-PPP)**.

3.3.2 Crystallographic studies of TEP and Zn(TEP)

Suitable Crystals of **TEP** for single X-ray diffraction were obtained by layering a solution of the compound dissolved in CH₂Cl₂ with CH₃OH (precipitating agent). In addition, crystals of **Zn(TEP)** were directly achieved from the recrystallization of the solid (coordination compound) in CH₂Cl₂. The POV-Ray views of both systems are depicted in Figure 2 and 3 respectively, and crystallographic details are shown in Table A3.1.

TEP crystallizes in a monoclinic space. The structure shows a flat porphyrin core substituted at the *meso*-positions by methyl ester groups. Figure 2a shows it is centrosymmetric, having an inversion point in the centre of the porphyrinic core. The molecules present partial overlapping by π - π interactions of the porphyrinic rings with a staircase type arrangement with an average distance among them of 3.779 Å (N2...N2) (Figure 2b), indicating the formation of J-aggregates in the one-dimension. The 3D supramolecular packing of **TEP** is shown in Figure A3.1.

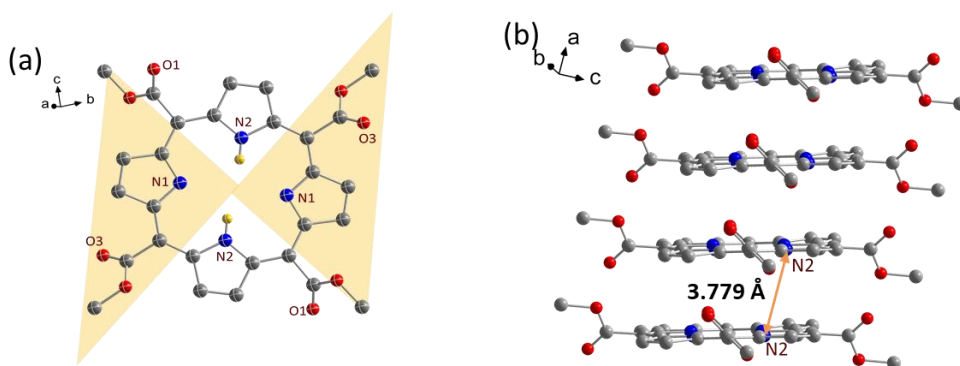


Figure 2. (a) Molecular structures of **TEP**. (b) The packing of **TEP** exhibiting π - π interactions.

The structure of the metalloporphyrin **Zn(TEP)** shows units where the zinc atoms are coordinated at the centre of the porphyrinic rings with Zn-N_{Py} bond lengths of 2.049 and 2.060 Å (Figure 3a). Now, the crystal structure reveals a new rearrangement of the **Zn(TEP)** units forming a coordination polymer [**Zn(TEP)**]_∞ (Figure 3b). In [**Zn(TEP)**]_∞, the zinc centres are hexacoordinated to four equatorial pyrrolic nitrogen donor atoms from the porphyrin moiety and two axial C=O ligands from the methyl ester donor groups of two adjacent zinc(II) porphyrin neighbours. The *meso*-methyl ester groups are displayed at opposite sides in the porphyrin plane, increasing the symmetry of the final arrangement. The **Zn(TEP)** moieties are aligned in a parallel manner, which may minimize sterically unfavourable interactions between their substituents. Furthermore, the porphyrin cores overlap slightly but present displacement from an ideal axis to maximize Zn-O interactions, with bond lengths of 2.387 Å, which is in the range of other hexa-coordinate zinc(II) porphyrins described in the literature.^{12,13}

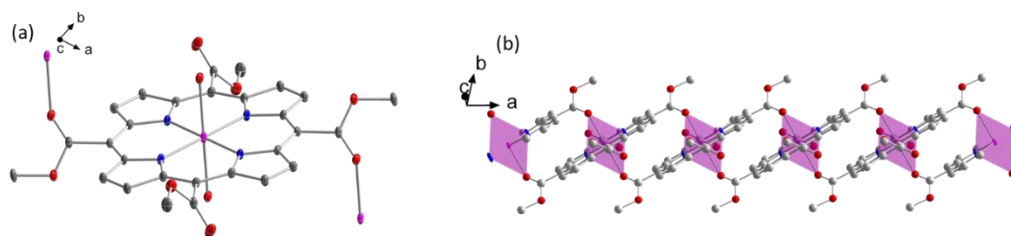


Figure 3. (a) Molecular structures of **Zn(TEP)**. (b) The 1D polymer formed by **Zn(TEP)**. Colour legend: Zn in purple, O in red, N in blue and C in grey.

3.4 Solution-processed BHJ OSCs based on porphyrin **TEP**

As it is described in previous chapter, the fabrication of a BHJ OSC device containing **TEP** molecules was tested in collaboration with the group of Dr. Mariano Campoy. In this way, thin films of **TEP**, P3HT, PCBM and their mixtures (**TEP**-P3HT and **TEP**-PCBM in a 1:1 ratio respectively) in chlorobenzene were prepared by blade coating on clean microscope slide glass substrates. Their UV-vis absorption spectra and photo-luminescent were obtained by measuring the films.

The UV-Vis absorption spectra of the blends films processed with P3HT and PCBM are shown in Figure 4a. Like the previous study on porphyrin **Zn(4R-PPP)**, the films of blends display the absorption of the combined contribution of porphyrin, **TEP**, and P3HT or PCBM. The free based porphyrin **TEP** presents a strong Soret absorption at 390 nm and four Q bands between 510 to 700 nm. For P3HT and PCBM, the main absorption bands are at 515 and 334 nm respectively. Due to the interaction of the binary combination within the films (**TEP**-P3HT and **TEP**-PCBM respectively) the overall spectra present wide absorption, in which the main band clearly shifts. Photoluminescence quenching results shown in Figure 4b provide evidence of the photoinduced charge transfer process from **TEP** to PCBM. The phenomenon occurs when it is energetically favourable for the electron, in the excited state of the donor, to be transferred to the acceptor. In this case the more electronegative PCBM results in an effective quenching of the excitonic photoluminescence of porphyrin donor.¹⁴⁻¹⁶ In the case of **TEP** mixing with P3HT, the quenching was not observed (Figure A3.2). Furthermore, the HOMO and LUMO energy levels calculated for **TEP** (-5.30 and -3.54 eV respectively) obtained from electrochemical measurements (Figure 5) are above the energy levels of PCBM (-5.93 and -3.94 eV), indicating that **TEP** may work better with PCBM as a donor material.

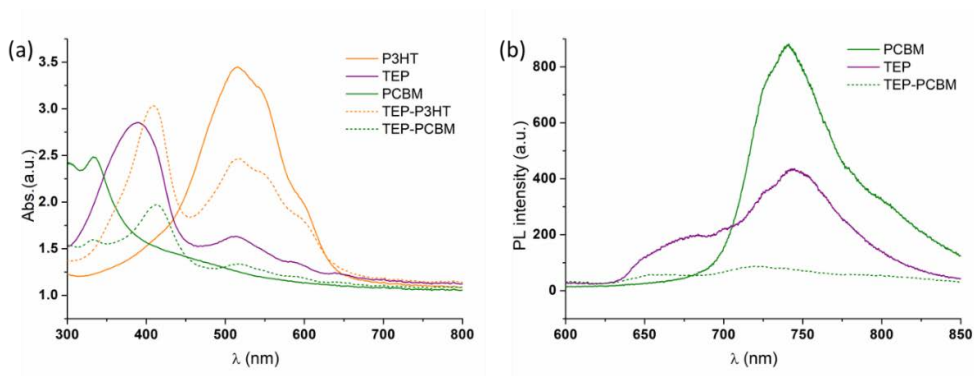


Figure 4. (a) UV-Vis absorption spectra of the compounds and the blend films (1: 1, w/w). (b) Photoluminescence quenching of **TEP** and **PCBM**.

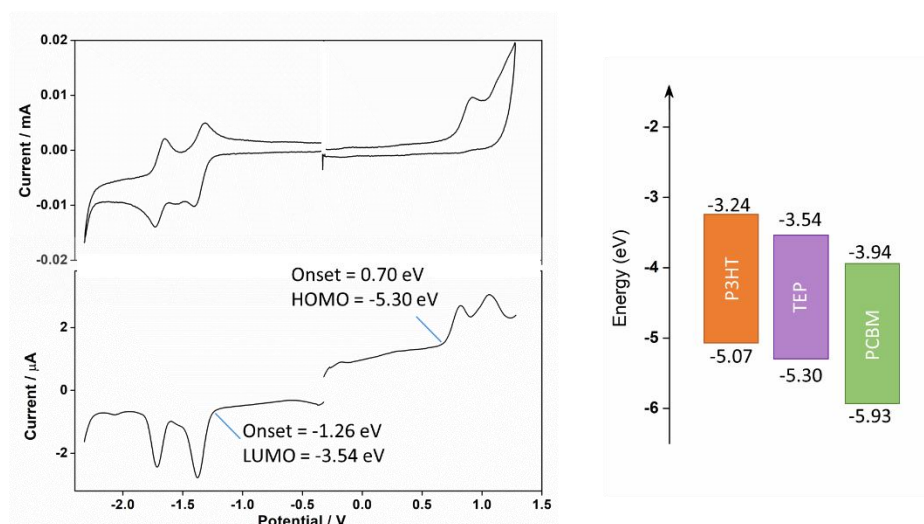


Figure 5. CV and DPV of **TEP** (0.5 mM) in 0.1 M TBAPF_6 CH_2Cl_2 solution. Potentials vs. Fc/Fc^+ .

Typical $J-V$ characteristic curves of an ITO/PEDOT:PSS/**TEP**:PCBM/Al cell have been plotted in Figure 6a at different light intensities from 0.1 to $100 \text{ mW}\cdot\text{cm}^{-2}$ at $T=300 \text{ K}$. Unfortunately, the device processed with **TEP** and PCBM did not exhibit values of V_{OC} and J_{SC} , pointing out an inefficient behaviour. The crude phase separation was also studied by microscopy (Figure 6b) to understand the key factor which may affect the performance of the device. A large-scale phase separation was observed, yielding almost no photocurrent processes. The latest results have been demonstrated by the detection of unquenched photoluminescence from PCBM in other reports.¹⁷

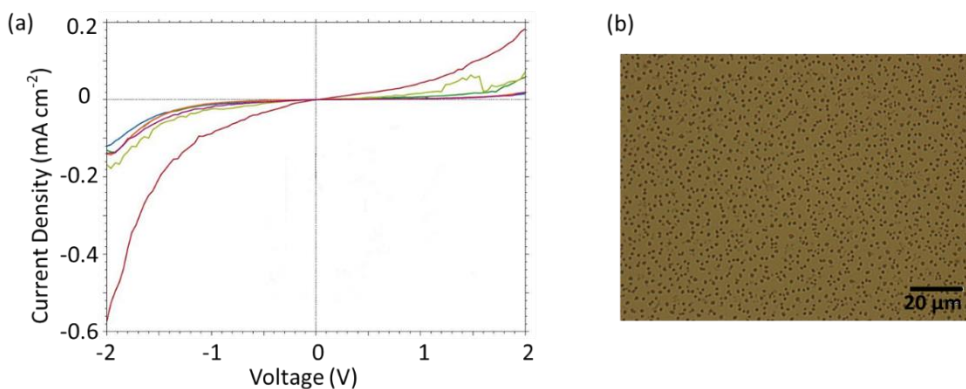


Figure 6. (a) J–V characteristics of the solar cells based on the **TEP**-PCBM blends (1:1, w/w) at different illumination intensities. (b) Top view of active layer of the device using microscopy.

3.5 Conclusions

Two small porphyrin units containing carbonyl moieties at the *meso*-positions were synthesized toward their supramolecular study (by single X-ray diffraction) and ultimately to be used as active components in BHJ OSCs. The first is a free-based porphyrin (**TEP**) which display strong π - π stacking interactions among the porphyrin cores, and the second is a Zn(II) porphyrin (Zn(II) coordinated to the free-based porphyrin, **Zn(TEP)**) which is well described as a 1D coordination polymer by the binding of the metal centre and carbonyl moieties from neighbours. Comparing **Zn(TEP)** with the metalloporphyrins **Zn(4R-PPP)** and **Zn(PPP)** presented in chapter II, the reducing of flexibility and steric hindrances in the *meso*-position substituents make the Zn(II) centres in **Zn(TEP)** more exposed toward coordination with adjacent porphyrins. In both case, the free-based and Zn(II) porphyrin present compact structures through intermolecular interactions or via coordination.

The suitable energy match and good photoluminescence quenching resulting from the mixing of **TEP** and PCBM, encouraged the use of **TEP** as prospective candidate as donor in BHJ OSCs experiments. The unsuccessful results regarding the performance of the final prototype indicates that further efforts toward morphology control and the process of device fabrication must be improved.

Experimental Section:

Synthesis Methods.

1. methyl 2-oxoacetate

To a solution of dimethyl tartrate (1.178 g, 6.6 mmol) in ether (12 mL) stirred under N₂ periodic acid dihydrate (1.501 g, 6.6 mmol) was added in portions (5 × 0.3 g) over the course of 20 min. The solution was stirred over 30 min, then decanted from the solid precipitate, dried (using MgSO₄), followed by filtering and the solvent was evaporated in vacuum to provide crude **G3** which was immediately used without further purification. Further analysis of the crude was not pursued because of the glyoxylic esters polymerized easily making their characterization difficult. Hence, it was always made freshly and immediately used in the synthesis of **TEP**.

2. TEP

G3 (1.028 g, 11.7 mmol), CH₂Cl₂ (0.8 L) and freshly distilled pyrrole (812 μL) were added into a 2-L round-bottomed flask with a N₂ inlet, the setup was covered with foil. The reaction mixture was stirred for 5 min and then BF₃·OEt₂ (2.30 mL, 18.7 mmol) was added dropwise. The reaction was monitored by the formation of the corresponding Soret band through UV-vis absorption spectrometry. After a stirring period of 2h at R.T., DDQ (1.992 g, 8.8 mmol) was added. The reaction mixture was stirred for another 5h at RT. The reaction mixture was filtered through Celite, after evaporation of solvents a crude solid mixture was adsorbed onto silica gel (15 g). Purification by column chromatography on Al₂O₃ (CH₂Cl₂: Et₃N: CH₃OH 200:1:0.1 as eluent) provided porphyrin **TEP** (220 mg, 14 %) as a dark solid. ¹H NMR (300 MHz, Chloroform-*d*) δ 9.50 (s, 8H), 4.61 (s, 12H), -3.33 (s, 2H).

3. Zn(TEP)

TEP (150 mg, 277 μmol) was dissolved and refluxed in 38 mL of CH₂Cl₂ under N₂ atmosphere. A solution of Zn(CH₃COO)₂·2H₂O (210 mg, 959 μmol) in a mixture of CH₃OH/CH₂Cl₂ (9 ml: 9 ml) was added dropwise. The reaction was monitored by absorption UV-Vis absorption spectroscopy (~3 h). Afterward, the final solution was washed with NaHCO₃ saturated aqueous solution, brine and distilled water. The organic phase was extracted using CH₂Cl₂. The removal of the solvent gave the desired product as a purple solid with a yield of 153 mg (91 %).

References:

- (1) Günes, S.; Neugebauer, H.; Sariciftci, N. S. *Chemical reviews* **2007**, *107*, 1324.
- (2) Beaujuge, P. M.; Fréchet, J. M. *Journal of the American Chemical Society* **2011**, *133*, 20009.
- (3) Van Der Poll, T. S.; Love, J. A.; Nguyen, T. Q.; Bazan, G. C. *Advanced Materials* **2012**, *24*, 3646.
- (4) Zhou, J.; Zuo, Y.; Wan, X.; Long, G.; Zhang, Q.; Ni, W.; Liu, Y.; Li, Z.; He, G.; Li, C. *Journal of the American Chemical Society* **2013**, *135*, 8484.
- (5) Li, L.; Huang, Y.; Peng, J.; Cao, Y.; Peng, X. *Journal of Materials Chemistry A* **2013**, *1*, 2144.
- (6) Qin, H.; Li, L.; Guo, F.; Su, S.; Peng, J.; Cao, Y.; Peng, X. *Energy & Environmental Science* **2014**, *7*, 1397.
- (7) Huang, Y.; Li, L.; Peng, X.; Peng, J.; Cao, Y. *Journal of Materials Chemistry* **2012**, *22*, 21841.
- (8) Li, L.; Huang, Y.; Peng, J.; Cao, Y.; Peng, X. *Organic Electronics* **2013**, *14*, 3430.
- (9) Zhang, Y.; Zhang, S.; Yao, L.; Qin, L.; Nian, L.; Xie, Z.; Yang, B.; Liu, L.; Ma, Y. *European Journal of Inorganic Chemistry* **2014**, *2014*, 4852.
- (10) Trova, M. P.; Gauuan, P. J. F.; Pechulis, A. D.; Bubb, S. M.; Bocckino, S. B.; Crapo, J. D.; Day, B. J. *Bioorganic & medicinal chemistry* **2003**, *11*, 2695.
- (11) Lindsey, J. S.; Schreiman, I. C.; Hsu, H. C.; Kearney, P. C.; Marguerettaz, A. M. *The Journal of Organic Chemistry* **1987**, *52*, 827.
- (12) Suijkerbuijk, B. M.; Tooke, D. M.; Spek, A. L.; van Koten, G.; Klein Gebbink, R. J. *Chemistry—An Asian Journal* **2007**, *2*, 889.
- (13) Rui, X.; Zha, Q.-Z.; Wei, T.-T.; Xie, Y.-S. *Inorganic Chemistry Communications* **2014**, *48*, 111.
- (14) Sariciftci, N. S.; Smilowitz, L.; Heeger, A. J.; Wudl, F. *Science* **1992**, *258*, 1474.
- (15) Chirvase, D.; Chiguvare, Z.; Knipper, M.; Parisi, J.; Dyakonov, V.; Hummelen, J. *Journal of Applied Physics* **2003**, *93*, 3376.
- (16) Hoppe, H.; Sariciftci, N. S. *Journal of materials research* **2004**, *19*, 1924.
- (17) Hoppe, H.; Niggemann, M.; Winder, C.; Kraut, J.; Hiesgen, R.; Hinsch, A.; Meissner, D.; Sariciftci, N. S. *Advanced Functional Materials* **2004**, *14*, 1005.

Chapter IV

Porphyrin-based binary self-assembling systems

4.1 Introduction

The study of intermolecular self-assembling systems based on porphyrins has delivered a wide variety of discrete molecular architectures and properties in recent years. These models have been investigated as monolayer rotors on surfaces,¹ light-harvesting metal-organic frameworks,² hierarchical and chiral multipart supramolecular architectures.³ Multi-porphyrin arrays can be formed via covalent as well as non-covalent synthetic methodologies. Covalent bonding plays an importance role in the synthesis of porphyrin functional materials, in this regard COFs (covalent organic frameworks) and MOFs (metal organic frameworks) are well-known examples where porphyrins are used as ligands to coordinate metal centres;⁴ another relevant type is well-defined isolable nanostructures from ionic self-assembly.⁵ On the other hand, thermodynamically labile intermolecular bonds (which facilitate the construction of defect-free large periodic arrays) and the non-covalent approaches⁶ (including hydrogen bonding, π - π stacking and van der Waals forces) are considerably useful to drive the self-assembly processes which can be modified later through external stimuli.⁷

In the previous chapters (II and III), well-ordered architectures have been formed by the coordination of metallo-porphyrins through the zinc centres and the carbonyl groups of the neighbours. In addition, the affinity of zinc centre to pyridine groups has been more often used to construct self-assembled porphyrin architectures shown in Figure 1.⁸ In this regard, Fleischer reported in 1991 a linear polymer with zigzag conformation formed by the coordination of one pyridine from the porphyrin periphery with the metal centre of an adjacent porphyrin.⁹ Some other cyclic tetramers based on Zn porphyrins bearing pyridyl groups have been solved by single crystal.¹⁰ Furthermore, the pyridine groups coming from other small molecules such as pyridine-4-yl-methanethiol or isonicotinic acid could be used as anchoring groups to fix Zn porphyrins on functional surfaces towards their use in molecular machinery¹ or dye sensitized solar cells.¹¹

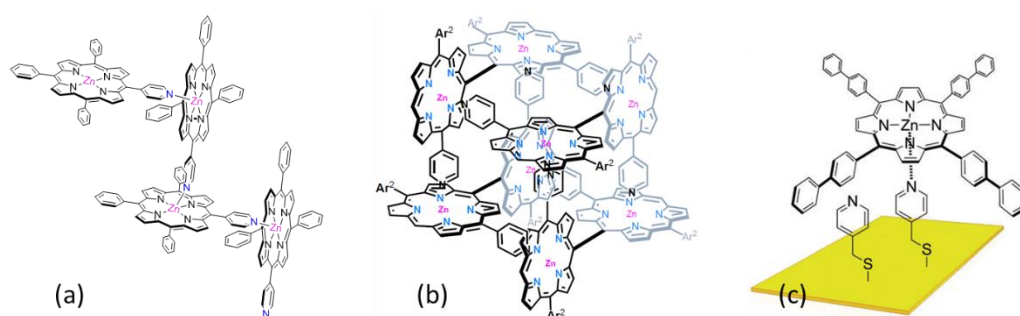


Figure 1. Structure and schematic views showing the interaction of zinc porphyrin and pyridine groups. (a) 1D polymer, (b) porphyrin box and (c) supramolecular rotor.

Another way to build well-defined structures based on the connection among porphyrins is by the use of their functional substituents exclusively, where again carboxylic or pyridyl porphyrins are commonly used. It is well known that (carboxyl)O-H \cdots N (pyridine)¹² and (pyridine)C-H \cdots O(carbonyl) hydrogen bonds can construct crystalline architectures because of

their strength and directionality.^{13,14} Besides, as mentioned above, coordination with metal centres to form MOFs is widely studied,^{2,4,15,16} in which the porphyrin groups, bearing carboxylic and pyridine, are frequently used as organic linkers.

For many applications, aggregations of porphyrins in solution are desired to produce discrete nanostructures by the use of straightforward synthetic methods, as ionic self-assembly for example, where two oppositely charged porphyrins in aqueous solution interact and the robust nature of these porphyrin-based materials allows the access to novel nanomaterials, with potential application in areas such as electronics, catalysis and sensors. Molecular recognition between the complementary arrangements of opposite charges, together with H-bond donors and acceptors on the porphyrin tectons, contribute to the ionic self-assembly processes. In this direction, Hone and co-workers^{5,17} have reported nanotubes formed by the mixture of $H_4TPPS_4^{2-}$ and metal compound tetrakis(4-pyridyl)porphyrin ($MTPyP^{4+}$) (Figure 2).

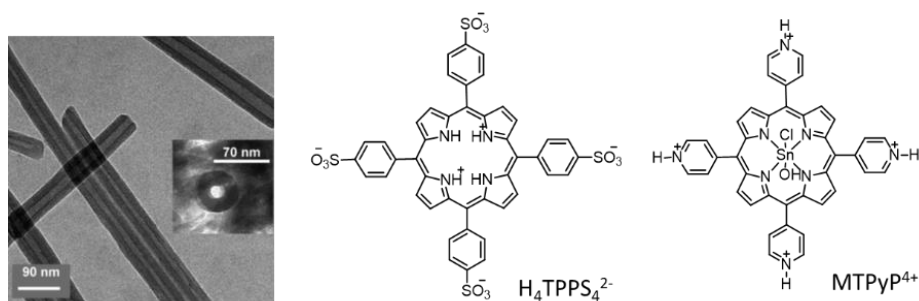


Figure 2. Porphyrins used in making the porphyrin nanotubes.

In view of the strategies mentioned above toward the achievement of intermolecular assembly of different porphyrins, a new symmetric porphyrin called **Zn(4R-CPP)** was designed and displayed in Figure 3, which contains four chiral centres and carboxyl groups in the *meso*-positions. Combining the effect of H-bonding of peripheral substitutions and weak coordination to the Zn(II) centre, the interaction of **Zn(4R-CPP)** with tetra(4-pyridyl) porphyrin (**TPyP**) (Figure 3) via bulk processes (meaning here standard solution methods) was studied with the intention of extrapolate the data to microfluid processes. A water-soluble porphyrin salt, **Zn(4R-CPP)^{m-}**, has been obtained from the deprotonation of the designed porphyrin. In the second step, some new nanostructures are presented by the binary porphyrin self-assembly with protonated **TPyP** (**H_nTPyPⁿ⁺**). Furthermore, considering the effects of chirality and metal centre coordination, a commercial tetra(4-carboxyphenyl) porphyrin (**TCPP**), which is a free-base (free ligand without metal centre) and achiral structure is used as reference. Figure 4 shows the porphyrins used in the intermolecular assembly study in this chapter.

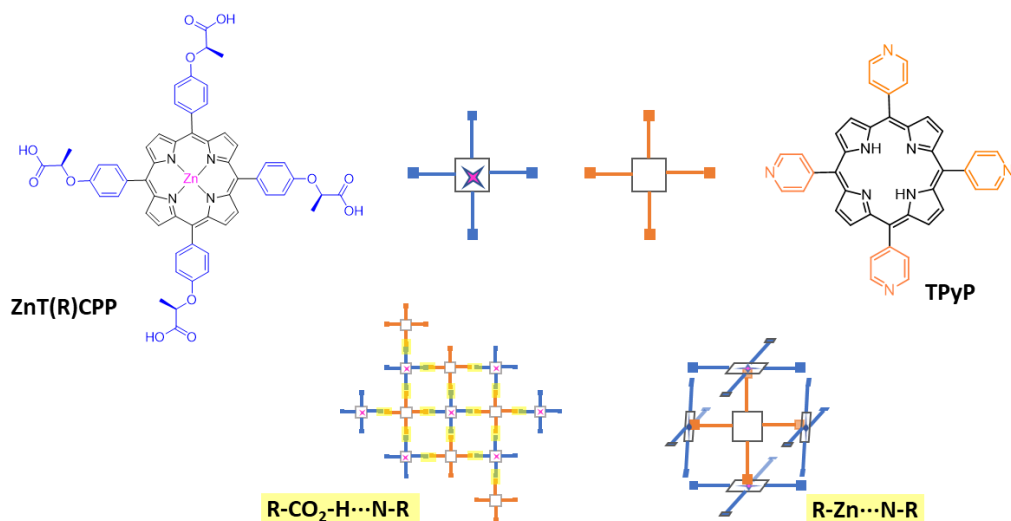


Figure 3. Prospective structures based on **Zn(4R-CPP)** and **TPyP** formed by H-bonding of peripheral substitution or weak coordination to the Zn(II) centre.

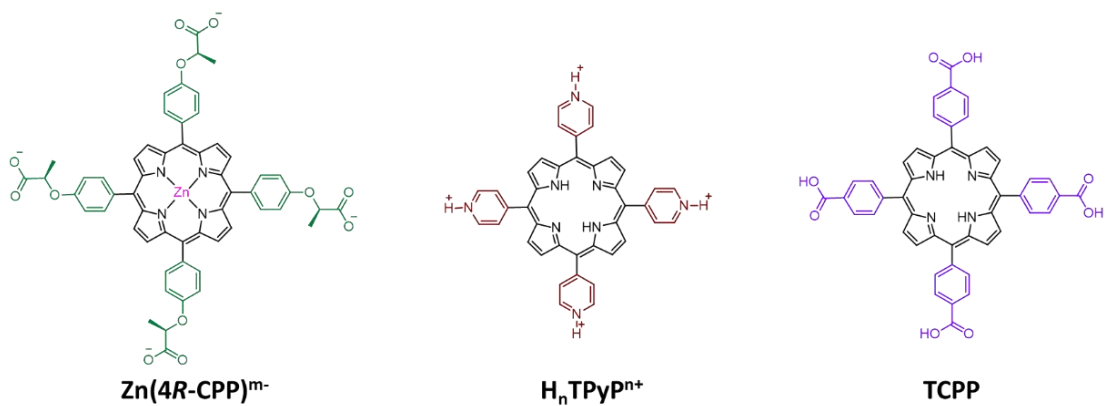


Figure 4. Chemical structures of the studied porphyrins.

4.2 Objectives

The Objective of this work is:

Exploration of self-assembling processes by the use of functional porphyrins through intermolecular interactions for their potential applications as nanomaterials.

The project focuses on the following aspects:

- (1) Synthesis of the tetracarboxylic chiral porphyrin **Zn(4R-CPP)** and the investigation of the self-assembly ability of this acidic porphyrin compared with **Zn(4R-PPP)** (from Chapter II).
- (2) Study of the interactions and the final assemblies between **Zn(4R-CPP)** and **TPyP** (Figure 3) in the appropriate solvent environment.
- (3) The comparative study, as a reference, between the commercial acidic porphyrin **TCP** and **TPyP**.
- (4) The creation of water-soluble porphyrin salts of the type **Zn(4R-CPP)^{m-}** by the deprotonation of the carboxyl porphyrin under study, and the construction of nanostructures together with the protonated form of **TPyP (H_nTPyPⁿ⁺)** via ionic self-assembly.

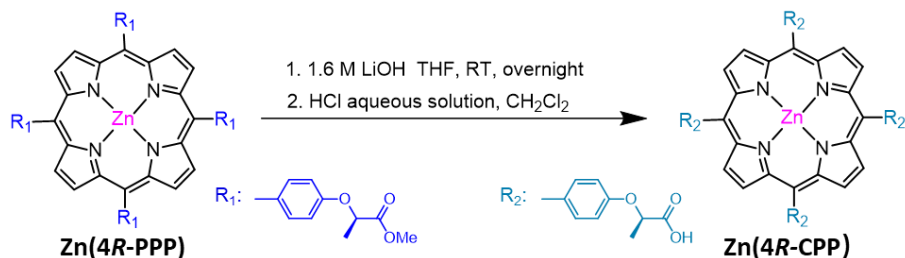
As it has been described in previous chapters, crystal structures of the resulting compounds are powerful tools to examine the final supramolecular arrangements. The achievement of single crystals has been pursued and successfully achieved in some cases. Here, we focus on the self-assembly process in solution under ambient condition. In the case of ionic self-assembly, due to the specific electrostatic interactions, the discrete self-assembled porphyrin nanostructures can be directly analysed by SEM.

4.3 Intermolecular self-assembly of porphyrins bearing carbonyl and pyridine groups

4.3.1 Synthesis of Zn(4R-CPP)

The desired porphyrin **Zn(4R-CPP)** was obtained firstly by the saponification reaction of the **Zn(4R-PPP)** (system described in chapter II) in an alkaline THF/H₂O mixed solution to remove the methyl groups, then titrated with an acidic aqueous solution and the final system extracted with the use of CH₂Cl₂ (Scheme 1). Comparing the direct hydrolysis reaction of **Zn(4R-PPP)** under acidic conditions with our two-steps synthesis, the second one provides a complete transformation of ester, leading to high yields of the final porphyrin that contains the carbonyl groups (87%) without need of further purification.

It is worth to mention that the metalloporphyrin with four carboxylic groups presents low solubility in most common solvents, and the -COOH protons easily exchange with those from the solvents, such as CD₃OD, providing unclear ¹H NMR spectra. Therefore, the study of this compound by ¹H NMR was performed in DMSO-d₆ solvent in which it was totally soluble.



Scheme 1. Synthesis of chiral acidic metalloporphyrin, **Zn(4R-CPP)**.

4.3.2 Self-assembly studies of Zn(4R-CPP)

4.3.2.1 Crystals of Zn(4R-CPP)

Taking into account that the interactions described in the former chapter and due to the existence of a large amount of carboxyl groups here, it is intuitive to expect a high number of intermolecular interactions, most of which are H-bonding, in the final molecular structure. Besides, the ability of coordination by the Zn(II) centre and oxygen from carbonyl group was proved in our previous studies and should also be taken into account in the case of **Zn(4R-PPP)**. In a first step, before performing the intermolecular self-assembly studies with different porphyrins, the possible self-assemble processes of **Zn(4R-CPP)** was explored.

Single crystals of **Zn(4R-CPP)** are shown in Figure 5; they could be achieved by evaporation of a mixture solvents. The flake-like crystals were obtained in THF/MCH (MCH = methylcyclohexane, Figure 5a), meanwhile the dendritic crystals named here **Zn(4R-CPP)-b** grew from a CH₃OH/CH₂Cl₂ mixture. Resolution by single X-ray diffraction was unfeasible because of bad diffraction of the crystals in both cases (even by the use of synchrotron sources). Powder X-ray diffraction was performed with the latest sample because of the scarce yield of crystalline material. Comparing the powder XRD diffractograms of **Zn(4R-CPP)-b** with **1a** and **1b** crystals (described in Chapter II) which was obtained from porphyrin **Zn(4R-PPP)** (that contains ester groups therefore having different periphery ending substituents) (Figure 6), the carboxyl groups have effects on the molecular self-assembly because of the different patterns even in the same crystallization conditions of **1a** (CH₃OH/CH₂Cl₂). Pointing out that the effects of having carboxyl groups instead of esters in the ending arms of the molecules would provide additional or different interactions apart from those observed and described for **1a** and **1b**.

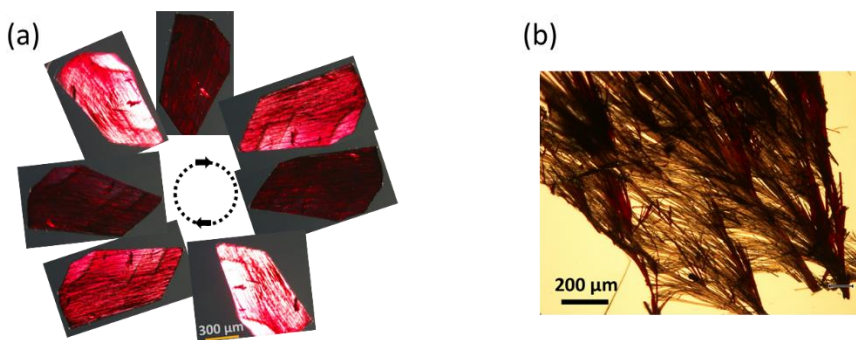


Figure 5. Microscope images of **Zn(4R-CPP)** crystals obtained from (a) THF/MCH and (b) CH₃OH/CH₂Cl₂.

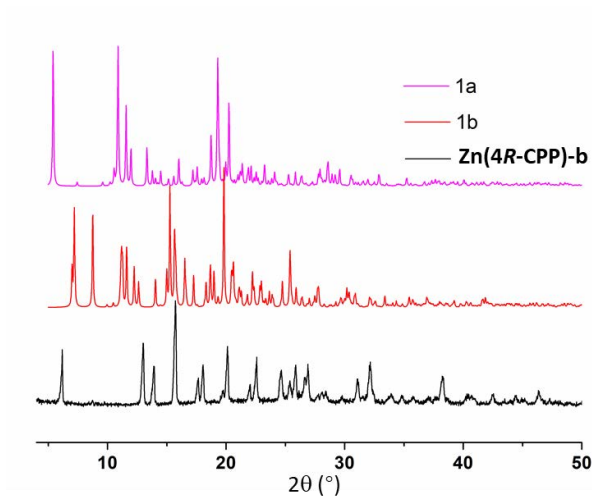


Figure 6. Powder X-ray diffraction patterns of **Zn(4R-CPP)-b** comparing with **1a** and **1b**.

4.3.2.2 Self-assembly studies by UV-Vis absorption and circular dichroism

In this chapter, studies in solution are emphasized towards the analysis of the formation of aggregates with the new tetracarboxyl porphyrin by the use of UV-Vis absorption spectroscopy and circular dichroism. In the previous study, the chiral groups attached to the porphyrin core are far away from the chromophore and therefore they do not present CD activity in the given solvent, unless supramolecular interactions provide them. The solutions of **Zn(4R-CPP)** in THF,

methylcyclohexane (MCH) and H₂O respectively, with low concentrations (5×10^{-6} M), were prepared to study the self-assembly of the system under the presence of different solvents. And the parallel studies were performed with the compound **Zn(4R-PPP)** (compound **1** in chapter II) as reference.

Considering the good solubility for both systems in THF (solvent chosen as mother solution, 1.5×10^{-4} M), mixture containing the tested solvent (H₂O or MCH respectively) was prepared by adding 0.1 mL mother solution into 3 mL solvent in a second step. MCH is an apolar solvent and it may favour the formation of H-bonding between molecules;¹⁸ water, on the other hand, being polar may provide different interactions. This also relates to Chapter II, where **1a** contains a molecule of water coordinated to the Zn(II) centres. In addition, all the solvents are suitable for the study of optical properties of the aggregation since they are transparent in the visible and near ultraviolet region where porphyrins have absorption.

As solvent plays an important role in the self-assembly process of porphyrins, several changes in the UV-Vis absorption bands were expected once the solvent was performed.^{19,20} In the case of **Zn(4R-PPP)**, the molecules did not present evidences of self-aggregation in MCH solvent, behaving as isolated chromophores surrounded by solvent molecules. On the contrary, **Zn(4R-PPP)** showed a wide absorption of the Soret band in H₂O, which probably related to asymmetry of metalloporphyrin introduced by the interaction of zinc ion with neighbouring molecules (Figure 7a).²¹ Comparing such results with the CD experiments, the same phenomenon is observed, where **Zn(4R-PPP)** did not self-assemble significantly in the THF or MCH-THF mixture. However, in H₂O, **Zn(4R-PPP)** showed strong Cotton effects at the position of the band associated with the coordination of the Zn centre. The weak one at 410.2 nm, the high intense positive Cotton effect with maxima at 427.6 nm and huge negative CD signal at 444.6 nm indicated the clear co-existence of monomer metalloporphyrin and the extension of the intermolecular interactions within chromophores (Figure 8a).

Zn(4R-PPP) did not show clear changes (that could be related to aggregation processes) in THF and H₂O from the spectra achieved using both spectroscopies, UV-Vis and CD (Figure 7b and 8b). Nevertheless, the negative Cotton effect at 425.4 nm and positive signal at 444.2 nm were observed in MCH, suggesting the formation of aggregates. Performing the experiments at -10 °C, the Cotton effect showed the same orientation like at room temperature and the isosbestic point at 435.6 nm could be referred to the possible equilibrium between the monomer and new superstructures.²²

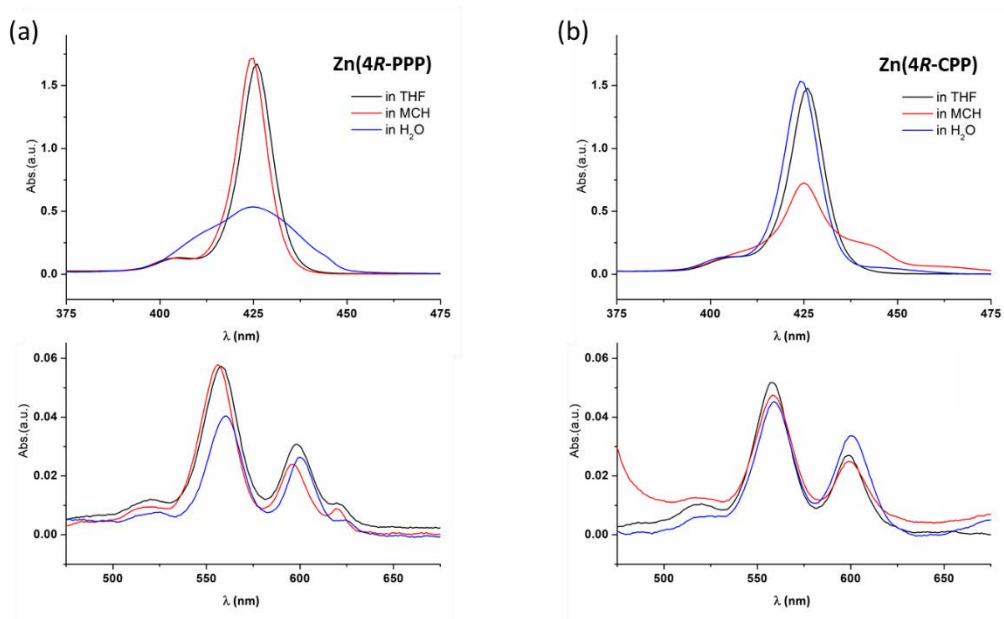


Figure 7. UV-Visible absorption spectra of (a) Zn(4R-PPP) and (b) Zn(4R-CPP) in different solvents.

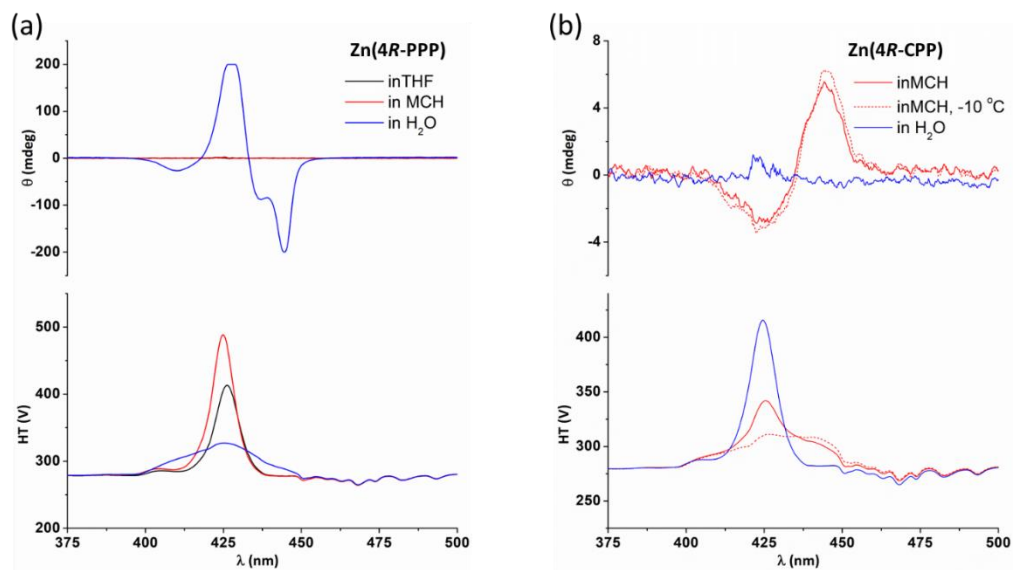


Figure 8. CD spectra and corresponding absorption signals from CD spectrometer for compounds (a) Zn(4R-PPP) and (b) Zn(4R-CPP) in different solvents.

4.3.3 Supramolecular organization of porphyrin-Py compounds

4.3.3.1 Titration studies of Zn(4R-CPP) with pyridine

In the next sections the interactions between the metalloporphyrin, which contains chiral and carboxylic groups in the *meso*-positions, and the **TPyP**, which is a commercially available one containing four pyridine groups, are described. In an initial step, the conditions and coordination ability of pyridine with our porphyrin, **Zn(4R-CPP)** were explored. Hence, titration studies of **Zn(4R-CPP)** with pyridine were followed by UV-Visible absorption spectroscopy. As it is mentioned, this study was performed as a reference for further experiments with **TPyP**. Previous studies in the literature indicated the increase of the electron density of the porphyrin ring after the coordination of the pyridine with the metalloporphyrin, shown by a red-shift in the absorption band of the Zn(II) porphyrins under study.⁹

Here, the experiments were carried out at room temperature in THF, toluene and CH₂Cl₂ respectively, fixing the concentrations, and adding quantitatively the pyridine system (Figure 9). As it can be observed in the UV-Vis spectra, initially all the experiments showed the Soret band related to the isolated compound but at different wavelengths depending on the solvent, which corresponded to 426.0 nm in THF, 427.6 nm in toluene and 422.2 nm in CH₂Cl₂. As the concentration of pyridine increased in the solution, the relative intensity for the Soret band decreased in all the cases. In THF (Figure 9a), there is no indication that pyridine bonded to the Zn(II) core even at the highest concentrations of pyridine. This may be due to the strong interaction of THF molecules with the porphyrin providing a solvent sphere that hinders the insertion of pyridine. When the porphyrin was treated in toluene (Figure 9b), the non-coordinative solvent, a bathochromic shift was observed which could correspond to the pyridine-compound. But it was observed only at a high concentration of pyridine, presumably because of the partial solubility of **Zn(4R-CPP)** in toluene and the addition of 20 μ L THF to improve solubility. Ultimately, UV-visible absorption spectroscopy in CH₂Cl₂ indicates efficient binding between **Zn(4R-CPP)** and pyridine molecules (Figure 9c). The increase of pyridine in the solution results in obvious red-shifts for the Soret and Q bands. An important shift was evidenced after the addition of 300 eq of pyridine, where the Soret band changed from 422.2 nm to 429.8 nm, the higher energy Q-band (Q _{α}) shifted from 549.8 nm to 562.6 nm, and the lower energy Q-band (Q _{β}) was from 589.4 nm to 604.8 nm. Moreover, the relative intensity for Q _{α} band decreased while the Q _{β} had a clearly increase when the content of pyridine exceeded 30 eq.²³ These results demonstrated the possibility of having penta-coordinated metalloporphyrin formed by one pyridine unit coordinated to the zinc metal ion.²⁴ Therefore, in this case CH₂Cl₂ was proposed as the best candidate compared to other solvents, and it was clear the effect of the surroundings and the necessity of excessive amount in the process of the linking material to carry out coordination.

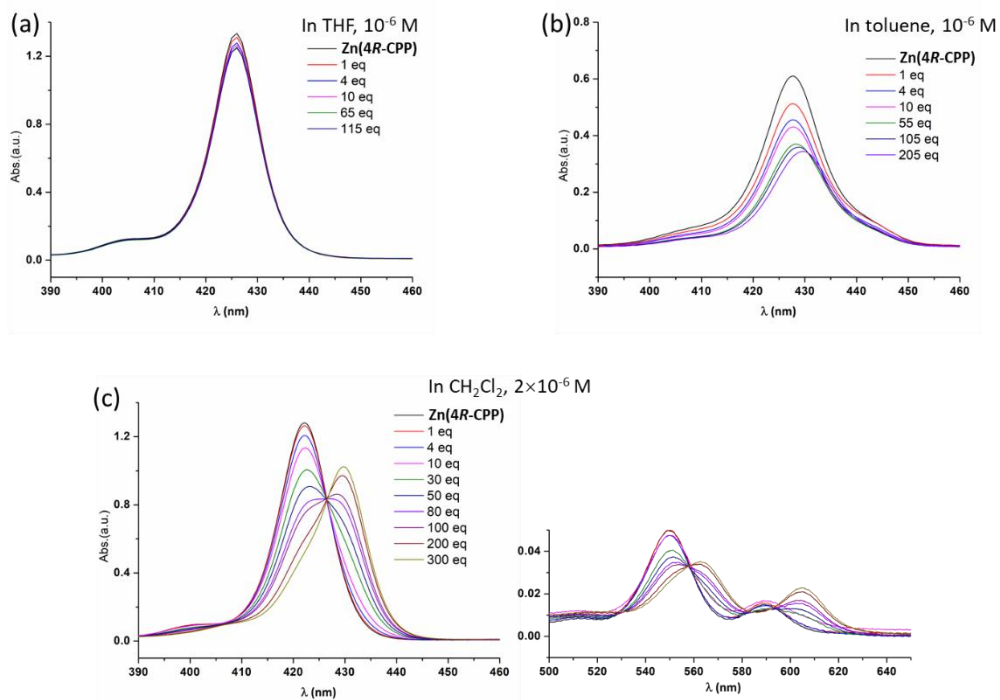


Figure 9. Titration of **Zn(4R-CPP)** with pyridine in (a) THF (10^{-6} M), (b) toluene (10^{-6} M), (a) CH_2Cl_2 (2×10^{-6} M).

4.3.3.2 Self-assembly studies in solution of Zn(4R-CPP) and TPyP

Here, it is worth to mention that both porphyrins, **Zn(4R-CPP)** and **TPyP**, have poor solubility in most of the common organic solvents, which limited in great manner of their study in solution. The solubility in a number of solvents was carefully tested in order to find out suitable solvents for the desired supramolecular aggregated that would contain both. In all the experiments, 0.2 mg of **Zn(4R-CPP)** were added in individual vials and then 194 μL of the candidate solvent was added (Figure 10 shows the list of solvents screened), to provide a final concentration of 10^{-3} M. **TPyP** was treated in the same way, and each vial contained 0.1 mg with 163 μL solvent (10^{-3} M). After sonication process, it appeared that **Zn(4R-CPP)** dissolved completely in THF and DMF, meanwhile the best solvent to solubilize **TPyP** was CHCl_3 . A compromised choice for both porphyrins was to perform the self-assembly experiments in DMF or THF, the solvents where both systems were partially soluble, at lower concentrations.

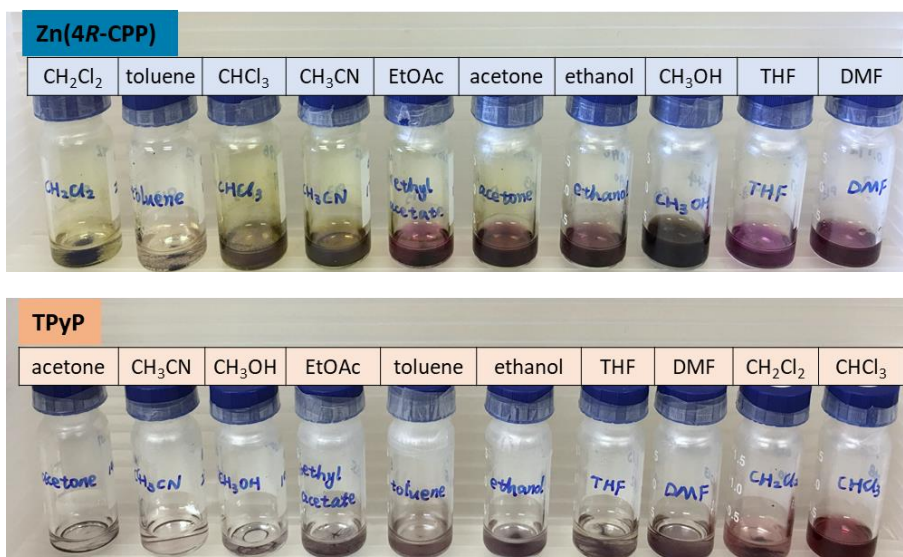


Figure 10. Solubility test of **Zn(4R-CPP)** and **TPyP** in different solvent (10^{-3} M).

In this way, the formation of aggregates was carried out at room temperature in DMF at 10^{-5} M for the porphyrin **TPyP** with the consecutive addition of **Zn(4R-CPP)**. In order to maintain the concentration of **TPyP** constant during the titration study, a mixture solution of **Zn(4R-CPP)** (10^{-4} M) and **TPyP** (10^{-5} M) in DMF was prepared for addition.

As observed in the UV-Vis spectra (Figure 11), the isolated porphyrin **TPyP** show a maximum absorption band at 415.6 nm for the Soret band and four absorptions at the range from 480 nm to 670 nm for the Q bands. As the carboxyl porphyrin **Zn(4R-CPP)** was added, the **TPyP** showed an increase in the absorbance bands. This effect may be as a result of increasing the solubility, caused by the interaction with **Zn(4R-CPP)** molecules. This result indicates the benefits of intermolecular self-assembly for the processing of this kind of porphyrin since **TPyP** is sparingly soluble in DMF in its pure form. To avoid precipitates from a saturated solution, 1.67 eq was the maximum amount used of **Zn(4R-CPP)**. The Soret band of **TPyP** present a bathochromic shift as well as a new peak appeared while increasing the content of **Zn(4R-CPP)**. Comparing the absorption spectra of the isolated **Zn(4R-CPP)** which is at 426.4 nm, the new peak corresponded to the Soret band of the latter could be identified. When the two porphyrins were mixed at the same concentration (10^{-5} M), the Soret band of both displayed a red shift of approximately of 1 nm, indicating efficient interaction of **Zn(4R-CPP)** and **TPyP** in solution even at low concentrations.

In addition, the characterization by ^1H NMR in DMSO- d_6 was attempted to observe the shifts resulting from the interaction of the two porphyrins. Nevertheless, clear NMR spectra could not be obtained because of the poor solubility and low concentration of the solution ($< 10^{-3}$ M).

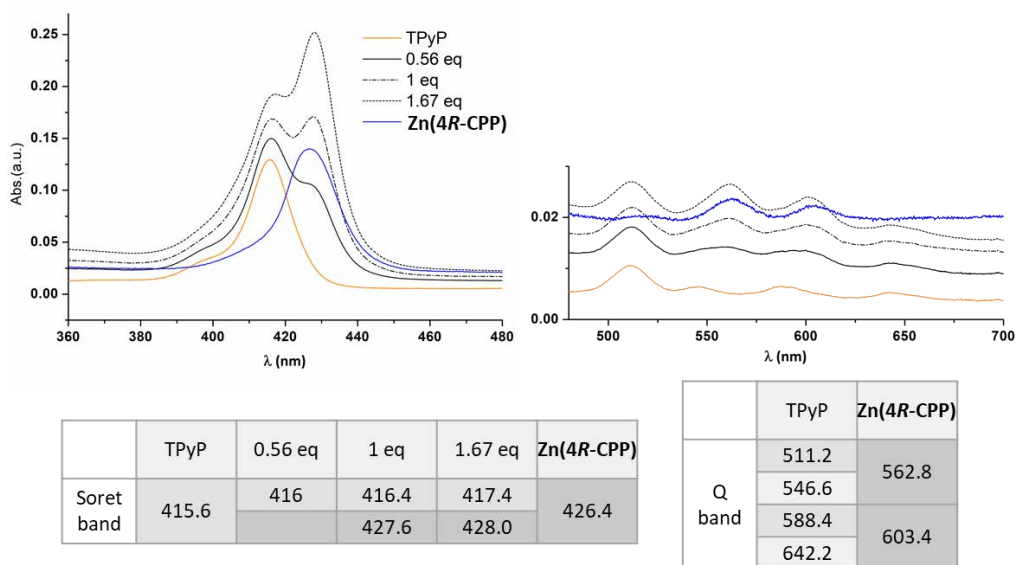


Figure 11. Titration of **TPyP** with **Zn(4R-CPP)** in DMF.

4.3.3.3 Self-assembly morphological studies of **Zn(4R-CPP)** and **TPyP**

DMF solutions of the two porphyrins **Zn(4R-CPP)** and **TPyP** at different concentration ratios were prepared (10 to 1, **Zn(4R-CPP)** vs. **TPyP**), and the final aggregates were analysed after precipitated on a copper grid support used for SEM analyses. The solid evolved after filtration and adsorption of the solvent by the use of a filter paper below the grid. The resulting porphyrin aggregates rested on the film of the grid (Figure 12). The samples were treated with gold coating to enhance the conductivity, and the measurement was performed under low vacuum and potential conditions to avoid overcharging the samples from the electron beam.

Figure 12 shows SEM images of the two isolated porphyrins and their mixtures. For **Zn(4R-CPP)** and **TPyP**, the two systems display nanoballs in both cases with homogenous sizes as well (Figure 12a and b). Probably because of the fast removal of the solvent, porphyrins cannot organize further providing bigger architectures and sizes.

Figure 12c presents the result from the ratio 10:1 (**Zn(4R-CPP)**): **TPyP**, the sample exhibits nanoballs as in previous cases but now the surface of the porphyrin nanoparticles become blurry. Once they appear to be at the same concentration (1:1) 10^{-5} M (Figure 12d), there is a clear absence of nanoballs on the grid and a roughness film can be appreciated. The change in the morphology suggests that a change in the way that molecules interaction appears when both are at the same concentration. However, in excess of one or the other, the recognition is different. Further experiments using others techniques (including microfluidics) should be carried out to gather more information. These experiments meant to explore the systems in their neutral states taking into account that the difference between them promotes hydrogen bonding interactions, but that coordination in the case of **Zn(4R-CPP)** appears as an additional

and competitive interaction with the **TPyP** units. Also, these preliminary experiments cannot discern the relevance of chirality in the final aggregates. Regarding this point, and as a way to glimpse the effect of some of these ideas, additional experiments using **TCPP** (Figure 13) and **TPyP** were discussed but not carried due to time limitations. Further analyses in this direction will be required.

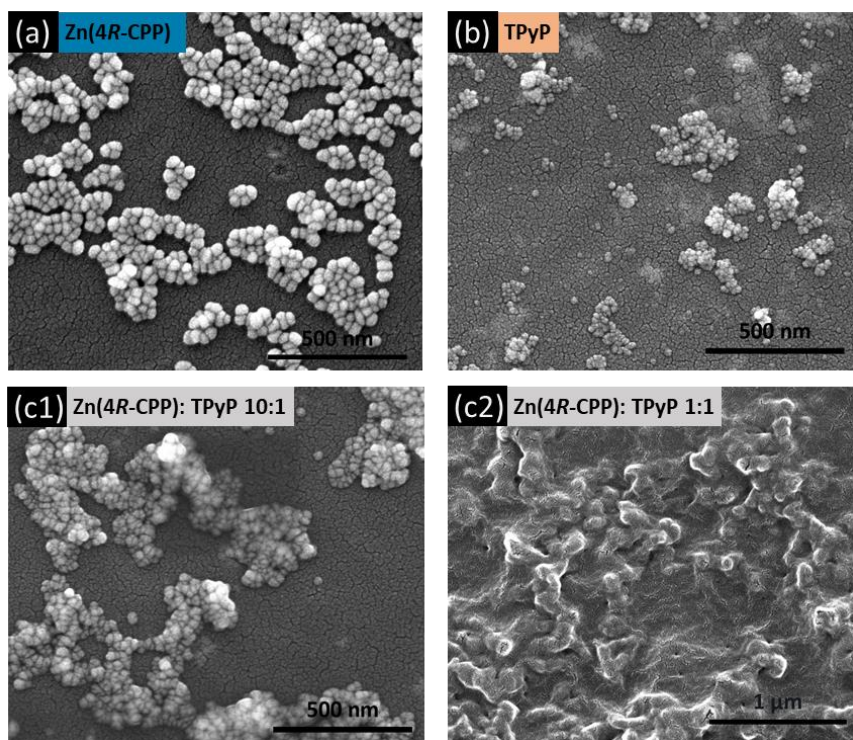


Figure 12. SEM images on copper grid of (a) **Zn(4R-CPP)** (10^{-5} M); (b) **TPyP** (10^{-5} M) and (c) mixture of **Zn(4R-CPP)** and **TPyP** (10^{-4} : 10^{-5} M or 10^{-5} : 10^{-5} M).

4.3.4 Self-assembly studies of **TCPP** and **TPyP**: titration experiments

Aggregates promoted by H-bonding and the creation of ordered architectures are particularly relevant in solids.^{25,26} In the past, 2D network structures made with **TCPP** molecules, were formed via intermolecular hydrogen bonding on Au (111) and were investigated by scanning tunnelling microscopy (STM).²⁵ The same studies show that when modified **TCPP** by replacing one of the 4-carboxyphenyl functions with a 3-pyridyl ring, a polar 2D grids can be formed by utilizing intermolecular (carboxyl...pyridyl) hydrogen bonding.²⁶

H-bonding is generally of limited stability, taking into account that **TCPP** and **TPyP** share the same porphyrin core and that the overall geometry structure is very similar, having each four symmetric functional groups. Here, titration experiments were performed using the two metal-

free porphyrins. The experiment was carried out in the same way described before, with fixing the concentration of **TPyP** and adding the mixture solution.

As the same phenomenon observed in the case of **TPyP** titrated with **Zn(4R-CPP)**, the Soret band increased and present a bathochromic shift when **TCPP** was added (Figure 13). During the whole titration procedure, only one Soret band appeared. Different from the combination of two isolated porphyrin bands, the clear band indicated the formation of homogeneous structure in solution. Due to the absent of metal in the porphyrin cores, the intermolecular coordination is negligible and the H-bonding is contributing to the self-assembly. These experiments stress the changes regarding to the interactions, and ignore the difficulty of detailed analyses and precise information regarding other subjects, for example the effect of the length or rigidity of the branches attached to the chromophore as well as the relevance of chiral centres in the final aggregates.

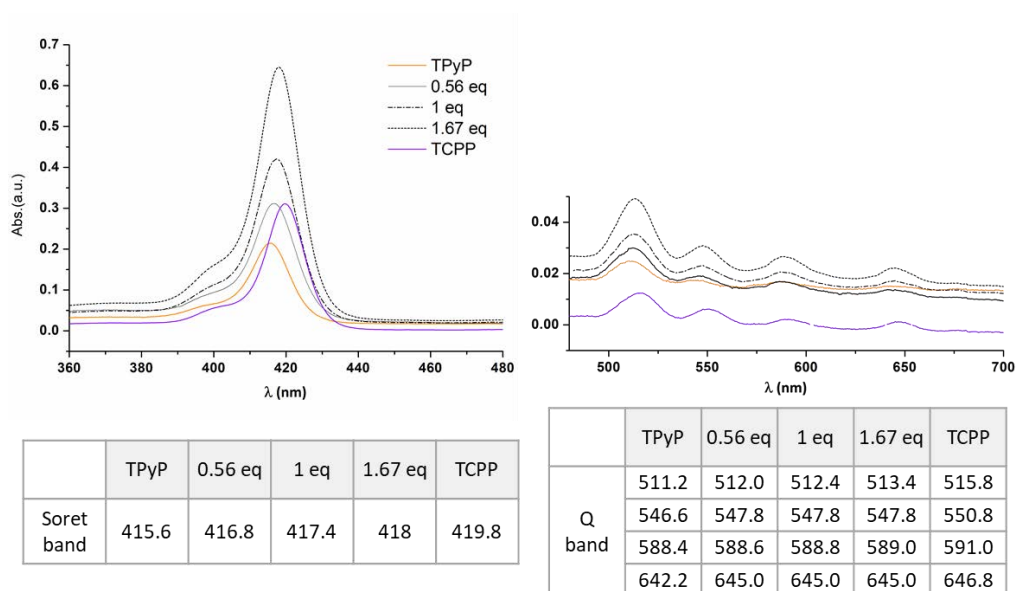


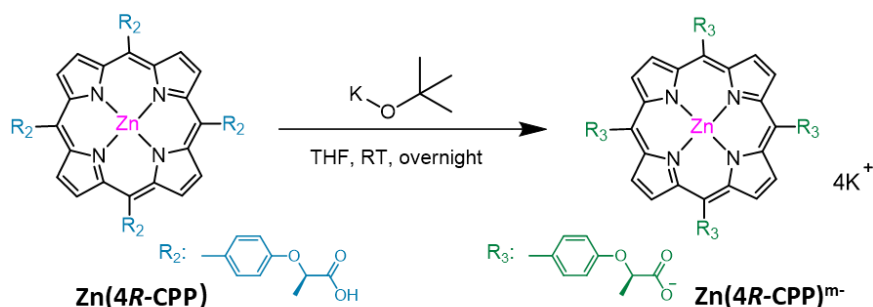
Figure 13. Titration of **TPyP** with **TCPP** in DMF.

4.4 Ionic self-assembly of water soluble porphyrins

4.4.1 Synthesis of **Zn(4R-CPP)^{m-}**

Taking into account the limited solubility of the systems under study and the possibility of improving the strength of the interactions, we deprotonated the carboxylic groups and protonated the pyridine, **Zn(4R-CPP)** and **TPyP** respectively, which allowed us to perform experiments in additional and biocompatible solvents, for example H₂O.

The water-soluble porphyrin $\text{Zn(4R-CPP)}^{\text{m-}}$ was achieved by the deprotonation of the carboxyl porphyrin Zn(4R-CPP) using potassium tert-butoxide in THF under mild conditions (Scheme 2). Once the porphyrin salt was formed, the pink product would precipitate from the THF solution with a yield of 96 %.



Scheme 2. Synthesis of chiral acidic metalloporphyrin Zn(4R-CPP) .

4.4.2 Synthesis of $\text{H}_n\text{TPyP}^{\text{n+}}$

Beer's law experiments carried out for **TPyP** by Robert F. Pasternack^{27,28} in H_2O at different pH have demonstrated that the porphyrin in the acid forms obey the law, and the temperature-jump study corroborated the finding that **TPyP** exists in aqueous solution in its monomeric form. In their study, **TPyP** was positively charged at the periphery at $\text{pH} = 2.3$ and the monomeric porphyrin unit contained two pyrrole hydrogens in the central region. Additional spectroscopy related to the protonation of **TPyP** in CH_2Cl_2 has been reported in the literature,²⁹ indicating that the protonation and aggregation behaviour are markedly influenced by the nature of the acid used in the procedure. Addition of large quantities of trifluoroacetic acid (CF_3COOH) to a CH_2Cl_2 solution of **TPyP** porphyrin produces a red shift of the Soret band together with the collapsing of the four Q-bands into two new bands. It has been established that the change from a D_{2h} (the free base) to a D_{2d} symmetry (the diacid species) of the porphyrin core confirms the fully protonated $\text{H}_6\text{TPyP}^{6+}$. In the case of increasing the HCl concentration, the Soret and Q-bands undergo gradual hypochromicity and bathochromic shifts, and a tetra-protonated species at the peripheral pyridyl groups $\text{H}_4\text{TPyP}^{4+}$ was observed during the process. And in another example, the bulky tetrakis(3,5-bis(trifluoromethyl)phenyl)borate anion (TFPB) led to the formation of unaggregated tetraprotonated ($\text{H}_4\text{TPyP}^{4+}$)(TFPB)₄ ion pairs due to the steric hindrance.

Considering all the above, HCl was chosen for acidizing **TPyP**, taking into account that our de-protonated system, $\text{Zn(4R-CPP)}^{\text{m-}}$, would contain K^+ ions as counterions and then KCl will be formed once both species contact. As it is mentioned above, the HCl aqueous solution at the $\text{pH} = 2.3$ ($[\text{H}^+] 5.01 \text{ mM}$) give rise to $\text{H}_4\text{TPyP}^{4+}$ species, and by using the 4:1 ratio one could calculate the concentration of porphyrin in the solution as 1.25 mM. Under this calculation, 7.75 mg of **TPyP** was added into 10 mL HCl aqueous solution ($\text{pH} = 2.3$). The **TPyP** was partly dissolved even after ultrasonication, which indicated that the concentration ratio of H^+ to **TPyP** should be larger

than 4:1 to have the possibility of H_4TPyP^{4+} species in solution. Besides, isolation of H_4TPyP^{4+} from solution was unfeasible because of the pH value changed as the volume of solvent decreased.

Previous report demonstrated that the macrocyclic centre of TPyP does not get affected by large ions such as TFPB,²⁹ so it is presumed that the interaction with $Zn(4R-CPP)^{m-}$ by ionic-assembly may happen exclusively at the peripheral positions. Therefore, the existence of H_4TPyP^{4+} or H_6TPyP^{6+} would not provide severe difference regarding the nature of the intermolecular interactions.

For our studies, it is worth to isolate first both systems, $Zn(4R-CPP)^{m-}$ and acidulated porphyrin H_nTPyP^{n+} . For this reason, 25 mg TPyP were added in 16 mL milli-Q water, then titrated by HCl aqueous solution (6 M, 200 μ L) dropwise and slowly until all the porphyrin dissolved. By means of ultrasonication, the TPyP and acid can blend sufficiently to keep a uniform green solution with a final pH of 1.29. The solution was left in oven (80 °C) until the evaporation of acid solvent and green crystals came out.

Figure 14 shows the crystal structure of H_nTPyP^{n+} by single crystal X-ray diffraction using a synchrotron source. The core of the molecule can be better described now as H_6TPyP^{6+} . Water molecules are present in the crystal lattice (oxygen depicted in red), and the H-bonding they provide result in the different pyridine environment of the porphyrin periphery. Chloride ions (green) are located around the four pyridine substitutions by $Cl \cdots H-N_{py}$ H-bonding with distances of 2.246 and 2.329 Å. In the porphyrin core, there are four hydrogen atoms binding to the corresponding nitrogen atoms and two chloride ions fixed at the both sides of the porphyrin plane by H-bonding. As chloride anions interlace between porphyrin units and interact with all the TPyP surrounding them, we could conclude that it is hexa-protonated of the TPyP in the crystal structure but the average charge for each porphyrin unit is less. A remarkable outcome from the crystals is the bending of the porphyrin. The conjugated core displays a conformation that differs in great manner from planar, pointing to the fact that should be taking into account for the planning of 2D webs containing such species together with the $Zn(4R-CPP)^{m-}$ systems.

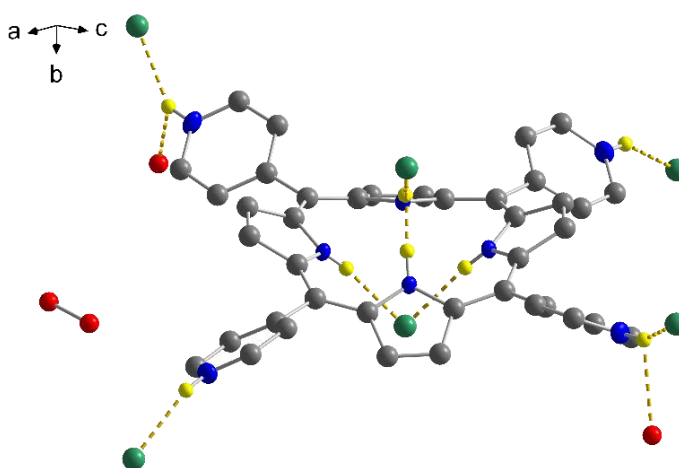


Figure 14. The crystal structure of acidizing H_nTPyP^{n+} . Parts of H-bonding are marked by yellow dash line. Colour legend: Cl in green, O in red, N in blue and C in grey.

4.4.3 Ionic self-assembly studies using Zn(4R-CPP)^{m-} and $\text{H}_n\text{TPyP}^{n+}$

There are only few reports related to the self-assembly of porphyrins in aqueous solution, one example is the *meso*-tetrakis(4-phosphonatophenyl)porphyrin (H_2TPPP) aggregates in various protonation equilibrium steps showing the pH-dependent homo-self-assembly.³ In the case of self-aggregation of opposite charged porphyrins, the anionic *meso*-tetrakis(4-sulfonatophenyl)porphine (H_2TPPS) and the cationic *meso*-tetrakis(N-methylpyridim-4yl)porphinato-copper(II) (CuT4) were proved to imprint chirality promoted by their assembly in solution.³ The change of the cationic unit by $\text{Sn}^{\text{IV}}\text{T(4-Py)P}^{4+}$ displayed a well-defined binary porphyrin nanostructure by ionic self-assembly.¹⁷

It is worth to mention that the new water-soluble porphyrins we synthesized break away the restricted conditions for the aggregation studies of general porphyrins in organic solvents, and the achievement of molecules soluble in water opens the door to future studies by microfluidics, since our systems can be introduced in microfluid ships which are made of polydimethylsiloxane (PDMS), a material non-resistant to common organic solvents. An initial characterization in the bulk (standard solution) was performed in this thesis to promote further microfluidic analyses. Following the examples reported,¹⁷ the straightforward mixing of equimolar solutions of Zn(4R-CPP)^{m-} and $\text{H}_n\text{TPyP}^{n+}$ in water was carried out and the outcomes were observed by SEM technique..

Figure 15 shows the aqueous solutions (10^{-3} M) of each porphyrin, Zn(4R-CPP)^{m-} and $\text{H}_n\text{TPyP}^{n+}$. The former is a clear dark green solution, while the latter is brick-red colour with a pasty texture. Once mixed the two compounds at the ratio 1:1, precipitate named **M1** formed immediately. As the two porphyrins were consumed completely, the solution became transparent. A drop of the solution containing the corresponding compound was placed on the pH paper, which was then dried for comparison. All of the three solutions were neutral (Figure 15), indicating that acidic porphyrin TPyP^{n+} was stable in the fresh prepared aqueous solution and the H^+ did not seem to be released from porphyrin molecules. In the case of the mixture, the remaining of neutral solvent illustrated that the charge of the two porphyrins were identical, and they achieved an equilibrium state to precipitate under the controlling of mole ratio.

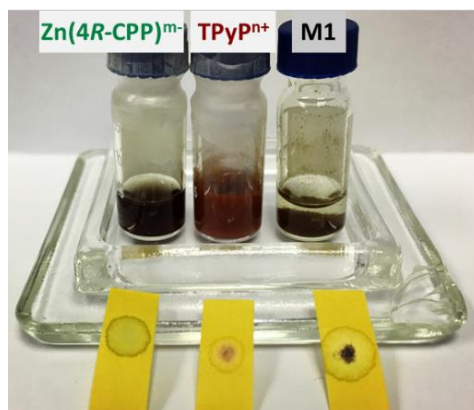


Figure 15. The aqueous solutions of Zn(4R-CPP)^{m-} , $\text{H}_n\text{TPyP}^{n+}$ and their mixture **M1**.

Droplets of $\text{Zn(4R-CPP)}^{\text{m-}}$ and $\text{H}_n\text{TPyP}^{\text{n+}}$ aqueous solutions were deposited on silicon substrates. After the evaporation of water, the remains were examined by using SEM. Figure 16a shows the morphologies of potassium $\text{Zn(4R-CPP)}^{\text{m-}}$. The porphyrin organized along certain directions, forming porphyrin flowers with six petals in big scale. The details of the surface reveal that they were composed by the compact stacking of slender fibres. Except the well-formed crystals, another aggregation which was in an amorphous state was found to spread on the substrate, and it has already displayed a tendency of dendritic developing.

In the case of $\text{H}_n\text{TPyP}^{\text{n+}}$ chloride, the porphyrin directly aggregated into flat bulks shown in Figure 16b. Most of the reports²⁷⁻²⁹ about acidic TPyP aggregations were investigated in organic solvents or in aqueous solution as we mentioned before ($\text{TPyP}^{\text{n+}}$ synthesis section). Here, the compound was concentrated on silicon surface, and the self-assembly of the porphyrin was purely visual. For a metallo-TPyP system from Li-Jun Wan *et al.*,³⁰ self-assembled structures displayed hollow hexagonal nanoprisms with the assistance of surfactant. However, acidic free-base porphyrin in this thesis presents a pretty different morphology.

When transferred the precipitate **M1** on the silicon substrate and studied by SEM, the final aggregates were composed by octahedral nanoparticles structures which were covered with amorphous film (Figure 16c). The SEM images reveal that the octahedrons are nanometres in size, and small crystals locate in the film seemed to be the initial growing point of the nanoparticles. Different morphologies formed in our experiment, indicates that the aggregations of the two water-soluble porphyrins happened very fast through the bulk process. To improve the conditions for introducing two kinds of porphyrins, a moderate way via microfluid processes is presumed in future.

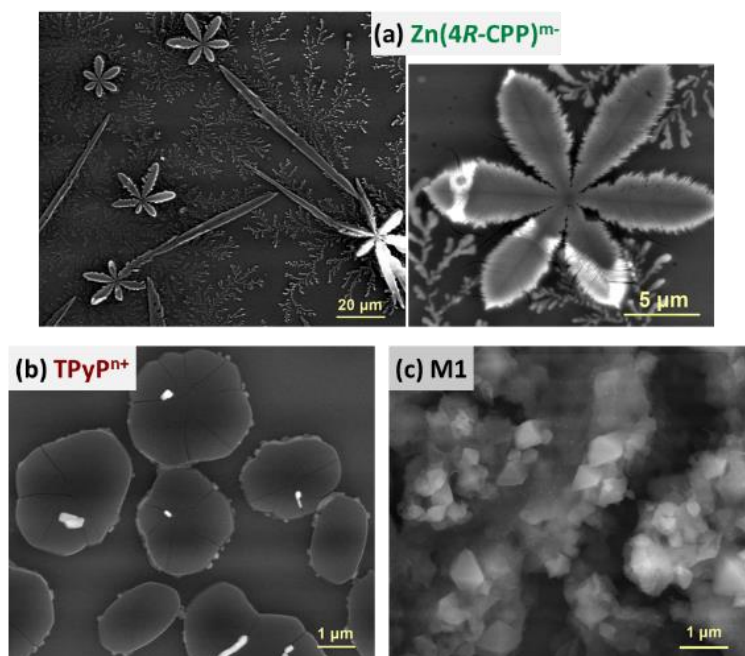


Figure 16. SEM images of porphyrins aggregations (a) potassium $\text{Zn(4R-CPP)}^{\text{m-}}$, (b) $\text{H}_n\text{TPyP}^{\text{n+}}$ chloride and (c) the mixture **M1**.

4.5 Conclusions

In this chapter, my work has been focused on developing porphyrin materials produced via non-covalent interactions such as particulate H-bonding motifs or various coordination centre of compounds. A series of studies of porphyrins which involved different groups have demonstrated that the non-covalent interactions were indeed formed in solution and in the solid state. Metalloporphyrin **Zn(4R-CPP)**, which contains a Zn(II) centre and four carbonyl groups at its *meso*-positions, appears to be well-organized in mixture solvent systems, resulting in a variety of single crystal morphologies. Comparing to **Zn(4R-PPP)**, which does not show any aggregation in common organic solvents, the formation of H-bonding is supported by the spectral signals in the apolar solution methylcyclohexane. The three titration experiments including **Zn(4R-CPP)** with pyridine and **TPyP**, as well as **TCPP** with **TPyP**, demonstrate the Zn(II) centre in this molecule could be affected by the pyridine groups when the coordinating ligands is in an excess amount in solution, while the H-bonding formed by -COOH...Py- substituents of the two different porphyrins contribute in great manner to the aggregations.

Furthermore, the self-assembly study in aqueous solutions has been performed by successful synthesis of the water-soluble porphyrins **Zn(4R-CPP)^{m-}** and **H_nTPyPⁿ⁺**, with small counterions Cl⁻ and K⁺ respectively. The different morphologies of the single porphyrin and the mixture indicate that the two compounds could interact by ionic-assembly and present new micron octahedral nanomaterial.

Experimental Section:

Materials.

The compounds of tetra(4-pyridyl) porphyrin (**TPyP**) and tetra(4-carboxyphenyl) porphyrin (**TCPP**) used in this study were purchased from PorphyrChem Co. Ultrapure water with a resistivity $\geq 18.2 \text{ M}\Omega \text{ cm}$ was produced using a Milli-Q apparatus (Millipore) and was filtered by an inorganic membrane with a pore size of $0.02 \mu\text{m}$ (Whatman International, Ltd.) just before use.

Synthesis Methods.

1. Acidic metalloporphyrin, Zn(4R-CPP)

100 mg of **Zn(4R-PPP)** was dissolved in 4.54 mL of THF (20 mM), then 1.51 mL of LiOH aqueous solution (1.6 M) was added, and the mixture was stirred at room temperature overnight. After removing the THF solvent, 20 mL H₂O and 20 mL of CH₂Cl₂ were added, being the porphyrin in the aqueous phase. Treatment of the aqueous solution with dilute HCl (1.2 M) dropwise promoted the displacement of the solid to the organic phase. After the collection of CH₂Cl₂

solution and vacuum drying process, the purple solid **Zn(4R-CPP)** was obtained without further purification. Yield: 81 mg, 87%. ¹H NMR (300 MHz, DMSO-d₆) (Figure A4.1) δ 13.20 (s, 4H), 8.77 (s, 8H), 8.06 (d, *J* = 8.9 Hz, 8H), 7.27 (d, *J* = 8.4 Hz, 8H), 5.14 (q, *J* = 7.1 Hz, 4H), 1.70 (d, *J* = 6.9 Hz, 12H). Maldi-TOF/MS *m/z* (%): 1026.90 ([M-H]⁺)

2. Metalloporphyrin potassium salt, Zn(4R-CPP)^{m-}

An alkaline potassium tert-butoxide solution in THF 10⁻³ M was prepared. Then 20 mg of **Zn(4R-CPP)** was dissolved in 77.5 mL of the alkaline solution (2.5×10⁻⁴ M), and the mixture was stirred at room temperature overnight. After the evaporation of solvent, pink powder crude product came out. The precipitate was dissolved in H₂O and filtered to remove unreacted porphyrin. The evaporation of H₂O followed by THF washing process, pure porphyrin product was obtained. Yield: 22 mg, 96%. ¹H NMR (300 MHz, Deuterium Oxide) (Figure A4.2) δ 8.99 (s, 8H), 8.10 (d, *J* = 8.4 Hz, 8H), 7.31 (d, *J* = 8.7 Hz, 8H), 4.97 (q, *J* = 6.7 Hz, 4H), 1.75 (d, *J* = 6.8 Hz, 12H).

References:

- (1) Puigmartí-Luis, J.; Saletta, W. J.; González, A.; Amabilino, D. B.; Pérez-García, L. *Chemical Communications* **2014**, 50, 82.
- (2) So, M. C.; Jin, S.; Son, H.-J.; Wiederrecht, G. P.; Farha, O. K.; Hupp, J. T. *Journal of the American Chemical Society* **2013**, 135, 15698.
- (3) Lauceri, R.; De Napoli, M.; Mammana, A.; Nardis, S.; Romeo, A.; Purrello, R. *Synthetic metals* **2004**, 147, 49.
- (4) Li, C.; Qiu, W.; Long, W.; Deng, F.; Bai, G.; Zhang, G.; Zi, X.; He, H. *Journal of Molecular Catalysis A: Chemical* **2014**, 393, 166.
- (5) Medforth, C. J.; Wang, Z.; Martin, K. E.; Song, Y.; Jacobsen, J. L.; Shelnut, J. A. *Chemical Communications* **2009**, 7261.
- (6) Oliveras-González, C.; Di Meo, F.; González-Campo, A. n.; Beljonne, D.; Norman, P.; Simón-Sorbed, M.; Linares, M.; Amabilino, D. B. *Journal of the American Chemical Society* **2015**, 137, 15795.
- (7) Goldberg, I. *Chemical Communications* **2005**, 1243.
- (8) Imamura, T.; Fukushima, K. *Coordination Chemistry Reviews* **2000**, 198, 133.
- (9) Fleischer, E. B.; Shachter, A. M. *Inorganic Chemistry* **1991**, 30, 3763.
- (10) Tsuda, A.; Nakamura, T.; Sakamoto, S.; Yamaguchi, K.; Osuka, A. *Angewandte Chemie International Edition* **2002**, 41, 2817.
- (11) Cao, J.; Liu, J.-C.; Deng, W.-T.; Li, R.-Z.; Jin, N.-Z. *Electrochimica Acta* **2013**, 112, 515.
- (12) Patra, R.; Titi, H. M.; Goldberg, I. *Crystal Growth & Design* **2013**, 13, 1342.
- (13) Zaman, M. B.; Tomura, M.; Yamashita, Y. *The Journal of organic chemistry* **2001**, 66, 5987.

- (14) Vishweshwar, P.; Nangia, A.; Lynch, V. M. *The Journal of organic chemistry* **2002**, *67*, 556.
- (15) Farha, O. K.; Shultz, A. M.; Sarjeant, A. A.; Nguyen, S. T.; Hupp, J. T. *Journal of the American Chemical Society* **2011**, *133*, 5652.
- (16) Lee, C. Y.; Farha, O. K.; Hong, B. J.; Sarjeant, A. A.; Nguyen, S. T.; Hupp, J. T. *Journal of the American Chemical Society* **2011**, *133*, 15858.
- (17) Wang, Z.; Medforth, C. J.; Shelnut, J. A. *Journal of the American Chemical Society* **2004**, *126*, 15954.
- (18) Balaban, T. S. *Accounts of chemical research* **2005**, *38*, 612.
- (19) van Hameren, R.; van Buul, A. M.; Castriciano, M. A.; Villari, V.; Micali, N.; Schön, P.; Speller, S.; Monsù Scolaro, L.; Rowan, A. E.; Elemans, J. A. *Nano letters* **2008**, *8*, 253.
- (20) Nappa, M.; Valentine, J. S. *Journal of the American Chemical Society* **1978**, *100*, 5075.
- (21) Stockett, M. H.; Musbat, L.; Kjær, C.; Houmøller, J.; Toker, Y.; Rubio, A.; Milne, B. F.; Nielsen, S. B. *Physical Chemistry Chemical Physics* **2015**, *17*, 25793.
- (22) Borovkov, V. V.; Lintuluoto, J. M.; Fujiki, M.; Inoue, Y. *Journal of the American Chemical Society* **2000**, *122*, 4403.
- (23) Gautam, R.; Chauhan, S. *Materials Science and Engineering: C* **2014**, *43*, 447.
- (24) Alessio, E. *STRUCTURE AND BONDING* **2006**, *1*.
- (25) Yuan, Q.; Xing, Y.; Borguet, E. *Journal of the American Chemical Society* **2010**, *132*, 5054.
- (26) Vinodu, M.; Goldberg, I. *CrystEngComm* **2005**, *7*, 133.
- (27) Pasternack, R. F.; Huber, P. R.; Boyd, P.; Engasser, G.; Francesconi, L.; Gibbs, E.; Fasella, P.; Cerio Venturo, G.; Hinds, L. d. *Journal of the American Chemical Society* **1972**, *94*, 4511.
- (28) Pasternack, R. F. *Annals of the New York Academy of Sciences* **1973**, *206*, 614.
- (29) De Luca, G.; Romeo, A.; Scolaro, L. M. *The Journal of Physical Chemistry B* **2005**, *109*, 7149.
- (30) Hu, J.-S.; Guo, Y.-G.; Liang, H.-P.; Wan, L.-J.; Jiang, L. *Journal of the American Chemical Society* **2005**, *127*, 17090.

Chapter V

Exploratory study of new curcuminoids

5.1 Introduction

In the previous Chapters (II and IV), intermolecular self-assembled structures based on porphyrins have been achieved by the unique design of our molecules. Taking the advantage of the chiral *meso*-substituents, the derivatives of 2-aryloxy propanoate or 2-aryloxypropanoic acid (Figure 1), various aggregation are obtained by the coordination of metal centre with substituents and non-covalent interactions, especially the H-bonding. And we pointed out well-organized structures of **Zn(4R-PPP)** were beneficial to a potential application in solution processed organic solar cell.

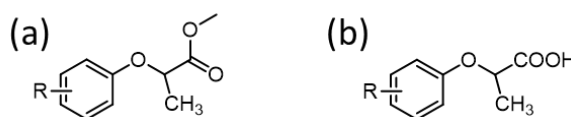


Figure 1. Chemical structures of racemic (a) 2-aryloxy propanoate and (b) 2-aryloxypropionic acid.

In this chapter, additional studies related to these ligands will be carried out because of their proved ability for self-assembly and other relevant properties. For example, some chiral systems based on 2-aryloxypropionic acids, especially the (*R*)-enantiomers, are pointed out as herbicides widely used for the pre- and post-emergence control of broadleaf weed.¹ In this case, extensive information on the degradation capacity of phenoxyalkanoic herbicides used against bacteria, soil microbes, and plant has been published in the last years.^{2,3} Several 2-aryloxypropionic acids also possess analgesic and anti-inflammatory properties but with less ulcerogenic activity comparing to ketoprofen or acetylsalicylic acid.⁴⁻⁶ Due to the importance of chiral 2-aryloxypropionic acids, both for agrochemical as well as for pharmaceutical applications, it is clear to combine this moiety with some bioactive components.

Curcuminoids (CCMoids, Figure 2), the bright yellow chemicals with a natural origin, were considerate. Their supposed pharmacological activities as anti-oxidant, anti-inflammatory,⁷ anti-virus and anti-tumoral responses demonstrated to be effective to a certain extent in recent medical treatments.^{8,9} Besides, the versatile chemistry of CCMoid molecules has opened new door to develop their applications in the functional materials fields, such as molecular electronics,¹⁰ host frameworks for drug delivery¹¹ and organic solar cells.¹²

CCMoids can be synthesized by the aldol condensation of β -diketone groups with aromatic aldehydes,¹³ and the modification of them at four different parts (Figure 2) create CCMoids-based multifunctional systems. In our work, chiral 2-aryloxy propanoate ligand was introduced into the CCMoid skeleton, which (as before it happened with the porphyrin units) can coordinate to a series of metallic atoms, such as Zn, Co, or metalloid atom as B, providing homoleptic or heteroleptic structures.^{14,15} In addition, the de-protection of the ester groups (the end of the CCMoid arms) providing two carboxylic groups makes the CCMoid a good candidate for the construction of multidimensional structures. It is important to mention that the presence of chiral groups attached to the CCMoid skeleton is not well developed in the literature; only few

publications regarding the optical chirality of CCMoids has been studied by the non-covalent interactions of polyphenolic type CCMoid with biomacromolecules, such as human serum albumin and nucleic acids.¹⁶⁻¹⁸

Taking into account all the above, CCMoids bearing chiral and achiral arms were synthesized and investigated in the same way. All the molecules under study in this chapter are listed in Figure 2.

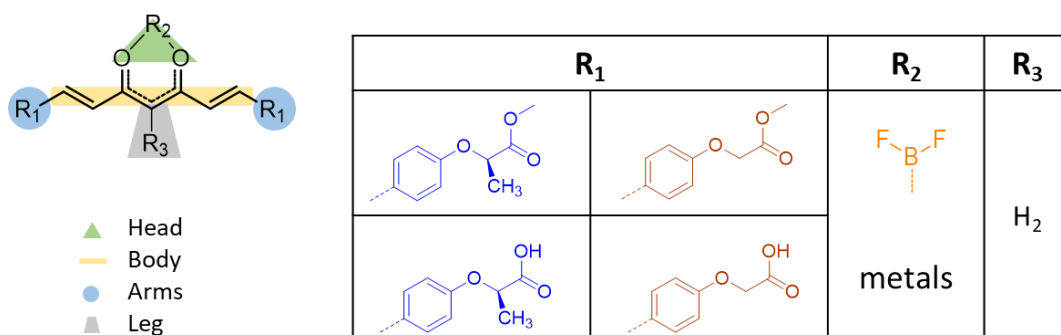


Figure 2. Schematic drawing of the target functionalized CCMoids.

5.2 Objectives

The main objects of this project are:

The synthesis of CCMoids containing chiral groups, in a similar manner as chapter II describes, as well as the study of the effect of chirality in such systems. In addition, research towards the achievement of terminal acid groups from the hydrolyzation of the ester groups (as chapter IV shows) would allow to investigate the possible creation of systems with different dimensionality (1D, 2D, MOFs, ...) as well as open the possibility of examining CCMoid systems soluble in aqueous solution for future applications as biomaterials.

The project will be carried out centring in the following aspects:

- (1) Preparation of CCMoids containing chiral ester groups (groups described in chapters II) and the creation of coordination compounds with such ligand.
- (2) Analogous studies with CCMoid that display carboxylic ending groups (in the arms) to increase the coordination points. Compare the differences of CCMoids with chiral and achiral arms in spatial assembly and also make comparison between CCMoids and porphyrins from previous chapters.

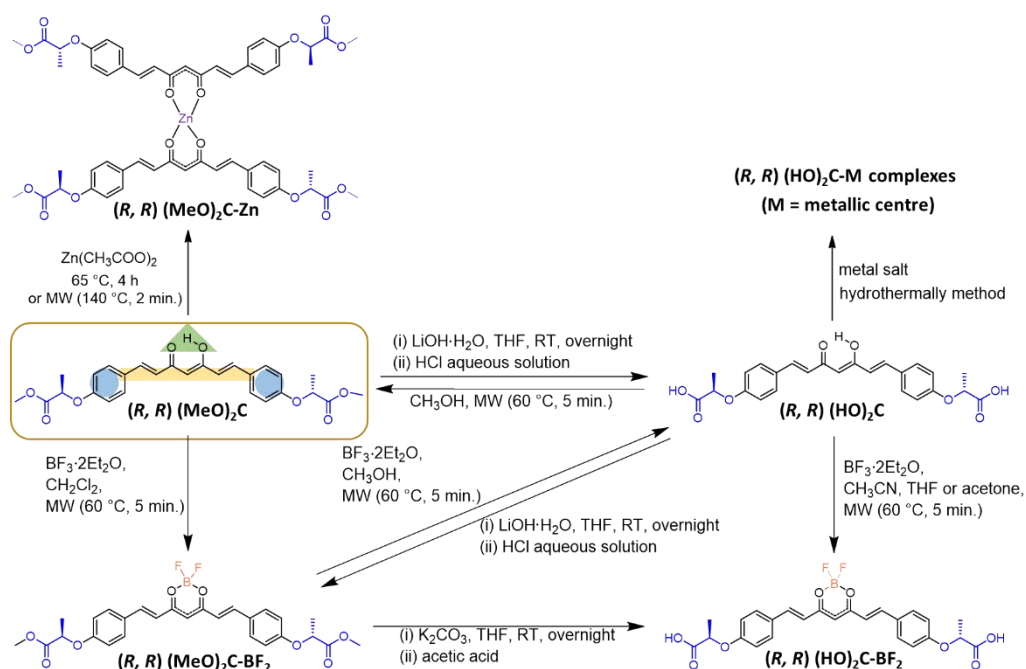
The β -diketone moiety, common for all CCMoids, can provide coordination to different metalloids or metal centres. On the other hand, the ester groups and the carboxylic groups from the ends of the molecule can assist in further reactions by coordinating with additional metal

ions to provide high dimensional structures. Finally, the chiral or achiral groups confers the molecule with unique properties toward recognition, function and self-assembly.

As it was shown before, a powerful method to study molecular assembly is single crystal X-ray diffraction, which reflects the molecule arrangement in space. In this chapter, the final systems were characterized by the use of such technique together with studies in solution, such as absorption spectroscopy and fluorescence spectroscopy, providing a general picture of the intrinsic properties and complex architectures of the molecules.

5.3 Synthesis and characterization

This section shows the synthetic pathways used to achieve a novel family of CCMoids. This set of molecules encloses chiral and achiral groups in the arms of the CCMoids (similar as it was performed in chapter II), which can be attached to ending ester groups or carboxylic systems (as shown for porphyrins in chapter IV). In addition, this section also introduces the coordination of these organic molecules with metal ion and metalloids (boron from BF₂- moiety) providing a number of different molecular structures. Taking the chiral system as an example, Scheme 1 presents the chemical combinations achieved with these CCMoids.



Scheme 1. Reactivity tested with CCMoids.

Figure 3 illustrates the two methodologies used for growing suitable crystals. One is by the evaporation of the mixed CCMoid solution, and the other is by slow diffusion of diethyl ether vapour into a compound solution.

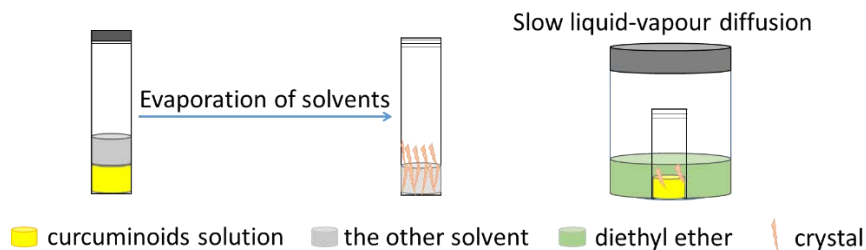
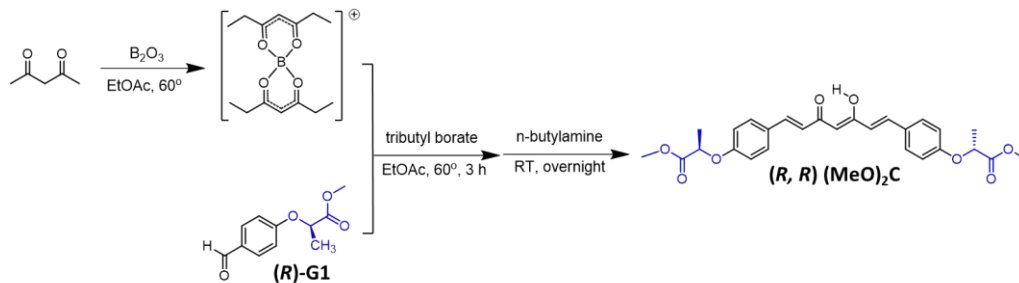


Figure 3. General description of the methodologies followed to re-crystallize CCMoids crystals.

5.3.1 Synthesis of CCMoids bearing chiral centres and ester groups

5.3.1.1 Synthesis and crystal structure of (*R, R*) (MeO)₂C



Scheme 2. Synthesis of the (*R, R*) (MeO)₂C

To perform the synthesis of the desired CCMoid a first step is required where the chiral aldehyde (*R*)-Methyl 2-(4-formylphenoxy) propanoate (**(*R*)-G1**) must be prepared. This is achieved by the use of the Mitsunobu reaction and further information has been already described in Chapter II. The new CCMoid ligand, (*R, R*) (MeO)₂C, was prepared by the modified method reported in the literature.^{13,19} Like in previous works, the first step involves the formation of a boron compound of 2,4-pentanedione under mild conditions. This prevents Knoevenagel reactions on the methylene group and activate the methyl positions of 2,4-pentanedione for aldol condensation once the mixture of (**(*R*)-G1**) and tributyl borate is added. Then, *n*-butylamine is incorporated as catalyst. Here, the boron compound decomposed without the use of dilute acids, giving the desired CCMoid. To purify, the achieved brown slurry material was separated from a residual transparent liquid (excess of tributyl borate) after the total evaporation of the

solvent. The solid part was washed with cold CH₃OH until it became yellow, resulting in the pure precipitate (**R, R**) (MeO)₂C with a 31 % of yield.

The compound of (**R, R**) (MeO)₂C is air-stable and highly soluble in most organic solvents. It was re-crystallized by slow liquid-liquid diffusion method in CH₂Cl₂/CH₃OH system, when in a final step, the sample was left open to air and most of the solvent evaporated, which is a similar manner as the porphyrin systems described in chapter II. As a result, crystals were analysed by single X-ray diffraction. Table A5.1 shows general crystal data information of the CCMoid species.

(**R, R**) (MeO)₂C crystallized from CH₂Cl₂/CH₃OH as a yellow crystal in the orthorhombic space group P₂₁₂₁₂₁, with CH₃OH molecules intercalated in the structure (Figure 4 and A5.1). The keto-enol form of the central moiety in the molecule was confirmed in the solid state. Distances of C(1)-C(2) and C(1)-C(15) have a slightly difference, intermediate between a single and double bond, indicating a conjugation with the CCMoid backbone. The two phenyl groups extend from the backbone with slight twist (torsion angles 171.20 and 15.42°), forming a conjugated backbone bended to be arched shown in Figure 4b, and the chiral moieties are flexible and point to different directions.

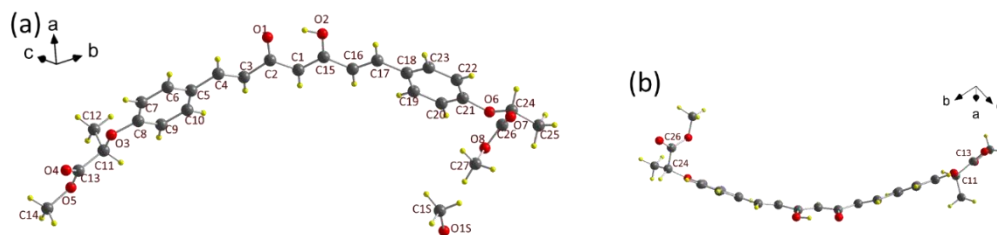


Figure 4. Molecular structure of (**R, R**) (MeO)₂C in different crystallographic projections. Colour legend: O in red, H in yellow and C in grey.

In the 2D packing of (**R, R**) (MeO)₂C (Figure 5) the carbonyl and methyl groups of the chiral centre provide weak hydrogen bonding with adjacent CCMoids. Furthermore, the π - π stacking from phenyl groups (3.856 and 3.751 Å) display CCMoids face to face. The final crystal structure was organized by layers with a distance of 5.334 Å (Figure A5.2).

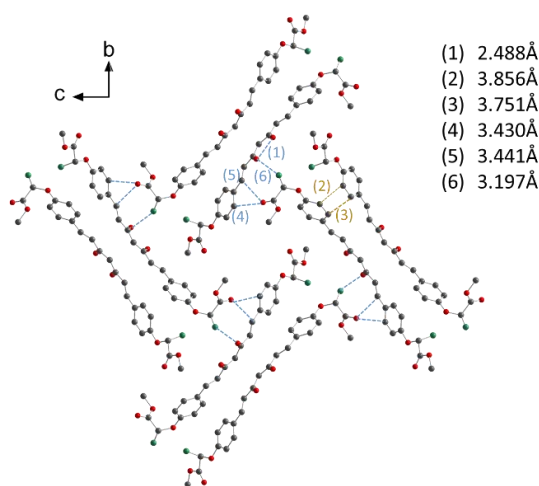
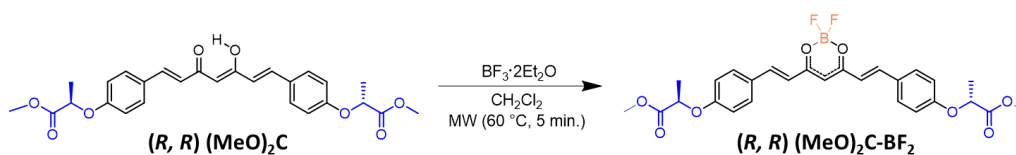


Figure 5. The molecular interactions in the structure of **(*R, R*) (MeO)₂C**.

5.3.1.2 Synthesis and crystal structure of **(*R, R*) (MeO)₂C-BF₂**



Scheme 3. Synthesis of the **(*R, R*) (MeO)₂C-BF₂**

In our study, BF₂-CCMoid could be directly prepared by the addition of borontrifluoride etherate (BF₃·Et₂O) to the free organic unit of **(*R, R*) (MeO)₂C** (Scheme 3). In some other reports,^{20,21} 1,3-diketodifluoroboronate species were produced successfully from the free ligands by the action of BF₃·Et₂O refluxing in CH₂Cl₂. In order to simplify the experiment and decrease the reaction time, we performed the reaction of **(*R, R*) (MeO)₂C** and BF₃·Et₂O (1:1.5) in CH₂Cl₂ under the irradiation in a microwave reactor, and the pure products were obtained in few minutes with a 95 % of yield.

Additionally, borondifluoride compounds could be obtained in a one-pot reactions by mixing the corresponding aldehyde, acetylacetone (or a *meso*-substituted analogue), and BF₃·Et₂O in EtOAc as solvent and in the presence of *n*-butylamine as a base.²² The aldol reactions between 2,4-pentanedione and the corresponding aromatic aldehydes have produced the “in situ generated BF₂-CCMoids” (e.g.: phenolic hydroxyl,²² *o*-propargyl phenyl,²³ triphenylamine groups¹²).

Figure 6 shows the comparison between the free ligand and the **(*R, R*) (MeO)₂C-BF₂** system. As it can be observed in the image, the proton shift from the –OH in the free ligand disappear and the proton shifts from the conjugated skeleton move to low fields. The rest of signals,

corresponding to the arms of the molecule that contain the chiral groups and ester were easily recognized and similar to those found for the porphyrin systems in previous chapters.

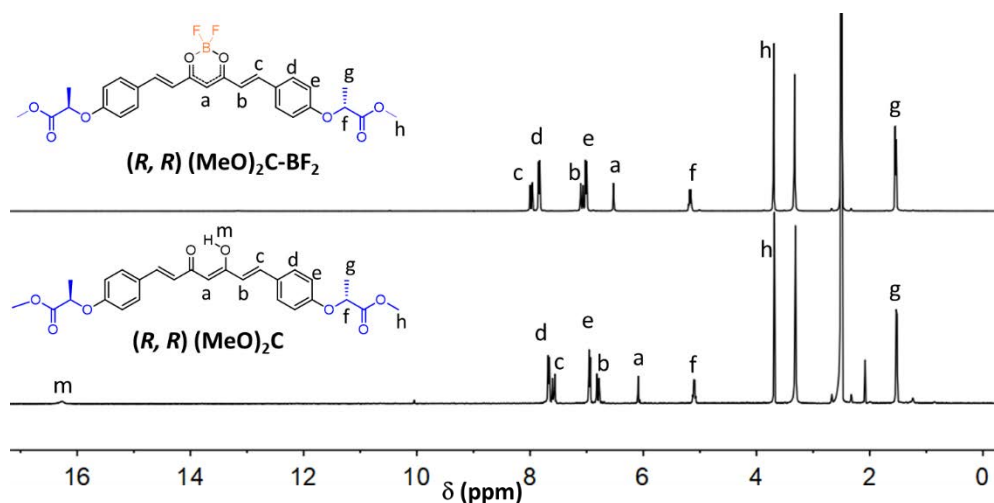


Figure 6. ¹H NMR spectrum of *(R,R)*-(MeO)₂C and *(R,R)*-(MeO)₂C-BF₂ in DMSO-d₆ at 20 °C.

Suitable crystals *(R,R)*-(MeO)₂C-BF₂ for single X-ray diffraction data (Table A5.1) collection were obtained by dissolving CCMoid (50 mg) in CH₂Cl₂ layered with n-hexane (after three days). The compound crystallized in a monoclinic crystal system with two molecules in the asymmetric unit (Figure A5.3) that display similarity of twisting at the aromatic rings than the previous system (Figure 7). This configuration is the same as the one found in a published CCMoid structure which bears two -OCH₃ on the phenyl groups,²⁴ but here the effect of the coordination of the boron with the β-diketone moiety provides a flatter structure, which is clearly evident if compared with the free ligand structure shown before. The torsion angle between the phenylate and the dioxaborine plane of the two molecules is in the range of 7.50-20.48 °, and the ending chiral moieties expand to opposite directions.

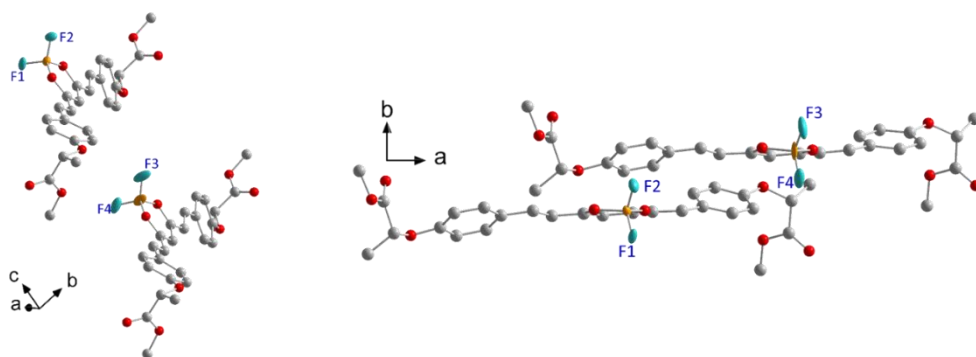


Figure 7. Molecular structure of *(R,R)*-(MeO)₂C-BF₂ in different crystallographic projections. Colour legend: O in red, B in orange, F in green and C in grey.

As observed in other types of $\text{BF}_2\text{-CCMoids}$,²⁵ the molecules are tightly packed in the solid state. They form staggered stacks parallel to the *c*-axis to minimize dipolar interactions and favour propanoate donor-dioxaborine acceptor interactions. The molecules interact by weak intermolecular $\text{C-H}\cdots\text{F}$ interactions with each other (Figure 8). For a single molecule, one of F atoms interacts with the methyl group of the chiral centre of a neighbour molecule (distances $\text{C}\cdots\text{F}$ are in the range 3.29-3.37 Å) extending such interactions along the *c*-axis. The crystal packing diagrams are shown in Figure A5.4 and A5.5.

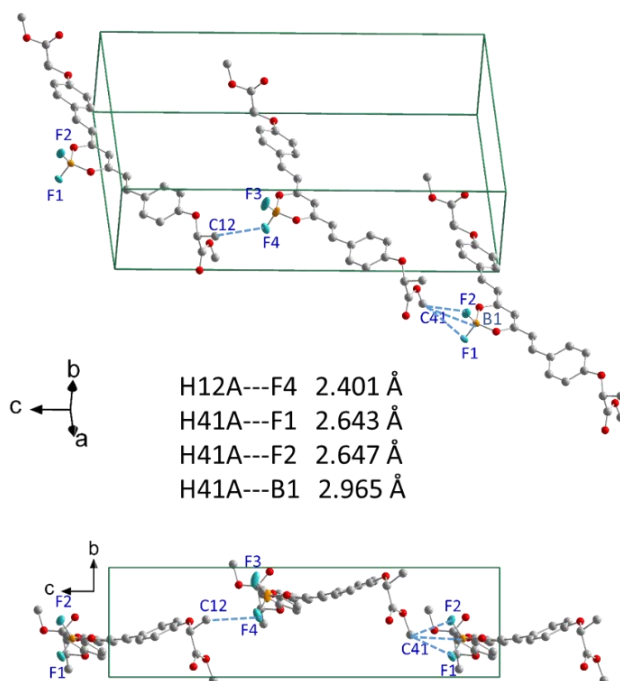
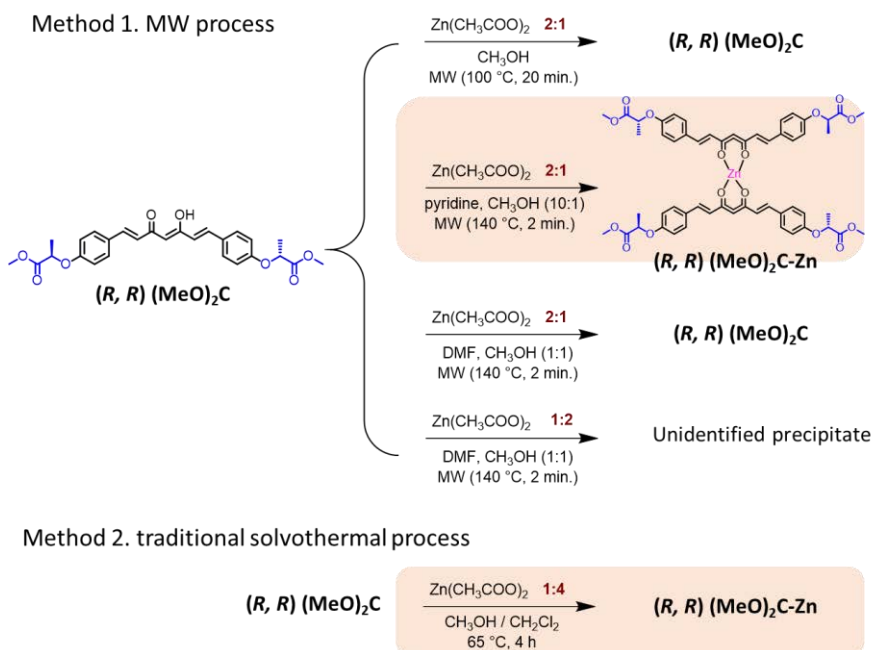


Figure 8. Molecular interaction between the two (*R, R*) $(\text{MeO})_2\text{C-BF}_2$ monomers in the cell unit.

5.3.1.3 Synthesis and crystal structure of (*R, R*) $(\text{MeO})_2\text{C-Zn}$

The coordination compound could be achieved by traditional solvothermal methods and by the use of a microwave reactor. To find the most efficient methodology to achieve pure (*R, R*) $(\text{MeO})_2\text{C-Zn}$, the two methods were tried, with zinc acetate as the metal source (Scheme 4).



Scheme 4. Representation of the methods used for the synthesis of **(R, R) (MeO)₂C-Zn**. Successful results are highlighted in orange.

The synthesis has been directed toward the coordination of the Zn(II) ions with the β -diketone moiety, as it has happened in the past with other systems described in the group, a putative scheme of the molecule would contain one metal ion attached to two CCMoid ligands.²⁶ Toward such interest, reactions having 2:1 moles of **(R, R) (MeO)₂C** and $\text{Zn}(\text{CH}_3\text{COO})_2$ respectively, in different solvents (CH_3OH , DMF and pyridine) with assisted microwave methodology were carried out. Those solvents were tried due to the successful achievement of similar compounds in the past.²⁶⁻²⁸ In the case of CH_3OH or DMF as solvents, the chelation reaction of **(R, R) (MeO)₂C** and $\text{Zn}(\text{CH}_3\text{COO})_2$ did not happen under the given conditions (100 °C, 20 min in CH_3OH or 140 °C, 2 min in DMF). Increasing the amount of $\text{Zn}(\text{CH}_3\text{COO})_2$ with respect to the initial proportion, gives rise to insoluble precipitates formed in DMF. Furthermore, in pyridine (containing small amount of CH_3OH), the MW reactions did not show any precipitate even when the solution cooled down, and the final product was extracted with a mixture of acetone/ H_2O .

On the other hand, traditional solvothermal methods using low boiling point solvents was the second method attempted for the achievement of coordination compounds. Normally deprotonation of the ligand is the first step toward the coordination of the metallic centres,²⁹ but here instead, the ratio of metallic salt was increased to promote coordination. In this way, a new ratio of 1:4 was used and the reagents dissolved in a $\text{CH}_3\text{OH}/\text{CH}_2\text{Cl}_2$ (v/v: 10/1). The reaction was heated at 65 °C during 4 hours and **(R, R) (MeO)₂C-Zn** was obtained in an 89 % of yield. This methodology provided higher yields than the assisted MW pathway, and it was also easier to purify the final system. The parameters used are similar to those used in porphyrin reactions, providing better results in this case.

Figure 9 shows the ^1H NMR spectrum of (R, R) $(\text{MeO})_2\text{C-Zn}$. The homoleptic structure was confirmed by the uniform protons shifts of the two CCMoid-type ligands. The signals relative to the arms were not affected (from the free ligand disposition) after the coordination due to the long distance from the Zn(II) centre. The rest of the protons from the conjugated skeleton shifted to high fields, especially the one corresponding to the methane group.

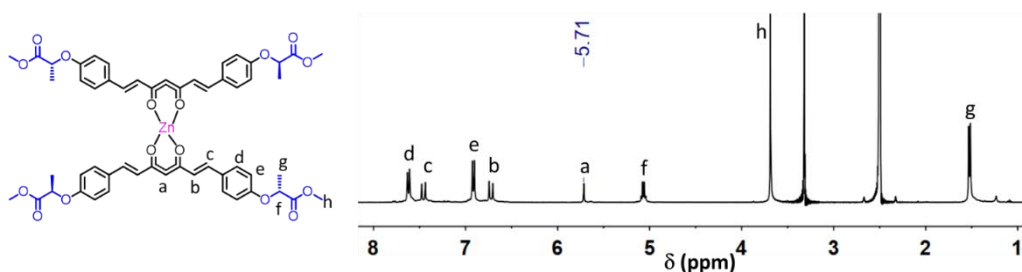


Figure 9. ^1H NMR spectrum of (R, R) $(\text{MeO})_2\text{C-Zn}$ in DMSO-d_6 at $20\text{ }^\circ\text{C}$.

CCMoid compounds containing Zn(II) metal ions are of particular interest due to the enhancement of biological activity, and several papers have reported their promising cytotoxic activity against human cancer cells as well as their potential use as diagnostic agents.^{28,30-33} However, very few CCMoid-Zn molecular structures appeared in the literature, and the first published one was in 2012 where zinc binds two 9Accm ligands (9Accm = 1,7-(di-9-anthracene)-1,6-heptadiene-3,5-dione) and one pyridine molecule, $[\text{Zn}(\text{9Accm})_2(\text{py})]$.²⁶ Another compound structure obtained through X-ray diffraction analysis has a penta-coordinated Zn(II) which is formed by one CCMoid ligand, bipy-9 and a chloride ion.³⁴ In our study, crystals were obtained by layering a THF solution of (R, R) $(\text{MeO})_2\text{C-Zn}$ with CH_3OH , and the general crystal data information of it is presented in Table A5.1.

A view of (R, R) $(\text{MeO})_2\text{C-Zn}$ is shown in Figure 10. There are two kinds of Zn centres in the asymmetric unit. One of them presents a pseudo-octahedral geometry and the other is penta-coordinated, showing a trigonal bipyramidal geometry. Both systems coordinate to two CCMoid ligands, having the extra positions for the two molecules of H_2O in the case of the former, or one molecule of CH_3OH in the case of the latter (Figures 10b and 10c). The distances of Zn to the diketone oxygen atoms vary from 1.99 to 2.05 Å, being similar to others found in the literature. The Zn ion binding to two H_2O molecules present distances of 2.33 and 2.22 Å, and they are longer than the distance of the Zn centre to the CH_3OH in the neighbouring molecule, which is 1.86 Å.

There are not major differences in the C-C distances (1.30-1.49 Å) between the single and double bonds ranges for the CCMoids in both molecules. The skeleton of all the CCMoids in the unit cell do not exhibit clearly twists, and overall the molecules present a linear shape. In addition, for each CCMoid, the two chiral groups are tilted (torsions approximately of $60\text{-}80^\circ$) breaking the linearity of the conjugated skeleton, showing the flexibility of the CCMoid and the different conformations that can present.

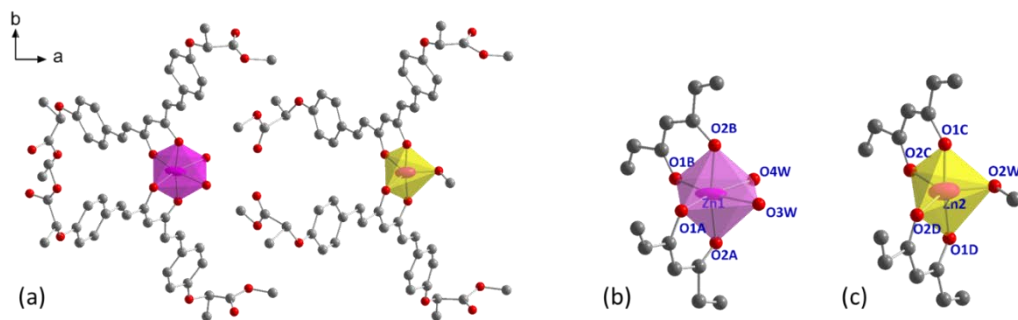
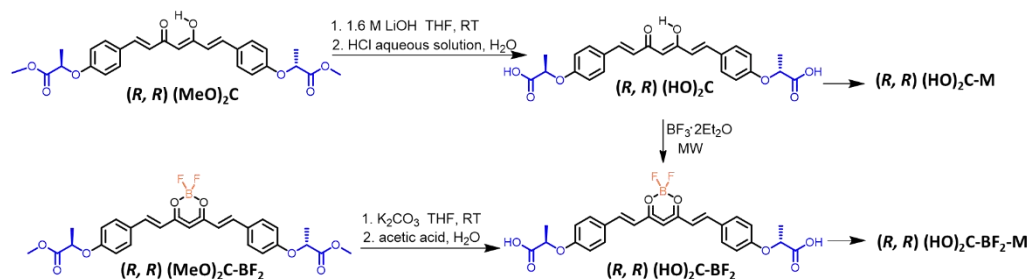


Figure 10. Crystal structure (a) and the central cores (b, c) of (R, R) $(\text{MeO})_2\text{C-Zn}$.

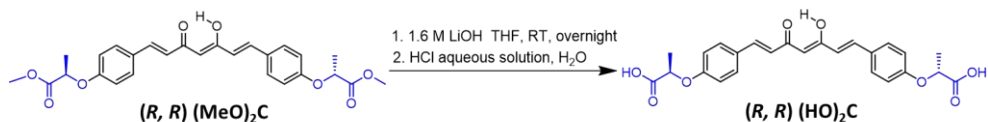
5.3.2 Synthesis of carboxylic CCMoids compounds bearing chiral centres

Chapter IV shows the evolution from porphyrin containing ester groups toward related systems containing acid groups in the terminal positions of the *meso*-substituted moieties. Here, a similar study was performed using CCMoids, where a new system called (R, R) $(\text{HO})_2\text{C}$ with chiral units and carboxylic groups in both ends of the molecule, has been synthesized. The complete synthetic route is shown in Scheme 5. In this case, a new coordination compound was achieved using such free ligand but containing a metalloid centre, $-\text{BF}_2$ (Scheme 5). In addition, we tried to construct the coordination network based on these CCMoid ligands with different metals.



Scheme 5. Synthesis of (R, R) $(\text{HO})_2\text{C}$ and metallo-CCMoids.

5.3.2.1 Synthesis of (*R,R*) (**HO**)₂**C**



Scheme 6. Synthesis of (*R,R*) (**HO**)₂**C**.

(*R,R*) (**HO**)₂**C** was obtained from the hydrolysis reaction of (*R,R*) (**MeO**)₂**C** by the same method described in chapter IV for the synthesis of **Zn(4R-CPP)**. The pure product precipitated directly from H₂O after HCl titration (yield: 97 %) (Scheme 6). This reaction deserves particular notice due to its quantitative yield (97 %). On the other hand, there is a limited literature on CCMoids containing carboxylic groups. At present, there is only one patent published by Choi *et al.*³⁵, where a CCMoid presents the direct attachment of the carboxylic groups at the *para*-positions of the benzene rings using the similar method described here (89 % yield). Furthermore, there is no previous data on systems that present chiral moieties in their structures. In our case, the ¹H NMR spectrum (Figure 11) displays clear evidences of the hydrolysis of the methyl ester groups under basic conditions, and the existence of the carboxylic acid groups (-COOH) formed after HCl titration. Indeed, the proton signal appeared at 3.68 ppm, which corresponds to the methyl groups of the ester, is now missing and a new signal corresponding to the protons from the carboxylic appears at 13.10 ppm.

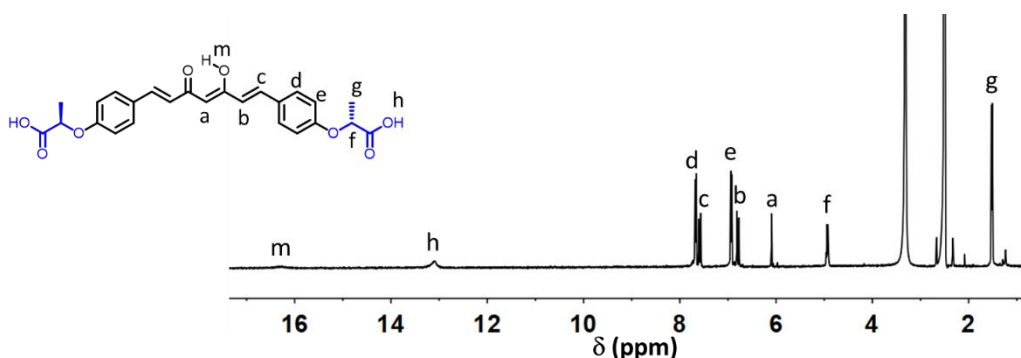


Figure 11. ¹H NMR spectrum of (*R,R*) (**HO**)₂**C** in DMSO-d₆ at 20 °C.

It is well known that the poor solubility of CCM and CCMoids in neutral aqueous media limits their biomedical applications and study, and the molecular degradation relates to the phenol groups and the creation of radicals in most cases.³⁶ In general, the CCM is extremely unstable at pH > 7, although degradation could be stopped by recovery of the neutral pH (e.g.: addition of HCl).^{37,38} In our case, a brown CCMoid aqueous solution was formed after adding LiOH, and the expected structure shown in Figure 12 was stable in the alkaline solution, which had been proved

by the successful achieving of **(R, R) (HO)₂C** in high yield. In future steps (not pursued here due to the lack of time) the isolation of the CCMoid salt will be studied due to the high solubility that presents in aqueous solutions (Figure 12).

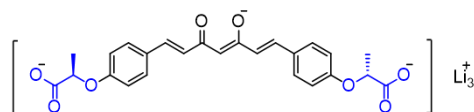


Figure 12. Schematic drawing of the CCMoid salt.

5.3.2.2 Synthesis of **(R, R) (HO)₂C-M** compounds (**M** = metallic centre)

Di-carboxylic organic systems³⁹ are of high interest due to their chelating properties regarding the binding of different metal centres as well as because they can provide metal-organic frameworks (MOFs) or coordination polymers (CPs).⁴⁰⁻⁴² In addition, supramolecular structures from such systems can be also studied due to their rich chemistry, providing 2D H-bonding networks.⁴³

Concerning this matter, **(R, R) (HO)₂C** is a dicarboxylic organic molecule as well as contains a diketone group which has been proved to be easily coordinated (previous experiments with the ester version). Inspired by the solvothermal methodology described for the synthesis of MOFs, solutions of **(R, R) (HO)₂C** in different solvents were prepared combining the use of different metal sources. Some of the reactions were performed with the assistance of additional acids or alkyl solutions, which are normally use to decrease the kinetics of the reaction, or to assist in the deprotonation. Table A5.2-5.6 in the appendix provides information of the experiments and conditions that presented crystalline material. In general, the final solutions were heated at 80 °C during 3 days, then the reaction vessels were allowed to cool down to room temperature (Figure 13).

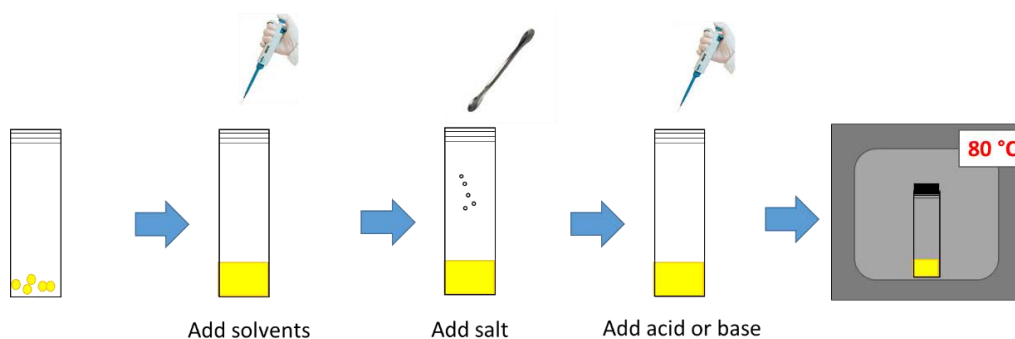


Figure 13. Schematic drawing of the **(R, R) (HO)₂C-M** compounds synthesis.

Taking into account the variety provided by this type of combinatorial synthesis, **(R, R) (HO)₂C** was reacted with a number of Zn(II), Zr(IV), Cu(II), Co(II) salts, and in some of the reactions additional organic ligands such as 4,4-bipyridyl and di(4-pyridyl) ethane were added for assisting the assembly towards the creation of highly dimensioned molecular-based systems.

Overall, different mixtures of solvents were used, due to the difference of solubility between the metal sources and the free CCMoid. In all the cases, with the exception of Zn(NO₃)₂·6H₂O, precipitates formed immediately once the metal salts were added into the solution that contained the ligand. In order to slow down the reaction, acidic conditions were performed in some cases to generate a proton exchange equilibrium between the **(R, R) (HO)₂C** and the media (both in the carboxylic and the enol positions). Decreasing the speed of the coordination could provide the system with more time to reorganize and precipitate in a well-organized manner, producing crystals. As a comparison, basic conditions were also studied for these reactions. Additional strategies including the use of preformed metallic clusters or of bipyridine derivatives were tried. Under these conditions, two reactions provided crystals suitable for single-crystal X-ray crystallographic analysis, which were obtained by evaporating the residual solution at room temperature with time (Table 1).

Table 1. Conditions for the achievement of crystals.

Nº	(R, R) (HO)₂C	metal salt	ratio	solvent
160725B	10 mg	Zn(NO ₃) ₂ · 6H ₂ O 20 mg	1:3	DMF: ethanol: KOH aqueous solution 1 ml: 0.5 ml: 0.5 ml (33 µl 1M KOH)
160725C	10 mg	Co(NO ₃) ₂ · 6H ₂ O 20 mg	1:3	DMF: ethanol: H ₂ O 1 ml: 0.5 ml: 0.5 ml

Some papers describe the possibility of DMF acting as a template in the formation of MOFs as in some cases ammonium salts do, which usually led to metal-formate framework of niccolite structures.^{44,45} In the present work, two novel systems were achieved through the decomposition of DMF when using the conditions shown in Table 1: **[Zn₂(HCOO)₆][COOH_x]** and **[Co(OH)_m(HCOO)_n]**. In both cases, the structures do not exhibit the coordination with the CCMoid.

The binodal **[Zn₂(HCOO)₆][COOH_x]** displays a perovskite-like topology (Figure 14a) with the distance of Zn···Zn is 5.985 Å. The structure contains one unique formate anion that bridges the metal ions Zn(II) in anti-anti mode (Figure 14b) to form a 3D framework, with one type of COOH_x that is disordered inside the cavities of the structure (Figure 14c). The Zn(II) ion presents octahedral geometry coordinated to six oxygen atoms from six formate anions (Figure 14b). DMF can decompose and evolve into formic acid and HN(CH₃)₂ under certain conditions,⁴⁶ providing the formate anions that we observed in the structure. In this case, there is an absence of ammonium units in the structure, showing exclusively -COOH moieties in the framework. Even though the possibility of degradation of CCM in alkaline conditions has been discussed, DMF provides the formic acid units here.

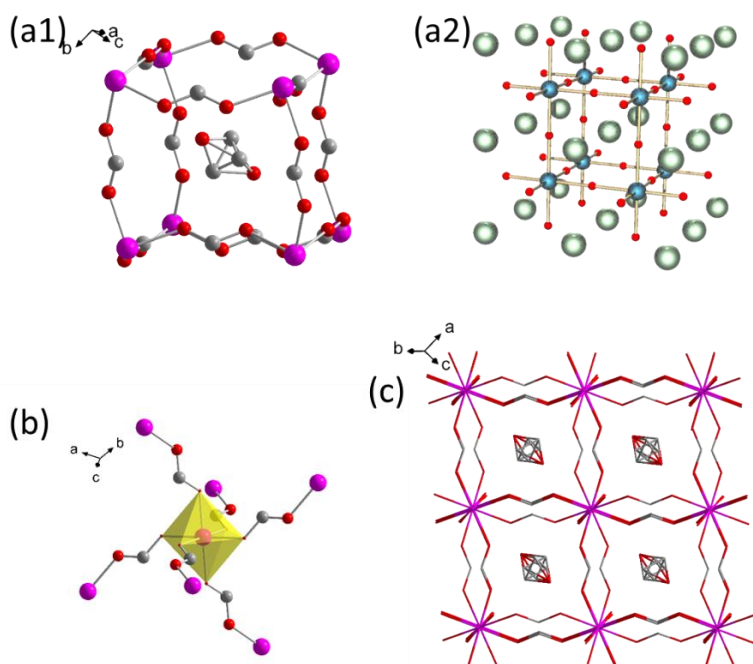


Figure 14. (a1) Perovskite structural topology of the compound $[\text{Zn}_2(\text{HCOO})_6][\text{COOH}_x]$. (a2) Perovskite structural picture from Wikimedia Commons. (b) Coordination and linkage modes of the ligands and metal ions in the compounds with the metal ions in polyhedron views. (c) 3D space-filling view of the framework with the cations filled in the cavities. Zn in pink, O in red, and C in grey.

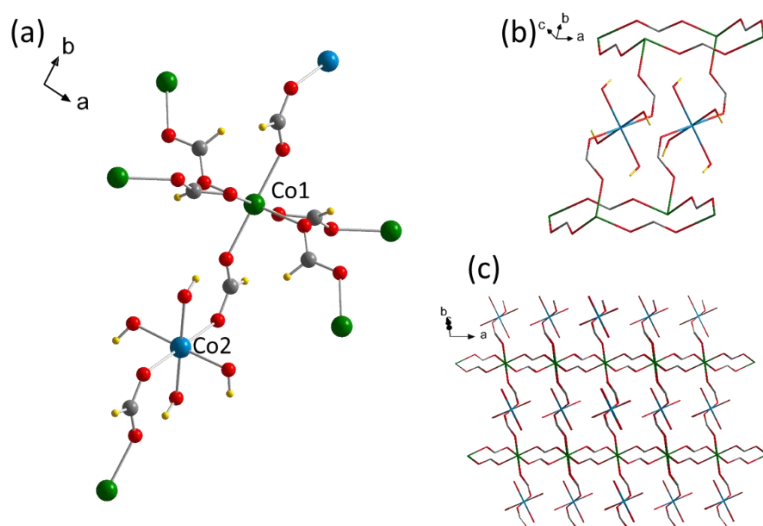


Figure 15. (a) Coordination and linkage modes of the ligands and metal ions in $[\text{Co}(\text{OH})_m(\text{HCOO})_n]$. (b) Representation of the existing the cage in the structure. (c) 3D space-filling view of the framework. Different Co in green and blue, O in red, and C in grey.

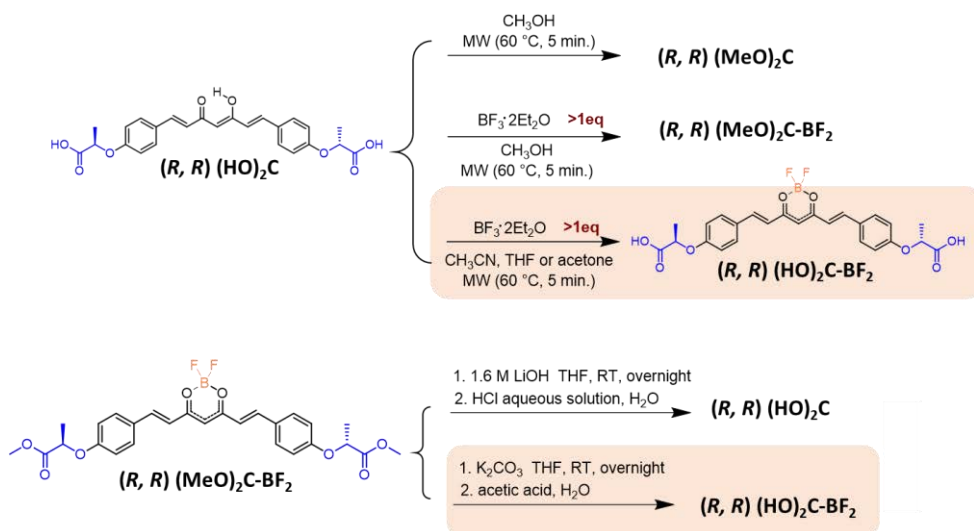
In the structure of $[\text{Co}(\text{OH})_m(\text{HCOO})_n]$ shown in Figure 15, there are two kinds of Co(II) ions. Both of them present octahedral geometry, the first type is connected to other six Co(II) through six oxygen atoms from the formate anions, like the previous Zn(II), And the second coordinates with two formate anions and four hydroxides (Figure 15a), acting as the linker between the parallel layers constructed only by Co(II) and formate anions (Figure 15b and 15c). As before, the existence of formic acid comes from the degradation of DMF as described in previous literature.^{47,48}

Taking into account the achievement of the final systems containing the desired CCMoid were not isolated in a crystalline form, we moved towards the coordination of the ligand with metalloids centres (boron ions) with the aim of getting new CCMoids containing BF_2^- groups (the purpose of such synthesis is described below) and exploring the possibility of capping the β -diketone, leaving only the carboxylic groups for further coordination.

5.3.2.3 Synthesis of $(R, R) (\text{HO})_2\text{C}-\text{BF}_2$

Considering an intermediate step towards the achievement of highly dimensioned systems, we attempted the protection of the β -diketone part of the CCMoid with the aim of using the two carboxylic groups towards the coordination with additional metals.

Here a BF_2^- group was coordinated with $(R, R) (\text{HO})_2\text{C}$ under microwave or by the hydrolyzation of $(R, R) (\text{MeO})_2\text{C}-\text{BF}_2$ (Scheme 7).



Scheme 7. Representation of the methods used for the synthesis of $(R, R) (\text{HO})_2\text{C}-\text{BF}_2$. Successful results are highlighted in orange.

Reactions in CH_3OH of $(R, R) (\text{HO})_2\text{C}$ varying the equivalents of $\text{BF}_3 \cdot \text{Et}_2\text{O}$ (from 1 to 3) were performed in an attempt to discern the different species which could be formed and to

investigate the possible competition between the β -diketone moiety and the carboxylic groups at the ends. The reactions were performed in a similar manner, firstly **(R, R) (HO)₂C** was dissolved in CH₃OH and BF₃·Et₂O was added in the second step; then the reaction mixture was irradiated in a microwave reactor at 60 °C for 5 minutes (specifics shown at the end of the chapter, in the synthetic section).

¹H NMR studies showed that under such conditions CH₃OH was not a suitable solvent. The **(R, R) (HO)₂C** system reacts with the CH₃OH molecules and methylation reactions are observed, where the ligand becomes **(R, R) (MeO)₂C** and the final compound is identical with the previous described ester ligand, **(R, R) (MeO)₂C-BF₂**. Previous reports explained the lack of stability of BF₂-CCM systems in polar solvents,^{23,49} where the coordination of BF₂- to CCM could be broken. Unlike these systems, **(R, R) (MeO)₂C-BF₂** remains stable in CH₃OH. Other solvents, such as CH₃CN, THF and acetone (2 mL), provided the desired system **(R, R) (HO)₂C-BF₂** in high yields (97 %) under the same conditions. Even an excess use of BF₃·Et₂O in the reaction with **(R, R) (HO)₂C** did not provide further coordination of the BF₂- moieties with the carboxylic groups, which has been demonstrated by following the reaction result with ¹H NMR. As it can be observed in the NMR spectrum of the target molecule (Figure 16), the proton shift from the -OH in the free ligand disappears and the proton shifts from the conjugated skeleton move to lower fields, and the rest of signals corresponding to the arms of the molecule related to the chiral groups and carboxylic acids.

Attempts to achieve the aimed compound by the direct hydrolysis of **(R, R) (MeO)₂C-BF₂** were carried out using LiOH and later a HCl aqueous solution. However, under such conditions the coordination compound is not stable, isolating only the free ligand. Then we modified the method following a previous strategy where potassium carbonate was used as a base with an analogous BF₂-CCM system,⁵⁰ and later titrated with acetic acid. This one provided the final **(R, R) (HO)₂C-BF₂**, but comparing with the assisted MW reaction, it presents lower yields (53 %) and the hydrolysis was incomplete implying additional steps in the final work out.

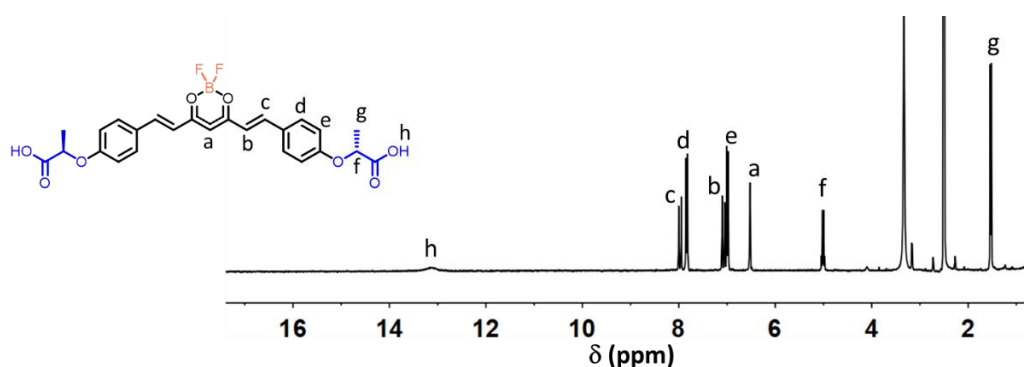


Figure 16. ¹H NMR spectrum of **(R, R) (HO)₂C-BF₂** in DMSO-d₆ at 20 °C.

5.3.2.4 Advanced synthesis using (*R, R*) (HO)₂C-BF₂

(*R, R*) (HO)₂C-BF₂ was used as starting material together with a number of Zn(II) sources in additional solvothermal reactions. Table A5.7 shows all the reactions carried out toward the achievement of crystalline products. In the case of using ZnCl₂, a precipitate was formed immediately once the metal salt was introduced. In other cases, they were still clear solutions after the Zn(II) salt was added, and after the reactions, the compounds were apt to adhere to the wall of the vial, not like the precipitate suspended in the solution in the previous (*R, R*) (HO)₂C-M reactions. Unfortunately, it was unsuccessful to isolate crystalline material from those reactions and additional paths should be designed in the future.

5.3.2.5 Crystallization of (*R, R*) (HO)₂C and (*R, R*) (HO)₂C-BF₂

(*R, R*) (HO)₂C and (*R, R*) (HO)₂C-BF₂ display great solubility in a number of solvents, and we attempted to crystallize them by using different methods, including slow evaporation of solvents and slow liquid-vapour diffusion (Table A5.8-5.9). It was difficult to achieve suitable crystals for the single X-ray analyses which was agree with the difficulties encountered for the achievement of MOFs or high organized structures with these carboxylic CCMoids. Nevertheless, both systems displayed a degree of crystallinity in CH₃OH/hexane mixtures for (*R, R*) (HO)₂C, and CH₃OH/toluene for (*R, R*) (HO)₂C-BF₂. The powder X-ray diffraction diffractograms found for such samples (Figure 17) present obvious differences from those found for the ester analogue systems, related probably to the existence of a large number of H-bonding in the structures of the former.

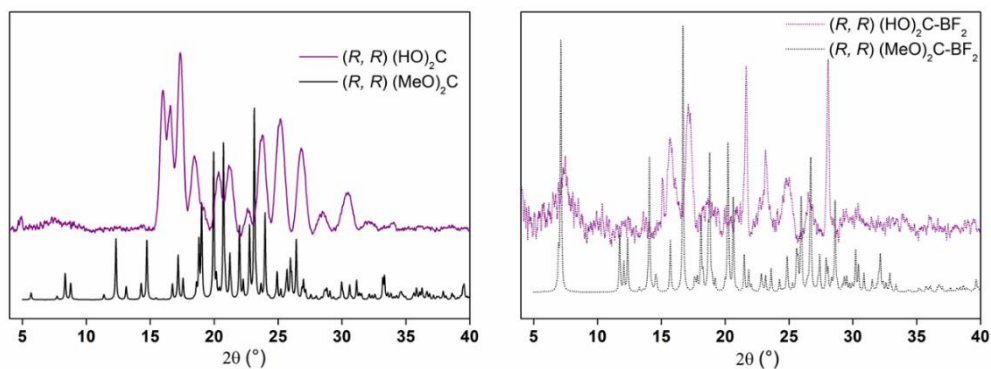
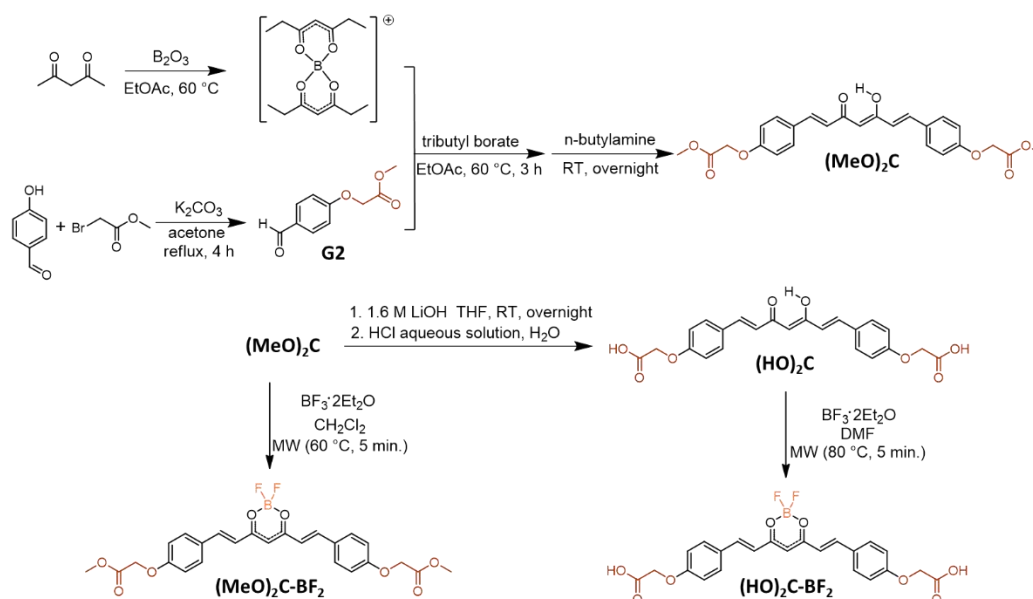


Figure 17. (Left) Comparison of (*R, R*) (HO)₂C (crystallized from CH₃OH/hexane) with (*R, R*) (MeO)₂C. (Right) Comparison of (*R, R*) (HO)₂C-BF₂ (crystallized from CH₃OH/toluene) with (*R, R*) (MeO)₂C-BF₂.

5.3.3 Synthesis and structures of CCMoid ligands bearing achiral groups

5.3.3.1 Synthesis and crystallization of CCMoids bearing achiral groups.

CCMoids based on $(\text{MeO})_2\text{C}$ with the achiral arms have been synthesized following the synthetic route showed in Scheme 8. Most of the reactions were following the same methods for the chiral systems.



Scheme 8. Synthesis of the $(\text{MeO})_2\text{C}$ molecule and derivatives.

$(\text{MeO})_2\text{C}$ was achieved by the reaction of boron oxide and methyl 2-(4-formylphenoxy)acetate (**G2** used in Chapter II) in EtOAc . The product was purified by dissolving the crude in hot CH_2Cl_2 and then precipitating the system with CH_3OH . The BF_2 -compound, $(\text{MeO})_2\text{C-BF}_2$, was synthesized in the same way as (R, R) $(\text{MeO})_2\text{C-BF}_2$ in CH_2Cl_2 , but with a lower concentration of free ligand. For the carboxylic $(\text{HO})_2\text{C}$, the purification was performed from hot THF and precipitated latterly with cold CH_2Cl_2 . $(\text{HO})_2\text{C-BF}_2$ was performed in DMF due to the poor solubility of $(\text{HO})_2\text{C}$ with an excess of $\text{BF}_3 \cdot \text{Et}_2\text{O}$ heating at $80\text{ }^\circ\text{C}$.

Compared to the CCMoids with chiral arms, which have extra methyl groups, the achiral family has less solubility. Table A5.10-12 displays the solubility test and results made with $(\text{MeO})_2\text{C}$, $(\text{MeO})_2\text{C-BF}_2$ and $(\text{HO})_2\text{C}$, respectively, using a number of common organic solvents.

Growing crystals for X-ray crystallography was difficult for the CCMoids because of the poor solubility and synchrotron source was mandatory. Several techniques such as slow evaporation of a single or multi solvent system and liquid-vapour slow diffusion were used to grow the final single crystals for analysis (Table A5.10-12). Table A5.13 shows the crystal information of the achiral CCMoid $(\text{MeO})_2\text{C}$, the boron compound $(\text{MeO})_2\text{C-BF}_2$, and $(\text{HO})_2\text{C}$.

5.3.3.2 Crystal structure of (MeO)₂C

(MeO)₂C crystallizes in the monoclinic space group P2₁/c. Suitable crystals were achieved by slow liquid-vapour diffusion (CH₂Cl₂/ether) (Table A5.10). Again, the molecule presents the keto-enol form with arched conjugated backbone, as it happens with the chiral analogue. (Figure 18).

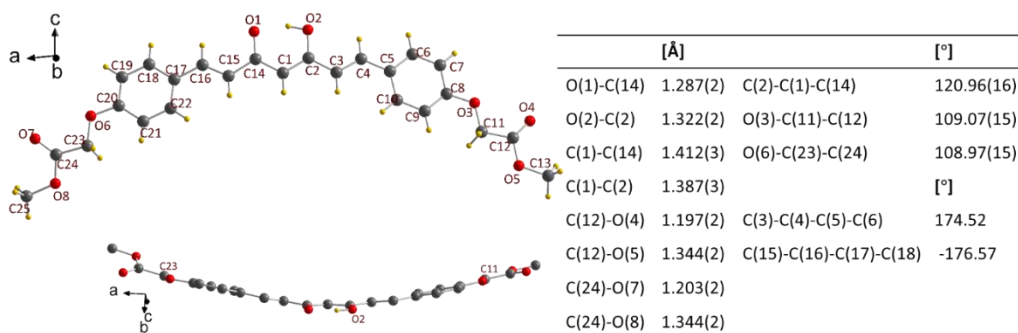


Figure 18. Molecular structure of (MeO)₂C and selected bond lengths [Å] and angles [°]. Colour legend: O in red, H in yellow and C in grey.

In the packing of (MeO)₂C, the molecules seem to be grouped in pairs (Figure 19). Inside the pair, the C12 from one molecule interacts with O5 from the other, forming similar pairs as in (*R*, *R*) (MeO)₂C.

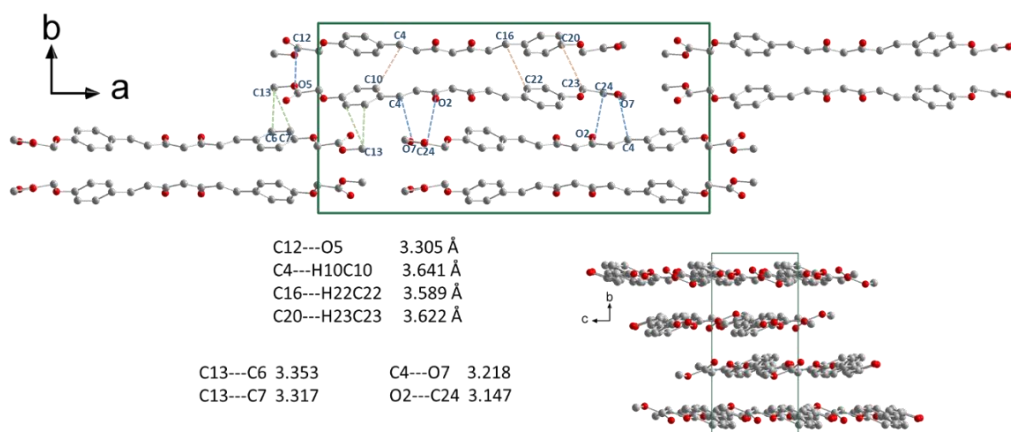


Figure 19. Crystal packing diagram of (MeO)₂C down the c-axis (top) and a-axis (bottom) direction.

5.3.3.3 Crystal structure of (MeO)₂C-BF₂

Table A5.11 shows the powder X-ray diffraction patterns of crystals growth in THF, acetone and CH₃CN. Suitable crystals for single X-ray diffraction analysis were obtained by dissolving (MeO)₂C-BF₂ in THF by slow evaporation.

The BF₂- group has two possible positions in the monomer. It is noticeable that the conjugated chain, in the two sides of the ligand, has a different conformation regarding the centre, either zig-zag (O1-C14-C15-C16) or boat shape (O2-C1-C2-C3), similar to other reported Co(II) CCMoid compounds,²⁷ which emphasizes the flexibility of the organic molecules. The two phenyl groups rotated in a way that the extended arms appear in the same dimension, where overall the molecule displays a “W” shape (Figure 20).

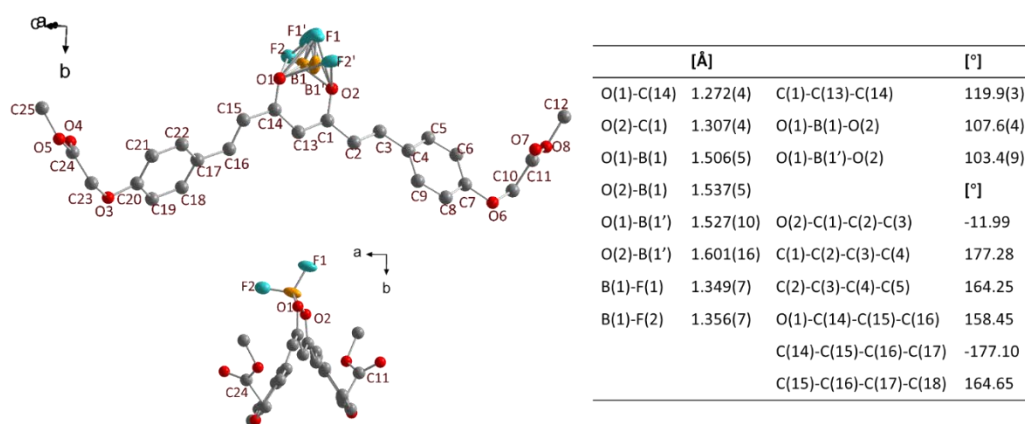


Figure 20. Molecular structure of (MeO)₂C-BF₂ and selected bond lengths [Å] and angles [°]. Colour legend: O in red, B in orange, F in green and C in grey.

Supramolecular 1D chains can be observed through weak H-bonding from one of the F atoms in the centre of the molecule and a proton from the ending methyl group of an adjacent molecule (Figure 21 F1---C12 and F2---C25), forming a straight line composed by the CCMoids head to head along the c axis. In addition, extra interactions between the achiral centres C10 and C23 with the oxygen atoms of two separately molecules expand the system in additional dimensions (Figure 21, left).

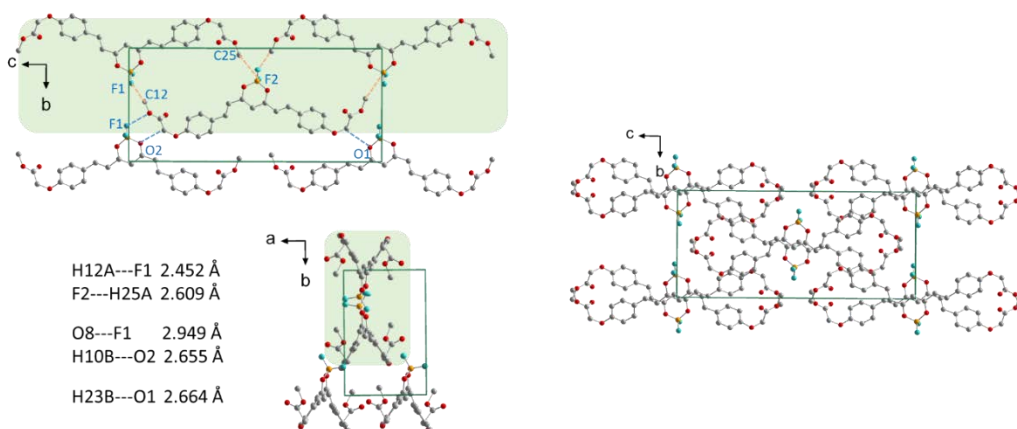


Figure 21. (Left) Molecule interaction in and between 1D chain. (Right) Crystal packing diagram of $(\text{MeO})_2\text{C-BF}_2$ down the a-axis direction.

5.3.3.4 Crystal structure of $(\text{HO})_2\text{C}$

$(\text{HO})_2\text{C}$ is sparingly soluble in most organic solvents compared with analogous systems. For crystallization, 2mg of $(\text{HO})_2\text{C}$ was dissolved in 5 ml of suitable solvents (acetone, THF, EtOH and CH_3OH , respectively) and then using slow evaporation method. In addition, the mixtures of solvents systems were tried by mixing toluene with the solvents mentioned above, using liquid-liquid diffusion, but open to air (as in Chapter II). The final single crystal for X-ray analysis was achieved from a CH_3OH /toluene mixture (Table A5.12).

The monomer of $(\text{HO})_2\text{C}$ is the unique structure so far of a CCMoid bearing two carboxylic endings at the arm position. The molecule is almost flat without torsion of the substituents, and all the carbon and oxygen atoms are nearly in one plain (Figure 22). This situation is peculiar, in non-conjugated heteroatom-containing compounds (the endings of the molecule), and it must be due to the packing with the rest of neighbours in the crystal.

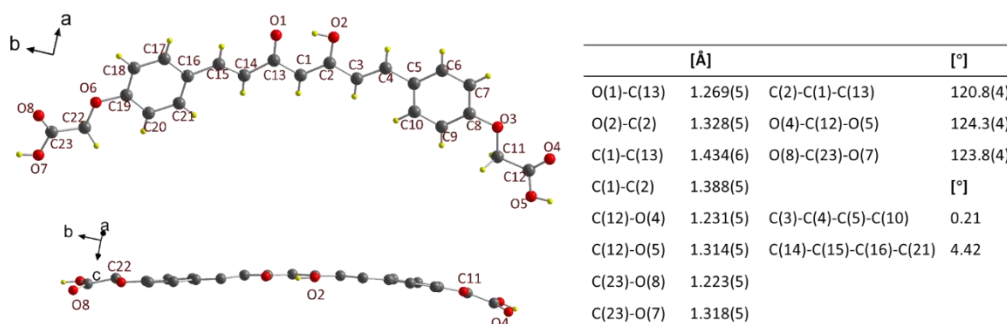


Figure 22. Molecular structure of $(\text{HO})_2\text{C}$ and selected bond lengths [Å] and angles [°]. Colour legend: O in red, H in yellow and C in grey.

Indeed, due to the H-bonding induced by the carboxylic groups, the molecules connected arms by arms through O8---O5 and O7---O4 along b-axis and O7---O8 along c axis, demonstrating a supramolecular 2D structure that expands displaying a wave shape (Figure 23). The supramolecular entity stacks layer by layer through the Vander Waals interaction between the surfaces along a-axis (Figure 24).

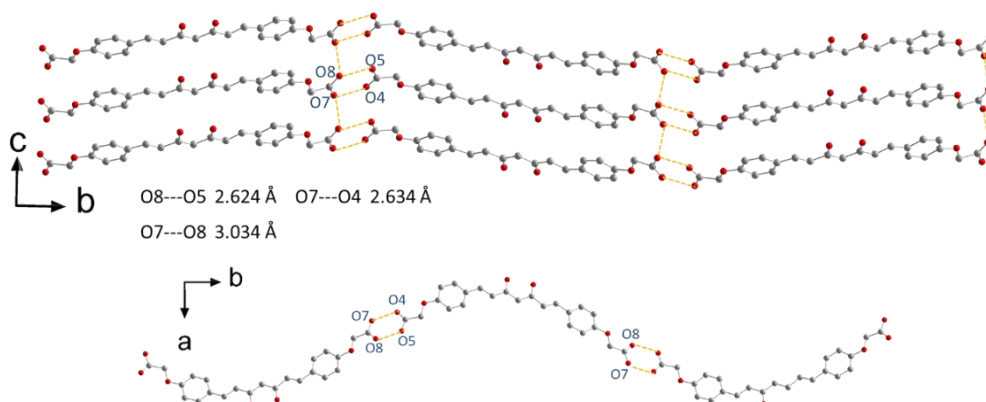


Figure 23. 2D surface formed by H-bonding in $(\text{HO})_2\text{C}$. Parts of H-bonding are marked by yellow dash line. Colour legend: O in red and C in grey.

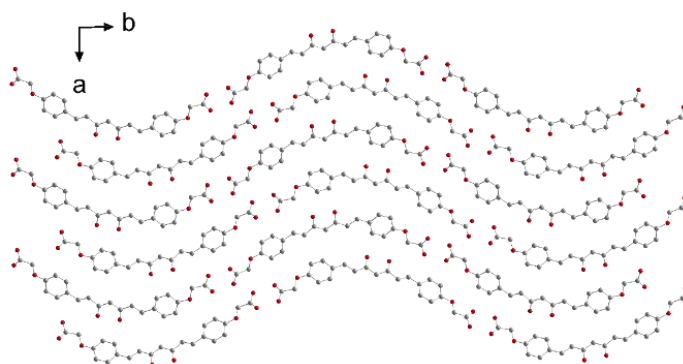


Figure 24. Crystal packing diagram of $(\text{HO})_2\text{C}$ in the c-axis direction.

5.3.4 Summary of the CCMoid structures of this chapter

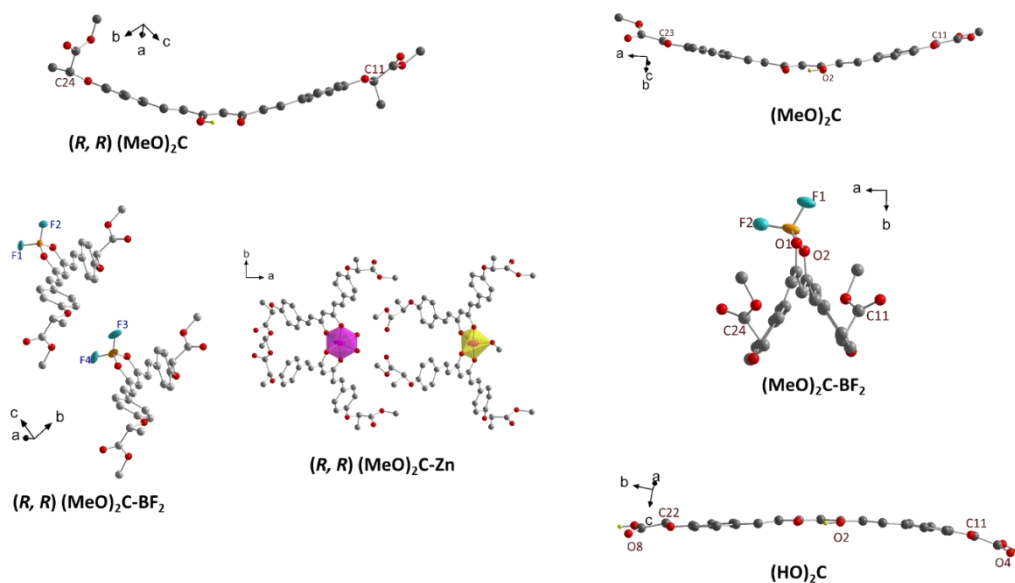


Figure 25. Summary of CCMoid structures.

(*R, R*) (MeO)₂C, (MeO)₂C and (HO)₂C present in their conjugated chain the combination of single-double C-C bonds connected in both sides with two phenyl groups. They differ on the final conformations, due to the chemical variety and the packing of the molecules. Overall, achiral centres display planar conformations.

In the case of the BF₂- compounds, (*R, R*) (MeO)₂C-BF₂ and (MeO)₂C-BF₂, the conjugated skeletons became also linear, appearing twisted the aromatic groups.

The only metallo-CCMoid resolved in this work is (*R, R*) (MeO)₂C-Zn, containing the same brands as the porphyrins in Chapter II. (*R, R*) (MeO)₂C-Zn did not crystallize under the given conditions for porphyrins (e.g.: Zn(4*R*-PPP), CH₂Cl₂/CH₃OH and CH₂Cl₂ / n-hexane) and it was difficult to obtain suitable crystals for X-ray diffraction. This is probably because the Zn(II) coordinates with two CCMoid ligands but has more probabilities of accommodate additional solvents, where in porphyrins the core has less flexibility.

5.4 Photophysical properties studies

BF₂-CCM species exhibits interesting photophysical and photochemical properties.⁵⁰⁻⁵² The absorption band of curcumin is approximately 408-430 nm in most organic solvents while the fluorescence spectrum is solvent-sensitive with emission wavelengths ranging from 460 to 560 nm. It is well known that the fluorescent BF₂- dyes could offer the advantages of optical properties^{53,54} including high emission quantum yields, large molar extinction coefficients and high sensitivity upon changes in solvent polarity. The addition of BF₂- moieties to diketone groups of CCMoids has been studied since the pioneering research of Montellano et al¹⁵ in 1993. Here, the optical properties of the CCMoids and its difluoroboron derivatives were compared by following the way of A. Chaicham et al⁵⁰ and the effect of chiral and achiral substituents in solution was investigated.

Based on the solubility tests from previous section, THF was selected to dissolve all of our CCMoids using a fixed concentration of 10⁻⁵ M where all displayed pale-yellow colours (Figure 26a). Under such conditions, the CCMoids exhibit strong absorptions and emission bands as shown in Figure 27, especially the two boron compounds display bright fluorescent emissions under the UV light (Figure 26b). It is found that the coordination with BF₂- shifts the maximum of the absorption band towards higher wavelengths, which did not happen in solution with the Zn compound (Figure 27a). The influence of chiral or achiral groups in the coordination compounds is negligible for optical properties in THF, which also relates to the absence of CD signal shown in Figure A5.6. Emission bands vary but overall BF₂-CCMoids display the most shifted and the highest wavelength values, which is observed on other systems containing such moiety.⁵⁰

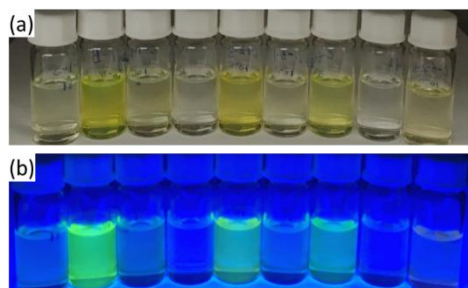


Figure 26. Pictures of CCMoids in THF under illumination: (a) white light and (b) UV light ($\lambda=365$ nm).

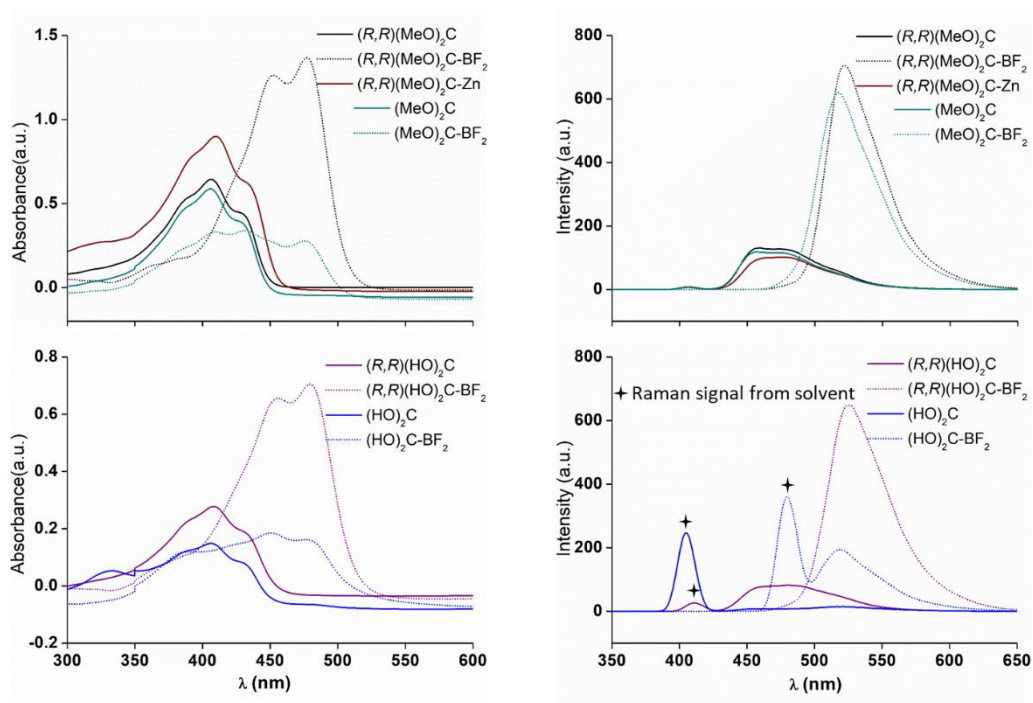


Figure 27. The UV-vis spectra (left) and fluorescence spectra (right) of CCMoids in THF (10^{-5} M).

5.5 Conclusions

Two new CCMoid ligands, with chiral and achiral moieties in the arms were synthesized. Such groups are identical to those described in chapter II for porphyrin moieties attached in the *meso*-substituents. The hydrolysis of the final ester groups gave rise to carboxylic groups, and the synthesis of metal organic frameworks and/or coordination compounds based on this type of CCMoids has been performed. To investigate the reactivity and diversity of the free organic ligands, coordination compounds containing BF_2^- moieties and Zn(II) ions compounds were synthesized by microwave and solvothermal methods.

The stability of these new CCMoids, as well as the conversional conditions among them have been studied. In the assisted microwave reactions, solvent is a notable parameter, and the carboxylic groups could undergo to esterification reactions when CH_3OH is used. The BF_2^- compounds could be synthesized directly by the free ligand with $\text{BF}_2 \cdot 2\text{Et}_2\text{O}$ in suitable solvents, and the yield increased by improving the solubility of the ligand in the solvents. The BF_2^- compounds are not stable in strong alkaline and acidic conditions.

Experimental Section:

Synthesis Methods.

1. (*R, R*) (MeO)₂C

1 g of Acetylacetone (10 mmol) and 0.5 g of B₂O₃ (7 mmol) were dissolved in 10 mL of EtOAc. The reaction mixture was heated until 60 °C for 30 min until a white paste formed. Then, a solution of 4.16 g of (*R*)-**G1** (20 mmol) and 9.2 g of tributyl borate (40 mmol) in 20 mL of EtOAc was added. The mixture was stirred 60 °C for further 3 h. After cooling down, n-butylamine (0.5 mL, 5 mmol) in EtOAc (10 mL) was added dropwise. The bright yellow solution became orange in 2 hours after n-butylamine was added, and the final reaction changed the colour to be brown after stirred at room temperature overnight.

Rotary evaporator was used to extract EtOAc completely, and then the brown slurry materials could be delaminated from the residual transparent liquid. After carefully removed the liquid, cold CH₃OH (10 mL) was poured into the brown paste, and precipitate separated out slowly under the action of the ultrasonication. The coloured solid was centrifuged and washed with CH₃OH many times to remove impurities until it became yellow. Yield: 1.49 g, 31 %. ¹H-NMR (400 MHz, DMSO-d₆) δ 16.27 (s, 1H), 7.67 (d, 4H), 7.58 (d, 2H), 6.95 (d, 4H), 6.80 (d, 2H), 6.09 (s, 1H), 5.12-5.07 (m, 2H), 3.68 (s, 6H), 1.53(d, 6H). ESI/MS m/z (%): 481.19 ([M+H]⁺), 983.35([2M+Na]⁺).

2. (*R, R*) (MeO)₂C-BF₂

In a 10 mL microwave vial, (*R, R*) (MeO)₂C (0.125 mmol, 60 mg) was dissolved in 2 mL of CH₂Cl₂. Then, BF₃·Et₂O (0.179 mmol, 22 μL) were added and the reaction mixture was irradiated in a microwave reactor to reach 60 °C and maintain for 5 min. After the cooling with a flow of compressed air, the solvent was removed and the remaining compound was washed with cold Et₂O and vacuum dried to afford 63 mg of (*R, R*) (MeO)₂C-BF₂ as an orange powder. Yield: 95 %. ¹H-NMR (400 MHz, DMSO-d₆) δ 7.98 (d, 2H), 7.84 (d, 4H), 7.09 (d, 2H), 7.01 (d, 4H), 6.53 (s, 1H), 5.18-5.15 (m, 2H), 3.70 (s, 6H), 1.54(d, 6H). ESI/MS m/z (%): 509.18 ([M-F]⁺), 529.18([M+H]⁺), 1074.39([2M+NH₄]⁺).

3. (*R, R*) (MeO)₂C-Zn

Microwave process:

In a 10 mL microwave vial, (*R, R*) (MeO)₂C (0.104 mmol, 50 mg) and Zn(CH₃COO)₂ (52 μmol, 9.5 mg) was dissolved in a mixture solvent of pyridine (2.5 mL) and CH₃OH (v/v 10:1). Then the reaction mixture was irradiated in a microwave reactor, then heated to 140 °C and hold for 2 min. After cooling with a flow of compressed air, the solvent was removed and the remaining compound was dissolved in acetone again. Then H₂O was added into the solution and the precipitated was filtered and washed with cold Et₂O. The process of extraction was repeated several times. The final (*R, R*) (MeO)₂C-Zn was found as a shining yellow powder. Yield: 18 mg, 34%.

Traditional solvothermal method:

(R, R) (MeO)₂C (0.666 mmol, 320 mg) was dissolved in a CH₃OH/CH₂Cl₂ mixture (10 ml: 1ml). The resulting yellow solution was kept stirring, and then a solution of Zn(CH₃COO)₂·2H₂O (2.664 mmol, 585 mg) in CH₃OH (10 ml) was added dropwise. The final solution was warmed up to 65 °C and left for four hours. A yellow precipitate was formed by concentrating the sample using rotary evaporation. The solid was washed with water and ether, and then dried under vacuum. Yield: 305 mg, 89 %. ¹H-NMR (400 MHz, DMSO-d₆) δ 7.62 (d, 4H), 7.46 (d, 2H), 6.92 (d, 4H), 6.72 (d, 2H), 7.51(s, 1H), 5.09-5.04 (m, 2H), 3.69 (s, 6H), 1.52(d, 6H).

4. **(R, R) (HO)₂C**

480 mg of **(R, R) (MeO)₂C** (1 mmol) was dissolved in 50 mL of THF (20 mM). Afterward, 16.8 mL of LiOH aqueous solution (1.6 M) was added, and the mixture was stirred at room temperature overnight. Then, the THF was removed leaving a yellowish aqueous solution. A yellow precipitate was formed from the titration of the solution with dilute HCl (1.2 M) drop by drop. The solid was filtered and washed with H₂O for three times, followed by CH₂Cl₂ wash to remove impurities. Yield: 439 mg, 97 %. ¹H-NMR (400 MHz, DMSO-d₆) δ 16.27 (s, 1H), 13.10 (s, 2H), 7.67 (d, 4H), 7.58 (d, J = 8.4 Hz, 4H), 6.93 (d, 2H), 6.79 (d, 2H), 6.09 (s, 1H), 4.96-4.91 (m, 2H), 1.52 (d, 6H). ESI/MS m/z (%): 451.15 ([M-H]⁻), 453.15([M+H]⁺).

5. **(R, R) (HO)₂C-BF₂**

Microwave process:

In a 10 mL microwave vial, **(R, R) (HO)₂C** (0.111 mmol, 50 mg) was dissolved in 2 mL of solvent (CH₃CN, THF or acetone). To the solution, excess BF₃·Et₂O (0.444 mmol, 56 μL, 4eq) was added and the reaction mixture was irradiated in a microwave reactor and heated to 60 °C, and then hold for 5 min. After cooling down with a flow of compressed air and removal of the solvent, the brown compound was washed with cold Et₂O and vacuum dried. Yield: 108 mg, 97%. ¹H-NMR (400 MHz, DMSO-d₆): δ 13.14 (s, 2H), 7.97 (d, 2H), 7.83 (d, 4H), 7.07 (d, 2H), 6.69 (d, 4H), 6.52 (s, 1H), 5.04-4.97 (m, 2H), 3.70 (s, 6H), 1.53 (d, 6H).

Hydrolyzation reaction:

50 mg of **(R, R) (MeO)₂C-BF₂** (95 μmol) was dissolved in 10 mL of THF (9.5 mM). Ten, 10 mL of an aqueous solution of K₂CO₃ (26 mg, 190 μmol) were added and the colour of solution became green. A brown solution was formed after stirring the reaction at room temperature overnight. Then, THF was removed and the rest of the aqueous solution was titrated with acetic acid drop by drop, giving rise to a brown precipitate. The solid was filtered and washed with H₂O for three times, and then CH₂Cl₂ was used furtherly to remove impurities. Yield: 53mg, 53%.

6. **(MeO)₂C**

0.5 g of Acetylacetone (5 mmol) and 0.25 g of B₂O₃ (3.55 mmol) were dissolved in 5 mL of EtOAc. The reaction mixture was heated to 60 °C and hold for 30 min until a white paste formed. Then, a solution of 1.94 g of **G2** (10 mmol) and 4.6 g of tributyl borate (20 mmol) in 10 mL of EtOAc were added. The mixture was stirred at 60 °C for further 3 h. After cooling down, *n*-butylamine (0.25 mL, 2.5 mmol) in EtOAc (5 mL) was added dropwise, and the final reaction was kept stirring at room temperature overnight. An orange precipitate came out in the next day. It was filtered and then dissolved in CH₂Cl₂ followed by heating up to 40 °C. After the compounds completely dissolved, CH₃OH was added slowly. Then the solution was left in an ice bath until yellow solid appeared. The solid was filtered and dried under vacuum condition. Yield: 1.4 g, 62 %. ¹H-NMR (400 MHz, DMSO-d₆): δ 16.28(s, 1H), 7.68 (d, 4H), 7.60 (d, 2H), 7.01 (d, 4H), 6.81 (d, 2H), 6.10 (s, 1H), 4.88 (s, 4H), 3.71 (s, 6H). ESI/MS m/z (%): 453.15([M+H]⁺), 927.28([2M+Na]⁺).

7. (MeO)₂C-BF₂

In a 10 mL microwave vial, **(MeO)₂C** (0.133 mmol, 60 mg) was dissolved in 4 mL of CH₂Cl₂. Then, BF₃·Et₂O (0.265 mmol, 32 μL) was added and the reaction mixture was irradiated in a microwave reactor and then heated to 60 °C and hold for 5 min. After the cooling of the reaction with a flow of compressed air and the removal of the solvent, the remaining compound was washed with cold Et₂O and vacuum dried to afford 64 mg of (MeO)₂C-BF₂ as an orange powder. Yield: 62 mg, 96 %. ¹H-NMR (400 MHz, DMSO-d₆): δ 7.80 (d, 2H), 7.85 (d, 4H), 7.10 (d, 2H), 7.06 (d, 4H), 6.55 (s, 1H), 4.93 (s, 4H), 3.71 (s, 6H).

8. (HO)₂C

500 mg of **(MeO)₂C** (1.105 mmol) were dissolved in 55 mL of THF (20 mM). Afterward, 18.5 mL of LiOH aqueous solution (1.6 M) was added and the reaction was stirred at room temperature overnight. Then, THF was removed, and a yellowish aqueous solution was left. Titration the final solution with dilute HCl (1.2 M) drop by drop provided a precipitate. The solid was filtered and dissolved in THF, and the solution was kept stirring at 65 °C. After the compound was completely dissolved, the reaction was cooled down and CH₂Cl₂ was slowly added. The solution was kept in an ice bath and a yellow solid finally appeared. The solid was filtered and washed with CH₂Cl₂. Yield: 450 mg, 96 %. ¹H-NMR (400 MHz, DMSO-d₆): δ 16.30 (s, 1H), 13.01 (s, 1H), 7.68 (d, 4H), 7.60 (d, 2H), 6.98 (d, 4H), 6.80 (d, 2H), 6.10 (s, 1H), 4.75 (s, 4H). ESI/MS m/z (%): 425.12([M+H]⁺), 423.12([M-H]⁻).

9. (HO)₂C-BF₂

In a 10 mL microwave vial, compound **(HO)₂C** (0.118 mmol, 50 mg) was dissolved in 2 mL of DMF. Then, BF₃·Et₂O (0.944 mmol, 116 μL) was added and the reaction mixture was irradiated in a microwave reactor for heating to 80 °C and hold for 5 min. After cooling with a flow of compressed air, H₂O was added dropwise into the solution, and then orange precipitate came out. The compound was filtered and washed with cold Et₂O, and then vacuum dried to afford 64 mg of **(HO)₂C-BF₂** as an orange powder. Yield: 49 mg, 88 %. ¹H-NMR (400 MHz, DMSO-d₆): δ 13.10 (s, 1H), 8.00 (d, 2H), 7.84 (d, 4H), 7.08 (d, 2H), 7.04 (d, 4H), 6.54 (s, 1H), 4.81 (s, 4H).

References:

- (1) Vinkovic, V.; Kontrec, D.; Sunjic, V.; Navarini, L.; Zanetti, F.; Azzolina, O. *Chirality* **2001**, *13*, 581.
- (2) Schneiderheinze, J.; Armstrong, D.; Berthod, A. *Chirality* **1999**, *11*, 330.
- (3) Kato, D.-i.; Mitsuda, S.; Ohta, H. *The Journal of organic chemistry* **2003**, *68*, 7234.
- (4) Marzo, A.; Quadro, G.; Bruno, G.; Treffner, E.; Reali, F.; Borrelli, G.; Stradi, R. *Arzneimittel-Forschung* **1983**, *33*, 198.
- (5) Astoin, J.; Lepage, F.; Fromantin, J.; Poisson, M. *Eur J Med Chem Chim Ther* **1980**, *15*, 457.
- (6) Azzolina, O.; Collina, S.; Vercesi, D.; Ghislandi, V.; Bonabello, A.; Galmozzi, M. *Farmaco (Societa chimica italiana: 1989)* **1997**, *52*, 449.
- (7) Menon, V. P.; Sudheer, A. R. In *The molecular targets and therapeutic uses of curcumin in health and disease*; Springer: 2007, p 105.
- (8) Pari, L.; Tewas, D.; Eckel, J. *Archives of physiology and biochemistry* **2008**, *114*, 127.
- (9) Kocaadam, B.; Şanlıer, N. *Critical reviews in food science and nutrition* **2017**, *57*, 2889.
- (10) Prins, F.; Barreiro, A.; Ruitenber, J. W.; Seldenthuis, J. S.; Aliaga-Alcalde, N.; Vandersypen, L. M.; van der Zant, H. S. *Nano letters* **2011**, *11*, 4607.
- (11) Su, H.; Sun, F.; Jia, J.; He, H.; Wang, A.; Zhu, G. *Chemical Communications* **2015**, *51*, 5774.
- (12) Archet, F.; Yao, D.; Chambon, S.; Abbas, M.; D'Aléo, A.; Canard, G.; Ponce-Vargas, M.; Zaborova, E.; Le Guennic, B.; Wantz, G. *ACS Energy Letters* **2017**, *2*, 1303.
- (13) Pabon, H. *Recueil des Travaux Chimiques des Pays-Bas* **1964**, *83*, 379.
- (14) Wanninger, S.; Lorenz, V.; Subhan, A.; Edelmann, F. T. *Chemical Society Reviews* **2015**, *44*, 4986.
- (15) Sui, Z.; Salto, R.; Li, J.; Craik, C.; de Montellano, P. R. O. *Bioorganic & medicinal chemistry* **1993**, *1*, 415.
- (16) Zsila, F.; Bikádi, Z.; Simonyi, M. *Biochemical and biophysical research communications* **2003**, *301*, 776.
- (17) Zsila, F.; Bikádi, Z.; Simonyi, M. *Organic & biomolecular chemistry* **2004**, *2*, 2902.
- (18) Zsila, F.; Bikádi, Z.; Simonyi, M. *Bioorganic & medicinal chemistry* **2004**, *12*, 3239.
- (19) Aliaga-Alcalde, N.; Marqués-Gallego, P.; Kraaijkamp, M.; Herranz-Lancho, C.; den Dulk, H.; Görner, H.; Roubeau, O.; Teat, S. J.; Weyhermüller, T.; Reedijk, J. *Inorganic chemistry* **2010**, *49*, 9655.
- (20) Felouat, A.; D'Aléo, A.; Fages, F. r. *The Journal of organic chemistry* **2013**, *78*, 4446.
- (21) Kamada, K.; Namikawa, T.; Senatore, S.; Matthews, C.; Lenne, P. F.; Maury, O.; Andraud, C.; Ponce-Vargas, M.; Le Guennic, B.; Jacquemin, D. *Chemistry-A European Journal* **2016**, *22*, 5219.
- (22) Liu, K.; Chen, J.; Chojnacki, J.; Zhang, S. *Tetrahedron letters* **2013**, *54*, 2070.
- (23) Weiss, H.; Reichel, J.; Görls, H.; Schneider, K. R. A.; Micheel, M.; Pröhl, M.; Gottschaldt, M.; Dietzek, B.; Weigand, W. *Beilstein Journal of Organic Chemistry* **2017**, *13*, 2264.
- (24) Caruso, F.; Pettinari, R.; Rossi, M.; Monti, E.; Gariboldi, M. B.; Marchetti, F.; Pettinari, C.; Caruso, A.; Ramani, M. V.; Subbaraju, G. V. *Journal of inorganic biochemistry* **2016**, *162*, 44.
- (25) D'Aléo, A.; Felouat, A.; Heresanu, V.; Ranguis, A.; Chaudanson, D.; Karapetyan, A.; Giorgi, M.; Fages, F. *Journal of Materials Chemistry C* **2014**, *2*, 5208.
- (26) Aliaga-Alcalde, N. r.; Rodríguez, L.; Ferbinteanu, M.; Höfer, P.; Weyhermüller, T. *Inorganic chemistry* **2011**, *51*, 864.
- (27) Díaz-Torres, R.; Menelaou, M.; Roubeau, O.; Sorrenti, A.; Brandariz-de-Pedro, G.; Sañudo, E. C.; Teat, S. J.; Fraxedas, J.; Ruiz, E.; Aliaga-Alcalde, N. *Chemical Science* **2016**, *7*, 2793.

- (28) Khalil, M. I.; AL-Zahem, A. M.; Qunaibit, M. M. *Medicinal Chemistry Research* **2014**, *23*, 1683.
- (29) Menelaou, M.; Weyhermüller, T.; Soler, M.; Aliaga-Alcalde, N. *Polyhedron* **2013**, *52*, 398.
- (30) Lu, W.-P.; Mei, X.-T.; Wang, Y.; Zheng, Y.-P.; Xue, Y.-F.; Xu, D.-H. *Environmental toxicology and pharmacology* **2015**, *39*, 515.
- (31) Mei, X.; Luo, X.; Xu, S.; Xu, D.; Zheng, Y.; Xu, S.; Lv, J. *Chemico-biological interactions* **2009**, *181*, 316.
- (32) Pucci, D.; Crispini, A.; Mendiguchía, B. S.; Pirillo, S.; Ghedini, M.; Morelli, S.; De Bartolo, L. *Dalton Transactions* **2013**, *42*, 9679.
- (33) Zhou, S.-S.; Xue, X.; Wei, D.; Jiang, B.; Wang, J.-F.; Lu, C.-H. *Chemical Research in Chinese Universities* **2012**, *28*, 647.
- (34) Pucci, D.; Bellini, T.; Crispini, A.; D'Agnano, I.; Liguori, P. F.; Garcia-Orduna, P.; Pirillo, S.; Valentini, A.; Zanchetta, G. *MedChemComm* **2012**, *3*, 462.
- (35) Choi, M. H. L., Yong Chan; Han, Ho Gyu In *Repub. Korean Kongkae Taeho Kongbo*; KR 2011133224: Korea, 2011.
- (36) Chakraborti, S.; Dhar, G.; Dwivedi, V.; Das, A.; Poddar, A.; Chakraborti, G.; Basu, G.; Chakraborti, P.; Surolia, A.; Bhattacharyya, B. *Biochemistry* **2013**, *52*, 7449.
- (37) Tønnesen, H. H.; Karlsen, J. *Zeitschrift für Lebensmittel-Untersuchung und Forschung* **1985**, *180*, 402.
- (38) Bernabé-Pineda, M.; Ramírez-Silva, M. a. T.; Romero-Romo, M.; González-Vergara, E.; Rojas-Hernández, A. *Spectrochimica Acta Part A: Molecular and Biomolecular Spectroscopy* **2004**, *60*, 1091.
- (39) Lim, C. S.; Van Noord, A. C.; Kampf, J. W.; Pecoraro, V. L. *European Journal of Inorganic Chemistry* **2007**, *2007*, 1347.
- (40) de Lill, D. T.; Gunning, N. S.; Cahill, C. L. *Inorganic chemistry* **2005**, *44*, 258.
- (41) Sun, Z.-G.; Ren, Y.-P.; Long, L.-S.; Huang, R.-B.; Zheng, L.-S. *Inorganic Chemistry Communications* **2002**, *5*, 629.
- (42) Anana, H.; Trifa, C.; Bouacida, S.; Boudaren, C.; Merazig, H. *Acta Crystallographica Section E: Crystallographic Communications* **2015**, *71*, m114.
- (43) Sadakiyo, M.; Yamada, T.; Kitagawa, H. *Journal of the American Chemical Society* **2014**, *136*, 13166.
- (44) Li, M. Y.; Kurmoo, M.; Wang, Z. M.; Gao, S. *Chemistry—An Asian Journal* **2011**, *6*, 3084.
- (45) Shang, R.; Chen, S.; Hu, K. L.; Wang, B. W.; Wang, Z. M.; Gao, S. *Chemistry—A European Journal* **2016**, *22*, 6199.
- (46) Wang, X.-Y.; Gan, L.; Zhang, S.-W.; Gao, S. *Inorganic chemistry* **2004**, *43*, 4615.
- (47) Wang, Z.; Hu, K.; Gao, S.; Kobayashi, H. *Advanced Materials* **2010**, *22*, 1526.
- (48) Shang, R.; Chen, S.; Hu, K.-L.; Jiang, Z.-C.; Wang, B.-W.; Kurmoo, M.; Wang, Z.-M.; Gao, S. *APL Materials* **2014**, *2*, 124104.
- (49) Raghavan, S.; Manogaran, P.; Narasimha, K. K. G.; Kuppusami, B. K.; Mariyappan, P.; Gopalakrishnan, A.; Venkatraman, G. *Bioorganic & medicinal chemistry letters* **2015**, *25*, 3601.
- (50) Chaicham, A.; Kulchat, S.; Tumcharern, G.; Tuntulani, T.; Tomapatnaget, B. *Tetrahedron* **2010**, *66*, 6217.
- (51) Bong, P. H. *Bulletin of the Korean Chemical Society* **2000**, *21*, 81.
- (52) Khopde, S. M.; Indira Priyadarsini, K.; Palit*, D. K.; Mukherjee, T. *Photochemistry and photobiology* **2000**, *72*, 625.
- (53) Bonardi, L.; Kanaan, H.; Camerel, F.; Jolinat, P.; Retailleau, P.; Ziessel, R. *Advanced Functional Materials* **2008**, *18*, 401.
- (54) Kamkaew, A.; Lim, S. H.; Lee, H. B.; Kiew, L. V.; Chung, L. Y.; Burgess, K. *Chemical Society Reviews* **2013**, *42*, 77.

Chapter VI

Py-CCMoid-coordination polymers

6.1 Introduction

Coordination polymers (CPs) are defined as the coordination networks created with organic ligands (linkers) containing potential voids designed to accommodate metal centres where such coordination entities can be repeated in: one dimension (with cross-links between individual chains), loops, spiro-links, or as coordination compounds extended through repeating coordination entities in two or three dimensions.¹ MOFs (metal-organic frameworks) are a particular case of CPs that can present exceptional high surface areas, tuneable pore apertures and low densities. Because of the fascinating structural topologies and their potential as functional materials in various applications, such as gas storage,² separation,³ catalysis,⁴ sensing,⁵ and bio applications,⁶ MOFs are some of the most promptly rising fields in chemical and material sciences.

In general, both metal centres and ligands require to be biologically friendly for CPs with biological applications.⁷ Beside the biologically acceptable metals (such as Ca, Mg, Zn, Fe, Ti, and Zr), chemists have paid increasing attention to biologically active linkers towards the creation of functional frameworks.⁸ Some small natural molecules such as formates,⁹ oxalates,¹⁰ succinates¹¹ and glutarates¹² have been used as linkers, as they all contain more than one coordinative groups.

Regarding the above, it is important to remark that CCMoids provide structural plurality which are capable of containing different functional groups connected through a conjugate backbone. It has been probed that they present an excellent ability to coordinate with metal ions, making them promising candidates for the creation of coordination polymers of all kind. In practice, only the natural occurring curcumin has been used as a building block to construct MOFs, being the exclusive system reported until now (Figure 1), where the compound displays stable porosity and putative drug delivery ability.¹³

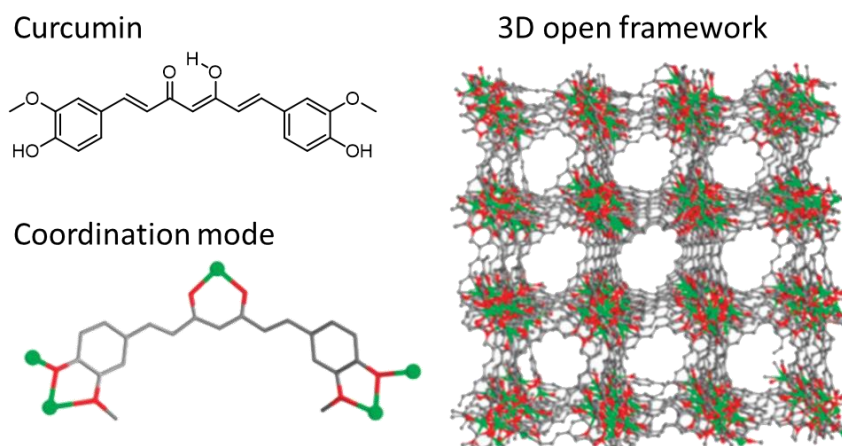


Figure 1. The crystal structure of a MOF constructed with curcumin ligand (Zn, green; C, grey; O, red).¹³

In this chapter, the chemistry structure of a CCMoid containing pyridine moieties at its endings has been explored. In general, bidentate organic ligands and more precisely, bipyridine groups, are commonly used to increase the dimensionality and rigidity of the final frameworks, including the possibility of generating accessible pores by sharing the simultaneous coordination of two kinds of linkers with one metal centre,¹⁴ or by the reaction of preformed metal clusters with bipyridine linkers¹⁵ (Figure 2).

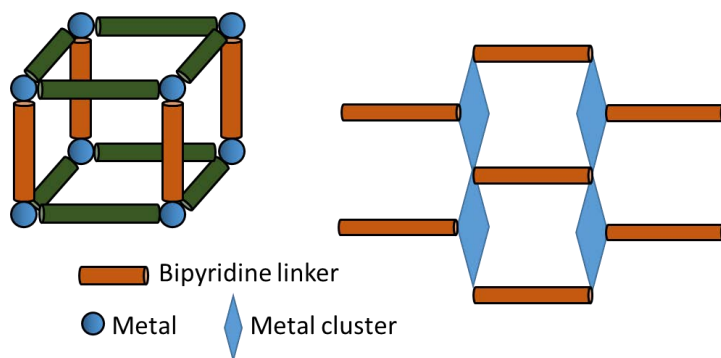


Figure 2. Two ways to introduce bipyridine linkers in the synthesis of MOFs.

Integrating the outstanding properties of CCMoids and they versatility toward the combination of different functional groups, here we made use of a CCMoid named **3Py-CCM** bearing two pyridine groups at both arms (Figure 3). The ligand was synthesized in the group of Dr. Mònica Soler at the University of Chile, and this chapter presents the exploratory work regarding the application of such ligand as a linker for the creation of novel CPs. This work shows initial steps towards the use of such organic system in the creation of a variety of coordinated networks which may extend the potential technological applications of CCMoids.

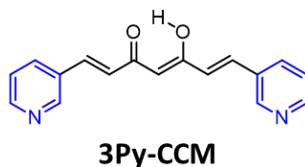


Figure 3. Chemical structure of **3Py-CCM**.

6.2 Objectives

The Objective of this chapter is:

To explore the synthesis of CPs/networks by the use of **3Py-CCM**.

The work will be focused on the following aspects:

- (1) Synthetic studies regarding the creation of CPs containing the **3Py-CCM** ligand with a variety of metal centres using solvothermal synthesis and the investigation of the different structures obtained by varying reaction conditions.
- (2) Studies of the deposition of the systems on different surfaces.

3Py-CCM is a symmetrical ligand and contains three coordination groups: two pyridine groups at the ends of the molecule and a β -diketone moiety in the middle. The latter has a great tendency to coordinate with a number of metallic centres,¹⁶ where the coordination number of the metal varies depending on their nature. In some cases, the metal centres coordinate to one CCM-type ligand and to additional co-ligands, normally N,N-chelating ligands as for example 3-azo-phenyl-4,4'-bipyridine¹⁷ and bathophenanthroline.¹⁸ Here, due to the introduction of pyridine groups in the molecule, our CCMoid could connect with each other creating networks without the assistance of extra ligands using the metal centres exclusively. Moreover, the three coordination moieties, from the molecule, provide more opportunities to grow in different dimensions. Figure 4 illustrates some possible coordination networks.

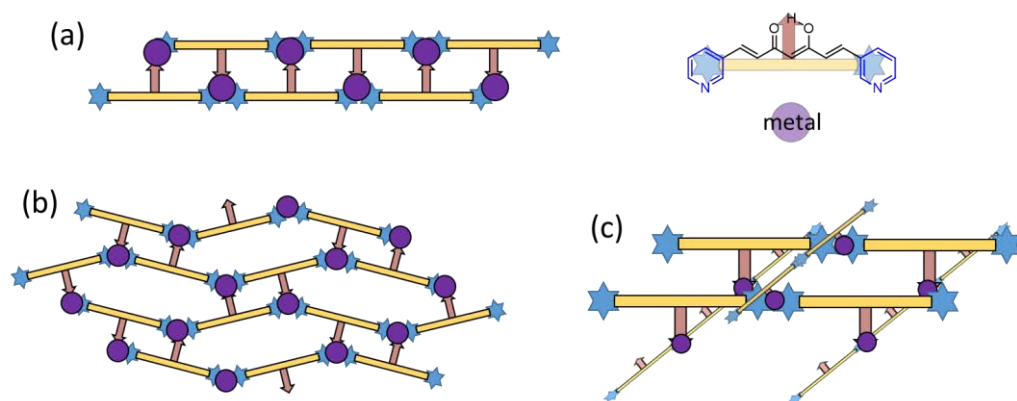
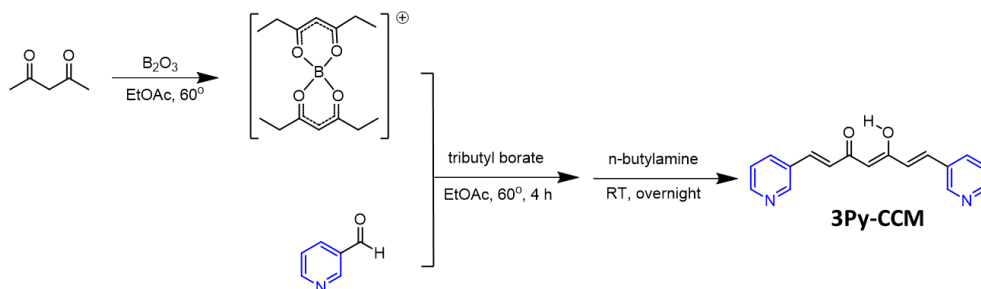


Figure 4. Prospective structures of coordination networks based on **3Py-CCM** and metal ions, formed by (a) cross-links between 1D-CPs, (b) 2D-CPs and (c) 3D-CPs.

6.3 Synthesis and characterization of CPs based on Py-CCMoid

6.3.1 Synthesis and structure of 3Py-CCM ligand



Scheme 1. Synthesis of the **3Py-CCM** molecule.

As mentioned above, the synthesis of 3Py-CCM ligand (Scheme 1) was developed in the group of Dr. M. Soler from the Universidad de Chile, varying the classic synthetic method described from H. J. J. Pabon.¹⁹ In this case, the use of a diluted acidic solution is avoided; instead, water is sufficient to break the boron-compound and to achieve the final system. The method was used in this work to achieve quantities of the free ligand for latter reactions towards the synthesis of CPs. Previous to this research, the structure of **3Py-CCM** was also achieved (Figure 5). As expected, it consists in a highly conjugated 1,3-diketone moiety which exist in the keto-enol form, with the two pyridine groups rotated in opposite directions with small torsion angles (-9.69 and 6.36, respectively). The molecule is almost linear, which may benefit the formation of porous and stable frameworks.

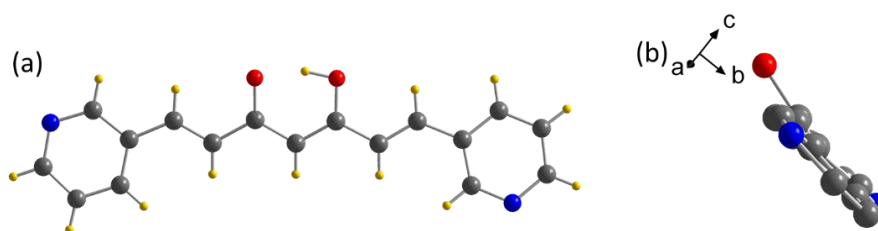


Figure 5. (a) Crystal structure of **3Py-CCM**. (b) Structure of **3Py-CCM** shown in a different crystallographic projection. Colour legend: O in red, N in blue, H in yellow and C in grey.

6.3.2 Synthesis and characterization of Py-CCMoid CPs

6.3.2.1 General methods to obtain the CPs based on 3Py-CCM

CPs based on **3Py-CCM** were synthesized following the method described before in chapter V, and the conditions required for the achievement of crystalline material were summarized in Table 1. Several reactions were performed towards such goal where basically $\text{Zn}(\text{NO}_3)_2 \cdot x\text{H}_2\text{O}$ and 3Py-CCM were mixed in different ratios and solvents. The final solutions were stored in closed vessels at 80 °C for 3 days to achieve crystals suitable for single crystal X-ray analyses. The solvents used in the synthesis of systems **PyC-Zn1** and **PyC-Zn2** were DMF/ CH_3OH (0.5 ml vs 1.5 ml) and DMA/EtOH (0.5 ml vs 1.5 ml), respectively. The crystals were collected and then washed with corresponding alcohols before their single crystal X-ray analyses. In the case of **PyC-Zn3**, two distinguished types of crystals came out, named here **PyC-Zn3-1** and **PyC-Zn3-2**.

Table 1. General conditions towards the synthesis of coordination polymers based on **3Py-CCM**.

N°	ligand	metal salt	solvent	conditions	results
PyC-Zn1	3Py-CCM 5 mg	$\text{Zn}(\text{NO}_3)_2 \cdot x\text{H}_2\text{O}$ 16 mg	DMF: CH_3OH 0.5 ml: 1.5 ml	80 °C, 3 days	crystal
PyC-Zn2			DMA: ethanol 0.5 ml: 1.5 ml		crystal
PyC-Zn3			DMF: ethanol 0.5 ml: 1.5 ml		PyC-Zn3-1 PyC-Zn3-2

Preliminary ATR-FTIR (Figure A6.1) spectra indicated that **PyC-Zn1** and **PyC-Zn3-2** were similar, meanwhile compounds **PyC-Zn1**, **PyC-Zn2** and **PyC-Zn3-1** displayed different spectra.

6.3.2.2 Crystal structures of PyC-Zn1 and PyC-Zn2

The crystallographic structures of **PyC-Zn1** and **PyC-Zn2** were resolved by the use of synchrotron source. In the period of writing of this thesis, **PyC-Zn3** remained unresolved due to the requirement of the optimized synthetic process towards the achievement of bigger sized crystals. For the other two, single crystal X-ray diffraction revealed that **PyC-Zn1** and **PyC-Zn2** are different types of CPs. **PyC-Zn1** is a 1D structure meanwhile **PyC-Zn2** presents a 2D network. They crystallize in the space groups $C2/c$ and $P2_1/n$, respectively. Crystallographic dates are shown in Table A6.1.

For the CP found for **PyC-Zn1**, there is one type of Zn(II) atom and also one type of CCMoid **3Py-CCM** in the asymmetric unit. Figure 6a shows that each Zn atom bridges four CCMoid units, forming an octahedron in hexa-coordination, which is binding to two 1,3-diketone moieties from two CCMoids in a *cis* disposition and to two N atoms from the pyridine rings with a *cis* distribution as well. For the CCMoid ligand, one of the pyridinic rings participates as a linker for the structure, meanwhile the other pyridine remains free (Figure 6b). The distance between Zn and the two O atoms of the diketone are a bit different, being the metallic centre closer to the side that

contributes to the coordination structure (Zn-O1 2.026 Å). Within the coordination chain, the disposition of the **3Py-CCM** ligand is similar to the free ligand described before, keeping the planarity of the conjugated system and the two different directions of N atoms of the side pyridine groups.

As shown in Figure 6a and 6c, one pair of **3Py-CCM** ligand forms a loop with a total length of 9.271 Å (Zn...Zn), and the extension in one direction of this moiety provides the final Zn-CCMoid chain. The chains interact with the neighbours through weak molecular interactions providing a final supramolecular 3D packing (Figure 6d).

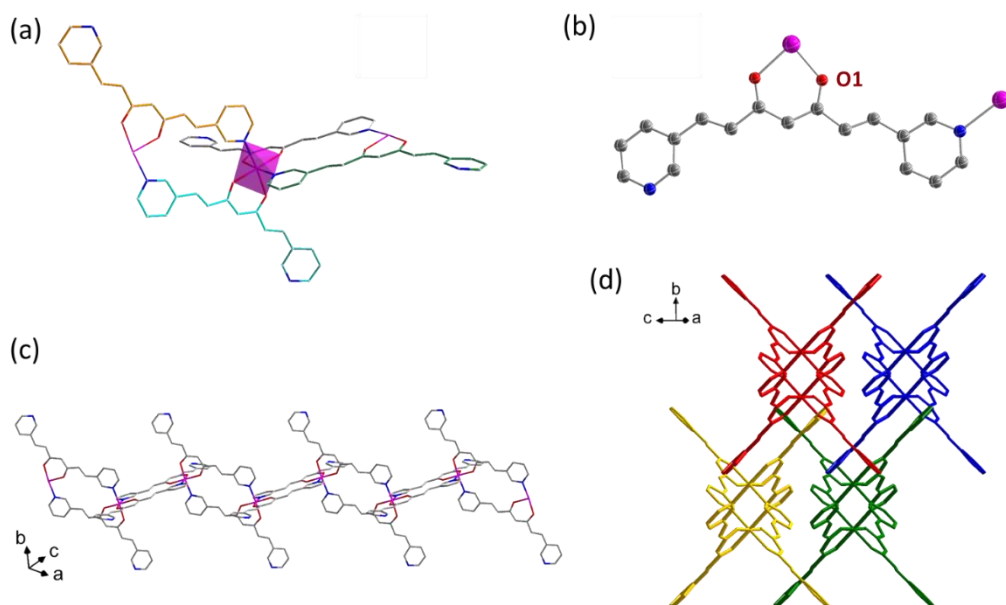


Figure 6. Crystal structure of **PyC-Zn1**: (a) Zn(II) polyhedral representation; (b) coordination modes of **3Py-CCM** in the chain; (c) Zn-CCMoid chain, **PyC-Zn1**; (d) the framework displays the interactions of different Zn-CCMoid chains (with different colours representing each chain). (Zn, pink; C, grey; O, red; N, blue; H are omitted for clarity).

When the reaction was performed in DMA/EtOH, **PyC-Zn2** was achieved, displaying a different coordination network. Figure.7a shows the coordination around the Zn centre in the case of **PyC-Zn2**. Each Zn(II) centre is hexa-coordinated as before, but now coordinates to two oxygen atoms from one 1,3-diketone moiety, two nitrogen atoms from 3Py-CCM ligands and two oxygen atoms from one nitrate anion. The latest is obtained from the metallic source, $M(\text{NO}_3)_2 \cdot x\text{H}_2\text{O}$, also observed in other cases of CPs that contain bipyridine ligands.^{20,21} Different from the previous system **PyC-Zn1**, both of the two pyridine sides in **3Py-CCM** are now twisted and involved the coordination network, affording infinite 2D layers along the b axis. In a single layer, two types of loops can be distinguished, the smallest presents Zn...Zn distances of 9.03 Å, similar to that found in **PyC-Zn1** (Figure 6c); the biggest void displays a rhomboid shape with

Zn...Zn distance of 22.060 Å which is almost three times bigger than the former (Figure. 7c). The assembly of the layers is shown in Figure.7d, parallel closely to each other, having the nitrate groups inserted in the bigger voids. The layers are separated from a distance of 4.53 Å.

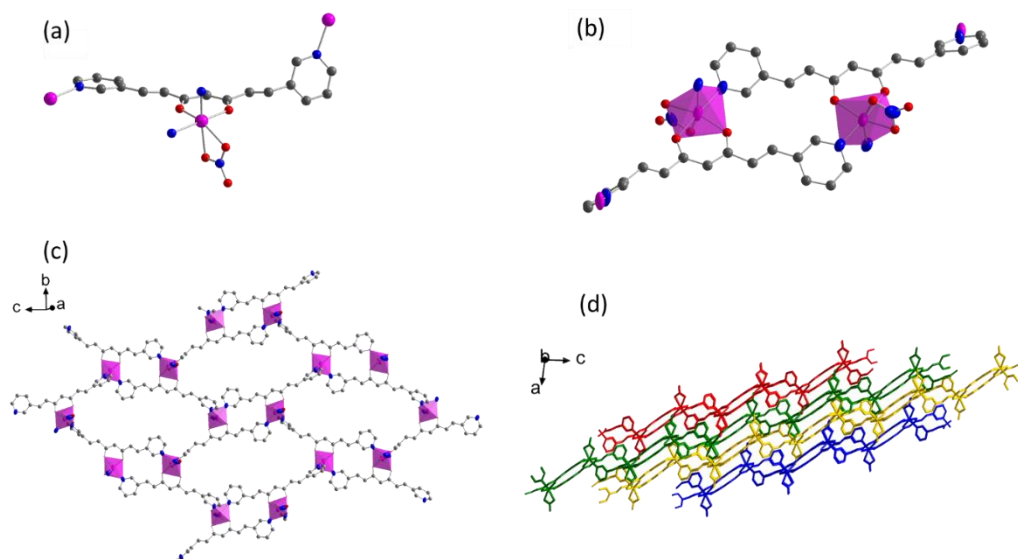


Figure 7. Crystal structure of **PyC-Zn2**: (a) Representation with the coordination of one Zn(II) centre and coordination mode of one CCMoid; (b) picture of the smallest loop in the layer; (c) 2D Zn-CCMoid layer; (d) framework consisting on packed Zn-curcumin layers (with different colours represent the layers). (Zn, pink; C, grey; O, red; N, blue; H are omitted for clarity).

6.3.2.3 Stability of PyC-Zn1, PyC-Zn2 and PyC-Zn3

At room temperature and kept in alcohol solutions, all the crystals were stable within long periods of time (> months). In the solid state, the effect of an external force was investigated for all of them, taking into account the variety of systems encountered. Few milligrams of crystals were grounded on plates for 10 minutes. All the crystals became fine and yellow powders (Figure 8 top). The powder X-ray diffraction spectra in Figure 8 shows the consistency of the patterns before and after grinding, which indicated there is not transformation of the structure, demonstrating the stability of all the coordination network under low pressure. In the case of **PyC-Zn1** and **PyC-Zn2**, the powder X-ray patterns match well with the single X-ray simulation, indicating the uniformity and reproducibility of the crystals. Furthermore, in the process it was found that **PyC-Zn3-1** and **PyC-Zn3-2** are different, presenting **PyC-Zn3-2** the same crystallographic pattern as **PyC-Zn1**, confirming what it was observed by FT-IR spectra. The final structure of **PyC-Zn3-1** remains unsolved.

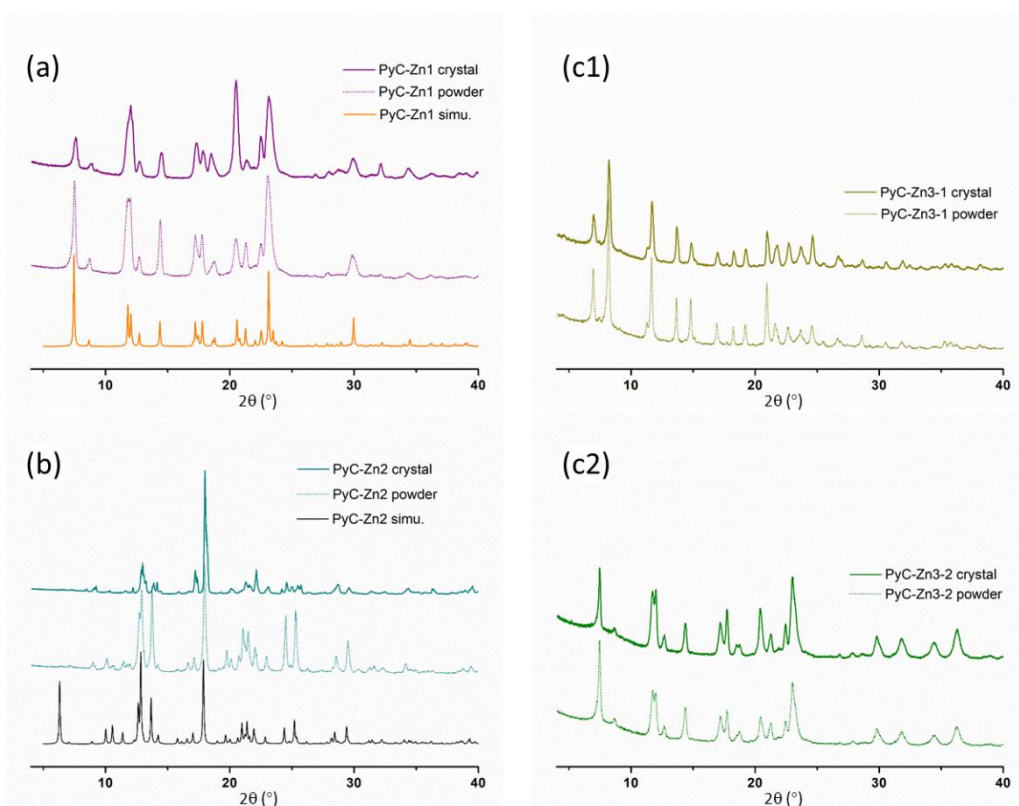
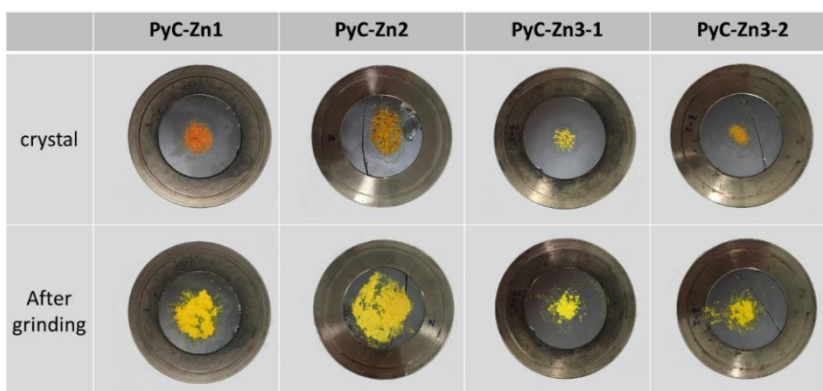


Figure 8. (Top) Comparison of the crystals before and after grinding. (Down) Powder X-ray diffraction for all the compounds.

Simultaneously thermal analysis STA(TG-DSC) was used toward the thermostability study of the free ligand and the coordinated networks. The results are shown in Figure 9, where the thermogravimetry (TG) and differential scanning calorimetry (DSC) techniques used are compared. For the free ligand **3Py-CCM**, a remarkable loss of weight happened at 185 °C. In the case of **PyC-Zn1**, the 1D system begins to decompose at 325 °C and **PyC-Zn2** does it at 262 °C.

DSC analyses show clearly the strenuous decompositions occurring between 600 and 700°C, corresponding to exothermic processes. These two coordinated networks based on the same free ligand, present different stability by comparing their TG curves, indicating **PyC-Zn1** is more stable than **PyC-Zn2**. This phenomenon probably due to the nitrate anions in the **PyC-Zn2** structure do not provide strength to the final system.

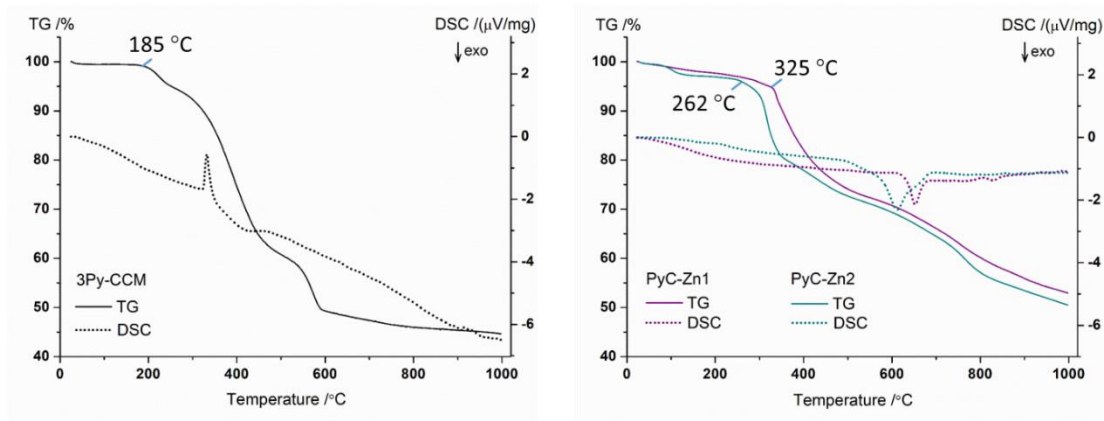


Figure 9. TG-DSC analyses of **3Py-CCM**, **PyC-Zn1** and **PyC-Zn2**, respectively.

6.4 Top-down exfoliation of crystalline **PyC-Zn2** towards the study of nanoscale aggregates

It is of great interest the development of approaches to prepare stable single layer.^{22,23} Taking into account the structure of **PyC-Zn2**, we explored the exfoliation and deposition of this 2D polymer. Since the crystal structure shows small voids and a conjugated network (based on the **3Py-CCM** ligand coordinated through Zn centres), **PyC-Zn2** may have interesting electronic properties at the nanoscale. The work performed by chemical and mechanical exfoliation on **PyC-Zn2** crystals was presented here.

6.4.1 The effect of washing with DMA

PyC-Zn2 was synthesized in a mixture of solvents: DMA/EtOH. The shiny crystals were picked up and then washed and kept in EtOH. Powder XRD spectra shown in Figure 10a demonstrate that the treatment in EtOH including wash and conservation, does not affect the structure of **PyC-Zn2**, as the crystals have the same pattern before and after, and both of them are in agreement with the simulated pattern of the tested crystal. However, when pure DMA was used to keep the crystals, the crystals of **PyC-Zn2** lost transparency and crystallinity over time (Figure 10b).

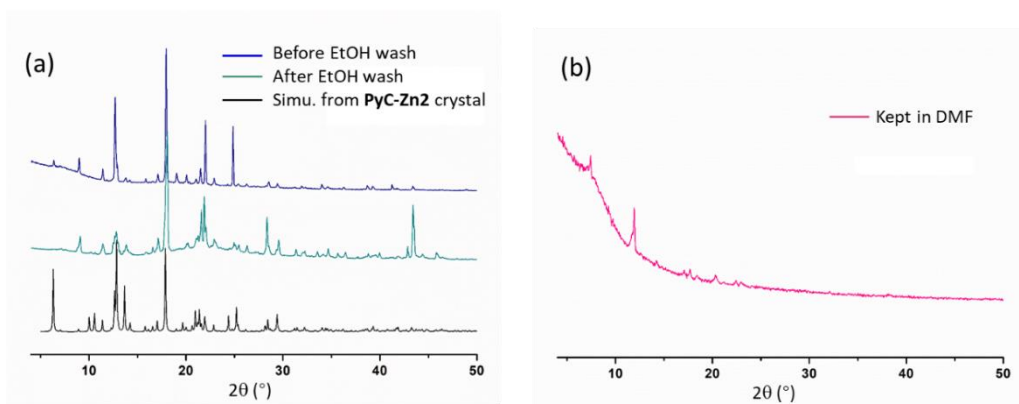


Figure 10. Powder XRD patterns of **PyC-Zn2** (a) before and after EtOH treatment, (b) kept in DMA overnight.

As **PyC-Zn2** is formed by the stacking of 2D layers, the effect of DMA on the crystal structure was explored. Figure 11 shows the ATR-FTIR spectra of the free ligand **3Py-CCM**, the crystal **PyC-Zn2** and the precipitate got from DMA. Compared to the free ligand **3Py-CCM**, the small peak at 3031 cm^{-1} disappears and another one at 1571 cm^{-1} shifts once the pyridine group coordinates to the Zn atoms in **PyC-Zn2** and in the case of treatment with DMA. In the case of the crystals before and after addition of DMA, the solids present similar spectra differing only in the area from 1675 to 1600 cm^{-1} . This region relates to the C=O stretching vibrational mode from the β -diketone moiety and the appearance of solvent, which is the case of the molecules treated. A broad peak appears probably due to the existence of DMA solvent. The ATR-FTIR spectra indicated that the DMA solvent can induce gradual erosion of the **PyC-Zn2** (the system redissolves again the solvent), and the crystals were cracked and lost the macroscopic shine.

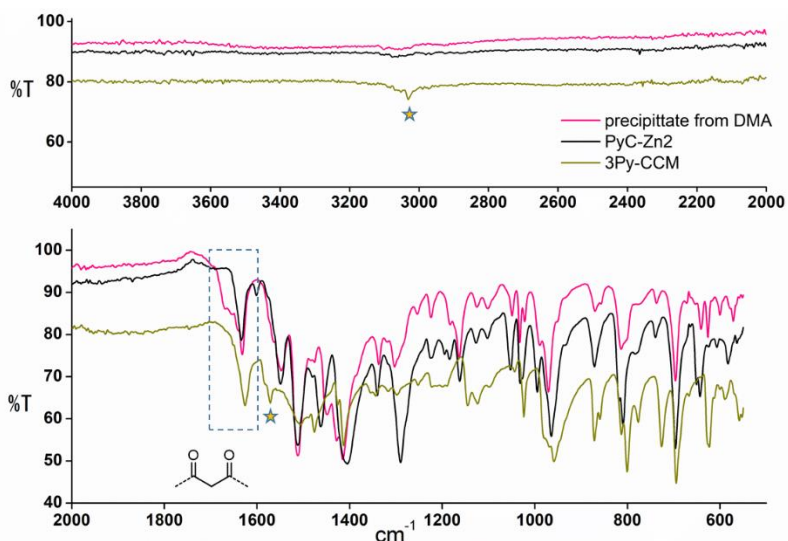


Figure 11. ATR-FTIR spectra of the free ligand **3Py-CCM**, the crystal **PyC-Zn2** and the precipitate obtained from DMA.

When kept the **PyC-Zn2** in DMA, the shining crystals became less crystalline and shiny, and the remained solution also changed to be yellowish, indicating the crystal is partially soluble in DMA. In order to understand the stability of the compound, the free ligand **3Py-CCM** and the **PyC-Zn2** system were tested by ^1H NMR in DMF-d_7 , solvent that has similar properties as DMA (Figure 12). The spectra of both compounds are different, demonstrating that after treatment with DMF, and probably happening the same with DMA, **PyC-Zn2** provides coordination compounds and not the free ligand. The absence of enol H at 16.12 ppm for the **PyC-Zn2** solution may indicate that the dissolved compound is still a CCMoid-metal system. The NMR spectrum shows a clean pattern with well-defined signals, similar to related coordination compounds (mononuclear Zn-CCM systems).²⁴ Comparing the disposition of the protons from the pyridine groups with those of the backbone, the latest are significantly shifted demonstrating that the 1,3-diketone moiety is the most affected, probably by the coordination to Zn. This is consistent with the strong bonding of oxygen atoms to the Zn in the structure (around 1.985 Å). Nevertheless, the existence of the hexa-coordination of Zn(II) as it appears in the structure, **PyC-Zn2**, cannot be confirmed through this test. MALDI studies did not show free charged ligand or big charged systems (the molecular weight found were below 1000) but were not conclusive, being impossible to suggest a putative structure for the solution part at the moment (Figure A6.2).

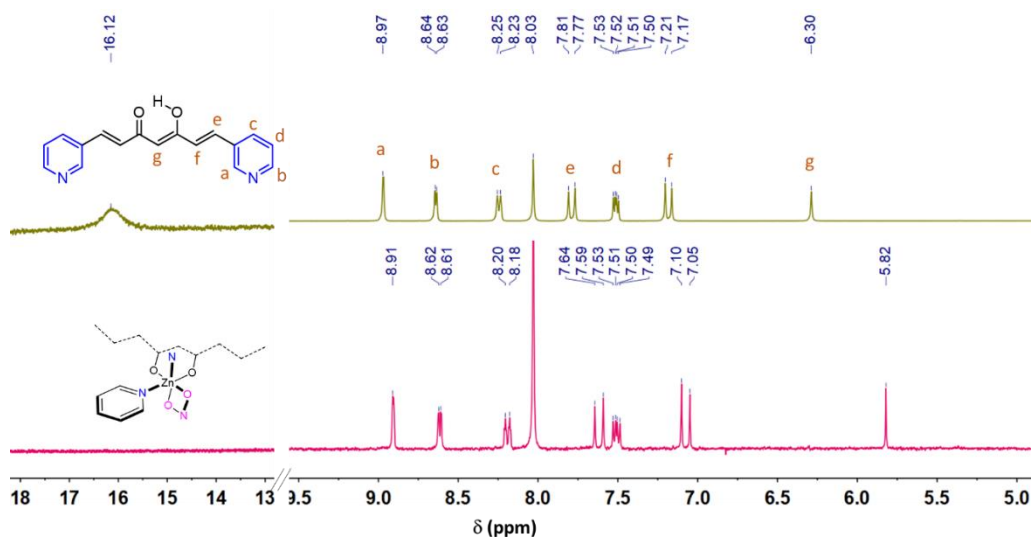


Figure 12. ^1H NMR spectra of **3Py-CCM** and the **PyC-Zn2** in DMF-d_7 .

The aggregation and morphology of the solid **PyC-Zn2** after washing with DMA have been investigated by SEM on different substrates. The solution and precipitate, named **PyC-Zn2a** and **PyC-Zn2b**, respectively, were separated, followed by drop casting on silicon wafer, mica and HOPG, correspondingly. Figure 13 a1-a3 show the aggregation of **PyC-Zn2a** (solution) after DMA completely evaporated for all the surfaces described. There is a significant effect on the final morphologies which are all obviously different. On the silicon wafer and HOPG, **PyC-Zn2a** molecules present higher order and crystallinity, forming flakes (Figure 13 a1) for the former or

sticks, for the latest (Figure 13 a3). However, the molecules spread out in an amorphous way in mica (Figure 13 a2). The morphologies found for **PyC-Zn2a** are distinctively different to those found for the free ligand, **3Py-CCM**, under the same conditions and substrates (Figure 14), emphasizing the idea that the dissolved systems from DMA may not be the free ligand.

The solid part, **PyC-Zn2b**, also differs from the results for the solution. The precipitate can be described as homogenous cubes with an average size of 1 μm , distributed on the different substrates (Figure 13 b1-b3).

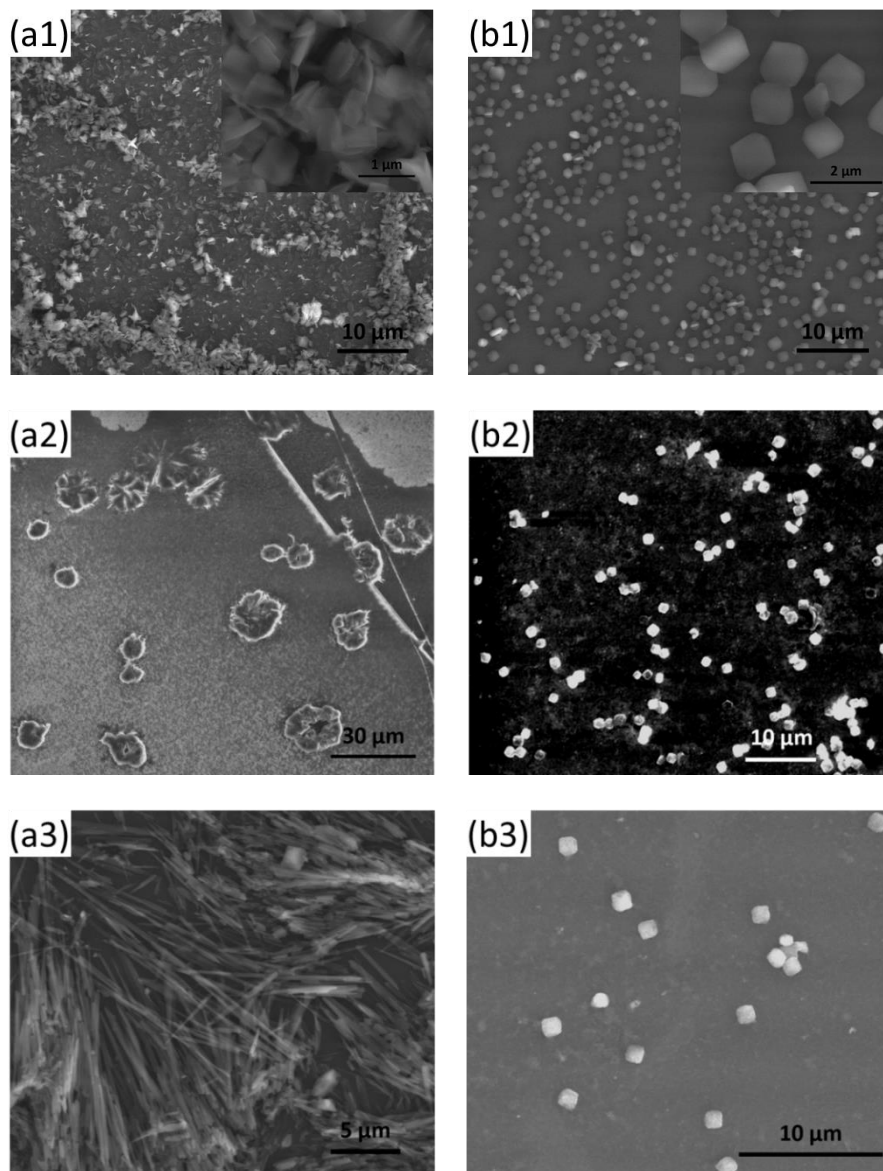


Figure 13. SEM images on different substrates of **PyC-Zn2a** and **PyC-Zn2b**, respectively. (a1-a3) **PyC-Zn2a** on silicon wafer, mica and HOPG; (b1-b3) **PyC-Zn2b** on silicon wafer, mica and HOPG.

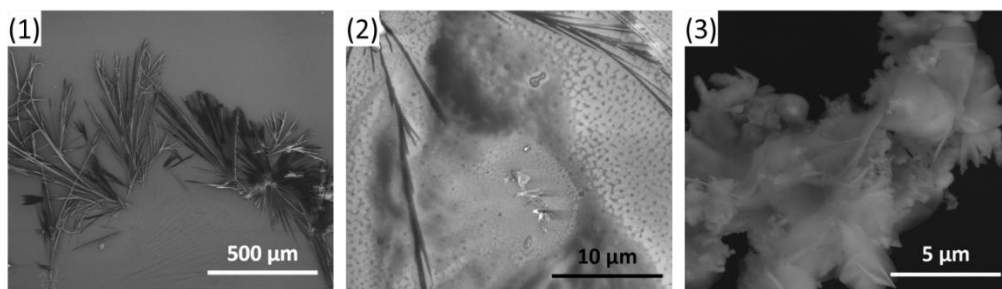


Figure 14. SEM images of the CCMoid ligand **3Py-CCM** on different substrates (1) silicon wafer, (2) mica and (3) HOPG.

The flakes (**PyC-Zn2a**) and cubes (**PyC-Zn2b**) found on silicon wafers were imaged by using atomic force microscopy (AFM). Figures 15 and 16 show the final outcomes. Due to the significantly reduction of contact force,²⁵ the tapping mode AFM method is very useful to generate reproducible images of the topography. The pictures in Figure 15 represent the surface topography of **PyC-Zn2a** flakes obtained at different zooms. The so named flakes, from the SEM picture, are now clearly amorphous aggregates of different heights (average 1 μm) having the appearance of mountain ranges. The morphology of the **PyC-Zn2b** cubes is kept in the AFM images; they can be characterized as rough and isolated islands with width dimensions ranging from 1 to 1.5 μm and height around 0.5 μm (Figure 16). The images indicate that the cubes are eventually digested by the solvent and became the structures that are later in solution. No further information regarding the disposition of the sheets (taking into account the crystallographic data) on the surface could be extracted from this data, although advance studies should be performed to understand the disposition and to measure conductivity of the final structures; the latest should be performed on conductive surfaces.

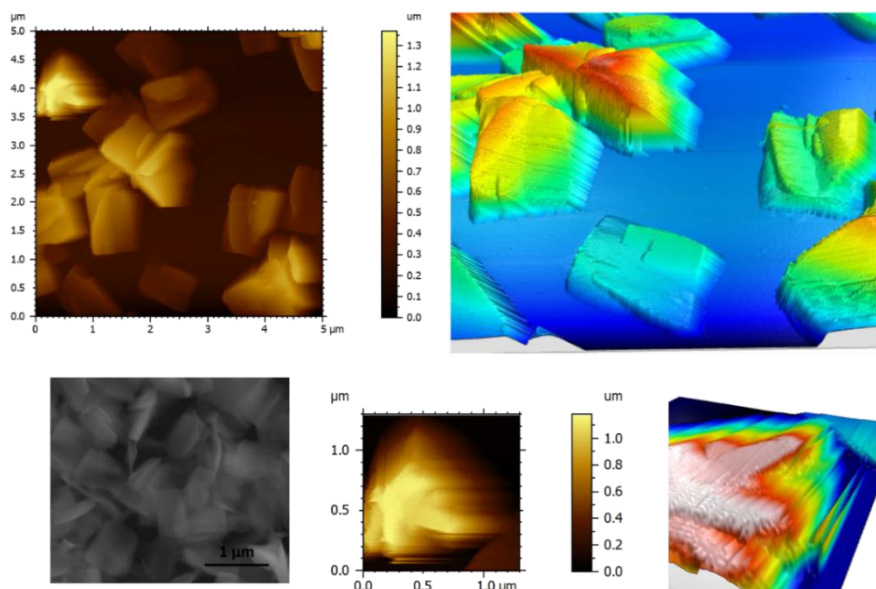


Figure 15. (Top) AFM images of **PyC-Zn2a** flakes obtained with tapping mode. (Down) The enlarged scan area.

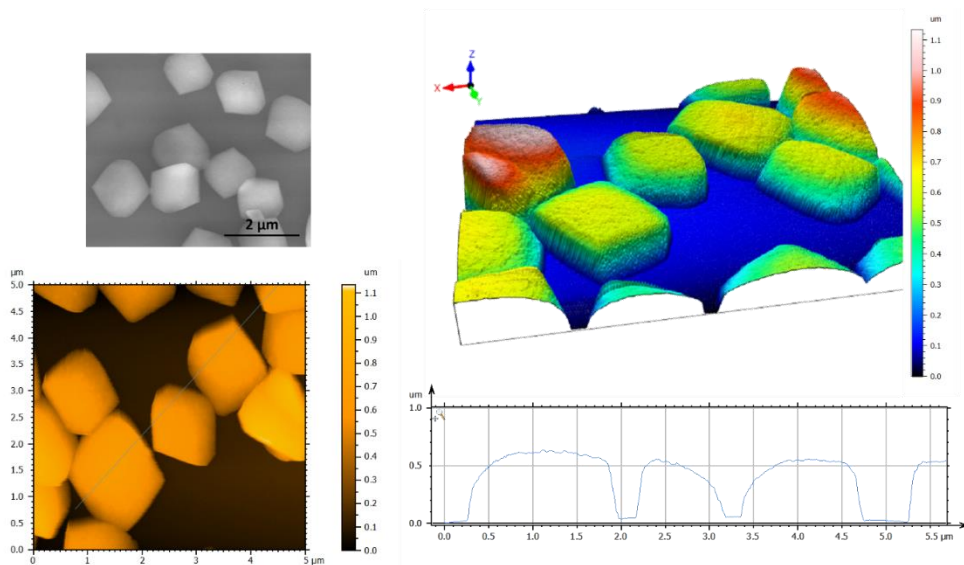


Figure 16. AFM images of **PyC-Zn2b** cubes obtained with tapping mode.

6.4.2 Exfoliation studies using EtOH, CH₃OH and acetone

Inspired by the 2D structure of **PyC-Zn2** and the works in the literature describing the exfoliation of graphite and other layered MOFs,^{23,26-30} further studies with this system were performed with the aim of finding a methodology that allowed us the separation of the layers. Sonication was selected as the mechanical force to compete with interlayer interactions from our coordination polymer. Delamination of **PyC-Zn2** by sonication in various solvents (CH₃OH, EtOH, and acetone) was explored, where the free ligand **3Py-CCM** was used for comparative reasons.

In this way, **3Py-CCM** (1 mg) was completely dissolved in all the chosen solvents (1 mL) without further treatment at room temperature, resulting in clear yellow solutions for all the cases (Figure 17a). Performing in an identical manner with crystals of **PyC-Zn2** (1 mg) dissolved in 1 mL of CH₃OH, EtOH and acetone respectively, the crystals remained unchanged in EtOH and acetone after 24 hours. However, in CH₃OH the solution was transparent but yellowish, having crystals partially dissolved (Figure 17b); perceptible Tyndall effects (scattering of light) could not be identified in the methanolic solution (Figure 17c) corroborating the partial dissolution of the sample or due to the small low concentration of nanoscale polymers in the solvent.

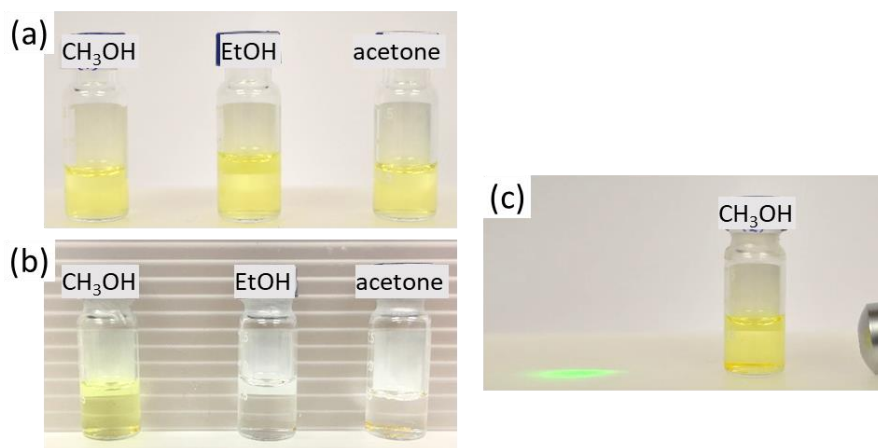


Figure 17. Photographs of (a) the solutions of **3Py-CCM** in CH₃OH, EtOH and acetone with the content of 1 mg·mL⁻¹ (b) the crystals of **PyC-Zn₂** 1 mg·mL⁻¹ kept 24 hours in CH₃OH, EtOH and acetone (c) the light beam incident from the side to demonstrates there is not the Tyndall effect in **PyC-Zn₂** CH₃OH solution.

However, once ultrasonic was used (100W, 42KHz) for **PyC-Zn₂** in CH₃OH, EtOH and acetone for about 15 minutes at room temperature, Tyndall light scattering (Figure 18) was observed for all the suspensions. Longer times were required for shining crystal to disappear under such concentrations and conditions. Then, the suspensions were kept quietly for 24 hours (for sedimentation) followed with taking the upper-layer colloidal suspensions for further studies.



Figure 18. The Tyndall effect of the **PyC-Zn₂** colloidal suspensions after ultrasonication 15 minutes in CH₃OH, EtOH, and acetone.

Atomic force microscope was employed to obtain morphological images of the delaminated **PyC-Zn₂** nanosheets. Samples were prepared by adding few drops of the colloidal suspension (10 μL) onto a freshly cleaved mica substrate, and the measurements were carried out at room temperature with an AFM tapping mode. Figures 18-21 show that the compounds have spherical shapes with nanoscale heights and the absence of flakes corresponding to the lamellae seen before in the solutions of the crystals of **PyC-Zn₂** in DMA. Our studies show large amounts of aggregates on the substrates, where nanosheets could not be observed. In CH₃OH, the particles were in the range of 30-40 nm high, while in ethanol the particles were bigger with the height between 100-150 nm. Acetone provided the smallest sized particles which are 20 nm high.

Further investigation of the sedimentation process (longer times, temperature, further centrifugation processes) were not performed for the lack of time but should be taken into account to accomplish a robust exfoliation process.

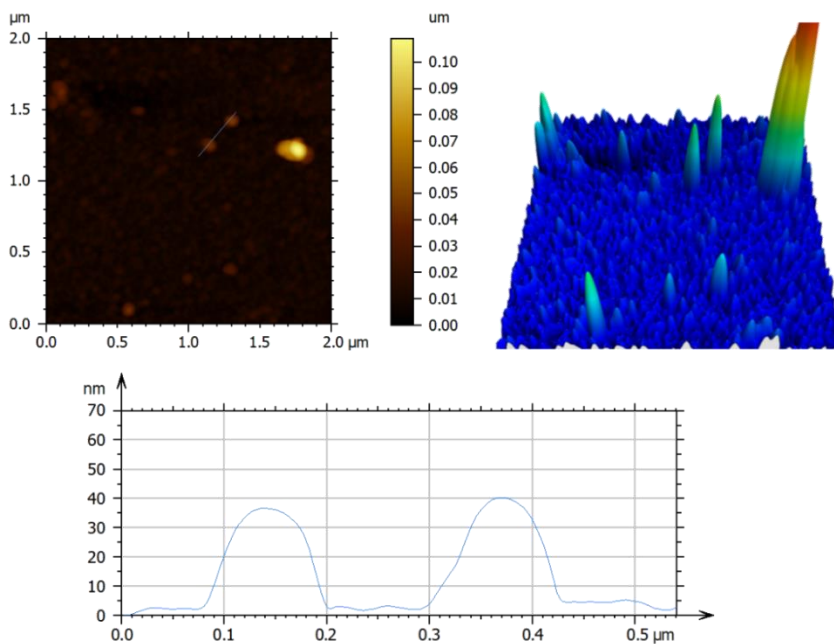


Figure 19. AFM images and height profiles corresponding to blue lines for nanoparticles formed by **PyC-Zn₂** exfoliation in CH_3OH .

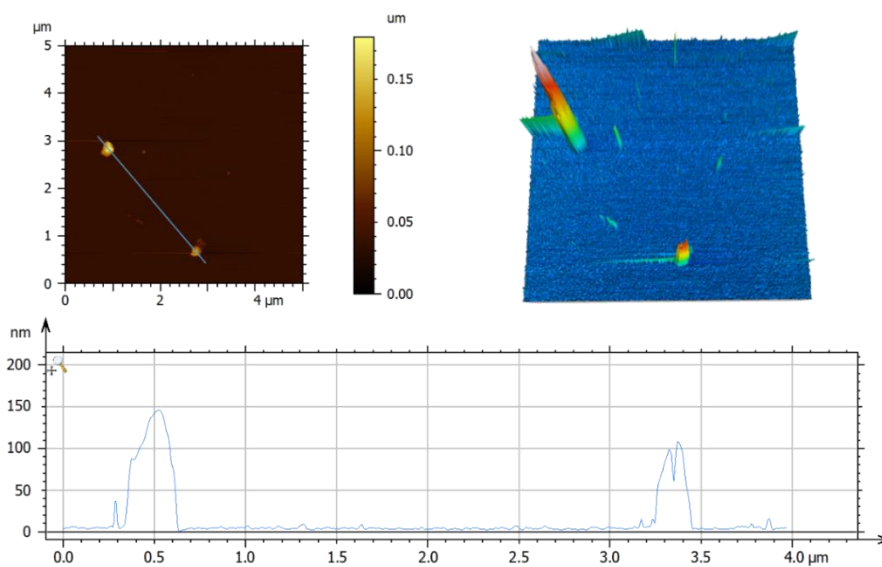


Figure 20. AFM images of nanoparticles of **PyC-Zn₂** exfoliation in EtOH .

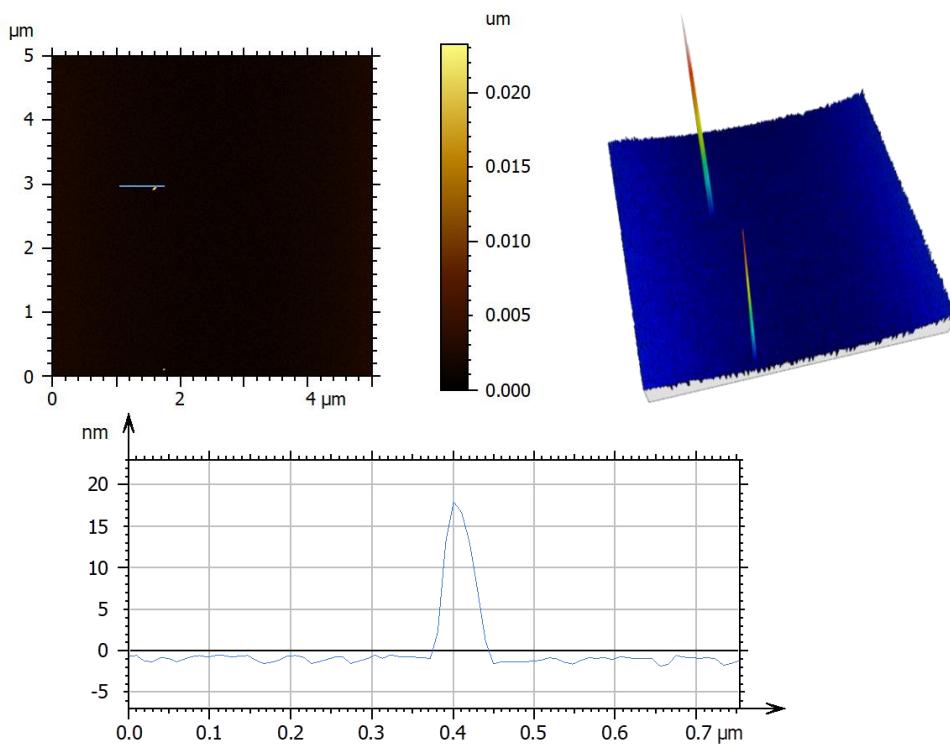


Figure 21. AFM images of nanoparticles of **PyC-Zn₂** exfoliation in acetone.

On the other hand, studies of the sediment were also performed by means of SEM (Figure 22). The images below show the morphologies found for the three solvents. From the pictures, instead of the big crystals of **PyC-Zn₂**, the solid was replaced by small aggregates with the shape of sticks, balls and flakes in CH_3OH , EtOH and acetone, respectively. In acetone, the system has the appearance of flakes and also compact structures, giving the impression that the nanosheets or flakes undergo to a re-stacking process after the sonication.

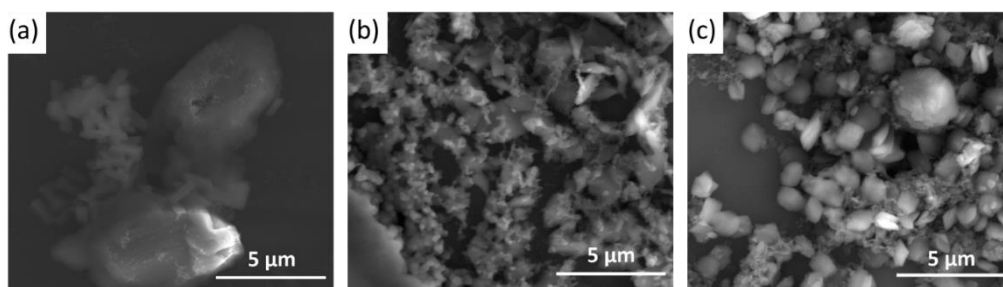


Figure 22. SEM images of the sedimentation exfoliated from different solvents on silicon wafer, (a) in CH_3OH , (b) EtOH and (c) acetone.

6.4.3 Exfoliation studies in H₂O, chlorobenzene and hexane

Studies regarding the possible effects of the solvents polarity, additional solvents were investigated for the exfoliation process. For that, three new solvents were tested: chlorobenzene and hexane, apolar solvents (polarity of 0.188 and 0.009, respectively), and H₂O is the other extreme. Using the same methodology as before, ultrasonic was used until no crystals were visible to the eye. Then, as explained above, the suspensions were deposited on silicon wafer, mica and HOPG, respectively. Figure 23 shows SEM images of the sonicated system treated in H₂O. The different morphologies found from the three substrates may indicate the strong effect of the solvent together with the surface, where the systems re-assemble in various ways depending on the substrates. In the case of chlorobenzene, the crystals seem to crack into small amorphous pieces (Figure 24). And in hexane, irregular blocks and sticks were found (Figure 25). Importantly, the solutions of both apolar solvents remained colourless after the exfoliation of **PyC-Zn2**. Further AFM studies should be performed toward a better analysis of the solvent and substrate effects.

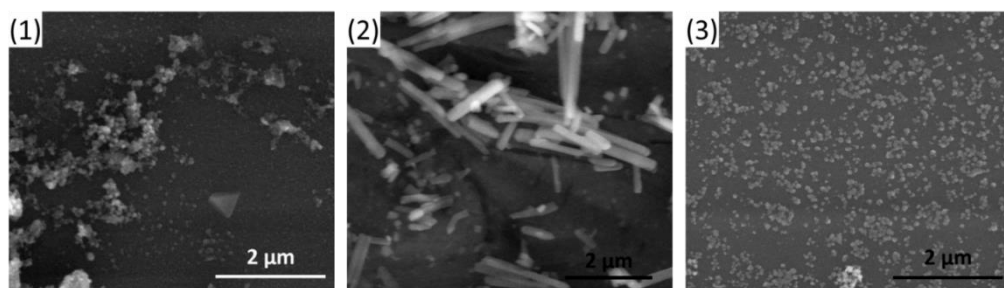


Figure 23. SEM images of **PyC-Zn2** exfoliated in H₂O on substrates of (1) silicon wafer, (2) mica and (3) HOPG.

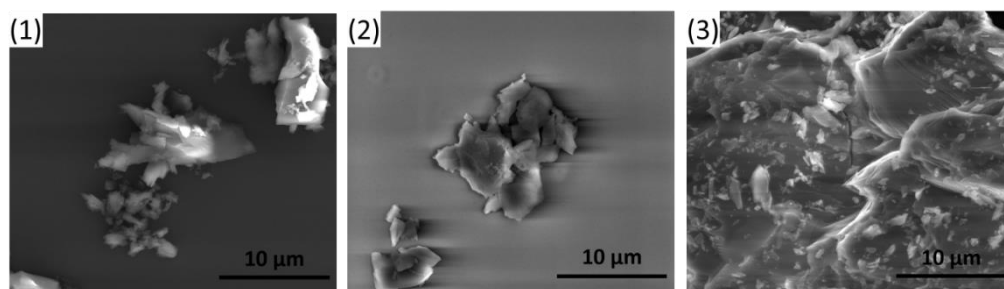


Figure 24. SEM images of **PyC-Zn2** exfoliated in chlorobenzene on substrates of (1) silicon wafer, (2) mica and (3) HOPG

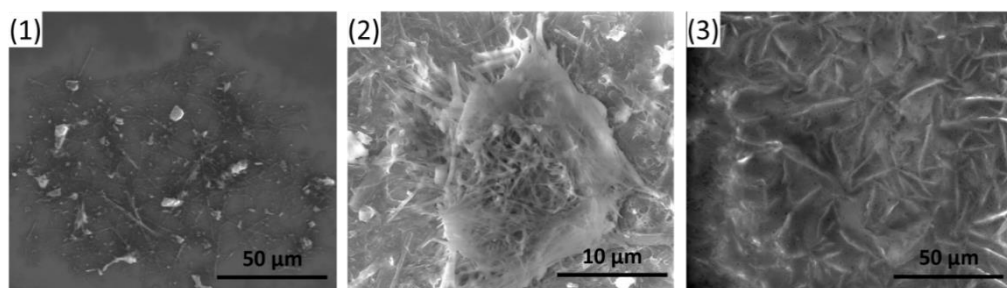


Figure 25. SEM images of **PyC-Zn2** exfoliated in hexane on substrates of (1) silicon wafer, (2) mica and (3) HOPG.

6.5 Conclusions

The free ligand **3Py-CCM** was used, for the first time, as a linker for the creation of coordination polymers. The molecule contains two pyridine groups at the sides of the molecule and one 1,3-diketone moieties in the middle of the conjugated skeleton providing a variety of possibilities towards coordination with metal centres and therefore assemblies. **PyC-Zn1** and **PyC-Zn2** have been achieved by using Zn(II) as the metallic source together with **3Py-CCM** as the linker. Both **PyC-Zn1** and **PyC-Zn2** have different structures demonstrating the versatility of the new ligand in coordination chemistry.

PyC-Zn1 can be described as a 1D coordination chain, which displays small loops. Coordination to the Zn ions is through one of the pyridine units and the β -diketone moiety. In the case of **PyC-Zn2**, it is a 2D network that possesses two different porous sizes; the conjugated sheets stacked layer by layer in a stable way.

A variety of analytical methods have been used toward the study of the exfoliation of the 2D network. The combination of SEM and AFM techniques provide valuable information about the effect of different solvents and surfaces. The ultrasonication process with acetone or apolar solvents, such as chlorobenzene and hexane, were found to be suitable.

Experimental Section:

Synthesis Methods.

1. 3Py-CCM

0.7 g of Acetylacetone (7 mmol) and 0.35 g of B₂O₃ (5 mmol) were dissolved in 8 mL of EtOAc. The reaction mixture was heated at 70 °C for 30 min until a white paste was formed. Then, a solution of 1.5 g of 3-pyridinecarboxyaldehyde (14 mmol) and 3.22 g of tributyl borate (14 mmol) in 3 mL of EtOAc was added. The mixture was stirred and refluxed (70 °C) for further 4 h. After cooling down, a solution of n-butylamine (0.4 mL, 4 mmol) in EtOAc (1 mL) was added dropwise, and the final reaction kept stirring at room temperature overnight. The reaction turned to a yellow colour with precipitate in next day. This suspension was filtered, washed with EtOAc and dried to afford a yellow solid. Then the solid was suspended in 30 mL of H₂O and stirred for 3 hours at room temperature, followed by filtering, washing process with H₂O and finally vacuum dried. The pure compound of 3Py-CCM was achieved by cooling down recrystallization from hot acetonitrile. Yield: 1.56g, 80%.

¹H NMR (400 MHz, DMSO-d₆) δ 15.96 (s, 1H), 8.91 (d, J = 1.7 Hz, 2H), 8.59 (dd, J = 4.8, 1.7 Hz, 2H), 8.19 (d, J = 8.0 Hz, 2H), 7.69 (d, J = 16.1 Hz, 2H), 7.48 (dd, J = 7.9, 4.8 Hz, 2H), 7.13 (d, J = 16.1 Hz, 2H), 6.22 (s, 1H). Elemental analysis (%) calculated for C₁₇H₁₄ N₂O₂ · 0.15 H₂O: C 72.66, H 5.13, N 9.97; found C 72.18, H 4.43, N 10.07. MALDI-MS m/z (%): 277.04 ([M-H]⁻), 279.03 ([M+H]⁺).

References:

- (1) Batten, S. R.; Champness, N. R.; Chen, X.-M.; Garcia-Martinez, J.; Kitagawa, S.; Öhrström, L.; O’Keeffe, M.; Suh, M. P.; Reedijk, J. *Pure and Applied Chemistry* **2013**, *85*, 1715.
- (2) Farha, O. K.; Yazaydin, A. Ö.; Eryazici, I.; Malliakas, C. D.; Hauser, B. G.; Kanatzidis, M. G.; Nguyen, S. T.; Snurr, R. Q.; Hupp, J. T. *Nature chemistry* **2010**, *2*, 944.
- (3) Chen, B.; Liang, C.; Yang, J.; Contreras, D. S.; Clancy, Y. L.; Lobkovsky, E. B.; Yaghi, O. M.; Dai, S. *Angewandte Chemie* **2006**, *118*, 1418.
- (4) Chughtai, A. H.; Ahmad, N.; Younus, H. A.; Laypkov, A.; Verpoort, F. *Chemical Society Reviews* **2015**, *44*, 6804.
- (5) Kreno, L. E.; Leong, K.; Farha, O. K.; Allendorf, M.; Van Duyne, R. P.; Hupp, J. T. *Chemical reviews* **2011**, *112*, 1105.
- (6) Horcajada, P.; Chalati, T.; Serre, C.; Gillet, B.; Sebrie, C.; Baati, T.; Eubank, J. F.; Heurtaux, D.; Clayette, P.; Kreuz, C. *Nature materials* **2010**, *9*, 172.

- (7) Giménez-Marqués, M.; Hidalgo, T.; Serre, C.; Horcajada, P. *Coordination Chemistry Reviews* **2016**, *307*, 342.
- (8) McKinlay, A. C.; Morris, R. E.; Horcajada, P.; Férey, G.; Gref, R.; Couvreur, P.; Serre, C. *Angewandte Chemie International Edition* **2010**, *49*, 6260.
- (9) Saravanan, K.; Nagarathinam, M.; Balaya, P.; Vittal, J. J. *Journal of Materials Chemistry* **2010**, *20*, 8329.
- (10) Sun, Y.-G.; Yu, W.; Wang, L.; Rong, S.-T.; Wu, Y.-L.; Ding, F.; Zhang, W.-Z.; Gao, E.-J. *Inorganic Chemistry Communications* **2010**, *13*, 479.
- (11) Wang, Z.; Liu, H.; Wang, S.; Rao, Z.; Yang, Y. *Sensors and Actuators B: Chemical* **2015**, *220*, 779.
- (12) Hwang, I. H.; Bae, J. M.; Kim, W.-S.; Jo, Y. D.; Kim, C.; Kim, Y.; Kim, S.-J.; Huh, S. *Dalton Transactions* **2012**, *41*, 12759.
- (13) Su, H.; Sun, F.; Jia, J.; He, H.; Wang, A.; Zhu, G. *Chemical Communications* **2015**, *51*, 5774.
- (14) Modrow, A.; Zargarani, D.; Herges, R.; Stock, N. *Dalton transactions* **2011**, *40*, 4217.
- (15) Vaidhyanathan, R.; Bradshaw, D.; Rebilly, J. N.; Barrio, J. P.; Gould, J. A.; Berry, N. G.; Rosseinsky, M. J. *Angewandte Chemie* **2006**, *118*, 6645.
- (16) Wanninger, S.; Lorenz, V.; Subhan, A.; Edelmann, F. T. *Chemical Society Reviews* **2015**, *44*, 4986.
- (17) Hussain, A.; Somyajit, K.; Banik, B.; Banerjee, S.; Nagaraju, G.; Chakravarty, A. R. *Dalton Transactions* **2013**, *42*, 182.
- (18) Shahabadi, N.; Falsafi, M.; Moghadam, N. H. *Journal of Photochemistry and Photobiology B: Biology* **2013**, *122*, 45.
- (19) Pabon, H. *Recueil des Travaux Chimiques des Pays-Bas* **1964**, *83*, 379.
- (20) Kondo, M.; Yoshitomi, T.; Matsuzaka, H.; Kitagawa, S.; Seki, K. *Angewandte Chemie International Edition* **1997**, *36*, 1725.
- (21) Barnett, S. A.; Champness, N. R. *Coordination chemistry reviews* **2003**, *246*, 145.
- (22) Ding, Y.; Chen, Y.-P.; Zhang, X.; Chen, L.; Dong, Z.; Jiang, H.-L.; Xu, H.; Zhou, H.-C. *Journal of the American Chemical Society* **2017**, *139*, 9136.
- (23) Amo-Ochoa, P.; Welte, L.; González-Prieto, R.; Miguel, P. J. S.; Gómez-García, C. J.; Mateo-Marti, E.; Delgado, S.; Gómez-Herrero, J.; Zamora, F. *Chemical Communications* **2010**, *46*, 3262.
- (24) Aliaga-Alcalde, N. r.; Rodríguez, L.; Ferbinteanu, M.; Höfer, P.; Weyhermüller, T. *Inorganic chemistry* **2011**, *51*, 864.
- (25) Zhong, Q.; Inniss, D.; Kjoller, K.; Elings, V. *Surface Science Letters* **1993**, *290*, L688.
- (26) Li, P.-Z.; Maeda, Y.; Xu, Q. *Chemical Communications* **2011**, *47*, 8436.
- (27) Beldon, P.; Tominaka, S.; Singh, P.; Dasgupta, T. S.; Bithell, E.; Cheetham, A. *Chemical Communications* **2014**, *50*, 3955.
- (28) Peng, Y.; Li, Y.; Ban, Y.; Jin, H.; Jiao, W.; Liu, X.; Yang, W. *Science* **2014**, *346*, 1356.
- (29) Foster, J. A.; Henke, S.; Schneemann, A.; Fischer, R. A.; Cheetham, A. K. *Chemical Communications* **2016**, *52*, 10474.
- (30) Xu, H.; Gao, J.; Qian, X.; Wang, J.; He, H.; Cui, Y.; Yang, Y.; Wang, Z.; Qian, G. *Journal of Materials Chemistry A* **2016**, *4*, 10900.

Chapter VII

Studies of porphyrin derivatives and
curcuminoids for single molecular
electronics experiments

7.1 Introduction

Porphyrin and curcuminoid molecules are promising building blocks for the construction of bio-inspired functional molecular devices.^{1,2} Both of them are well-defined conjugated systems that can contain aromatic groups and can be tuned chemically. Taking into account these features, they are particularly attractive in molecular electronics as candidates for the creation of stable and robust nanodevices. These systems present energy gaps that are in a realistic operational range,³ and indicate the oxidations and or reductions processes as other types of systems measured by the use of the MCBJ technique.⁴ Depending on the substituents attached to their conjugated cores (porphyrinic or CCMoid nature), the molecules can present lengths in the range of 1.5 to 2 nm (Figure 1). In addition, both types of ligands could bind most metal ions and non-metallic elements from the periodic table, which further could modulate the electronic and photonic properties of the final coordination compounds.^{5,6}

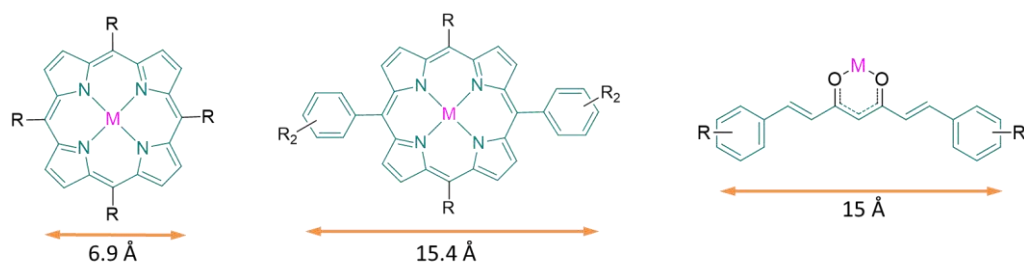


Figure 1. Conjugated system of porphyrin derivatives and CCMoids.

A critical point for an optimal electronic transport through a single-molecular junction is the electrodes–molecule interface. Therefore, depending on the nature of the electrodes, it is important to investigate reliable anchoring groups for the molecules to cleavage the electrodes.⁷ A number of anchoring groups have been investigated in the past using porphyrin derivatives and CCMoids systems for single molecular electronics applications, and the list of the groups that perform the best includes: amino (–NH₂),^{8,9} cyanide (–CN),¹⁰ thiophene,^{2,11} pyridyl (–PY),^{12,13} thiol (–SH),^{5,6,14} isothiocyanide (–SCN),¹⁵ methylthio (–SCH₃),¹⁶ hydroxyl (–OH),³ carbodithiolate,¹⁷ and thiochroman-based moieties.^{3,18} Sulphur-based groups (SR-) are some of the most frequently used because of their high affinity toward Au (surfaces, electrodes). The work presented here shows the studies in the field using porphyrin derivatives and CCMoids as main backbone/core structures with a range of different anchoring groups.

7.2 Objectives

This chapter is devoted to the design of new porphyrin derivatives containing SR- anchoring groups for their application in single molecular electronics together with the study of their electronic properties in solution and solid state. In addition, a family of CCMoids has also been

analysed in a similar manner as the porphyrin derivatives, with the aim of gathering information to improve their molecular design for electronic applications.

The porphyrin derivatives under study are depicted in Figure 2. As shown in the picture, the porphyrinic core is attached to two 3-thiophene (Figure 2, left) or methylthio (Figure 2, right) moieties (*meso*-positions) which function as terminal groups to anchor the molecule with gold electrodes. The two systems are named **th₂(^tBuph)₂P** and **MeS₂(^tBuph)₂P**, respectively. In **th₂(^tBuph)₂P**, 3-thiophene moieties were chosen because of their improvement on conductance with respect to 2-thiophene relatives.² On the other hand, thiophene-based molecules proved to be very promising toward the combination of electronic properties with optical or redox properties of porphyrin functional compounds.^{11,19-23} In both systems, the triple bond or phenyl, inserted between the porphyrin cores, were planned to increase conjugation and/or planarity of the molecules. The whole designed molecular system is symmetric containing in addition two benzyl tertbutyl branches (*meso*-positions). These bulky groups will suppress the possible aggregation of the molecules and will assist in the solubility of the final systems. These molecules were capable of locating a metal ion in the centre of the porphyrinic cavity with the aim of studying the effects of diamagnetic and paramagnetic centres. The last step hasn't been carried out due to the lack of time, however it is still mentioned here due to the possible repercussion on the final electronic properties.

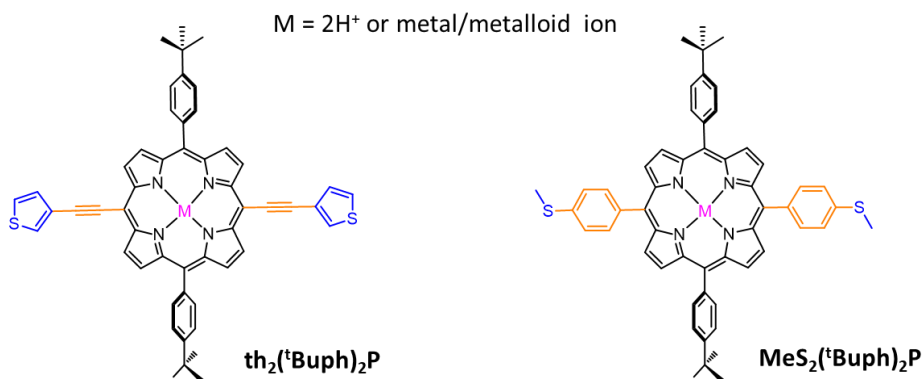


Figure 2. Designed porphyrin molecules.

CCMoids can be achieved at the gram scale from straightforward methodologies compared with porphyrin derivatives. Here, working together with the PhD candidate Álvaro Etcheverry from the group of Dr. M. Soler (Universidad de Chile), the electronic properties of a family of curcuminoids molecules (Figure 3) with SR- anchoring groups including methylthio, thiophene and thiocarbamate have been studied. The study also includes modifications of the 1,3-diketone moiety, by chelating or capping the upper part. In this way, boron and copper ions were used to coordinate the diketone part. In addition, the formation of heterocyclic aromatic rings (pyrazole and isoxazole) was also explored. To further analyse the electronic properties of such CCMoids, shorter molecules (acetylacetonate backbone, acac) and coordination compounds with such

ligands were prepared to gain insight on the effect of the molecular length in the electronic properties of the molecules.

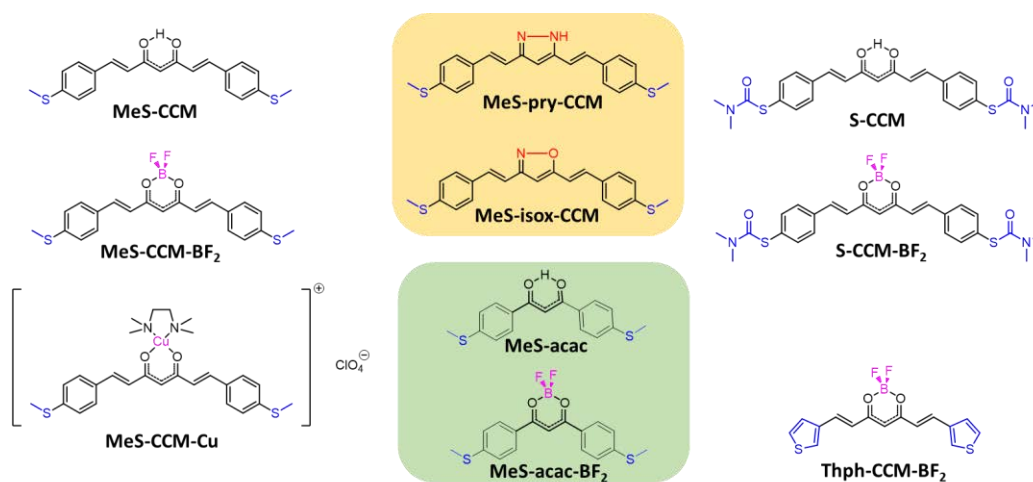
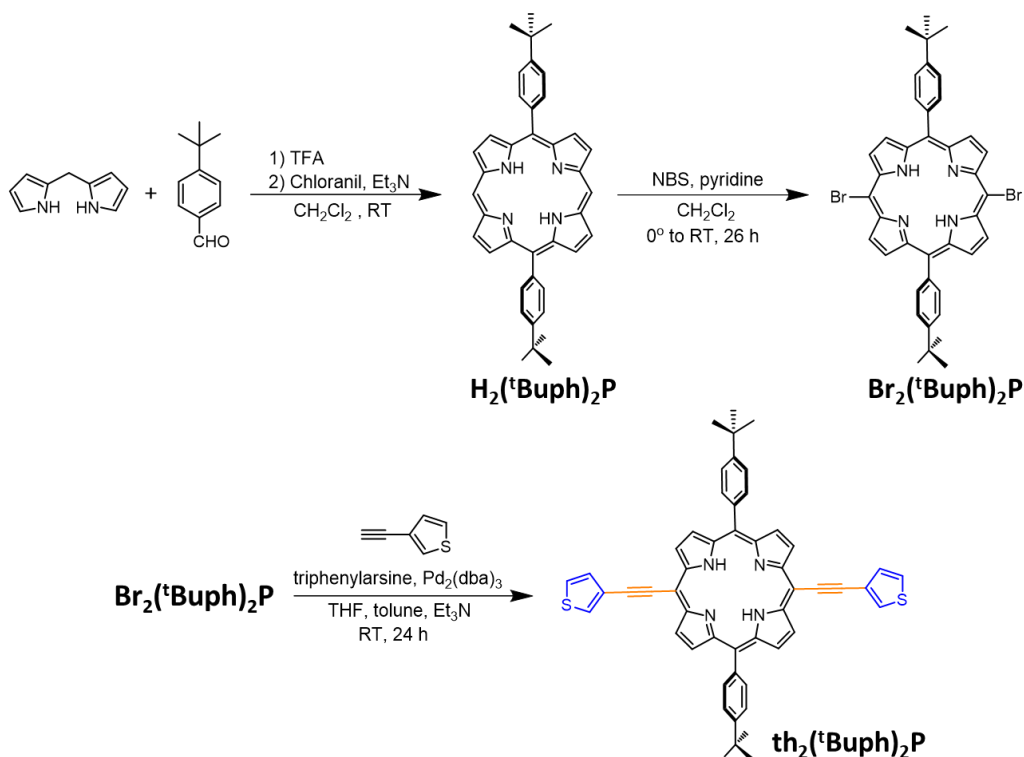


Figure 3. Designed CCMoids and analogues.

7.3 Synthesis

7.3.1 Synthesis of porphyrin **th₂(^tBuph)₂P**

In this work, *trans*-A₂B₂-porphyrin **th₂(^tBuph)₂P**, containing triple bonds or substituted phenyl units at two of the *meso*-positions, has been achieved following the synthetic route showed in Scheme 1. For the preparation of the desired porphyrin, the synthetic route was started with the addition of the benzyl tertbutyl branches following a “2+2” condensation procedure with the corresponding aldehyde and unsubstituted dipyrromethene. The reaction was performed as described in the Scheme 1 to afford A₂-porphyrin, **H₂(^tBuph)₂P**. Afterward, the bromination of **H₂(^tBuph)₂P** with N-bromosuccinimide (NBS) led to the corresponding bromoporphyrin, **Br₂(^tBuph)₂P**, then through a condensation reaction with 3-ethynylthiophene, provided the final compound, **th₂(^tBuph)₂P**.



Scheme 1. Synthesis of the **th₂(^tBuph)₂P** molecule.

5,15-bis(4-*tert*-butylphenyl)porphyrin, **H₂(^tBuph)₂P**, has been commonly used as a block unit to construct advanced A2BC-type or *trans*-A2B2 porphyrins, such as artificial metallo-DNAs.²⁴ Following the methods described by Yamada²⁴ and Handayani²⁵, **H₂(^tBuph)₂P** was prepared using the well-known Lindsey method, having the condensation of the 4-*tert*-butylbenzaldehyde with commercial available 2,2'-dipyrrromethane under mild conditions (yield: 24%). The bromination using *N*-bromosuccinimide (NBS) of **H₂(^tBuph)₂P** in the other two unsubstituted *meso*-positions of the porphyrinic core is a key step, where depending on the number of NBS equivalents it is possible to achieve the monobrominated or dibrominated versions. Hence, the intermediate molecule, 5,15-dibromo-porphyrin, **Br₂(^tBuph)₂P**, was obtained according to literature procedure^{24,26-28} with an excess of NBS (yield: 75%). In all the steps, after purification by chromatography, the formed porphyrins were fully characterized by ¹H NMR spectroscopy (Figure 4) and Maldi-TOF MS. The NH- of the free-based porphyrins located around -3 ppm and the absence of proton signals at 10.31 ppm after bromination, provide clear evidences of the achievement of the final systems.

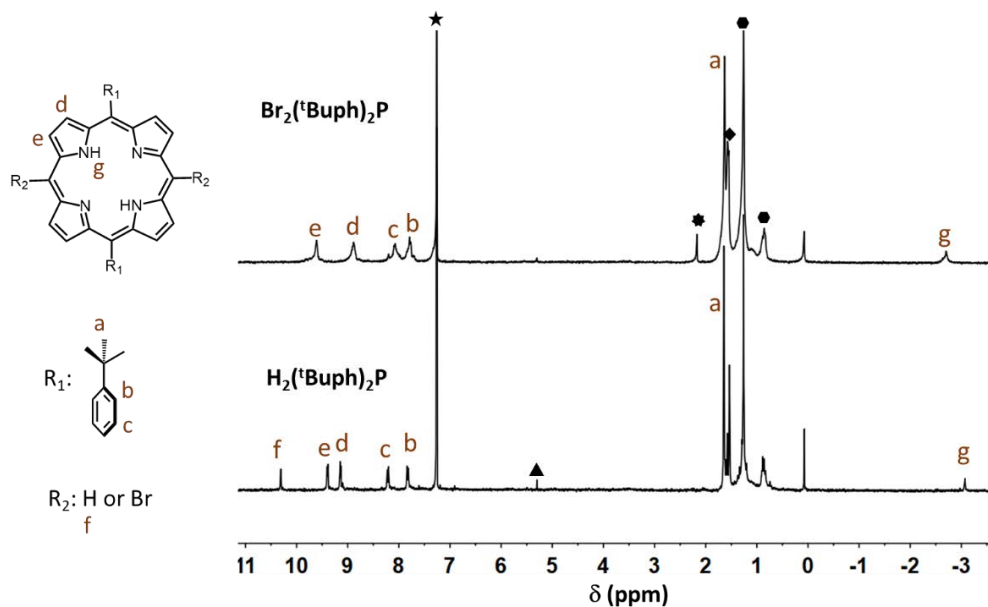


Figure 4. ^1H NMR of $\text{H}_2(\text{tBuph})_2\text{P}$ and $\text{Br}_2(\text{tBuph})_2\text{P}$ in CDCl_3 . ★ Solvent CDCl_3 , ▲ CH_2Cl_2 , ★ acetone, ◆ H_2O , ● n-hexane.

Regarding the final structure, the thiophene rings may not be coplanar within the porphyrin plane, having the freedom of rotating. Thus, the insertion of a triple bond as spacer group seemed to be advantageous, increasing conjugation and inducing planarity.²⁹ The final molecule, **th₂(tBuph)₂P**, was obtained following Sonogashira reaction,³⁰ which allows the direct cross-coupling of terminal alkynes with aryl halides catalyzed by tris(dibenzylideneacetone) dipalladium(0) ($\text{Pd}_2(\text{dba})_3$) and triphenylarsine (AsPh_3).^{22,27,31} To improve the purification process from reported porphyrins,²⁷ the crude mixture was filtered through celite to remove the residual AsPh_3 and $\text{Pd}_2(\text{dba})_3$ first. In addition, taking advantage of the high solubility of the crude in CH_2Cl_2 , a mixture of n-hexane/ CH_2Cl_2 (200:100 ml) was used as eluent in the silica gel chromatography. The crude was well separated in the column and the colour of the collecting solution changed from red to green and then to yellow (Figure 5a). Through the analysis of each coloured solid, the desired system was identified in the green area. For purification, thin layer chromatography plates were also used, being possible the identification of each part (Figure 5b). At the final step, a careful wash of the compound with ethanol, to remove the dibenzylideneacetone produced from $\text{Pd}_2(\text{dba})_3$, provided the pure product (24 mg, 51 %).

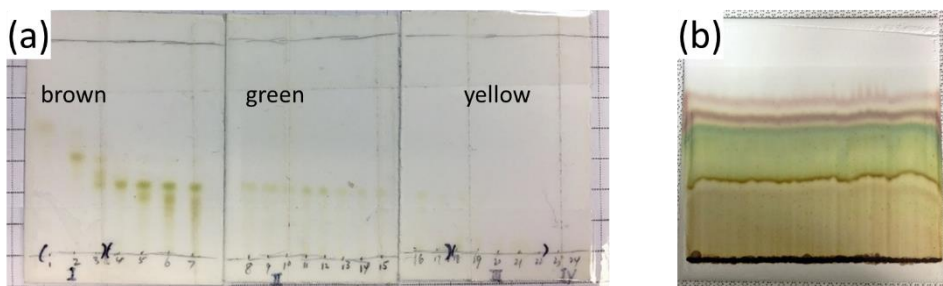


Figure 5. Illustration of the products collected (a) from column chromatography, (b) on thin layer chromatography plate.

The ^1H NMR spectra shown in Figure 6 demonstrates the availability of the purification method used for the final compound $\text{th}_2(\text{tBuph})_2\text{P}$. As expected, most of the proton signals were in the region from 9.7 to 7.5 ppm.

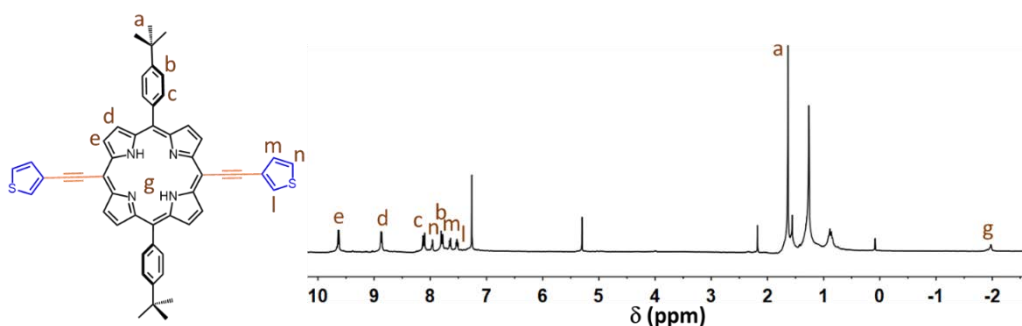
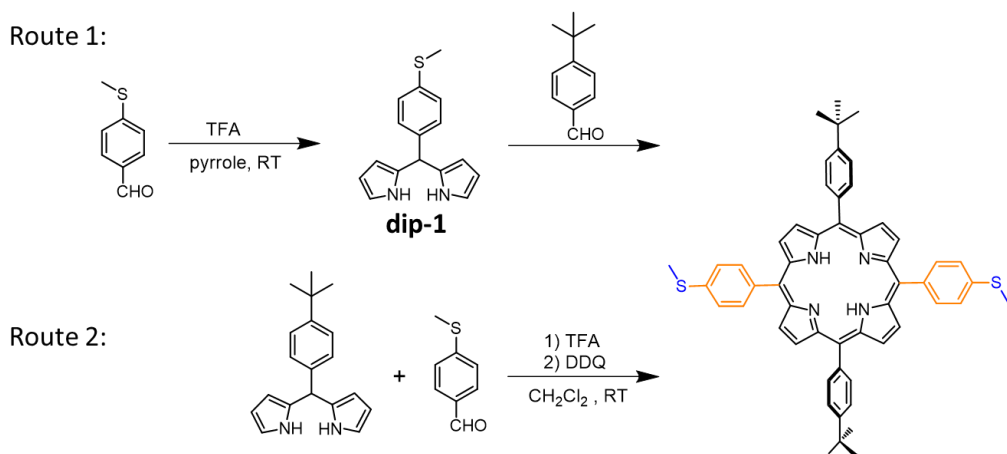


Figure 6. ^1H NMR spectrum of $\text{th}_2(\text{tBuph})_2\text{P}$ in CDCl_3 at 20°C . Other peaks are from solvents indicated in Figure 4.

7.3.2 Synthesis of $(\text{MeS})_2(\text{tBuph})_2\text{P}$

As it was mentioned above, the second porphyrinic system under study was $(\text{MeS})_2(\text{tBuph})_2\text{P}$, which is with phenyl methylthio units. It was expected to be synthesized via two conceivable pathways showed in Scheme 2. Our first attempt involved the reaction of 4-(methylthio) benzaldehyde with pyrrole units to give the corresponding 5-(4-Methylthiophenyl)dipyrromethane (**dip-1**), followed by the addition of tert-butylbenzaldehyde. The other attempt involved the direct reaction of the commercially available tert-butylphenyldipyrrolemethane with methylthiobenzaldehyde.



Scheme 2. Proposed synthetic routes for $(\text{MeS})_2(\text{t}^{\text{Buph}})_2\text{P}$.

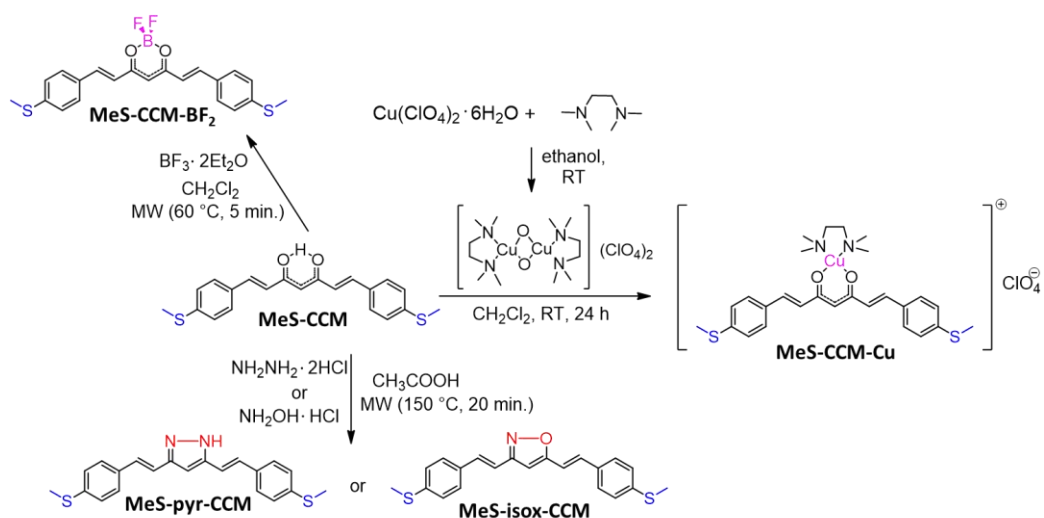
Regarding the first methodology, the possibility of synthesizing $(\text{MeS})_2(\text{t}^{\text{Buph}})_2\text{P}$ through this route was abandoned due to the unsuccessful achievement of pure 5-(4-Methylthiophenyl)dipyrromethane (**Dip-1**), even though the one-flask synthesis of dipyrromethanes has been reported before, in which an aldehyde was dissolved in a 40-fold excess of pyrrole with a catalytic amount of an acid at room temperature in the absence of any other solvent.³²⁻⁴¹ The main obtained product in our reaction was probably of dipyrromethane nature, tripyrrane or related polymers. **Dip 1** was not achieved by direct crystallization from the reaction mixture after removing the excess of pyrrole, and flash chromatography purification on silica was considered toward such goal.³³ For that, mildly basic media (cyclohexane or hexane : ethyl acetate : Et_3N = 80 : 20 : 1) was used, to prevent decomposition of the dipyrromethane on slightly acidic silica columns. Unfortunately, none of the efforts provided separation of the desired system.

Hence, according to the literature procedure,^{34,35} the second route toward the design of $(\text{MeS})_2(\text{t}^{\text{Buph}})_2\text{P}$ was tried, via the condensation of commercial dipyrromethane derivative 4-tert-butylphenyldipyrromethane with the 4-methylthiobenzaldehyde, using the Lindsey method described before. Purification was achieved with a considerable high number of chromatographic circles. The final system was achieved but in a low yield (< 2%), still containing some by-products from the reaction (Figure A7.1).

7.3.3 Characterization of SR-CCMoids

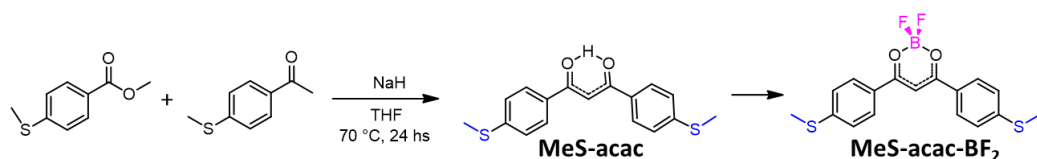
Scheme 3 shows the ligand **MeS-CCM** and all the reactions performed toward the achievement of derivatives, including coordination and capping of the β -diketone moiety through with diverse groups. As it was mentioned above, these compounds were synthesized by Álvaro Etcheverry. As other symmetric CCMoids, **MeS-CCM** was synthesized by the classic method developed by H. J. J. Pabon.³⁶ In this way, **MeS-CCM** was prepared from the mixing of 4-

(methylthio)benzaldehyde and acetylacetone in the presence of B_2O_3 , butyl borate and butylamine. The BF_2 -compound **MeS-CCM-BF₂** was produced from the free ligand by the addition of borontrifluoride diethyletherate in CH_2Cl_2 .³⁷ In the synthesis of **MeS-CCM-Cu**, a hydroxyl-bridged binuclear Cu compound³⁸ was formed at first and then chelated with the free ligand under mild conditions. The pyrazole and isoxazole derivatives, **MeS-pyr-CCM** and **MeS-isox-CCM**, were synthesized by modifying the method of Changtam,³⁹ using a microwave reactor for decreasing the reaction time, the amount of solvent and improving the yields.



Scheme 3. Reagents and conditions for the preparation of **MeS-CCM** analogues.

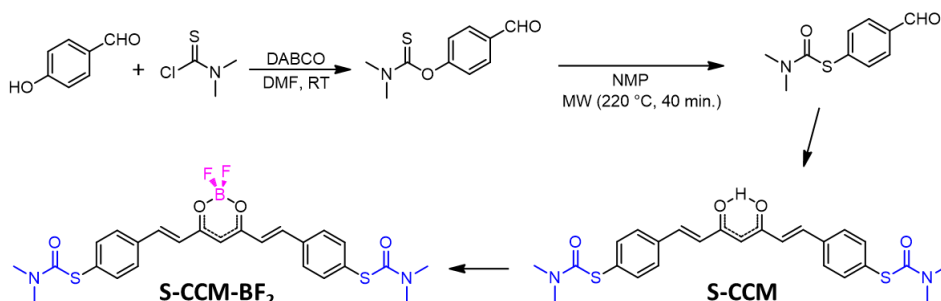
Following the procedure for the synthesis of β -ketoester,⁴⁰ yellow crystalline **MeS-acac** was condensed from the reaction of methyl 4-(methylthio)benzoate and 4-(methylthio)acetophenone in anhydrous alkaline THF solution under reflux (Scheme 4). And the BF_2 -compound, **MeS-acac-BF₂**, was achieved by using the same method described for CCMoid boron compounds.



Scheme 4. Condensation for synthesis of **MeS-acac**.

For the CCMoids **S-CCM**, the required aldehyde has been prepared following the literature.⁴¹ The (O-(4-formylphenyl) dimethylcarbamothioate) was synthesized from

hydroxybenzaldehyde and dimethyl thiocarbamoyl chloride, then the compound was transferred to (S-(4-formylphenyl) dimethylcarbamothioate) through Newman-Kwart rearrangement reaction after the microwave irradiation at a temperature of 220 °C for 40 min. **S-CCM** and **S-CCM-BF₂** were achieved by the general synthesis methods for CCMoids (Scheme 5).



Scheme 5. Synthesis of **S-CCM**.

7.4 MCBJ experiments with th₂(^tBuph)₂P

7.4.1 Redox properties of th₂(^tBuph)₂P

The reduction–oxidation processes of molecules can be related to the HOMO-LUMO energy gap of the systems and this is important for the later attachment of the molecule to the electrodes, where such energy will vary when cleavage with the gold electrodes happens. If the energy of the molecule is far away from the Fermi level of the electrode, charge carrier transport may be not effective or even impossible to happen. There is still no direct correlation of the HOMO-LUMO gap from the free molecule and the final conductance once the molecule connects to the electrodes and further studies must be performed to gather information toward such point. Porphyrin derivatives have been studied extensively for the application as component units in molecular electronics.^{42,43} In this work, the redox properties of porphyrins were studied by cyclic voltammetry (CV) and differential pulse voltammetry (DPV), which were performed to estimate the values of the highest occupied molecular orbital (HOMO) and the lowest unoccupied molecular orbital (LUMO) energy levels of our systems.

Figure 7 shows the CV and DPV of a solution 0.5 mM of th₂(^tBuph)₂P in CH₂Cl₂ containing 0.1 M of TBAPF₆ as electrolyte. All the potentials are vs. Fc/Fc⁺, used here as internal reference. The CV results exhibit two close irreversible oxidations in the +0.1 to +1.0 V range, related to the thiophen groups, showing features that are similar to other thiophene species reported in the literature.^{44,45} The possible reversibility of the first reduction process was further analysed by the methods of peak separation potential (26 mV) and current ratios ($i_{p,r}/i_{p,f} = 0.4$). Therefore, two irreversible oxidations and one possible quasi-reversible reductions followed by an irreversible reduction under such conditions could be identified.

A closer look at the DPV data presents the first oxidation and reduction of $\text{th}_2(\text{tBuph})_2\text{P}$ processes at +0.28 and -1.34 V, respectively referred vs. Fc/Fc^+ . As a result, the corresponding HOMO and LUMO energy levels are -5.08 and -3.46 eV for $\text{th}_2(\text{tBuph})_2\text{P}$ according to the calculation (they appear described in the Appendix). Hence, the electrochemical band gaps E_g^{ec} is 1.62 eV. This indicates the semiconductor nature of the molecule, as it can be seen in others small molecules and even polymers.^{46,47}

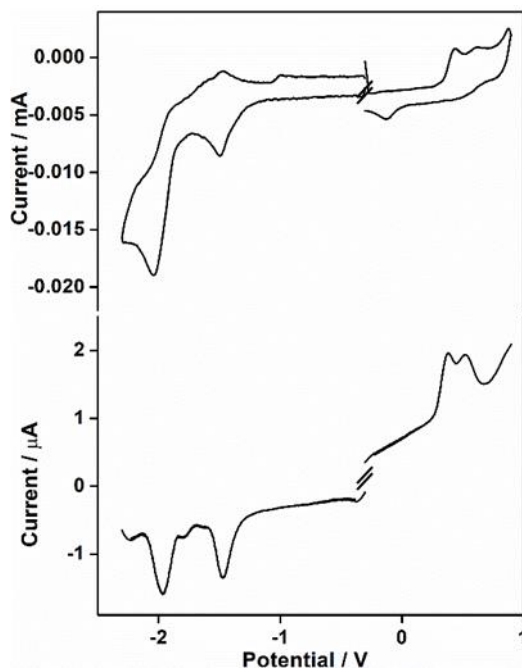


Figure 7. Cyclic voltammograms (CV) (top) and differential pulse voltammograms (DPV) (bottom) of $\text{th}_2(\text{tBuph})_2\text{P}$. Potentials vs. Fc/Fc^+ .

7.4.2 Single-molecule break-junction experiments of $\text{th}_2(\text{tBuph})_2\text{P}$

The transport properties of $\text{th}_2(\text{tBuph})_2\text{P}$ were studied by using MCBJ technique. Such experiments were performed by the group of Dr. Diana Dulić from the Universidad de Chile. In all cases, $\text{th}_2(\text{tBuph})_2\text{P}$ was dissolved in CH_2Cl_2 (10^{-4} μM) and deposited on the unbroken electrodes by drop casting before the measurements. Two thiophene groups on opposite sides of the molecule will be the anchoring groups (Figure 9). After the deposition, the junctions are broken at ambient conditions.

Before performing experiments with $\text{th}_2(\text{tBuph})_2\text{P}$, blanks of the nanodevice were accomplished where the gold electrode was cleaned with plasma ozone firstly (Figure A7.2). After the addition of the drop containing our molecule, the tunnel current became wider than in the blanks but did not show conductance peaks even when the V_{bias} and piezo speed varied

(Figure 8). An extra device, which bare gold without ozone cleaning treatment, displayed histograms that show the same behaviour after the molecule was deposited (Figure A7.3). Therefore, it was concluded that our molecule did not provide right contacts with the gold electrodes and conductance values were impossible to be measured. This result was related to the 3-thiophene groups and probably as well to the bulky aromatic groups at the opposite sides.

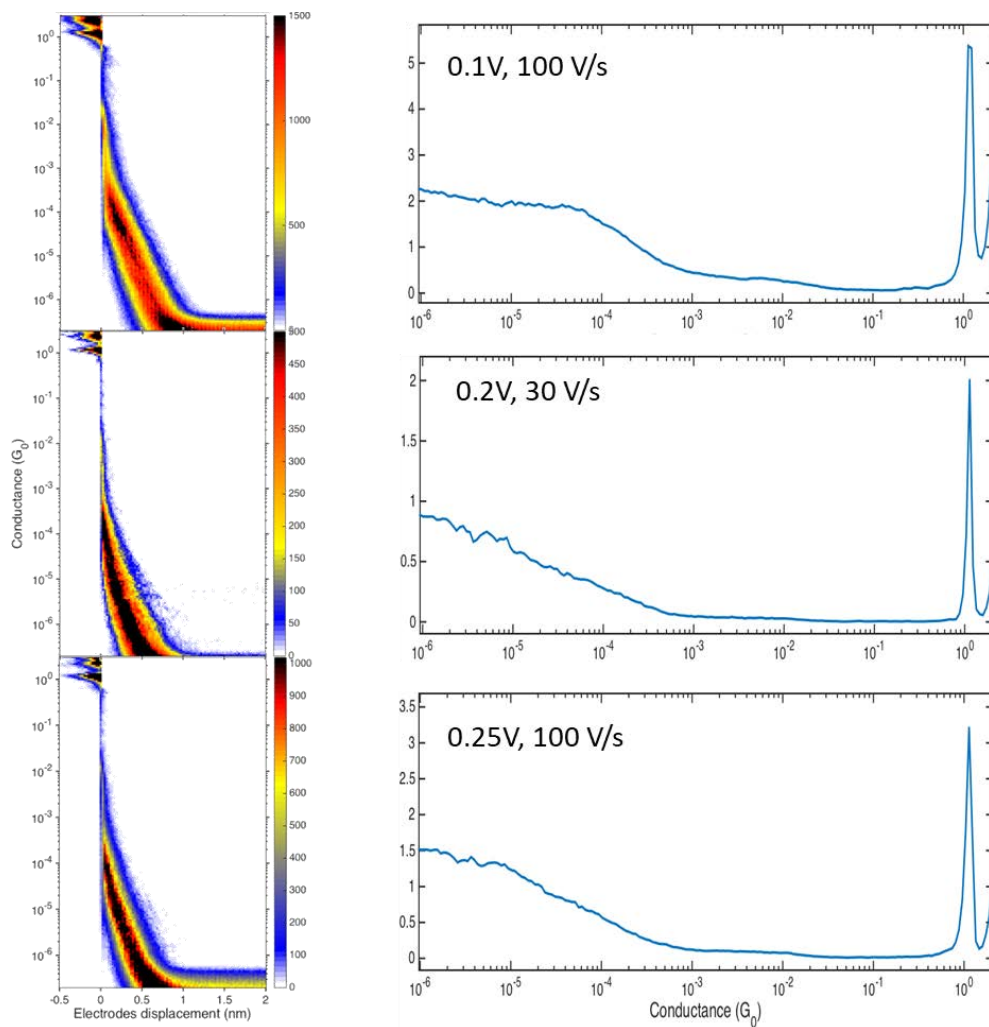


Figure 8. Conductance measurements of $\text{th}_2(\text{'Buph})_2\text{P}$ employing a MCBJ recorded with different V_{bias} and piezo speed. Conductance-distance traces (left) and 1D conductance histograms (right).

If the molecule would be sandwiched between both gold electrodes, a plateau would appear as a step shape in the 2D histograms. In our case, none of the trace histograms obtained for junction exposed to this molecule show such horizontal features, being impossible to distinguish signals different from the blank in the conductance histograms. This fact indicates a very low

probability of trapping one molecule between the electrodes that form the junction. Leaving the unsuccessful results aside, reasonable explanations toward such facts were searched. In this case, two possible answers were provided.

From a structural point of view, the molecule can be seen as a core with branches along the *meso*-positions in two axes. Unlike the other porphyrin-oligothiophenes,²¹⁻²³ in **th₂(^tBuph)₂P** the both types of branches, yet different, have similar length and rigidity. As reported in the literature,⁴⁸ steric hindrances can affect the trapping of the molecule in great manner and this would result in poor stability. As Figure 9 shows, this may lead to the dramatic reduction of suitable orientations for the molecule to approach the electrodes in an effective way.

Another reason could be the labile bond between the thiophene sulphur atoms and the gold atoms. Thiophene was chosen as a terminal group because of the previous experience in the group with a related CCMoid system (lineal conjugated system with thiophene groups on the sites of the diarylheptanoid skeleton) with successful results regarding MCBJ measurements.² Nevertheless, the coordination interaction here between the sulfur atoms and the gold electrodes is not as strong as expected, affecting the final measurements.

Considering the final results and the possible explanations toward the lack of conductance, the removal of the bulky *tert*-butyl branches would be a possibility toward a better design of the molecule. This group meant to avoid π - π stacking of porphyrin macrocycle by the steric hindrance, and to improve solubility, demonstrated in other similar porphyrin molecules with much longer alkyl chain.^{3,6,18} Another important change in the design would be the replacement of the anchoring groups, for instance, by methylthio groups.¹⁷

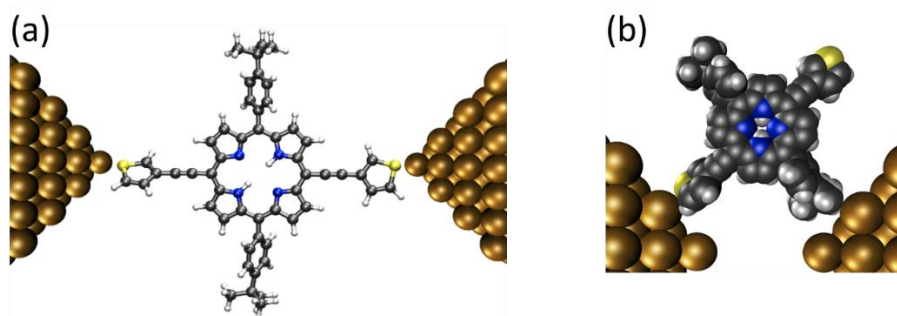


Figure 9. Sketches representing the different trapping probabilities shown by the **th₂(^tBuph)₂P**.

7.5 Electron transport studies with CCMoids

7.5.1 Single-molecule measurement MCBJ experiments on CCMoids

Measurements for all the CCMoids and related molecules depicted in Figures 3 and Schemes 3-5 were performed using CH_2Cl_2 and by means of the MCBJ method at ambient conditions. In parallel, two research groups worked with the same molecules to achieve better statistical analyses: the group mentioned before led by Dr. Diana Dulić and the group of Prof. H. S. J. van der Zant in TUDelft. Figure 10 displays six 2D-histograms of the CCMoid bearing different anchor groups introduced in Figure 3. Comparing the conductance vs. displacement histograms, a characteristic feature is the difference in the plateau length depending on the designed anchor groups. The order of plateau length is thiophene < methyl sulfide < thiocarbamate, indicating the thiocarbamate is most stable being as the anchor while thiophene the weakest. This corroborates one of our hypothesis in the previous porphyrin studies.

A closer look of the two-dimensional histograms shows that **MeS-CCM-BF₂** (Figure 10b) has a broad molecular feature that extends from zero displacement to the breaking point, corresponding to a double-peak structure in the conductance distribution of this molecule in one-dimensional conductance histograms (Figure 11b). This unique feature only appeared in the case of the **MeS-CCM-BF₂** system, and it was not observed in the rest of CCMoids even after the application of different bias voltages. In the case of the analogous shorter molecules, **MeS-acac** and its BF₂- compound **MeS-acac-BF₂**, only the second one presents again double peaks with conductance distributions similar to **MeS-CCM-BF₂** (Figure 12). Double-peaks also appear in the conductance histograms of pyrazole and isoxazole derivatives, **MeS-pyr-CCM** and **MeS-isox-CCM** (Figure 12); however, the mechanism is different. In this case, it is found that the pyrazole and isoxazole groups can provide an additional anchoring for the molecules, resulting in the different paths for their electrons transfer and having clearly higher conductance values.

Regarding the observation of two peaks on the BF₂- compounds, such phenomenon was connected with the existence of MeS- and BF₂- groups at the same time. Theoretical calculations have shown the relation between them, which is related to the difference in the dipolar moment of the molecule once connected to the gold electrodes. The dipolar moment of the molecule may affect the conductance and can vary the rotation of the methyl groups of the anchoring group. The different dispositions of those may provide the dual conductance.

Taking into account that the double peaks can interconvert depending on the voltage for the **MeS-CCM-BF₂** and **MeS-acac-BF₂** molecules, further analyses of the electronic properties of these molecules were performed from a chemical point of view by means of CV in CH_2Cl_2 and UV-Vis absorption spectra in the solid state.

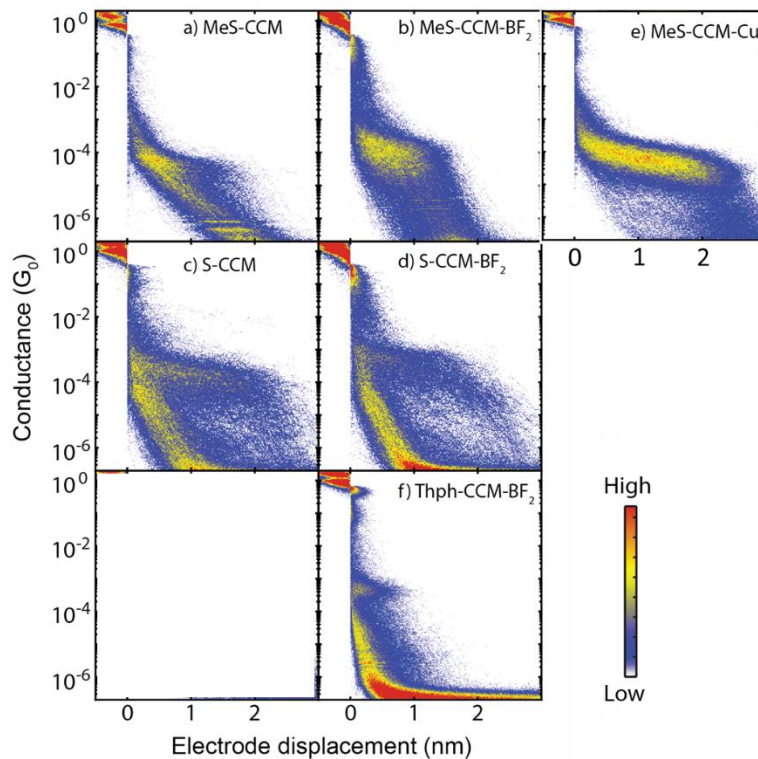


Figure 10. 2D conductance vs. displacement histograms of the full data sets of a representative sample of a) **MeS-CCM**, b) **MeS-CCM-BF₂**, c) **S-CCM**, d) **S-CCM-BF₂**, e) **MeS-CCM-Cu** and f) **Thph-CCM-BF₂**.

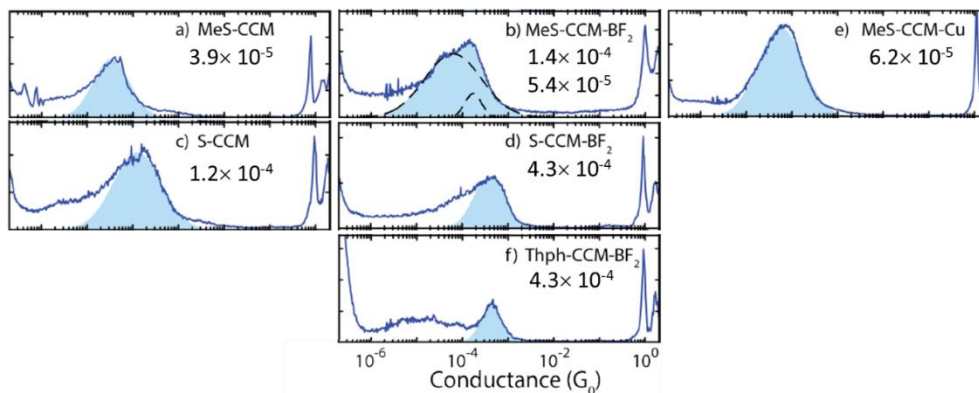


Figure 11. 1D conductance histograms and the most probable conductance value of the CCMoids: a) **MeS-CCM**, b) **MeS-CCM-BF₂**, c) **S-CCM**, d) **S-CCM-BF₂**, e) **MeS-CCM-Cu** and f) **Thph-CCM-BF₂**.

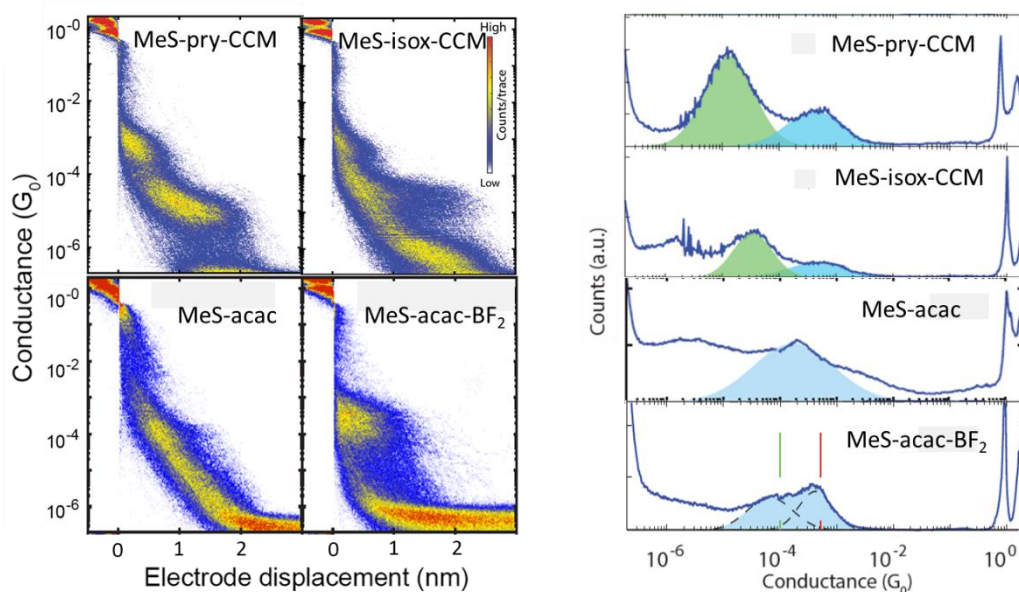


Figure 12. 2D conductance vs. displacement histograms (left) and One-dimensional conductance histograms (right) of **MeS-pyr-CCM**, **MeS-iso-CCM**, **MeS-CCM** and **MeS-CCM-BF₂**.

7.5.2 Stability of boron compounds

Borontrifluoride has been used to coordinate CCMoids by the β -diketone moiety group,⁴⁹ but this binding can be broken under certain conditions such as microwave irradiation in aqueous methanol.⁵⁰ Here, the stability of the BF₂- molecules in solution was tested to ensure their robustness in CH₂Cl₂ before their addition to the break junction. In this case, the three BF₂-compounds under study: **MeS-CCM-BF₂**, **S-CCM-BF₂** and **Thph-CCM-BF₂** were dissolved in dichloromethane-d₂ (CD₂Cl₂) with the controlled concentrations as well (5 mM in all cases). ¹H MNR were performed periodically every 24 hours for a total of five days. This is taking into account that once the drop was added then the MCBJ experiments would be taken at least three days. The ¹H NMR spectra of **MeS-CCM-BF₂** and **Thph-CCM-BF₂** are shown in Figure 13 and Figure A7.4(b) respectively. In both cases the signals observed correspond exclusively to the initial compounds, demonstrating the stability of the molecules in CD₂Cl₂ at room temperature. However, **S-CCM-BF₂** (shown in Figure A7.4(a)) displayed small peaks from the free ligand, showing that the system is less stable than the formers. In addition, when varying the temperature from R.T. to -90°C, the ¹H MNR (Figure A7.5) of **MeS-CCM-BF₂** did not present shifts or extra peaks, indicating the stability also of the configuration. Experiments of **MeS-CCM-BF₂** using DMSO-d₆ show that the unbinding is solvent dependent, presenting signals from the free ligand after time at ambient conditions. MCBJ experiments were performed exclusively in CH₂Cl₂ no longer than three days.

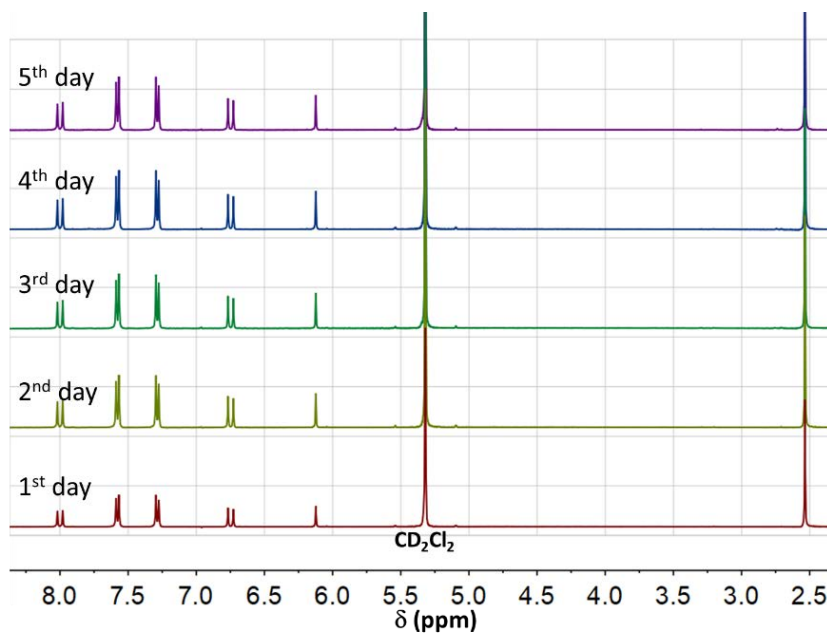


Figure 13. ^1H NMR spectrum of the **MeS-CCM-BF₂** in CD_2Cl_2 at room temperature with days.

7.5.3 Solid state UV-Vis absorption studies of CCMoids

By the use of solid-state UV-Vis absorption spectroscopy is possible to obtain the gap between the HOMO and the LUMO energy in molecules and polymers. In our case, diffuse reflectance technique was used to analyse the samples. For an isolated conjugated system with aromatic groups, one of the structural factors which define HOMO and LUMO energies is the introduction of different substituents.⁵¹ Here, to facilitate the discussion of the results obtained, the CCMoid systems are divided into two groups: (A) CCMoids with different anchoring groups and (B) CCMoids and acac derivatives (**MeS-acac** and **MeS-acac-BF₂**) that contain methylthio substituents. The limited amount achieved for the pyrazole and isoxazole derivatives, **MeS-pyr-CCM** and **MeS-isox-CCM**, restricted their measurements. Figure 14 displays the diffuse reflectance spectra of the rest of compounds. Then, by using the graphical method described in the Appendix, it was possible to determine the band gap for all the compounds by taking the crossed point between the lines obtained by the extrapolation of the long-wavelength edges of the absorbance bands with the horizontal ground lines.⁵² These results are summarized in the Table 1.

As in the case of the porphyrin molecule, the gaps found are of the order of 1.9 to 2.6 eV, displaying a semiconductor nature for all of them. In all the compounds, a pronounced bathochromic shift is observed (between 100 and 200 nm difference) for pairs **MeS-CCM/MeS-CCM-BF₂**, **S-CCM/S-CCM-BF₂** and **MeS-acac/MeS-acac-BF₂** and therefore it was expected that the BF₂- compounds present smaller band gaps when compare them with their respective free

ligands. It has been established that the incorporation of the BF_2 - group assist in the electronic delocalization by charge transfer from the major aromatic donor groups to the difluoroboron β -diketone acceptor,⁵³ resulting in the decrease of the energy difference between the HOMO and LUMO. This is corroborated in all the compounds under study. In addition, **MeS-CCM-Cu** shows the lowest band gap, probably due to coordination and to the factor that is the only compound charged among the ones under study.

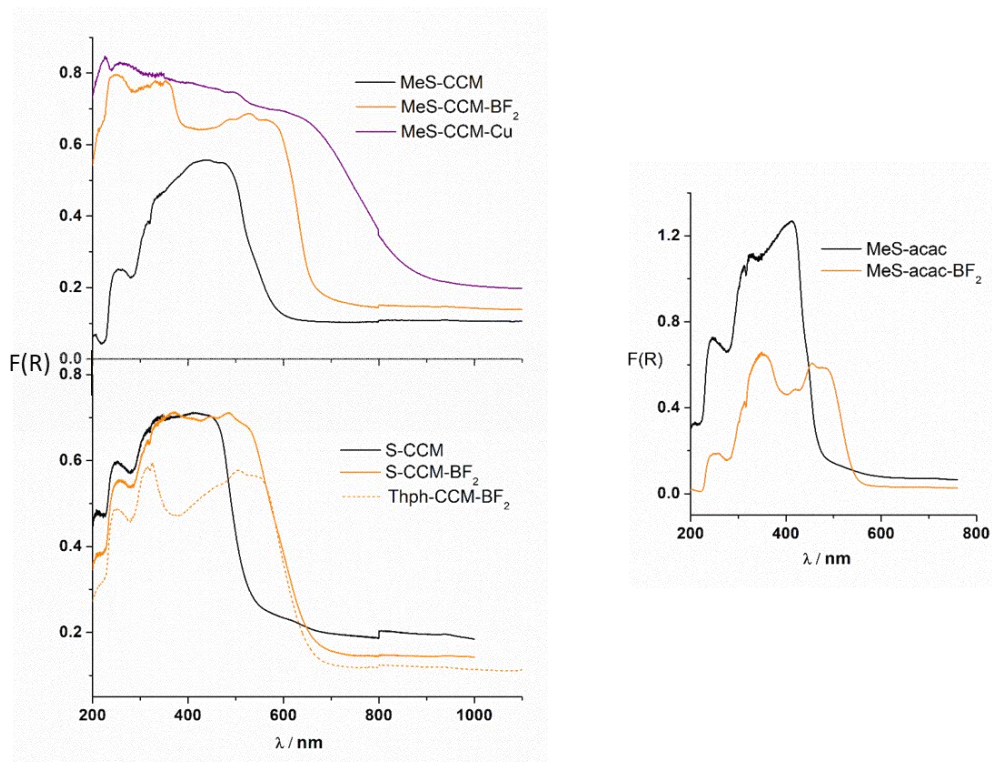


Figure 14. Diffuse reflectance spectra of the compounds.

Table 1. Band gap energy values and wavelengths from diffuse reflectance measurements.

	MeS-CCM	MeS-CCM- BF_2	MeS-CCM-Cu	S-CCM	S-CCM- BF_2	Thph-CCM- BF_2	MeS-acac	MeS-acac- BF_2
λ / nm	577	661	859	529	657	641	470	544
E_g^{op} (eV) solid	2.15	1.88	1.44	2.34	1.89	1.93	2.64	2.28

7.5.4 CV and DPV measurements of CCMoids

As mentioned before in this chapter, both cyclic voltammetry (CV) and differential pulse voltammetry (DPV) allows us to analyse the redox properties of the studied compounds, thus estimate the energies of the HOMO and of the LUMO. Figure 15 shows the curves for all the compounds with MeS- anchoring groups; the rest of systems are displayed in Figure A7.6. For a donor group, such is methylthio, the oxidation and reduction potentials are significantly affected by the nature of the binding of the β -diketone. The BF₂-compounds have the similar behaviour with previous reports,⁵⁴ that the first oxidation can be attributed to the electron donor moiety MeS- while the first reduction corresponds to the acceptor moiety, in this case the boron ring formed with the β -diketone moiety. The cyclic voltammograms for the electrochemical reduction of the studied copper-CCMoid exhibit small waves in the range of 0 to -2 V, which can be attributed to the reduction of the amine group from the second chelating ligand.⁵⁵ In the case of pyrazole and isoxazole derivatives, which are also the donor groups, the reduction potentials are very low and difficult to be observed under the tested conditions.

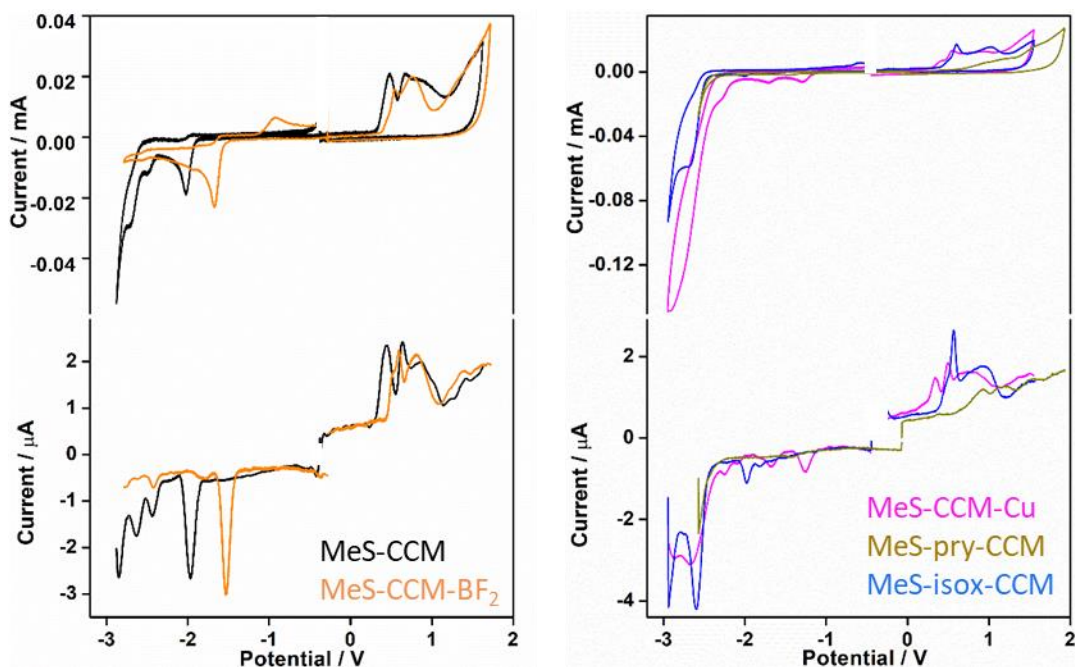


Figure 15. Cyclic voltammograms (CV) and differential pulse voltammograms (DPV) of compounds with methyl sulfide anchor groups. Potentials vs. Fc/Fc⁺.

The HOMO and LUMO obtained from electrochemical potentials of the first oxidation and reduction of the compounds were determined in CH₂Cl₂ and the data are presented in Figure 16 and Table A7.1 (vs. ferrocene/ferrocenium). The band gaps calculated from the electrochemical measurement match well with the values obtained from diffuse reflectance spectra.

At this point, it is impossible to clearly observe a correlation between the conductance values found in the single molecule MCBJ experiments and the energy gaps of them before anchoring the gold electrodes. When exclusively compared the molecules with the same anchoring groups (MeS-), it is possible to see that the LUMO is the one modified the most with respect to the HOMO values. However, most of the molecules provide similar conductance values, therefore it is supposed that the conductance may be through the HOMO orbitals, similar for all of them.

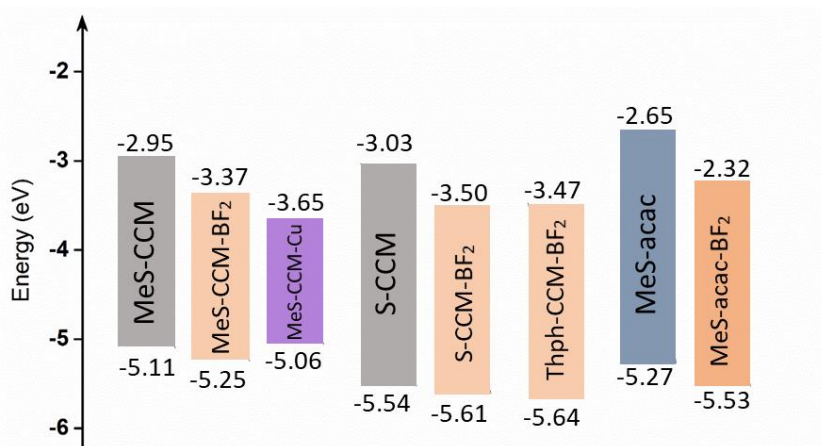


Figure 16. Frontier orbital values for the studied system.

7.6 Conclusions

Two porphyrin derivatives, **th₂(^tBuph)₂P** and **MeS₂(^tBuph)₂P**, were designed and synthesized, and characterization measured by MCBJ technique has been done with the first one containing thiophene anchoring groups. Taking into account all the intermediated systems and purification steps, the overall yield of the global reaction was approximately 5 %. Further studies regarding coordination were not pursued due to the low amount of compound achieved. The MCBJ experiments did not show distinctive signals from the blank probably because of the poor capacity of the thiophene groups to coordinate gold and the negative effect of the bulky groups at the opposite sites of the former. For that reason, a second porphyrin derivative was designed, this time containing MeS- groups at the sites to cleavage the gold electrodes. Unfortunately, it was impossible to get the compound pure and the quantities achieved in the final step were very low.

On the other hand, the physicochemical properties of a series of CCMoids involving a variety of anchoring groups have been studied by means of CV, DPV and solid-state UV-Vis absorption spectroscopies. This family includes coordination compounds of some of the free ligands attached to boron and copper ions. The electronic properties of these molecules were of interest because the MCBJ experiments show that the most part of these compounds exhibit stable molecular junctions and statistical analyses of the data were possible. Electrochemical

experiments (CV and DPV) of the CCMoids systems were performed towards the calculation of their HOMO-LUMO energy gaps. Here our aim was to achieve further information that would allow the design of molecules with improved electronic properties, which would be analysed later by MCBJ technique. Overall, HOMO and LUMO varied but the highest changes (upon coordination or capping of the molecules) were observed for the LUMO. The molecules displayed similar single electron transfer behaviour and this could imply that the conductance is through the HOMO in all the cases. This has to be corroborated by theoretical calculations and by the comparison of additional systems towards the creation of a library that could be applied for the nano gap. Presently, our results are in an initial stage and further studies would be performed.

Experimental Section:

Synthesis Methods.

1. Synthesis of 5,15-bis(4-tert-butylphenyl)porphyrin, H₂(^tBuph)₂P

Dipyrromethene (726 mg, 5.0 mmol) and 4-tert-butylbenzaldehyde (0.83 mL, 5.0 mmol) were dissolved in dry CH₂Cl₂ (500 mL). The yellowish solution was purged with Ar₂ for 30 min to remove oxygen completely. After adding trifluoroacetic acid (0.66 mL, 8.9 mmol) to the solution, the resulting scarlet mixture was stirred for 30 min at room temperature in dark. Then p-chloranil (1.83 g, 7.5 mmol) was added and the resulting solution was stirred for 1 h. Followed by adding Et₃N (1.1 mL, 7.9 mmol) and stirring for further 2 h. The reaction mixture was filtered to remove the oxidant solid, then the solvent was evaporated to afford a black residue, which was purified by silica gel column chromatography (7.5 cm × 20 cm, CH₂Cl₂: hexane: Et₃N = 50: 50: 1) to give a pure purple solid from the first part (Figure 17) of the column (350 mg, 24 %). ¹H NMR (300 MHz, Chloroform-*d*) δ 10.31 (s, 2H), 9.39 (d, *J* = 4.6 Hz, 4H), 9.14 (d, *J* = 4.5 Hz, 4H), 8.21 (d, *J* = 7.9 Hz, 4H), 7.83 (d, *J* = 7.9 Hz, 4H), 1.64 (s, 18H), -3.07 (s, 2H). MALDI-MS *m/z* (%):574.25 ([M]⁺).

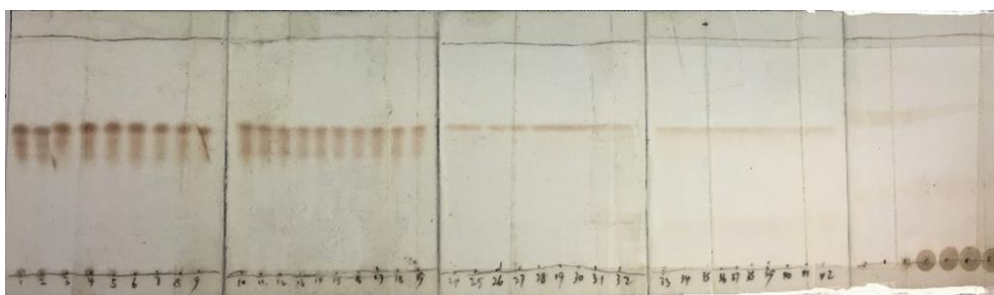


Figure 17. The illustration of product grading on silica plate collected from column chromatography.

2. Synthesis of 5,15-dibromo-10,20-bis(4-*tert*-butylphenyl)porphyrin Br₂(^tBuph)₂P

N-Bromosuccinimide (156 mg, 0.877 mmol) was added to a stirring mixture of porphyrin H₂(^tBuph)₂P (200 mg, 0.347 mmol) and pyridine (1.42 mL, 17.5 mmol) in CH₂Cl₂ (218 mL) at 0 °C. The mixture was stirred for 26 h at RT. Afterward, the bromination reaction was quenched by the addition of acetone (60 mL) and the solvent was evaporated. The residue was washed with CH₃OH and EtOAc and pure compound Br₂(^tBuph)₂P (190 mg, 75%) was achieved as a brown solid. ¹H NMR (300 MHz, Chloroform-*d*) δ 9.61 (d, *J* = 4.3 Hz, 4H), 8.88 (d, *J* = 4.2 Hz, 4H), 8.09 (d, *J* = 6.3 Hz, 4H), 7.78 (d, *J* = 6.3 Hz, 4H), 1.63 (s, 18H), -2.70 (s, 2H). MALDI-MS *m/z* (%): 732.12 ([M]⁺), 810.15([M+2K]⁺).

3. Synthesis of th₂(^tBuph)₂P

The mixture of Br₂(^tBuph)₂P (43.7 mg, 0.06 mmol) and 3-ethylthiophene (14.9 μL, 0.15 mmol) in THF (7.5 mL) with toluene (0.75 mL) and Et₃N (1.5 mL) was deoxygenated by freeze-pump-thaw cycles and purged with Ar gas in a Schlenk flask. AsPh₃ (9.2 mg, 0.03 mmol) and Pd₂(dba)₃ (41.2 mg, 45 μmol) were added and the reaction mixture was stirred at 30 °C in the dark for 24 hours. The crude mixture was filtered through celite and the solvent was removed under reduced pressure. The crude green product was first purified by silica gel chromatography using hexanes/CH₂Cl₂ as an eluent and washing later with ethanol. ¹H NMR (300 MHz, Chloroform-*d*) δ 9.63 (d, *J* = 4.8 Hz, 4H), 8.87 (d, *J* = 4.8 Hz, 4H), 8.12 (d, *J* = 8.2 Hz, 4H), 7.97 (dd, *J* = 3.0, 1.1 Hz, 2H), 7.79 (d, *J* = 8.2 Hz, 4H), 7.65 (dd, *J* = 5.0, 1.2 Hz, 2H), 7.58 – 7.47 (m, 2H), 1.64 (s, 18H), -1.98 (s, 2H). MALDI-MS *m/z* (%): 786.32 ([M]⁺).

4. 5-(4-Methylthiophenyl)dipyrromethane (dip-1).

Following the general procedure^{33,56}, distilled fresh pyrrole (50.0 mL, 720 mmol) and 4-(methylthio)benzaldehyde (3.75 mL, 28.8 mmol) were added to a flask and degassed with a stream of Ar. Afterward, TFA (0.22 mL, 2.9 mmol) was added and the red solution was stirred under Ar at RT for 5 min and finally quenched with 0.1 M NaOH (20 mL) until the solution became orange. Ethyl acetate was then added, and the organic phase was washed with water and dried with Na₂SO₄. The Removal of the solvent by distillation gave a yellow oil. All the procedure should be done under Ar to avoid the oxidation of pyrrole producing dark compounds. The oil was diluted in EtOH and then added dropwise into the water. In this way, a yellowish suspension came out. The achieved compound was filtered and dried. Then flash chromatography purification on silica (cyclohexane or hexane: ethyl acetate: Et₃N = 80: 20: 1) (Figure 18) was performed several times although the compound could not be separated from impurities.

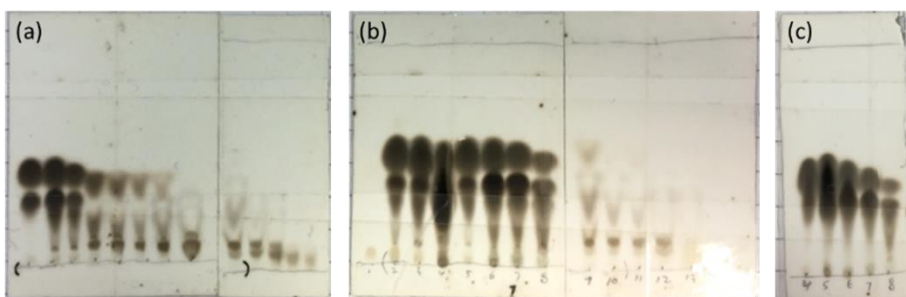


Figure 18. The illustration of product collected from column chromatography. (a) First chromatography by hexane/AcOEt/Et₃N = 80/20/1. (b) Second chromatography by hexane/AcOEt/Et₃N = 80/20/1. (c) third chromatography by cyclohexane/AcOEt/Et₃N = 80/20/1

5. Formation of the (MeS)₂(^tBuph)₂P via commercial dipyrromethane derivative.

The synthesis of (MeS)₂(^tBuph)₂P was tried according to literature procedures.^{34,35} A solution of 4-tert-Butylphenyldipyrromethane (1.114 g, 4 mmol) and 4-methylthiobenzaldehyde (0.761 g, 5 mmol) in dry CH₂Cl₂ (500 mL) was purged with Ar for 10 min, covered with aluminium foil, and then trifluoroacetic acid (0.276 mL, 3.6 mmol) was added. The resulting mixture was stirred at room temperature for 3 h after which dicyanodichloroquinone (1.544 g, 6.8 mmol) was added. Then the mixture was further stirred for 30 minutes followed by filter treatment. Concentrated it and poured into a column of silica gel packed with hexanes. Hexane:CH₂Cl₂:Et₃N = 50:50:1 was used as eluent and the first green colour band coming out was collected. The chromatography was repeated as before in cycles (Figure 19) until the desired porphyrin came out as a crude product. The yield was very low (< 2%) and the product was still impure. ¹H NMR (300 MHz, Chloroform-*d*) δ 8.87 (s, 8H), 8.53 (d, *J* = 8.5 Hz, 4H), 8.15 (d, *J* = 8.4 Hz, 4H), 7.76 (d, *J* = 8.2 Hz, 4H), 7.24 (d, *J* = 8.2 Hz, 4H), 2.76 (s, 6H), 1.62 (s, 18H), -2.74 (s, 2H).

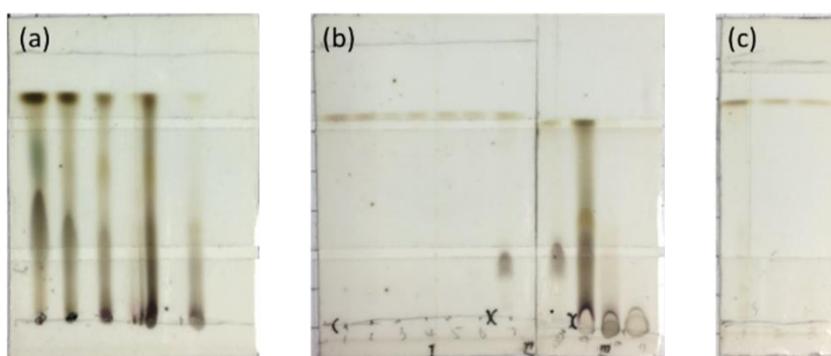


Figure 19. The illustration of product collected from column chromatography (hexane:CH₂Cl₂:Et₃N = 50:50:1). (a) First chromatography. (b) Second chromatography. (c) Third chromatography.

References:

- (1) Jurow, M.; Schuckman, A. E.; Batteas, J. D.; Drain, C. M. *Coordination chemistry reviews* **2010**, *254*, 2297.
- (2) Etcheverry-Berríos, A.; Olavarría, I.; Perrin, M. L.; Díaz-Torres, R.; Jullian, D.; Ponce, I.; Zagal, J. H.; Pavez, J.; Vásquez, S. O.; van der Zant, H. S. *Chemistry-A European Journal* **2016**, *22*, 12808.
- (3) Tanaka, Y.; Kiguchi, M.; Akita, M. *Chemistry-A European Journal* **2017**, *23*, 4741.
- (4) Parker, C. R.; Wei, Z.; Arroyo, C. R.; Jennum, K.; Li, T.; Santella, M.; Bovet, N.; Zhao, G.; Hu, W.; van der Zant, H. S. *Advanced Materials* **2013**, *25*, 405.
- (5) Perrin, M. L.; Prins, F.; Martin, C. A.; Shaikh, A. J.; Eelkema, R.; van Esch, J. H.; Briza, T.; Kaplanek, R.; Kral, V.; van Ruitenbeek, J. M. *Angewandte Chemie International Edition* **2011**, *50*, 11223.
- (6) Al-Galiby, Q. H.; Sadeghi, H.; Algharagholy, L. A.; Grace, I.; Lambert, C. *Nanoscale* **2016**, *8*, 2428.
- (7) Lörtscher, E.; Cho, C. J.; Mayor, M.; Tschudy, M.; Rettner, C.; Riel, H. *ChemPhysChem* **2011**, *12*, 1677.
- (8) Hybertsen, M. S.; Venkataraman, L.; Klare, J. E.; Whalley, A. C.; Steigerwald, M. L.; Nuckolls, C. *Journal of Physics: Condensed Matter* **2008**, *20*, 374115.
- (9) Sivanesan, A.; John, S. A. *Langmuir* **2008**, *24*, 2186.
- (10) Mishchenko, A.; Zotti, L. A.; Vonlanthen, D.; Bürkle, M.; Pauly, F.; Cuevas, J. C.; Mayor, M.; Wandlowski, T. *Journal of the American Chemical Society* **2010**, *133*, 184.
- (11) Takahashi, H.; Kanehara, M.; Teranishi, T. *Journal of Photopolymer Science and Technology* **2007**, *20*, 133.
- (12) Li, Z.; Smeu, M.; Ratner, M. A.; Borguet, E. *The Journal of Physical Chemistry C* **2013**, *117*, 14890.
- (13) Sedghi, G.; Esdaile, L. J.; Anderson, H. L.; Martin, S.; Bethell, D.; Higgins, S. J.; Nichols, R. J. *Advanced Materials* **2012**, *24*, 653.
- (14) Perrin, M. L.; Martin, C. A.; Prins, F.; Shaikh, A. J.; Eelkema, R.; van Esch, J. H.; van Ruitenbeek, J. M.; van der Zant, H. S.; Dulić, D. *Beilstein journal of nanotechnology* **2011**, *2*, 714.
- (15) Han, W.; Li, S.; Lindsay, S.; Gust, D.; Moore, T. A.; Moore, A. L. *Langmuir* **1996**, *12*, 5742.
- (16) Imahori, H.; Ozawa, S.; Ushida, K.; Takahashi, M.; Azuma, T.; Ajavakom, A.; Akiyama, T.; Hasegawa, M.; Taniguchi, S.; Okada, T. *Bulletin of the Chemical Society of Japan* **1999**, *72*, 485.
- (17) Li, Z.; Smeu, M.; Park, T.-H.; Rawson, J.; Xing, Y.; Therien, M. J.; Ratner, M. A.; Borguet, E. *Nano letters* **2014**, *14*, 5493.
- (18) Liu, Z.-F.; Wei, S.; Yoon, H.; Adak, O.; Ponce, I.; Jiang, Y.; Jang, W.-D.; Campos, L. M.; Venkataraman, L.; Neaton, J. B. *Nano letters* **2014**, *14*, 5365.
- (19) Shimidzu, T.; Segawa, H.; Wu, F.; Nakayama, N. *Journal of Photochemistry and Photobiology A: Chemistry* **1995**, *92*, 121.
- (20) Li, G.; Bhosale, S.; Tao, S.; Guo, R.; Bhosale, S.; Li, F.; Zhang, Y.; Wang, T.; Fuhrhop, J.-H. *Polymer* **2005**, *46*, 5299.
- (21) Zöllner, M. J.; Becker, E.; Jahn, U.; Kowalsky, W.; Johannes, H. H. *European Journal of Organic Chemistry* **2010**, *2010*, 4426.
- (22) Zöllner, M. J.; Frähmcke, J. S.; Elstner, M.; Jahn, U.; Jones, P. G.; Becker, E.; Kowalsky, W.; Johannes, H. H. *Macromolecular Chemistry and Physics* **2010**, *211*, 359.
- (23) Lyons, D. M.; Kesters, J.; Maes, W.; Bielawski, C. W.; Sessler, J. L. *Synthetic Metals* **2013**, *178*, 56.
- (24) Yamada, Y.; Kubota, T.; Nishio, M.; Tanaka, K. *Journal of the American Chemical Society* **2014**, *136*, 6505.

- (25) Handayani, M.; Gohda, S.; Tanaka, D.; Ogawa, T. *Chemistry-A European Journal* **2014**, *20*, 7655.
- (26) Koszelewski, D.; Nowak-Król, A.; Gryko, D. T. *Chemistry-An Asian Journal* **2012**, *7*, 1887.
- (27) Koszelewski, D.; Nowak-Król, A.; Drobizhev, M.; Wilson, C. J.; Haley, J. E.; Cooper, T. M.; Romiszewski, J.; Górecka, E.; Anderson, H. L.; Rebane, A. *Journal of Materials Chemistry C* **2013**, *1*, 2044.
- (28) Huang, Y.; Li, L.; Peng, X.; Peng, J.; Cao, Y. *Journal of Materials Chemistry* **2012**, *22*, 21841.
- (29) Odobel, F.; Suresh, S.; Blart, E.; Nicolas, Y.; Quintard, J. P.; Janvier, P.; Le Questel, J. Y.; Illien, B.; Rondeau, D.; Richomme, P. *Chemistry-A European Journal* **2002**, *8*, 3027.
- (30) Sonogashira, K. *Journal of Organometallic Chemistry* **2002**, 653, 46.
- (31) Kuo, M.-C.; Li, L.-A.; Yen, W.-N.; Lo, S.-S.; Lee, C.-W.; Yeh, C.-Y. *Dalton Transactions* **2007**, 1433.
- (32) Littler, B. J.; Miller, M. A.; Hung, C.-H.; Wagner, R. W.; O'Shea, D. F.; Boyle, P. D.; Lindsey, J. S. *The Journal of Organic Chemistry* **1999**, *64*, 1391.
- (33) Lee, C.-H.; Lindsey, J. S. *Tetrahedron* **1994**, *50*, 11427.
- (34) Abdelrazzaq, F. B.; Kwong, R. C.; Thompson, M. E. *Journal of the American Chemical Society* **2002**, *124*, 4796.
- (35) Noguchi, Y.; Nagase, T.; Kubota, T.; Kamikado, T.; Mashiko, S. *Thin Solid Films* **2006**, *499*, 90.
- (36) Pabon, H. *Recueil des Travaux Chimiques des Pays-Bas* **1964**, *83*, 379.
- (37) Felouat, A.; D'Aléo, A.; Fages, F. r. *The Journal of organic chemistry* **2013**, *78*, 4446.
- (38) Meek, D. W.; Ehrhardt, S. A. *Inorganic Chemistry* **1965**, *4*, 584.
- (39) Changtam, C.; Hongmanee, P.; Suksamrarn, A. *European journal of medicinal chemistry* **2010**, *45*, 4446.
- (40) Lu, T.; Jiang, Y.-T.; Ma, F.-P.; Tang, Z.-J.; Kuang, L.; Wang, Y.-X.; Wang, B. *Organic letters* **2017**, *19*, 6344.
- (41) Ge, C.; Wang, H.; Zhang, B.; Yao, J.; Li, X.; Feng, W.; Zhou, P.; Wang, Y.; Fang, J. *Chemical Communications* **2015**, *51*, 14913.
- (42) Roth, K. M.; Yasseri, A. A.; Liu, Z.; Dabke, R. B.; Malinovskii, V.; Schweikart, K.-H.; Yu, L.; Tiznado, H.; Zaera, F.; Lindsey, J. S. *Journal of the American Chemical Society* **2003**, *125*, 505.
- (43) Chen, F.; He, J.; Nuckolls, C.; Roberts, T.; Klare, J. E.; Lindsay, S. *Nano Letters* **2005**, *5*, 503.
- (44) Liu, D.; Gu, C.; Xiao, M.; Qiu, M.; Sun, M.; Yang, R. *Polymer Chemistry* **2015**, *6*, 3398.
- (45) Ozawa, H.; Baghernejad, M.; Al-Owaedi, O. A.; Kaliginedi, V.; Nagashima, T.; Ferrer, J.; Wandlowski, T.; García-Suárez, V. M.; Broekmann, P.; Lambert, C. J. *Chemistry-a European journal* **2016**, *22*, 12732.
- (46) Djurovich, P. I.; Mayo, E. I.; Forrest, S. R.; Thompson, M. E. *Organic Electronics* **2009**, *10*, 515.
- (47) Yu, C.-Y.; Chen, C.-P.; Chan, S.-H.; Hwang, G.-W.; Ting, C. *Chemistry of Materials* **2009**, *21*, 3262.
- (48) Ponce, J.; Arroyo, C. R.; Tatay, S.; Frisenda, R.; Gaviña, P.; Aravena, D.; Ruiz, E.; van der Zant, H. S.; Coronado, E. *Journal of the American Chemical Society* **2014**, *136*, 8314.
- (49) Rao, E. V.; Sudheer, P. *Indian journal of pharmaceutical sciences* **2011**, *73*, 262.
- (50) Raghavan, S.; Manogaran, P.; Narasimha, K. K. G.; Kuppusami, B. K.; Mariyappan, P.; Gopalakrishnan, A.; Venkatraman, G. *Bioorganic & medicinal chemistry letters* **2015**, *25*, 3601.
- (51) Roncali, J. *Macromolecular Rapid Communications* **2007**, *28*, 1761.
- (52) Murphy, A. *Solar Energy Materials and Solar Cells* **2007**, *91*, 1326.
- (53) Liu, T.; Zhang, G.; Evans, R. E.; Trindle, C. O.; Altun, Z.; DeRosa, C. A.; Wang, F.; Zhuang, M.; Fraser, C. L. *Chemistry-A European Journal* **2018**.

- (54) Kim, E.; Felouat, A.; Zaborova, E.; Ribierre, J.-C.; Wu, J. W.; Senatore, S.; Matthews, C.; Lenne, P.-F.; Baffert, C.; Karapetyan, A. *Organic & biomolecular chemistry* **2016**, *14*, 1311.
- (55) Zolezzi, S.; Spodine, E.; Decinti, A. *Polyhedron* **2002**, *21*, 55.
- (56) Clausen, C.; Gryko, D. T.; Yasserli, A. A.; Diers, J. R.; Bocian, D. F.; Kuhr, W. G.; Lindsey, J. S. *The Journal of organic chemistry* **2000**, *65*, 7371.

Appendix

Chapter II

Table A2.1. Crystallographic information of **1a-b** and **2a-c**.

	1a	1b	2a	2b	2c
formula	C ₆₀ H ₅₄ N ₄ O ₁₃ Zn	C ₆₀ H ₅₂ N ₄ O ₁₂ Zn	C ₅₆ H ₄₄ N ₄ O ₁₂ Zn	C ₅₆ H ₄₄ N ₄ O ₁₂ Zn	C ₆₀ H ₅₂ N ₄ O ₁₃ Zn, C ₄ H ₈ O
F _w	1104.44	1086.45	1030.34	1030.34	1174.53
crystal system	orthorhombic	orthorhombic	monoclinic	monoclinic	triclinic
space group	P 21 21 21	P 21 21 21	C 2/c	C 2/c	P-1
a [Å]	9.5790(2)	16.8600(0)	21.71000	20.76000	11.5044(17)
b [Å]	17.3042(3)	17.7400(0)	15.19000	11.92000	16.651(2)
c [Å]	32.6567(6)	17.9100(0)	14.35000	24.59000	16.712(2)
α [°]	90.00	90.00	90	90	65.654(2)
β [°]	90.00	90.00	104.2600	90.2100	86.591(2)
γ [°]	90.00	90.00	90	90	73.222(2)
V [Å ³]	5413.07(18)	5356.816	4586.458	6084.981	2786.0(6)
Z	4	4	4	4	2
ρ _{calcd} [Mg m ⁻³]	1.355	1.347	1.492	1.125	1.400
μ [mm ⁻¹]	0.524	1.225	0.818	0.617	0.514
F(000)	2304	2264	2136	2136	1228
crystal size [mm ³]	0.22 x 0.16 x 0.04	0.13 x 0.12 x 0.10	0.11 x 0.10 x 0.08		0.08 x 0.10 x 0.14
θ _{max} [°]	25.00	33.204	33.9	34.0	28.3
refl collected	9520	35749	33299	43301	18713
refl unique	7983	6842	5291	7606	12223
R(int)	0.0451	0.0600	0.030	0.018	0.024
Completeness (%)	99.6	72.6			
refl with I > 2σ(I)	9520	6842	5168	7404	10875
refined parameters	713	695	332	332	790
R ₁ [I > 2σ(I)]	0.0400	0.0358	0.0409	0.0633	0.0526
wR ₂ [I > 2σ(I)]	0.0894	0.0912	0.1180	0.2023	0.1263
R ₁ [all data]	0.0541	0.0399			
wR ₂ [all data]	0.0941	0.0922			
±Δρ _{max} [e Å ⁻³]	+1.015, -1.017	+0.333, -0.516	+0.67, -0.65	+1.97, -0.70	+1.15, -0.36

Table A2.2. Selected bond lengths [Å] and angles [°] for **1a**.

[Å]		[°]	
Zn(1)-N(4)	2.046(2)	N(4)-Zn(1)-N(2)	168.25(10)
Zn(1)-N(2)	2.052(2)	N(4)-Zn(1)-N(1)	90.08(9)
Zn(1)-N(1)	2.066(2)	N(2)-Zn(1)-N(1)	89.68(8)
Zn(1)-N(3)	2.082(2)	N(4)-Zn(1)-N(3)	89.11(9)
Zn(1)-O(13)	2.248(2)	N(2)-Zn(1)-N(3)	88.82(8)
O(13)-H(10)	0.828(10)	N(1)-Zn(1)-N(3)	168.71(9)
O(13)-H(20)	0.897(10)	N(4)-Zn(1)-O(13)	96.39(10)
C(5)-C(21)	1.503(4)	N(2)-Zn(1)-O(13)	95.16(10)
C(10)-C(27)	1.499(4)	N(1)-Zn(1)-O(13)	101.43(9)
C(15)-C(33)	1.504(4)	N(3)-Zn(1)-O(13)	89.85(10)
C(20)-C(39)	1.493(4)	Zn(1)-O(13)-H(10)	113(3)
C(45)-H(45)	0.9900	Zn(1)-O(13)-H(20)	122(3)
C(45)-C(46)	1.530(6)	O(1)-C(45)-C(46)	109.3(3)
C(45)-C(47)	1.522(6)	O(4)-C(49)-C(50)	109.0(3)
C(49)-H(49)	0.9900	O(7)-C(53)-C(54)	113.2(3)
C(49)-C(50)	1.517(5)	O(10)-C(57)-C(58)	108.2(2)
C(49)-C(51)	1.520(5)		
C(53)-H(53)	0.9900		
C(53)-C(54)	1.501(5)		
C(53)-C(55)	1.514(5)		
C(57)-H(57)	0.9900		
C(57)-C(58)	1.523(4)		
C(57)-C(59)	1.505(4)		
O(2)-C(46)	1.180(5)		
O(5)-C(50)	1.178(4)		
O(8)-C(54)	1.194(4)		
O(11)-C(58)	1.198(4)		

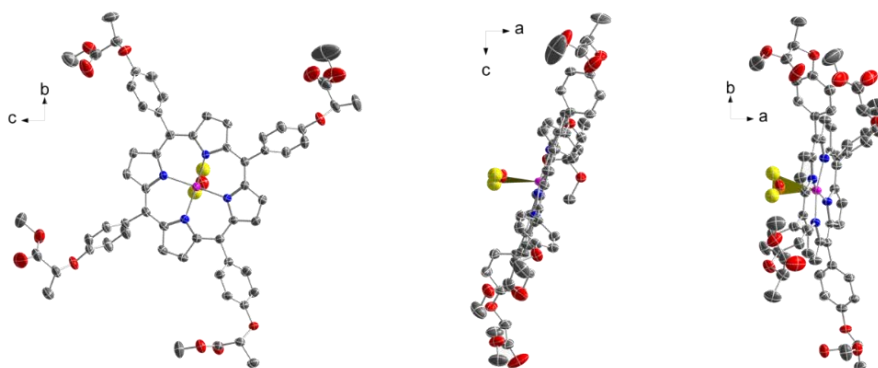
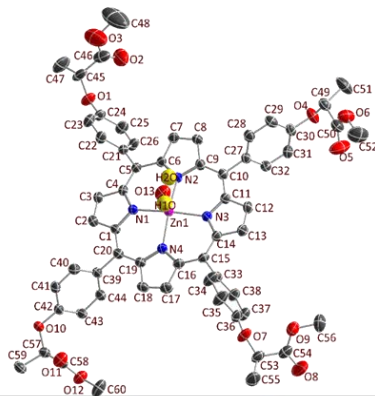
**Figure A2.1.** Different crystallographic projections of **1a**.

Table A2.3. Selected bond lengths [Å] and angles [°] for **1b**.

[Å]		[°]	
Zn(1)-N(4)	2.037(3)	N(4)-Zn(1)-N(1)	90.06(13)
Zn(1)-N(1)	2.054(3)	N(4)-Zn(1)-N(2)	169.67(14)
Zn(1)-N(2)	2.057(3)	N(1)-Zn(1)-N(2)	89.00(13)
Zn(1)-N(3)	2.068(4)	N(4)-Zn(1)-N(3)	89.92(14)
Zn(1)-O(5)	2.210(3)	N(1)-Zn(1)-N(3)	169.29(15)
C(2)-C(22)	1.494(6)	N(2)-Zn(1)-N(3)	89.10(13)
C(7)-C(32)	1.496(6)	N(4)-Zn(1)-O(5)	88.72(13)
C(13)-C(42)	1.492(6)	N(1)-Zn(1)-O(5)	104.21(14)
C(18)-C(52)	1.497(6)	N(2)-Zn(1)-O(5)	101.48(13)
C(28)-C(29)	1.481(8)	N(3)-Zn(1)-O(5)	86.50(14)
C(28)-C(30)	1.536(8)	O(1)-C(28)-C(30)	107.9(4)
C(28)-O(1)	1.449(6)	O(4)-C(38)-C(40)	110.8(4)
C(38)-C(39)	1.515(7)	O(7)-C(48)-C(50)	110.4(4)
C(38)-C(40)	1.503(7)	O(10)-C(58)-C(60)	110.6(4)
C(38)-O(4)	1.437(6)		
C(48)-C(49)	1.505(7)		
C(48)-C(50)	1.521(8)		
C(48)-O(7)	1.421(6)		
C(58)-C(59)	1.525(7)		
C(58)-C(60)	1.521(7)		
C(58)-O(10)	1.419(6)		

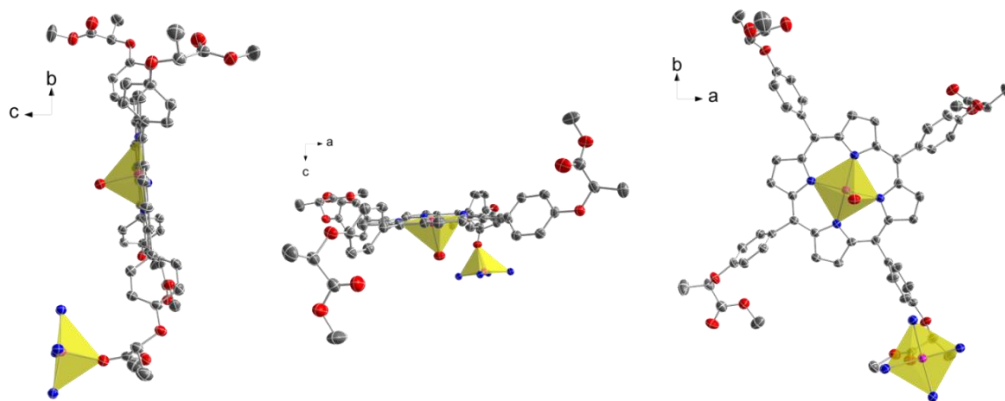
**Figure A2.2.** Different crystallographic projections of **1b**.

Table A2.4. Selected bond lengths [Å] and angles [°] for **2a**.

[Å]		[°]	
Zn(1)-N(1)	2.0365(13)	N(1)-Zn(1)-N(2)	90.06(13)
Zn(1)-N(2)	2.0476(13)	N(1)-Zn(1)-N(1')	180.00
C(2)-C(11)	1.495(2)	N(1)-Zn(1)-N(2')	89.40(5)
C(7)-C(20)	1.496(2)	N(2)-Zn(1)-N(2')	180.00
C(17)-O(1)	1.420(3)	O(1)-C(17)-C(18)	112.34(16)
C(17)-C(18)	1.514(3)	O(4)-C(26)-C(27)	107.56(16)
C(26)-O(4)	1.413(2)		
C(26)-C(27)	1.513(3)		

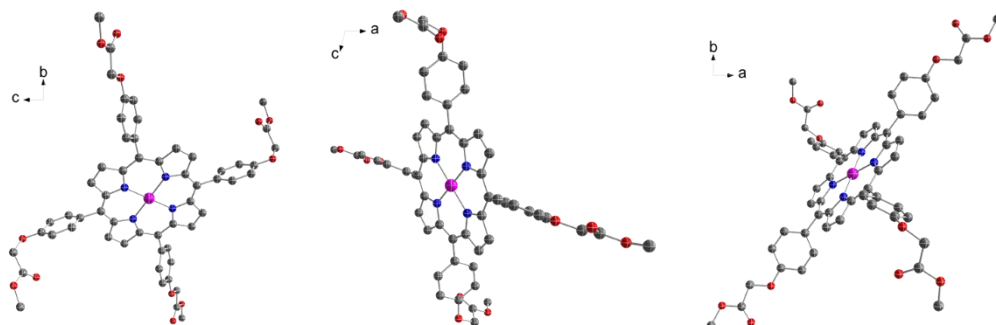
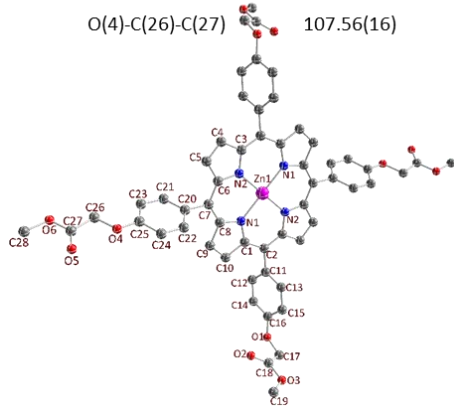


Figure A2.3. Different crystallographic projections of **2a**.

Table A2.6. Selected bond lengths [Å] and angles [°] for **2c**.

	[Å]		[°]
Zn(1)-N(1)	2.053(2)	N(1)-Zn(1)-N(2)	88.76(9)
Zn(1)-N(2)	2.061(2)	N(2)-Zn(1)-N(3)	88.88(9)
Zn(1)-N(3)	2.063(2)	N(3)-Zn(1)-N(4)	89.35(9)
Zn(1)-N(4)	2.062(2)	N(4)-Zn(1)-N(1)	89.41(9)
Zn(1)-O(13)	2.161(2)	N(1)-Zn(1)-N(3)	165.93(9)
		N(2)-Zn(1)-N(4)	165.20(9)
		N(1)-Zn(1)-O(13)	99.55(8)
		N(2)-Zn(1)-O(13)	101.77(8)
		N(3)-Zn(1)-O(13)	94.51(8)
		N(4)-Zn(1)-O(13)	93.02(8)
		O(1)-C(27)-C(28)	110.5(2)
		O(4)-C(36)-C(37)	110.7(2)
		O(7)-C(45)-C(46)	108.0(2)
		O(10)-C(54)-C(55)	111.0(2)

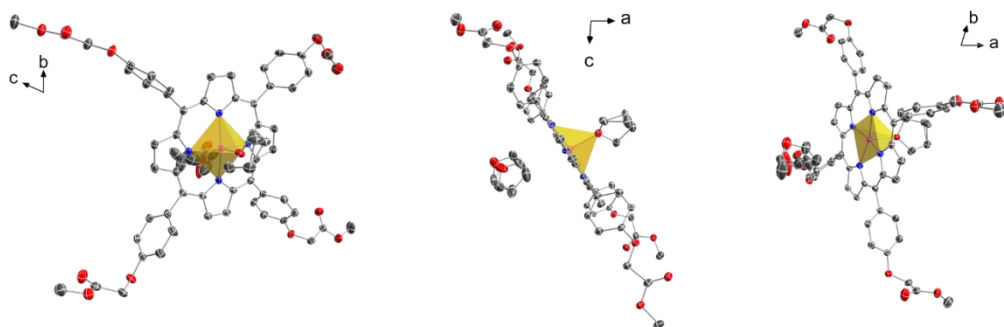
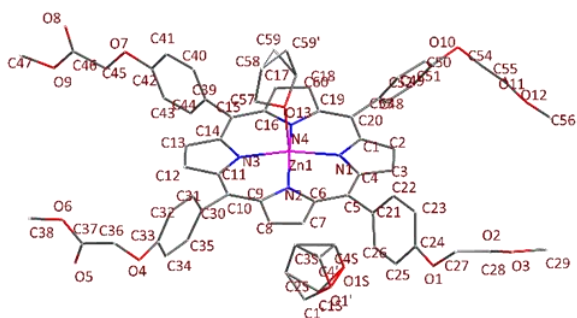


Figure A2.5. Different crystallographic projections of **2c**.

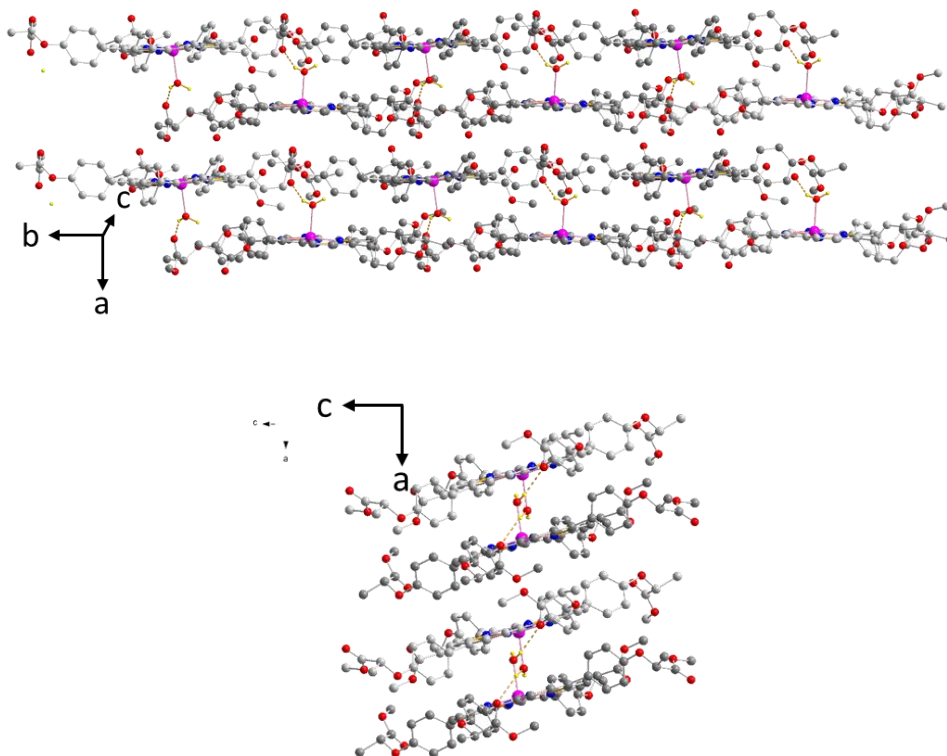


Figure A2.6. 2D organization of **1a** in different crystallographic projections.

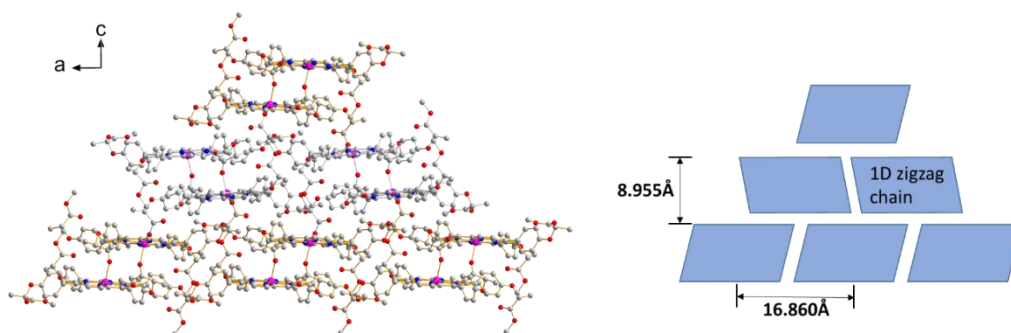


Figure A2.7. 3D supramolecular organization of **1b**.

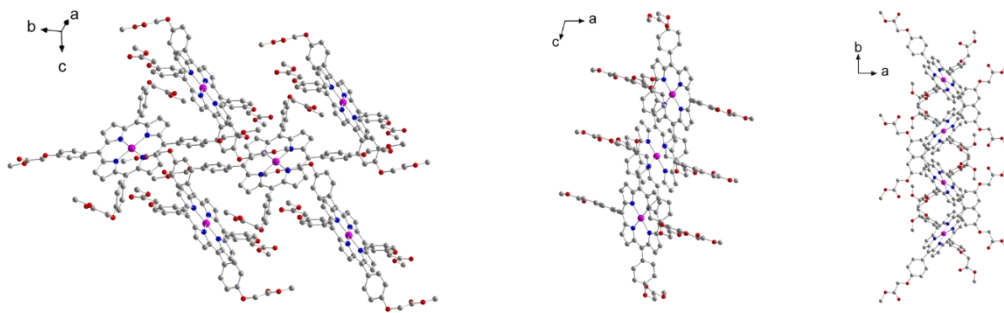


Figure A2.8. 2D structure of **2a**.

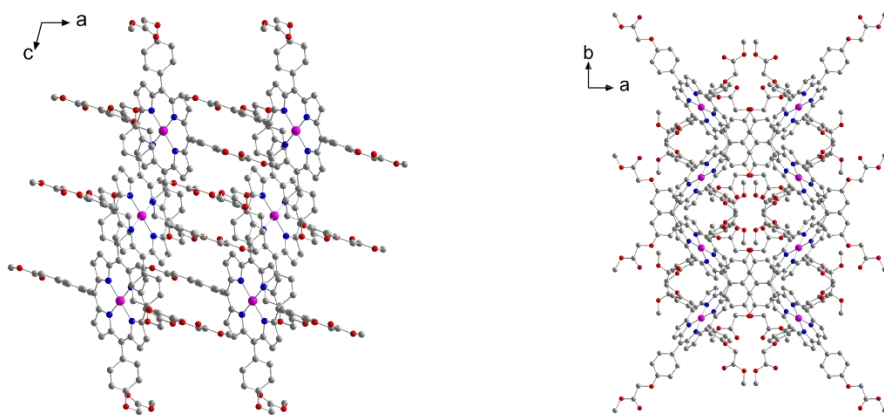


Figure A2.9. 3D supramolecular organization of **2a**.

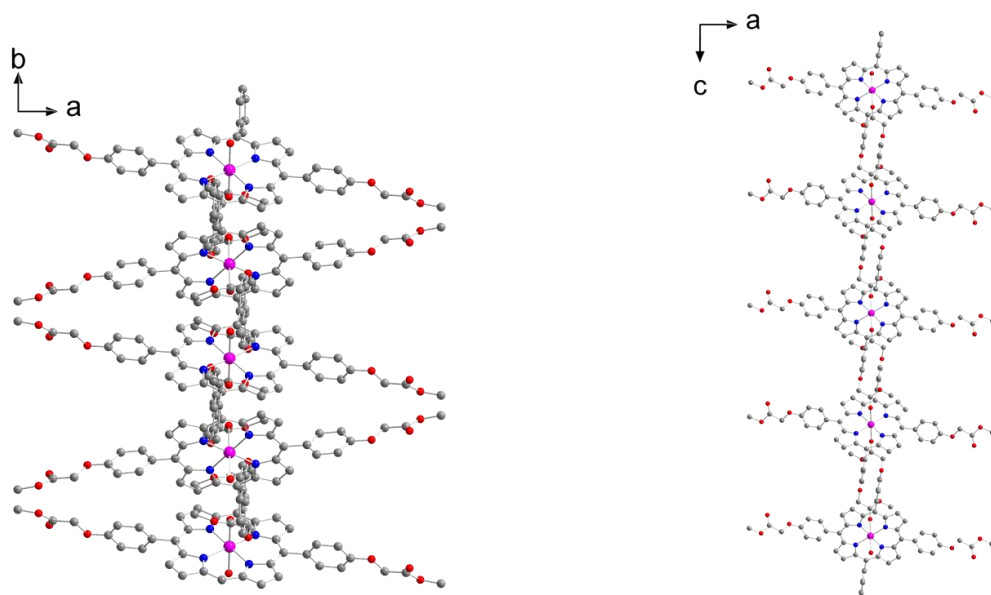


Figure A2.10. Different crystallographic projections of 2D network of **2b**.

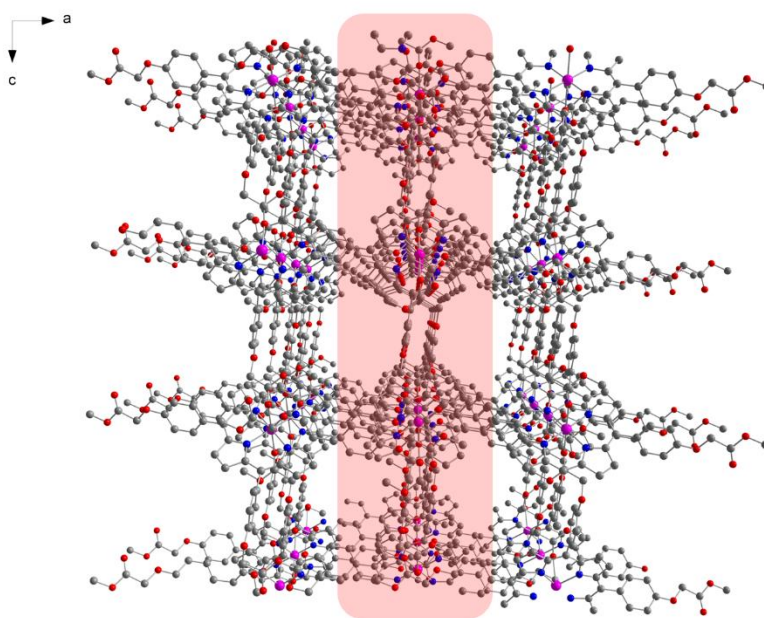


Figure A2.11. The crystal architecture of **2b** constructed by packing of 2D layers.

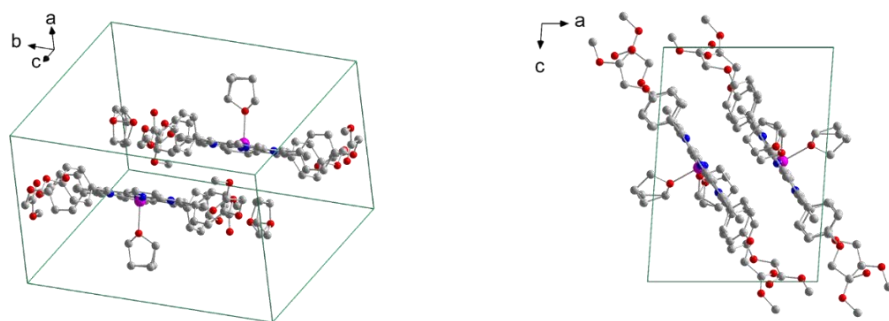


Figure A2.12. The unit cell of 2c.

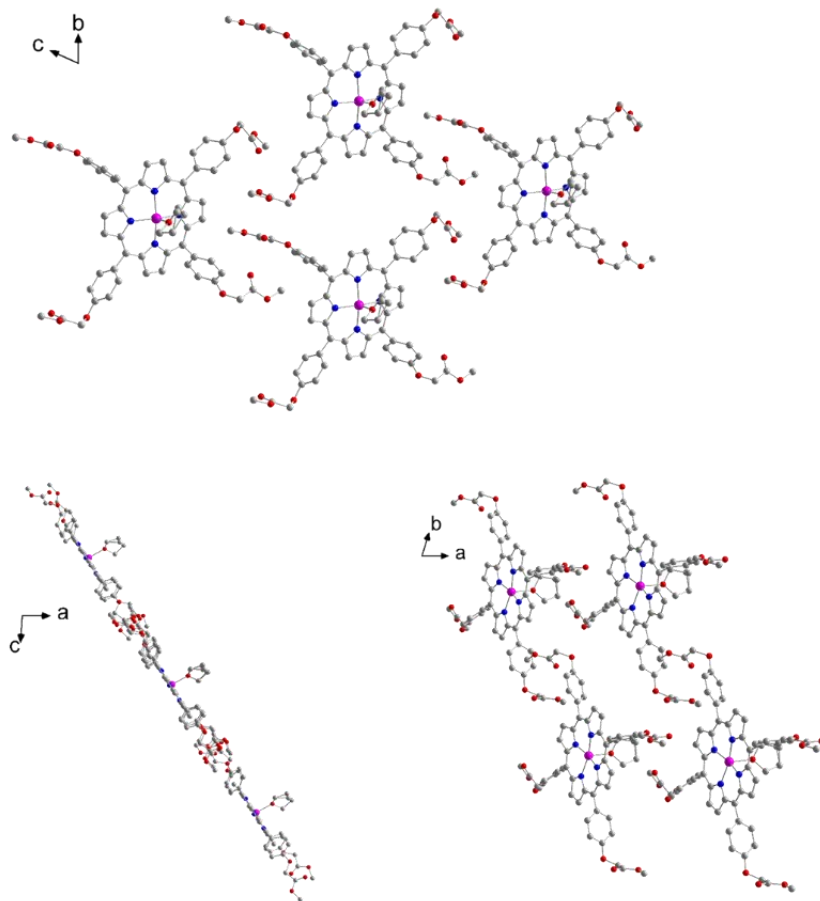


Figure A2.13. 2D supramolecular organization of 2c.

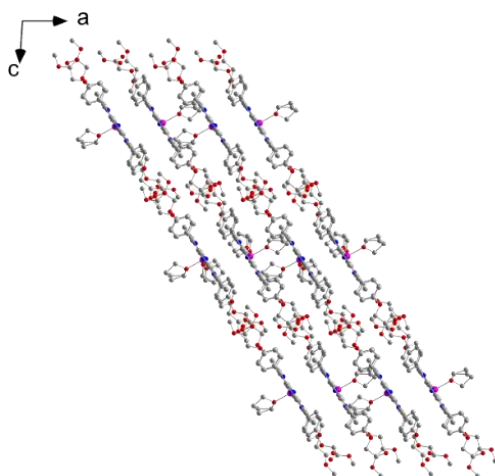


Figure A2.14. 3D supramolecular organization of **2c**.

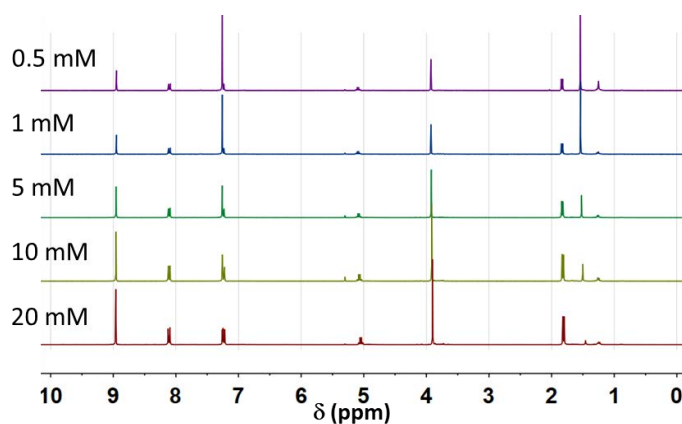


Figure A2.15. ^1H NMR of **1b** in different concentration in CDCl_3 .

Studies performed in solution by CD spectroscopies

In order to avoid the artificial signals related with the high absorption of the samples in the CD spectra, we fix the absorbance $A = 1$, and the molar absorptivity ϵ was obtained by UV-Vis spectrum (Figure A2.16) primarily.

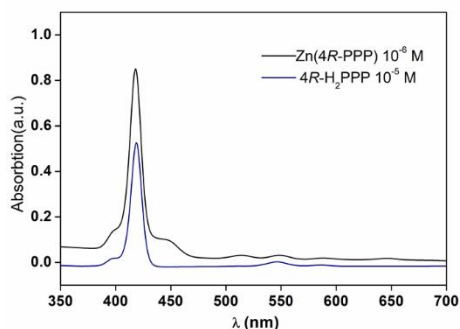


Figure A2.16. UV-Vis absorption spectrum of **Zn(4R-PPP)** (10^{-6} M) and **4R-H₂PPP** (10^{-5} M) in CH_2Cl_2 .

According to the Beer–Lambert law

$$A = \varepsilon c \ell$$

where ε is the molar attenuation coefficient of the material; c is the molar concentration; ℓ is the pathlength. We could calculate the molar absorptivity ε of **Zn(4R-PPP)** and **4R-H₂PPP** are $5.26 \times 10^5 \text{ M}^{-1} \cdot \text{cm}^{-1}$ and $8.51 \times 10^4 \text{ M}^{-1} \cdot \text{cm}^{-1}$ respectively. As the absorbance of porphyrins depend on the concentration of the species, when the value of A is 1 in the CD measurement, the concentration used for the two porphyrins are 1.90×10^{-6} M and 1.17×10^{-5} M. In case of broad absorption, different band widths (1 nm, 2nm, 5 nm and 10 nm) of the incident circularly polarized light were set to record CD spectra (Figure A2.17).

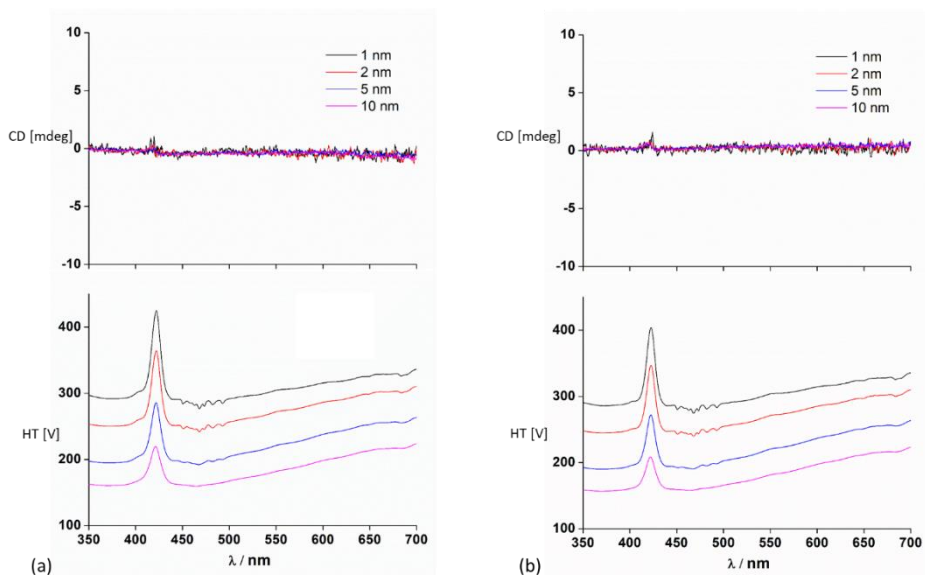


Figure A2.17. CD spectra and corresponding absorption signal from the CD spectrometer of (a) **Zn(4R-PPP)** (1.90×10^{-6} M) and (b) **4R-H₂PPP** (1.17×10^{-5} M) measured using different band widths in CH_2Cl_2 .

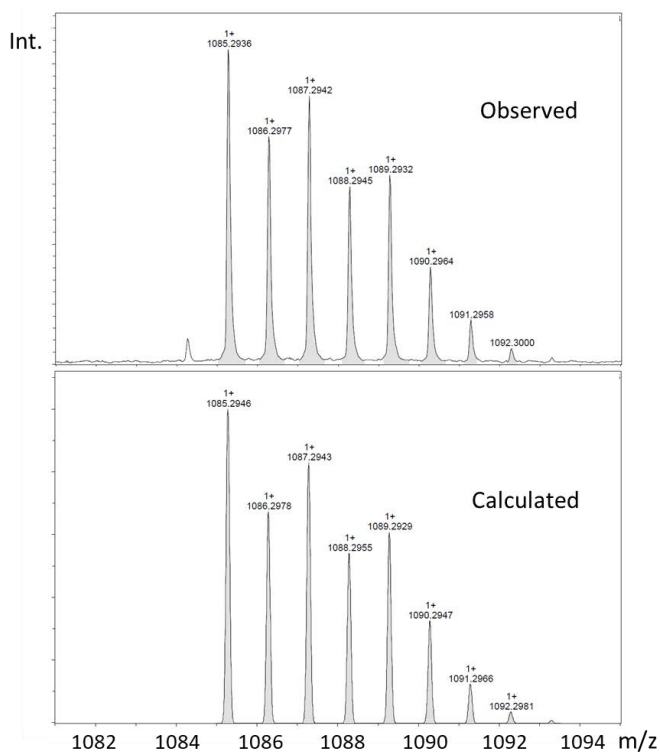


Figure A2.18. ESI-Mass spectra of **1a** in positive. (Top) The measured value. (Down) The predicted theoretical isotopic distribution.

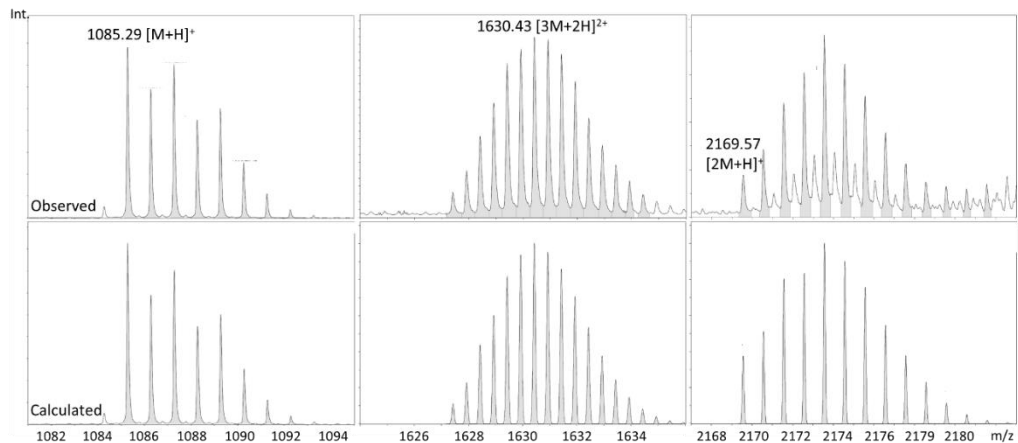


Figure A2.19. The predicted theoretical isotopic distribution and measured value of ESI-Mass spectra of **1b** in positive.

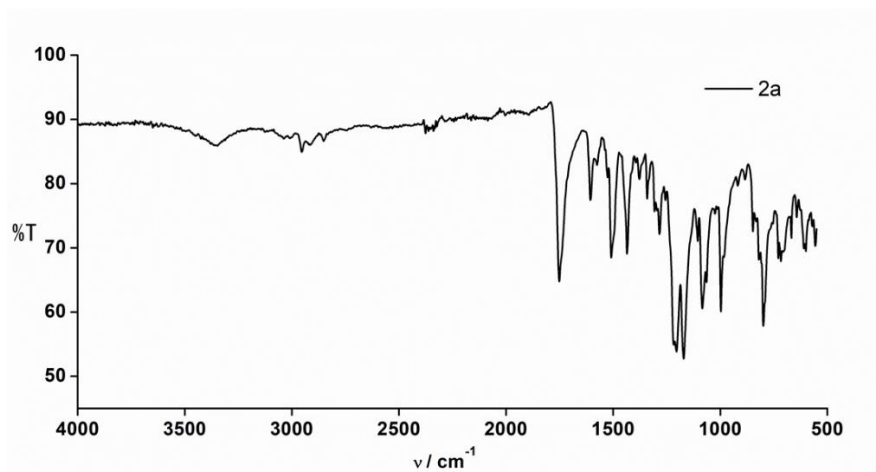


Figure A2.20. FT-IR of 2a.

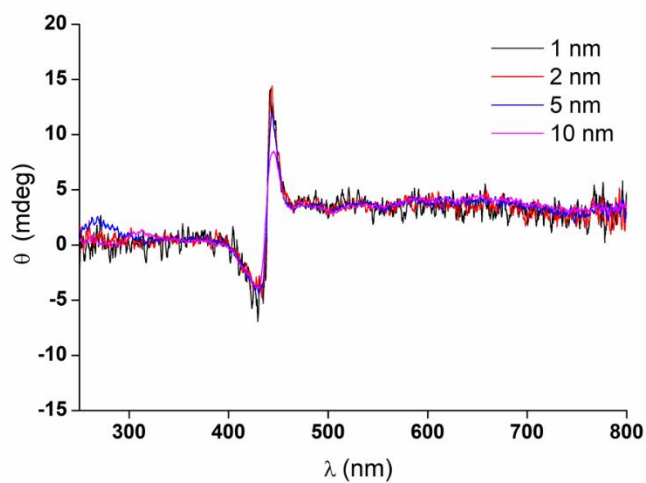


Figure A2.21. Solid-state CD spectra of compounds 1a.

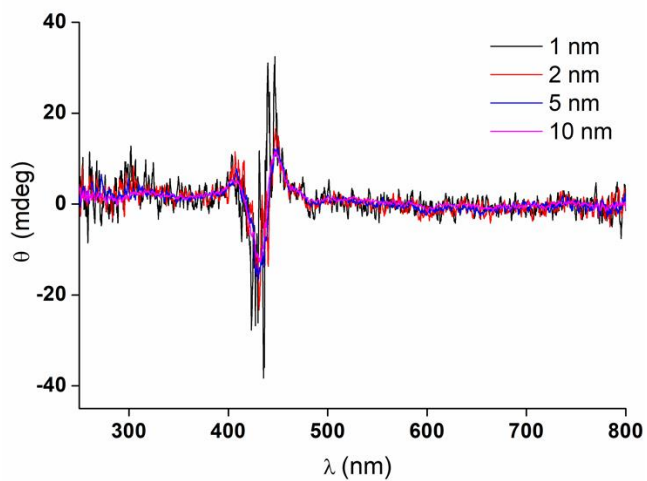


Figure A2.22. Solid-state CD spectra of compounds **1b**.

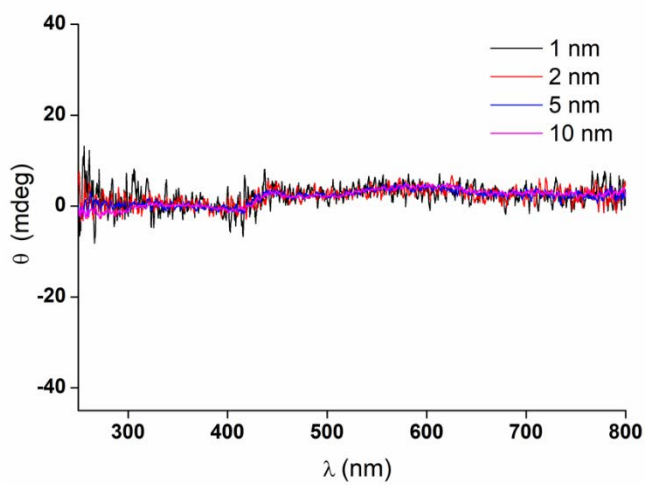


Figure A2.23. Solid-state CD spectra of compounds **2a**.

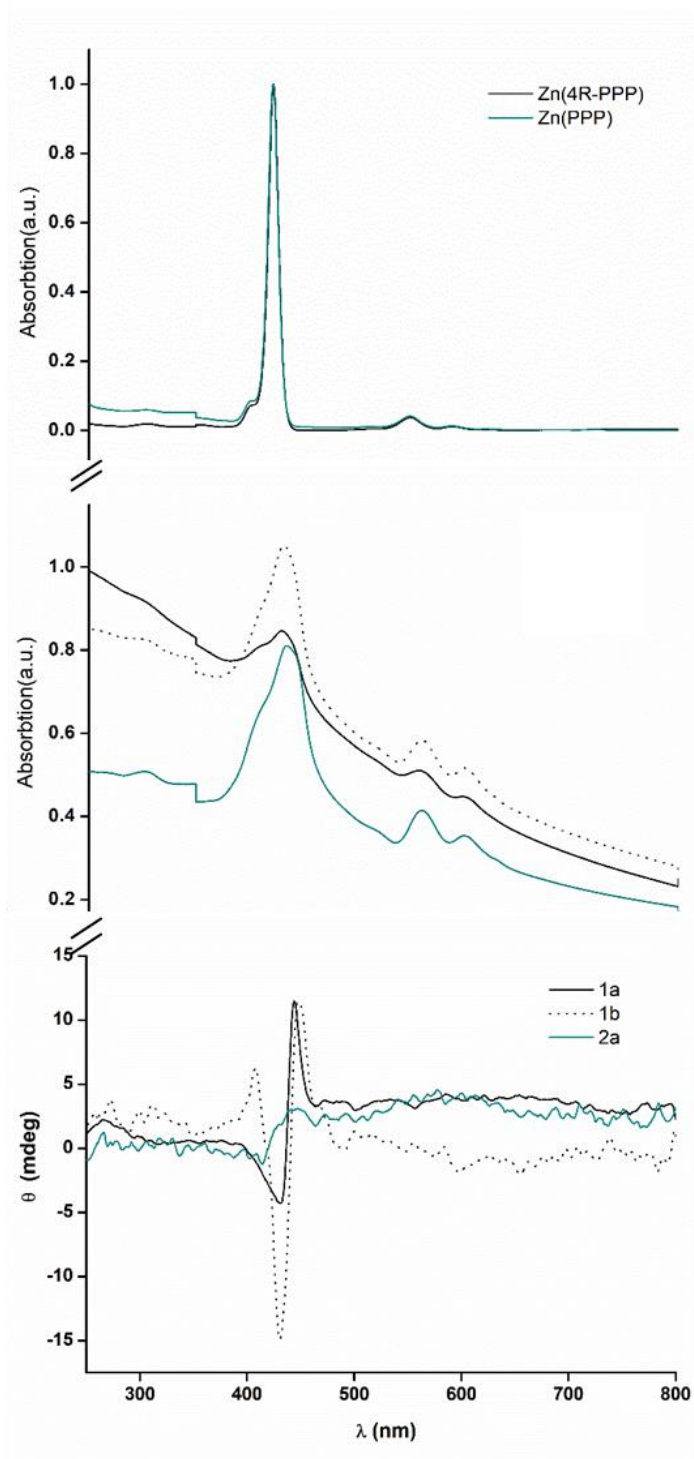


Figure A2.24. UV-Vis absorption spectroscopy of Zn-porphyrins in CH_2Cl_2 (upper). The solid-state UV-Vis of **1a**, **1b** and **2a** crystals (middle). Solid state CD spectra of **1a**, **1b** and **2a** (lower).

Solid-state VCD studies.

Experimentally, we achieved purple pellets by mixing/milling 2 mg of the samples and 150 mg of dry KBr. An 1800 cm^{-1} cut-off filter was used with two wavelengths, 1700 and 1300 cm^{-1} , in both cases providing similar spectra. A set of spectra (five each time) were collected for **1a** and **1b**, respectively, where each disk was rotated at intervals of 45 °.

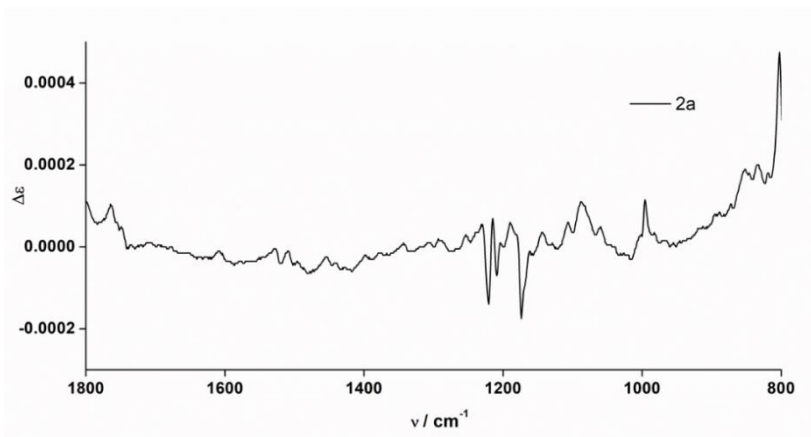


Figure A2.25. Solid-state VCD spectra of **2a**.

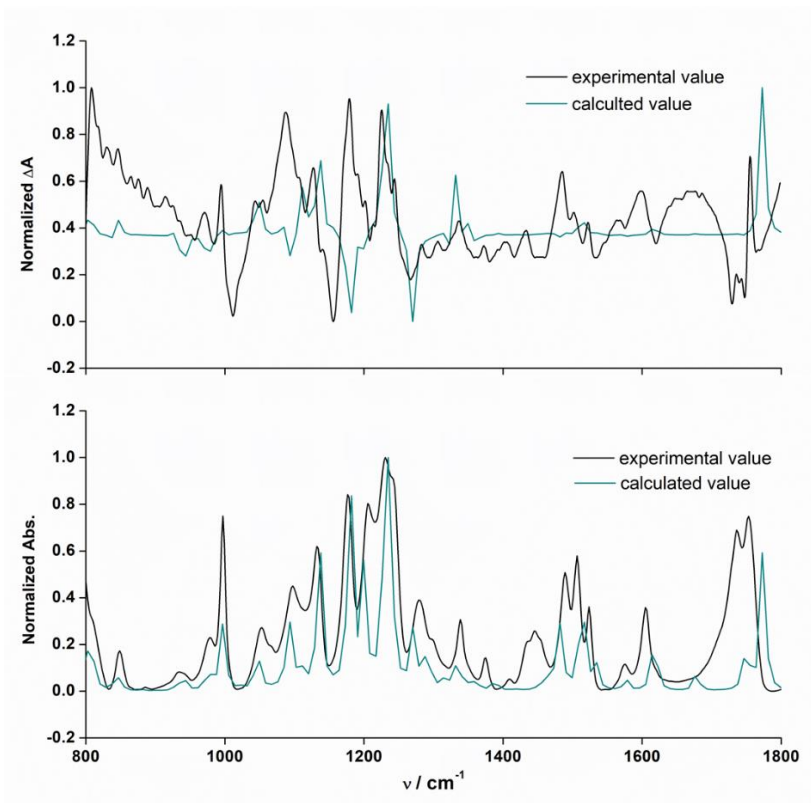


Figure A2.26. Theoretical calculation solid state IR and VCD spectra of **1a**.

Electrochemical properties

It is probable that the reduction–oxidation (redox) state of the molecule may be related to some form of molecular conductance switching. Porphyrins, due to their efficient charge carrier transport, have been studied extensively for applications such as organic solar cells,¹ molecular electronics components,^{2,3} et al. In this work, the redox properties of porphyrins are studied by cyclic voltammetry (CV) and differential pulse voltammetry (DPV), which were performed to estimate values of the highest occupied molecular orbital (HOMO) and the lowest unoccupied molecular orbital (LUMO) energy levels of our systems.

Perform the CV and DPV measurement on Pt electrode from a 0.5 mM porphyrin solution in 0.1 M TBAPF₆/CH₂Cl₂. A three-electrode cell consisting of a glassy carbon working electrode, a platinum wire counter electrode and another platinum wire reference electrode were used. The sample potential is swept at 100 mV/s from 0 V to 1.5 V and from 0 V to -2 V separately at room temperature under Ar. The potentials were internally calibrated using the Fc/Fc⁺ redox couple.

For organic semiconductors, the HOMO represents the energy required to extract an electron from the highest occupied molecular orbital, which is estimated from the first oxidation potential, corresponding to the ionization potential. And the LUMO is the energy necessary to inject an electron to the lowest unoccupied orbital, thus implying a reduction process, which is deduced from the first reduction potential, correlated with the electron affinity.⁴ To proceed with the calculations has to consider that the Fc/Fc⁺ has a potential of 4.80 eV below the vacuum level.⁵ Therefore, the HOMO and LUMO energy levels (E_{HOMO} and E_{LUMO}) of both molecules can be calculated according to the empirical equations:^{6,7}

$$E_{\text{HOMO}} = - (E_{\text{onset(ox)}} + 4.8) \text{ eV}$$

$$E_{\text{LUMO}} = - (E_{\text{onset(red)}} + 4.8) \text{ eV}$$

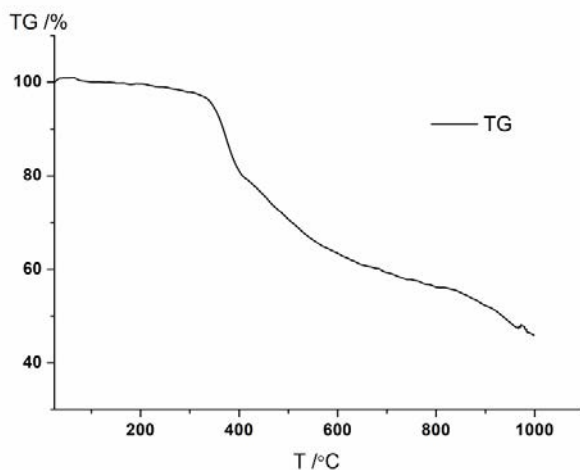


Figure A2.27. TG plot of Zn(4R-PPP).

Preparation of the films of the porphyrins and their blends with P3HT or PCBM

A concentration of 20 mg/mL in solvent (CH_2Cl_2 or chlorobenzene) was prepared for each compound. Different ratio mixtures of the porphyrin with P3HT and PCBM were achieved by stirring the two solutions at room temperature overnight. Deposition will be made by spin coating on the substrates. Following the same recipe used for normal devices by this deposition method, the revolutions per minute (RPM) was set at 800, and a volume of 200 μL of solution would be needed for covering the whole surface.

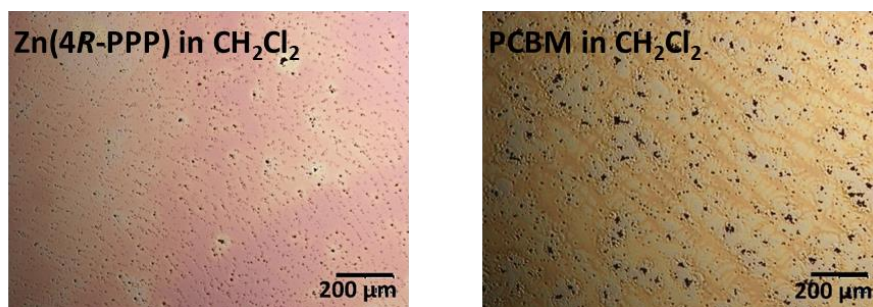


Figure A2.28. Microscope images of films by spin-coating CH_2Cl_2 solution of Zn(4R-PPP) (left) and PCBM (right).

Chapter III

Table A3.1. Crystallographic information of **TEP** and **Zn(TEP)**.

	TEP	Zn(TEP)
Formula	C ₂₈ H ₂₂ N ₄ O ₈	C ₂₈ H ₂₀ N ₄ O ₈ Zn
F _w	542.49	605.85
crystal system	monoclinic	triclinic
space group	P 2 ₁ /n	P
a [Å]	3.7790(8)	6.4350(13)
b [Å]	23.849(5)	10.090(2)
c [Å]	12.836(3)	10.395(2)
α [°]	90.00	66.44(3)
β [°]	96.08(3)	89.12(3)
γ [°]	90.00	76.65(3)
V [Å ³]	1150.3(4)	599.7(3)
Z	2	1
ρ _{calcd} [Mg m ⁻³]	1.566	1.678
μ [mm ⁻¹]	0.12	1.16
F(000)	564	310
θ _{max} [°]	33.4	30.0
refl collected	9254	10414
refl unique	2589	2948
R(int)	0.066	0.125
refl with I > 2σ(I)	2519	2799
refined parameters	184	189
wR ₂ [I > 2σ(I)]	0.041	0.062
wR ₂ [all data]	0.105	0.154
±Δρ _{max} [e Å ⁻³]	+0.36, -0.30	+1.63, -1.58

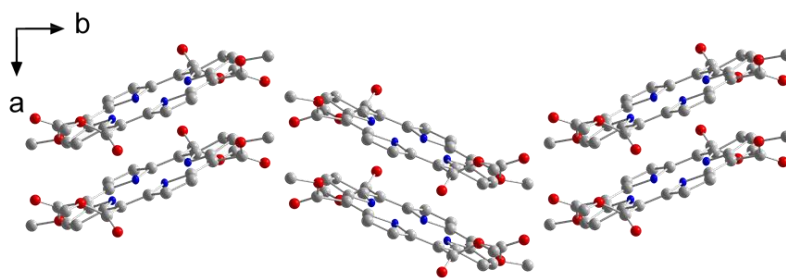


Figure A3.1. 3D organization of TEP.

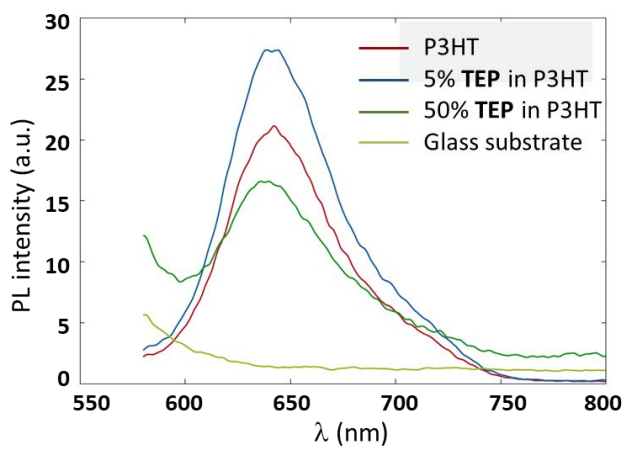


Figure A3.2. Photoluminescence spectra of TEP, P3HT and mixtures of both.

Chapter IV

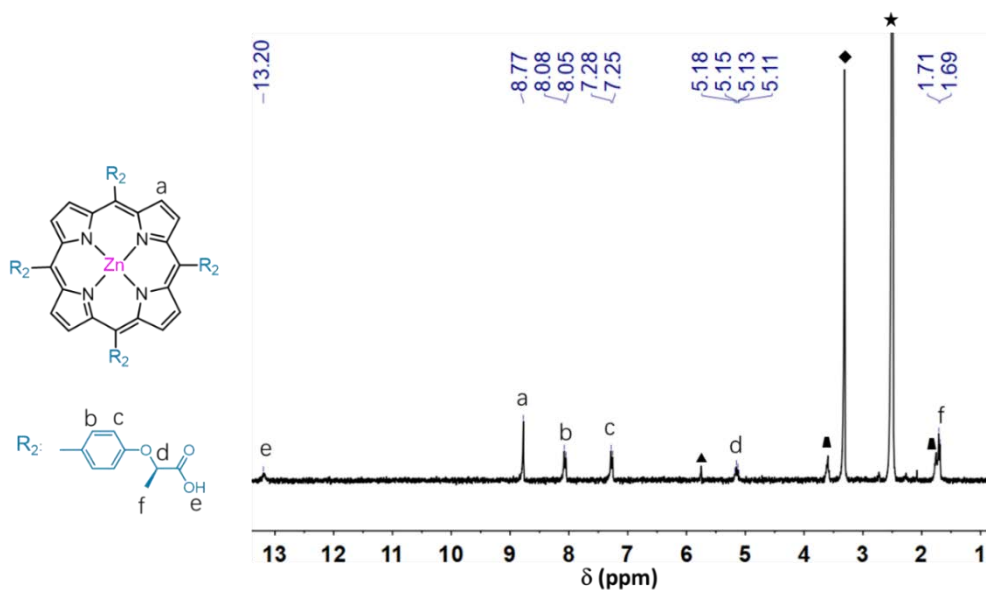


Figure A4.1. ^1H NMR of $\text{Zn}(4\text{R-CPP})$. \star Solvent DMSO- d_6 , \blacktriangle CH_2Cl_2 , \blacksquare THF, \blacklozenge H_2O .

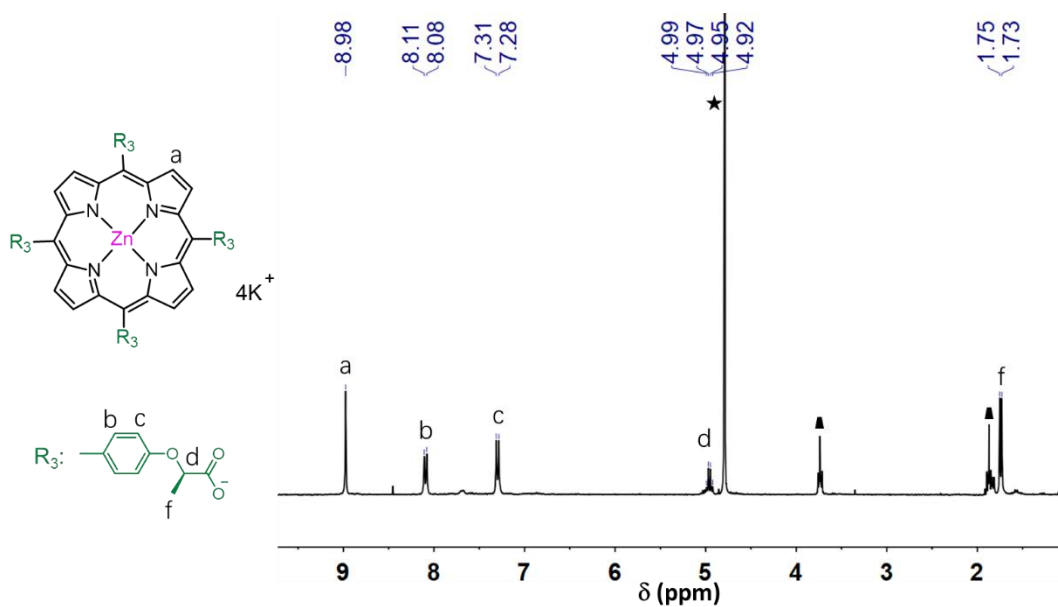
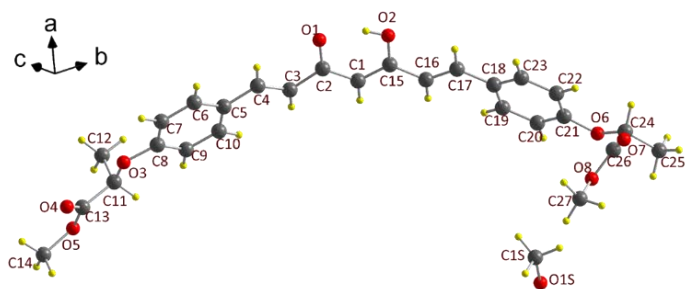


Figure A4.2. ^1H NMR of potassium $\text{Zn}(4\text{R-CPP})^{\text{m-}}$. \star Solvent Deuterium Oxide, \blacktriangle THF.

Chapter V

Table A5.1. Crystal and Experimental Data for *(R, R)* (MeO)₂C, *(R, R)* (MeO)₂C-BF₂ and *(R, R)* (MeO)₂C-Zn

	<i>(R, R)</i> (MeO) ₂ C	<i>(R, R)</i> (MeO) ₂ C-BF ₂	<i>(R, R)</i> (MeO) ₂ C-Zn
formula	C ₂₇ H ₂₈ O ₈ ·CH ₄ O	C ₂₇ H ₂₇ BF ₂ O ₈	C _{55.75} H _{56.50} O _{19.50} Zn
F _w	512.0	528.29	1103.88
crystal system	Orthorhombic	Monoclinic	Monoclinic
space group	P 2 ₁ 2 ₁ 2 ₁	P 2 ₁	P 2 ₁
a [Å]	5.3342(3)	15.076 (2)	13.174 (3)
b [Å]	21.1765(12)	6.9267 (9)	29.414 (6)
c [Å]	22.9045(13)	24.795 (3)	14.024 (3)
α [°]	90.00	90.00	90.00
β [°]	90.00	91.647 (9)	90.01
γ [°]	90.00	90.00	90.00
V [Å ³]	2587.3 (3)	2588.2 (6)	5434.3 (19)
Z	4	4	4
ρ _{calcd} [Mg m ⁻³]	1.316	1.356	1.349
μ [mm ⁻¹]	0.10	0.11	0.56
F(000)	1152	1104	2308
crystal size [mm ³]	0.50 × 0.06 × 0.05	0.19 × 0.18 × 0.04	
θ _{max} [°]	28.5	25.0	22.8
refl collected	30552	22954	90528
refl unique	5259	8659	13580
R(int)	0.077	0.069	0.097
refl with I > 2σ(I)	3903	5605	12576
refined parameters	340	693	1360
wR ₂ [I > 2σ(I)]	0.060	0.068	0.135
wR ₂ [all data]	0.155	0.217	0.423
±Δρ _{max} [e Å ⁻³]	+0.56, -0.44	+0.59, -0.49	+1.58, -0.53



	[Å]		[°]	
O(1)-C(2)	1.280(5)	C(2)-C(1)-C(15)	121.0(4)	
O(2)-C(15)	1.316(5)	O(3)-C(11)-C(13)	104.2(4)	
C(1)-C(2)	1.412(6)	O(6)-C(24)-C(26)	112.7(3)	
C(1)-C(15)	1.381(6)		[°]	
C(11)-C(12)	1.512(7)	C(3)-C(4)-C(5)-C(6)	171.20	
C(24)-C(25)	1.511(6)	C(16)-C(17)-C(18)-C(19)	15.42	

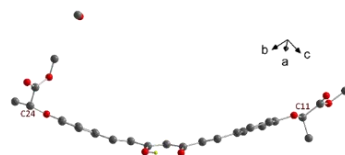


Figure A5.1. Molecular structure of **(*R,R*) (MeO)₂C** and selected bond lengths [Å] and angles [°].

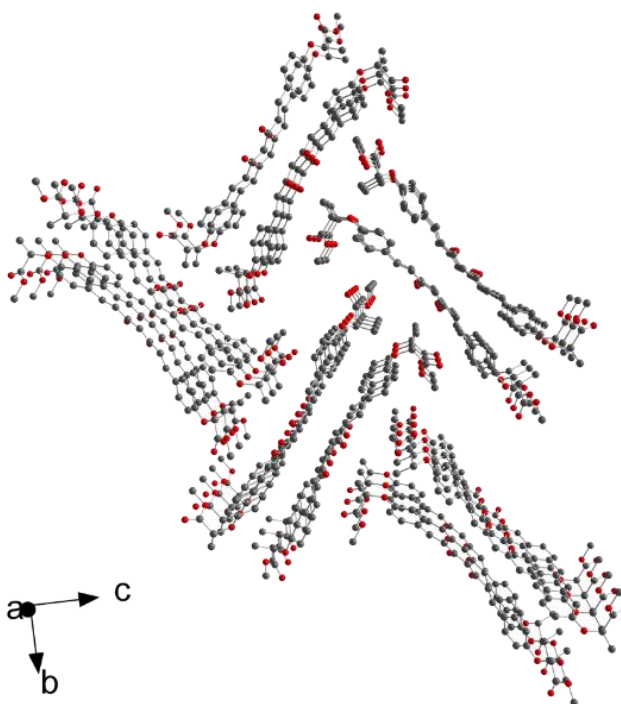
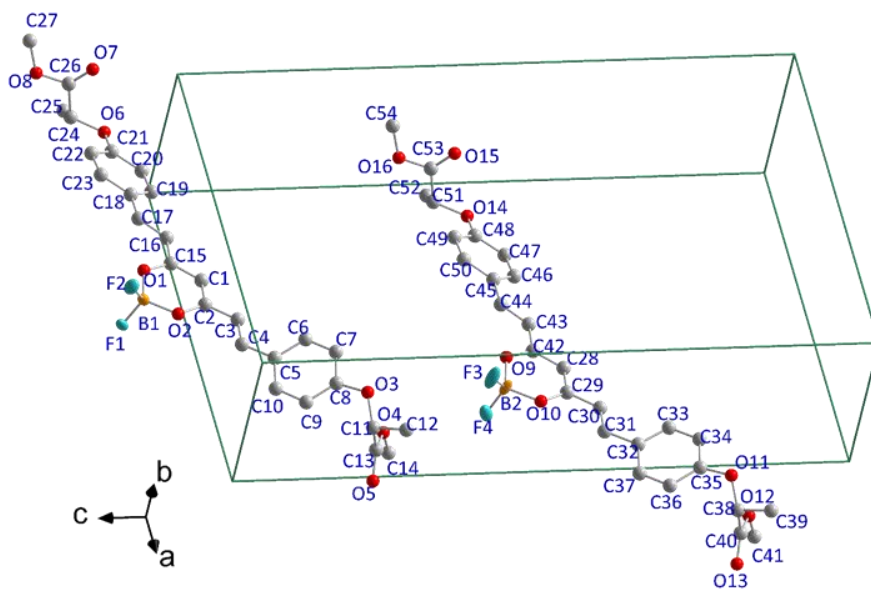


Figure A5.2. 3D self-assembly structure of molecular **(*R,R*) (MeO)₂C**.



	[Å]		[Å]
B(1)-F(1)	1.367(9)	B(2)-F(3)	1.324(12)
B(1)-F(2)	1.397(9)	B(2)-F(4)	1.391(12)
B(1)-O(1)	1.485(9)	B(2)-O(9)	1.484(10)
B(1)-O(2)	1.474(9)	B(2)-O(10)	1.488(10)
O(1)-C(15)	1.315(7)	O(9)-C(42)	1.312(8)
O(2)-C(2)	1.313(7)	O(10)-C(29)	1.324(8)
C(1)-C(2)	1.39(10)	C(28)-C(29)	1.369(10)
C(1)-C(15)	1.380(9)	C(28)-C(42)	1.373(10)
C(11)-C(12)	1.511(11)	C(38)-C(39)	1.520(11)
C(24)-C(25)	1.502(10)	C(51)-C(52)	1.528(11)
	[°]		[°]
C(2)-C(1)-C(15)	121.8(6)	C(29)-C(28)-C(42)	119.9(6)
O(3)-C(11)-C(13)	111.2(6)	O(11)-C(38)-C(40)	112.4(7)
O(6)-C(24)-C(26)	110.9(6)	O(14)-C(51)-C(53)	110.3(6)
	[°]		[°]
C(3)-C(4)-C(5)-C(6)	20.48	C(30)-C(31)-C(32)-C(33)	16.50
C(16)-C(17)-C(18)-C(19)	7.90	C(43)-C(44)-C(45)-C(46)	7.50

Figure A5.3. Scheme of the two molecules in the asymmetric unit of *(R, R)* (MeO)₂C-BF₂ (top) and selected bond lengths [Å], angles [°] and torsions [°].

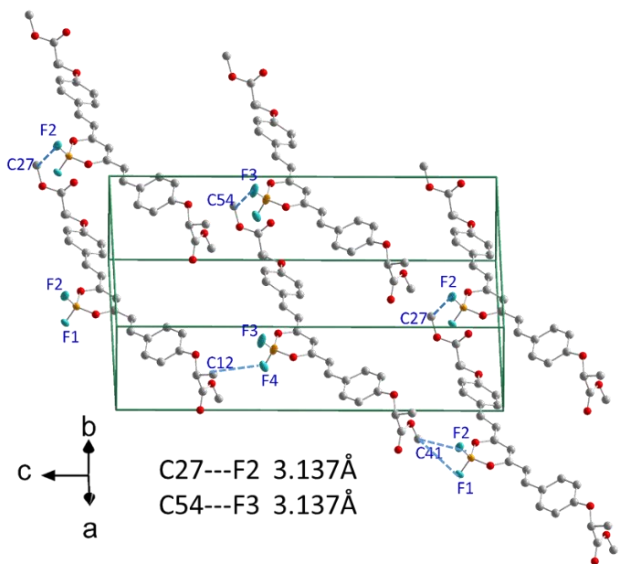


Figure A5.4. Representation of the expansion of *(R, R)* (MeO)₂C-BF₂ in one layer through molecular interactions

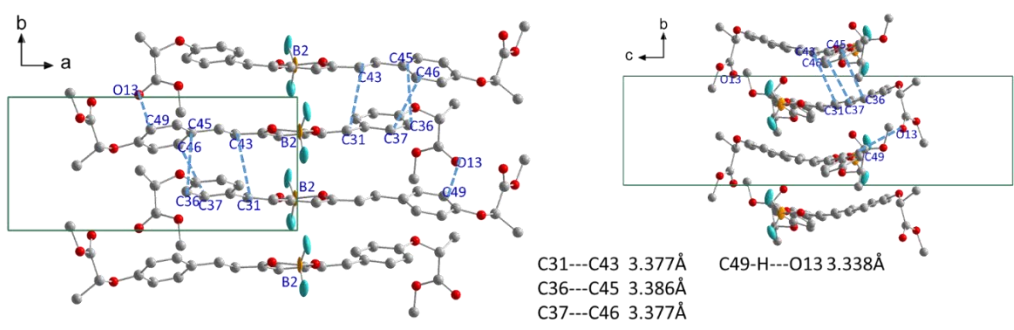


Figure A5.5. Crystal packing diagram of *(R, R)* (MeO)₂C-BF₂ in the c-axis (left) and a-axis (right) direction, displaying π-π stacking interactions.

Table A5.2. Reactions of (*R, R*) (HO)₂C with Zn(NO₃)₂ · 6H₂O in different solvent mixtures.

N°	(<i>R, R</i>) (HO) ₂ C	Zn(NO ₃) ₂ · 6H ₂ O	ratio	solvent
160701A	3 mg	3 mg	1:1.5	DMF 1 ml
160701B	3 mg	3 mg	1:1.5	DMF: ethanol 0.8 ml: 0.2 ml
160701C	3 mg	3 mg	1:1.5	DEF 1 ml
160701D	3 mg	3 mg	1:1.5	DEF: ethanol 0.8 ml: 0.2 ml
160719A	3 mg	5 mg	1:2.5	DMF: AcOH 1 ml: 5 µl
160719B	3 mg	5 mg	1:2.5	DMF: HNO ₃ 1 ml: 5 µl
160725A	10 mg	20 mg	1:3	DMF: ethanol: H ₂ O 1 ml: 0.5 ml: 0.5 ml
160725B	10 mg	20 mg	1:3	DMF: ethanol: KOH aqueous solution 1 ml: 0.5 ml: 0.5 ml (33 µl 1M KOH)

Table A5.3. Reaction of (*R, R*) (HO)₂C with different Zn salts.

N°	(<i>R, R</i>) (HO) ₂ C	Zn salt	ratio	solvent
161021A	10 mg	Zn(acac) ₂ 17.5 mg	1:3	DMF: ethanol 0.8 ml: 0.2 ml
161021B	10 mg	Zn acetate 12.2 mg	1:3	DMF: ethanol 1.6 ml: 0.4 ml
161021D	10 mg	Zn oxo acetate 11 mg	1:3	DMF: ethanol 1.6 ml: 0.4 ml
161104B	10 mg	Zn acetate · 2H ₂ O 13.7 mg	1:3	DMF: ethanol: AcOH 1.6 ml: 0.4 ml: 20 µl
161121A	5 mg	Zn acetate · 2H ₂ O 6.9 mg	1:3	DEA: ethanol: AcOH 0.8 ml: 0.2 ml: 40 µl

Table A5.4. Reaction of (*R, R*) (HO)₂C with different Zr salts.

N°	(<i>R, R</i>) (HO) ₂ C	Zr salt	ratio	solvent
161004A	10 mg	ZrCl ₄ 7.8 mg	1:1.5	DMF 2 ml
161004B	10 mg	ZrCl ₄ 7.8 mg	1:1.5	DMF: ethanol 1.6 ml: 0.4 ml
161004C	10 mg	ZrCl ₄ 7.8 mg	1:1.5	DMF: HNO ₃ 2 ml: 20 µl
161004D	10 mg	ZrCl ₄ 7.8 mg	1:1.5	DMF: KOH solution 2 ml: 63.3 µl
161007A	10 mg	ZrOCl ₂ · 8H ₂ O 10.7 mg	1:1.5	DMF 2 ml
161007B	10 mg	ZrOCl ₂ · 8H ₂ O 10.7 mg	1:1.5	DMF: ethanol 1.6 ml: 0.4 ml
161007C	10 mg	ZrOCl ₂ · 8H ₂ O 10.7 mg	1:1.5	DMF: HNO ₃ 2 ml: 20 µl
161007D	10 mg	ZrOCl ₂ · 8H ₂ O 10.7 mg	1:1.5	DMF: KOH solution 2 ml: 63.3 µl

Table A5.5. Reaction of (*R, R*) (HO)₂C with additional metal salts.

N°	(<i>R, R</i>) (HO) ₂ C	metal salt	ratio	solvent
160701E	3 mg	Cu(NO ₃) ₂ · 3H ₂ O 2.4 mg	1:1.5	DMF 1 ml
160701F	3 mg	Cu(NO ₃) ₂ · 3H ₂ O 2.4 mg	1:1.5	DMF: ethanol 0.8 ml: 0.2 ml
160701G	3 mg	Cu(NO ₃) ₂ · 3H ₂ O 2.4 mg	1:1.5	DEF 1 ml
160701H	3 mg	Cu(NO ₃) ₂ · 3H ₂ O 2.4 mg	1:1.5	DEF: ethanol 0.8 ml: 0.2 ml
160719C	3 mg	Cu(NO ₃) ₂ · 2.5H ₂ O 5 mg	1:3.2	DMF: AcOH 1 ml: 5 μl
160719D	3 mg	Cu(NO ₃) ₂ · 2.5H ₂ O 5 mg	1:3.2	DMF: HNO ₃ 1 ml: 5 μl
161021E	10 mg	Cu acetate· H ₂ O 13.2 mg	1:3	DMF: ethanol 1.6 ml: 0.4 ml
161121B	5 mg	Cu acetate· H ₂ O 6.6 mg	1:3	DEA: ethanol: AcOH 2 ml: 0.5 ml: 0.5 ml
160725C	10 mg	Co(NO ₃) ₂ · 6H ₂ O 20 mg	1:3	DMF: ethanol: H ₂ O 1 ml: 0.5 ml: 0.5 ml
160725D	10 mg	Co(NO ₃) ₂ · 6H ₂ O 20 mg	1:3	DMF: ethanol: KOH aqueous solution 1 ml: 0.5 ml: 0.5 ml (33 μl 1M KOH)

Table A5.6. Reaction of (*R, R*) (HO)₂C with additional ligands and Zn(NO₃)₂.

N°	(<i>R, R</i>) (HO) ₂ C	Guest ligand	ratio	solvent
160701E	3 mg	4,4-bipyridyl 2.4 mg	1:1.5	DMF 1 ml
160701F	3 mg	4,4-bipyridyl 2.4 mg	1:1.5	DMF: ethanol 0.8 ml: 0.2 ml
160701G	3 mg	4,4-bipyridyl 2.4 mg	1:1.5	DEF 1 ml
160701H	3 mg	4,4-bipyridyl 2.4 mg	1:1.5	DEF: ethanol 0.8 ml: 0.2 ml

Table A5.7. Reactions of (*R, R*) (HO)₂C-BF₂ and Zn salt in different conditions.

N°	(<i>R, R</i>) (HO) ₂ C-BF ₂	Metal salt	ratio	solvent	before and after reaction
		Zn(NO ₃) ₂ ·6H ₂ O			
170201C	10 mg	17.8 mg	1:3	DMA: ethanol 1.6ml: 0.4 ml	yellow solution----brown solution
		Zn acetate· 2H ₂ O			
170201A	10 mg	13.3 mg	1:3	DMA: ethanol 1.6ml: 0.4 ml	orange solution----shining film
170208A	5 mg	6.6mg	1:3	DMA 2 ml	orange solution----precipitate
170208B	5 mg	6.6mg	1:3	DMF: ethanol 1.5 ml: 0.5 ml	orange solution----shining film
170208C	5 mg	6.6mg	1:3	DMF: ethanol 1 ml: 1 ml	ligand partly soluble----shining film
		Zn(acac) ₂			
170201D	10 mg	15.8 mg	1:3	DMA: ethanol 1.6ml: 0.4 ml	orange solution----shining film
170209A	5 mg	7.9 mg	1:3	DMA 2 ml	orange solution----precipitate
170209B	5 mg	7.9 mg	1:3	DMF: ethanol 1.5 ml: 0.5 ml	orange solution----precipitate
170209C	5 mg	7.9 mg	1:3	DMF: ethanol 1 ml: 1 ml	ligand partly soluble----precipitate
		ZnCl ₂			
170530A	5 mg	13.7 mg	1:3	DMA: ethanol 1.5ml: 0.5 ml	precipitate----precipitate

Table A5.8 (Top) (*R, R*) (HO)₂C solubility test in common solvents (0.1 mg compound with 221 μL solvent, 10⁻³ M). (Bottom) Crystallization methods for (*R, R*) (HO)₂C by evaporation of different solvent systems and slow diffusion.



		Slow evaporation of solvent							
		(R,R)(HO) ₂ C 10 mg							
Solvent 1	CH ₃ OH 3 mL	ethanol 3 mL	THF 3 mL	acetone 5 mL	CH ₃ OH 3 mL	ethanol 3 mL	THF 5 mL	acetone 5 mL	
Solvent 2	toluene 3 mL	toluene 3 mL	toluene 3 mL	toluene 3 mL	hexane 3 mL	hexane 3 mL	hexane 3 mL	hexane 2 mL	

		Gas/liquid slow diffusion		
		(R,R)(HO) ₂ C 10 mg		(R,R)(HO) ₂ C 5 mg
Solvent 1	ethanol 1 mL	THF 2 mL	acetone 2 mL	
Solvent 2	ether 6mL	ether 6 mL	ether 6 mL	

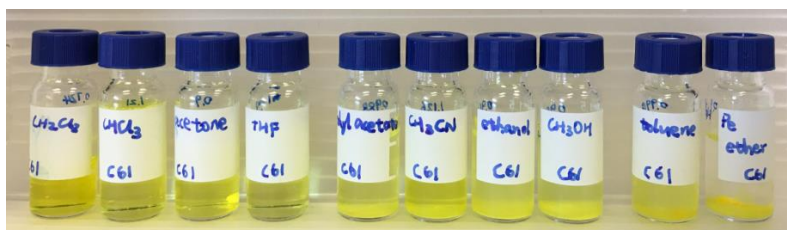
Table A5.9 (Top) *(R, R)* (HO)₂C-BF₂ solubility test in common solvents (0.1 mg compound with 100 μL solvent, 2×10⁻³ M). (Bottom) Crystallization methods for *(R, R)* (HO)₂C-BF₂ by evaporation of different solvent systems.



		Slow evaporation of solvent				
		<i>(R,R)</i> (HO) ₂ C -BF ₂ 10 mg				
Solvent 1	THF 3 mL	acetone 3 mL	CH ₃ CN 3 mL	CH ₃ OH 3 mL	CH ₃ OH 3 mL	CH ₃ OH 3 mL
Solvent 2	toluene 2 mL	toluene 2 mL	toluene 2 mL	toluene 3 mL	CH ₂ Cl ₂ 3 mL	hexane 3 mL

		Gas/liquid slow diffusion			
		<i>(R,R)</i> (HO) ₂ C -BF ₂ 5 mg			
Solvent 1	THF 0.5 mL	acetone 0.8 mL	CH ₃ CN 1.5 mL	CH ₃ OH 2 mL	
Solvent 2	ether 4 mL	ether 4 mL	ether 6 mL	ether 6 mL	

Table A5.10 (Top) (MeO)₂C solubility test in common solvents (0.1 mg compound with 110 μL solvent, 2×10⁻³ M). (Bottom) Crystallization methods for (MeO)₂C by evaporation of different solvent systems and slow diffusion.



		Slow evaporation of solvent							
		<i>(MeO)</i> ₂ C 10 mg				<i>(MeO)</i> ₂ C 5 mg			
Solvent 1	CH ₂ Cl ₂ 3 mL	THF 3 mL	acetone 8 mL	CH ₂ Cl ₂ 3 mL	CHCl ₃ 3 mL	THF 3 mL	acetone 8 mL	THF 3 mL	THF 3 mL
Solvent 2				CH ₃ OH 3 mL	CH ₃ OH 3 mL	CH ₃ OH 3 mL	CH ₃ OH 2 mL	Toluene 3 mL	hexane 3 mL

		Gas/liquid slow diffusion	
		<i>(MeO)</i> ₂ C 10 mg	<i>(MeO)</i> ₂ C 5 mg
Solvent 1	CH ₂ Cl ₂ 1 mL	THF 2 mL	acetone 2 mL
Solvent 2	ether 6 mL	ether 6 mL	ether 6 mL

Table A5.11 (Top) $(\text{MeO})_2\text{C-BF}_2$ solubility test in common solvents (0.1 mg compound with 100 μL solvent, 2×10^{-3} M). (Middle) Crystallization methods for $(\text{MeO})_2\text{C-BF}_2$ by evaporation of different solvent systems. (Down) Powder X-ray diffraction of $(\text{MeO})_2\text{C-BF}_2$ growing in THF, acetone and CH_3CN .



		Slow evaporation of solvent							
		$(\text{MeO})_2\text{C-BF}_2$ 10 mg			$(\text{MeO})_2\text{C-BF}_2$ 5 mg				
Solvent 1	THF 3 mL	acetone 5 mL	CH_3CN 7 mL	CHCl_3 5 mL	THF 3 mL	acetone 5 mL	CH_3CN 7 mL	CHCl_3 5 mL	CH_3OH 5 mL
Solvent 2					Toluene 3 mL	Toluene 3 mL	Toluene 3 mL	Toluene 3 mL	Toluene 3 mL

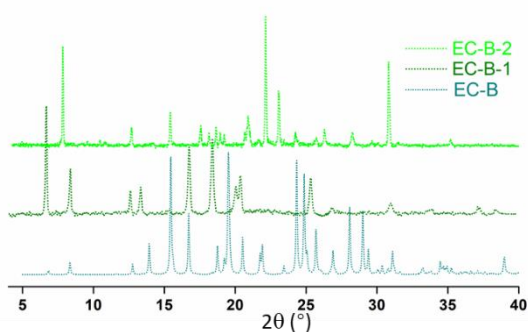


Table A5.12 (Top) $(\text{HO})_2\text{C}$ solubility test in common solvents (0.1 mg compound with 236 μL solvent, 10^{-3} M). (Bottom) Eight crystallization methods for $(\text{HO})_2\text{C}$ by evaporation of different solvent systems.



		Slow evaporation of solvent							
		$(\text{HO})_2\text{C}$ 2 mg							
Solvent 1	Acetone 5 mL	THF 5 mL	Ethanol 5 mL	CH_3OH 5 mL	Acetone 5 mL	THF 5 mL	Ethanol 5 mL	CH_3OH 5 mL	
Solvent 2					Toluene 3 mL	Toluene 3 mL	Toluene 3 mL	Toluene 3 mL	

Table A5.13. Crystal and Experimental Data for Structures **(MeO)₂C**, **(MeO)₂C-BF₂** and **(HO)₂C**.

	EC	EC-B	AC
formula	C ₂₅ H ₂₄ O ₈	C ₂₅ H ₂₃ BF ₂ O ₈	C ₂₃ H ₂₀ O ₈
F _w	452.44	500.24	424.39
crystal system	Monoclinic	Monoclinic	Orthorhombic
space group	P2 ₁ /c	P2 ₁ /c	P2 ₁ 2 ₁ 2 ₁
a [Å]	27.030(5)	7.5890 (15)	10.139(2)
b [Å]	13.028(3)	11.618(2)	48.382(10)
c [Å]	6.1460(12)	25.901 (5)	3.9400(8)
α [°]	90.00	90.00	90.00
β [°]	95.94(3)	90.81 (3)	90.00
γ [°]	90.00	90.00	90.00
V [Å ³]	2152.7(7)	2283.4 (8)	1932.7(7)
Z	4	4	4
ρ _{calcd} [Mg m ⁻³]	1.396	1.455	1.458
μ [mm ⁻¹]	0.11	0.17	0.12
F(000)	952	1040	888
crystal size [mm ³]			
θ _{max} [°]	23.9	34.2	29.5
refl collected	19478	40109	29129
refl unique	3079	5440	4936
R(int)	0.123	0.082	0.096
refl with I > 2σ(I)	2581	4848	4289
refined parameters	303	352	290
wR ₂ [I > 2σ(I)]	0.045	0.077	0.066
wR ₂ [all data]	0.120	0.202	0.217
±Δρ _{max} [e Å ⁻³]	+0.23, -0.25	+0.94, -0.37	+0.52, -0.57

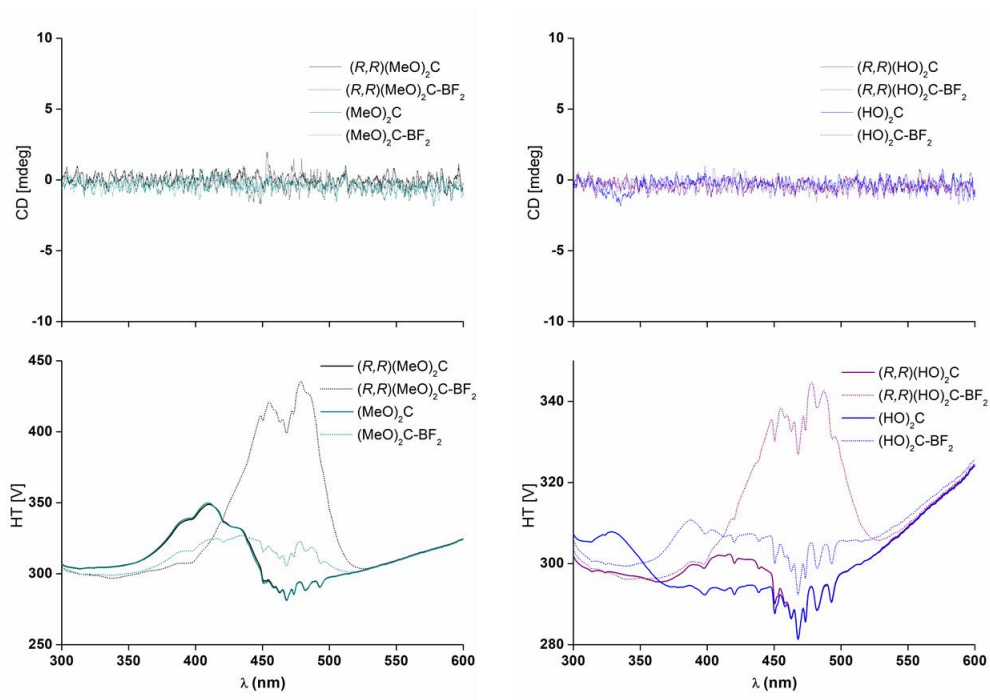


Figure A5.6. CD spectra and corresponding absorption signals of CCMoids (10^{-5} M) measured in THF.

Chapter VI

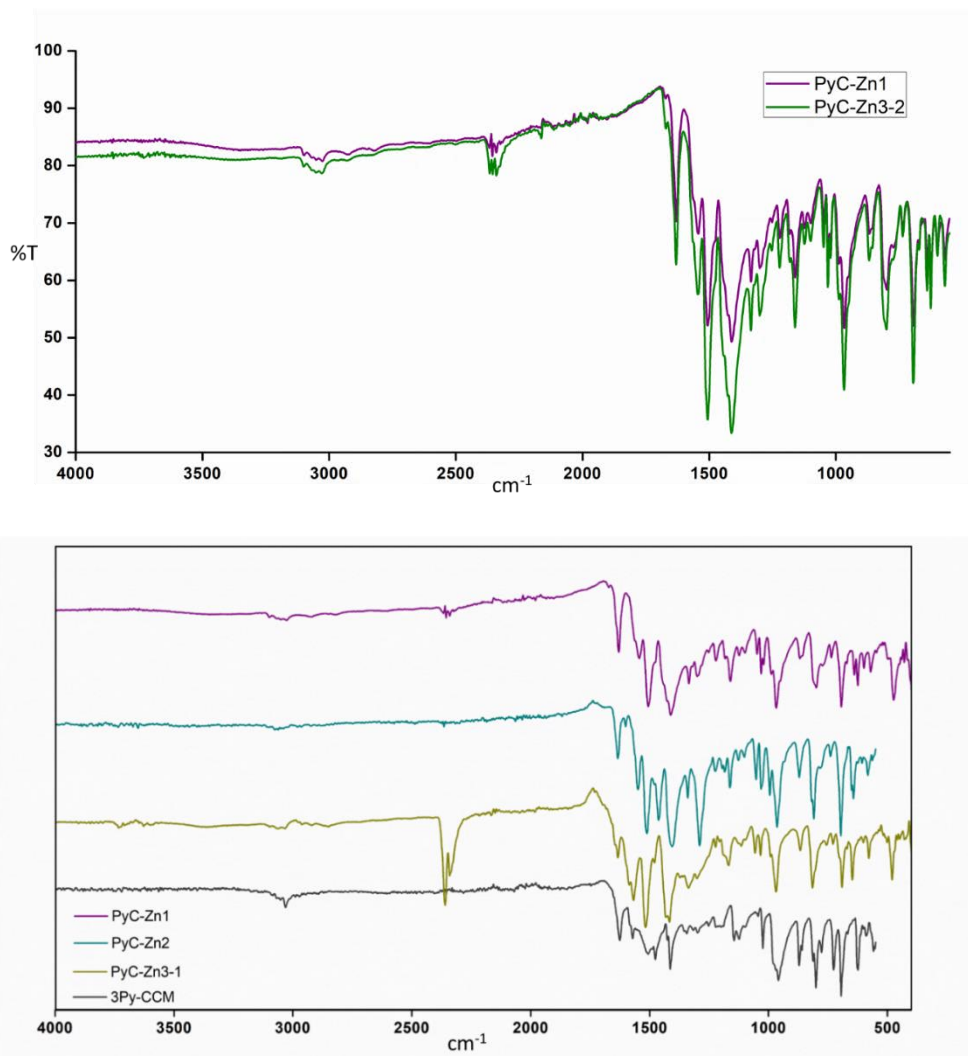
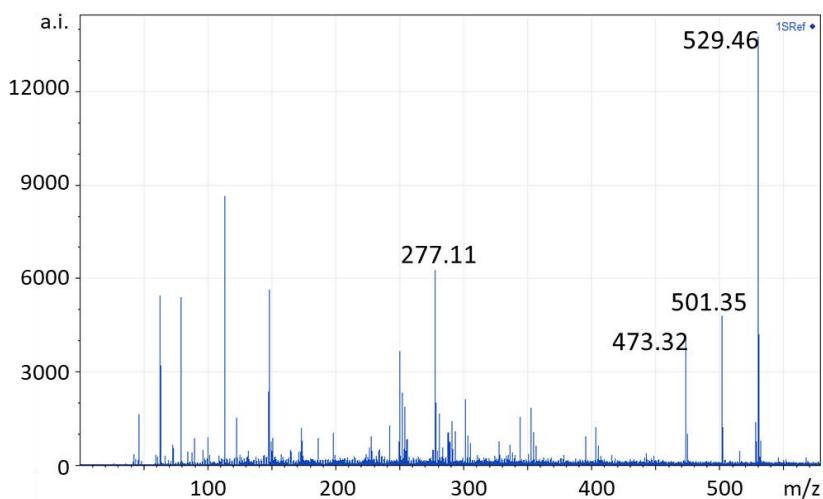


Figure A6.1. (Top) FT-IR spectra of **PyC-Zn1** and **PyC-Zn3-2**, (Down) FT-IR spectra of **PyC-Zn1**, **PyC-Zn2** and **PyC-Zn3-1** compared with ligand **3Py-CCM**.

Table A6.1. Crystal data and structure refinements for **PyC-Zn1** and **PyC-Zn2**.

	PyC-Zn1	PyC-Zn2
formula	C ₁₇ H ₁₃ N ₂ O ₂ Zn _{0.5}	C ₃₄ H ₂₆ N ₆ O ₁₀ Zn ₂
F _w	309.98	809.35
crystal system	Monoclinic	Monoclinic
space group	C2/c	P 2 ₁ /n
a [Å]	14.5539(12)	9.0611 (3)
b [Å]	20.3868(18)	14.0313 (4)
c [Å]	9.5213(8)	28.1117 (8)
α [°]	90.00	90.00
β [°]	91.462(3)	95.090 (1)
γ [°]	90.00	90.00
V [Å ³]	2824.1 (4)	3560.00(19)
Z	8	4
ρ _{calcd} [Mg m ⁻³]	1.458	1.510
μ [mm ⁻¹]	1.37	1.41
F(000)	1280	1648
crystal size [mm ³]		0.12 × 0.12 × 0.1
θ _{max} [°]	29.5	25.0
refl collected	13947	34882
refl unique	2377	6303
R(int)	0.049	0.055
refl with I > 2σ(I)	2172	4435
refined parameters	195	606
wR ₂ [I > 2σ(I)]	0.081	0.055
wR ₂ [all data]	0.186	0.159
±Δρ _{max} [e Å ⁻³]	+0.87, -0.56	+0.64, -1.09

**Figure A6.2.** The ESI-Mass spectrum of **PyC-Zn2** dissolved in DMA in negative.

Chapter VII

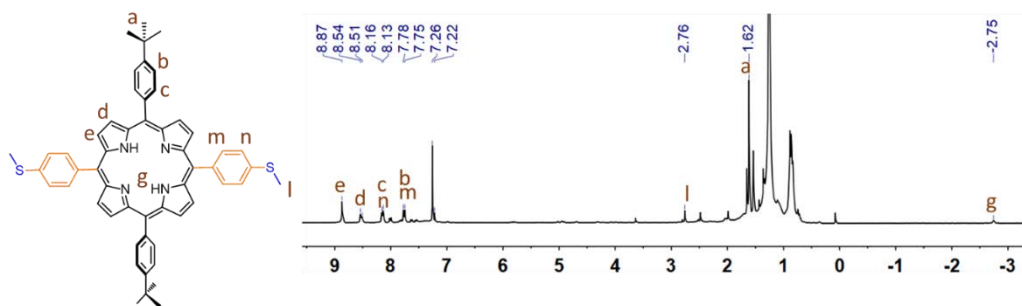


Figure A7.1. ^1H NMR spectrum of the crude $(\text{MeS})_2(^1\text{Buph})_2\text{P}$ in CDCl_3 at 20°C

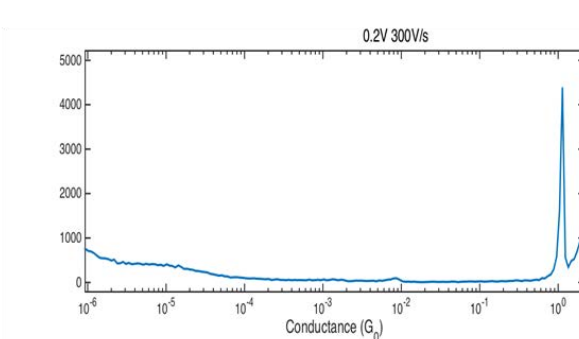
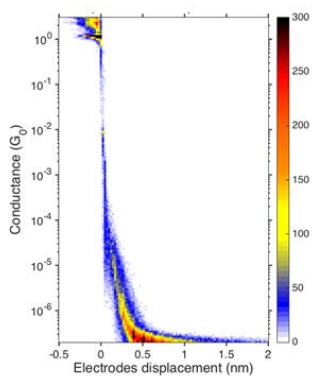


Figure A7.2 Conductance measurements of bare fold employing a MCBJ recorded with V_{bias} 0.2 V and piezo speed 300V/s. Conductance–distance traces (left) and 1D conductance histograms (right).

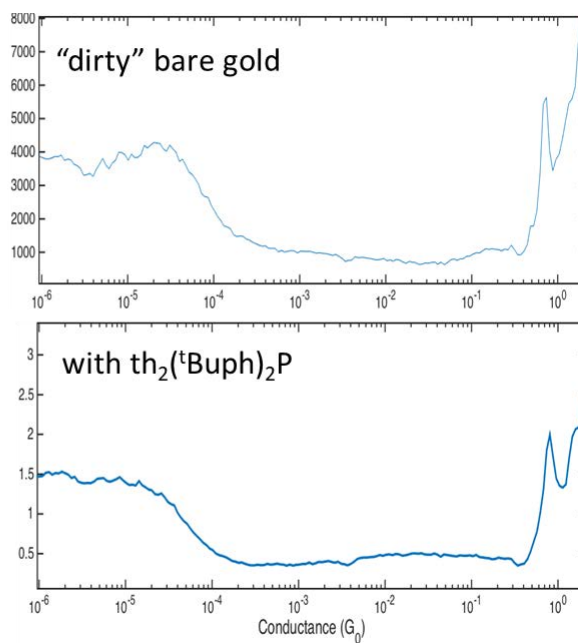
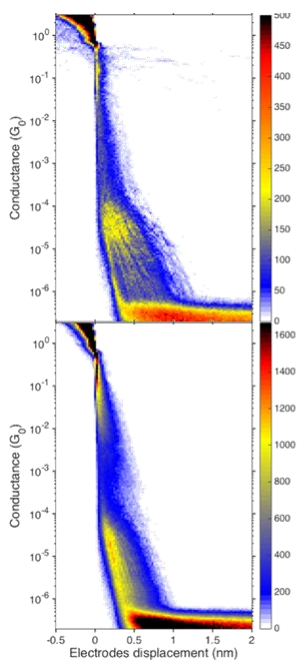


Figure A7.3 Conductance measurements of $\text{th}_2(\text{tBuph})_2\text{P}$ employing a MCBJ recorded with recorded with V_{bias} 0.1 V and piezo speed 300V/s.

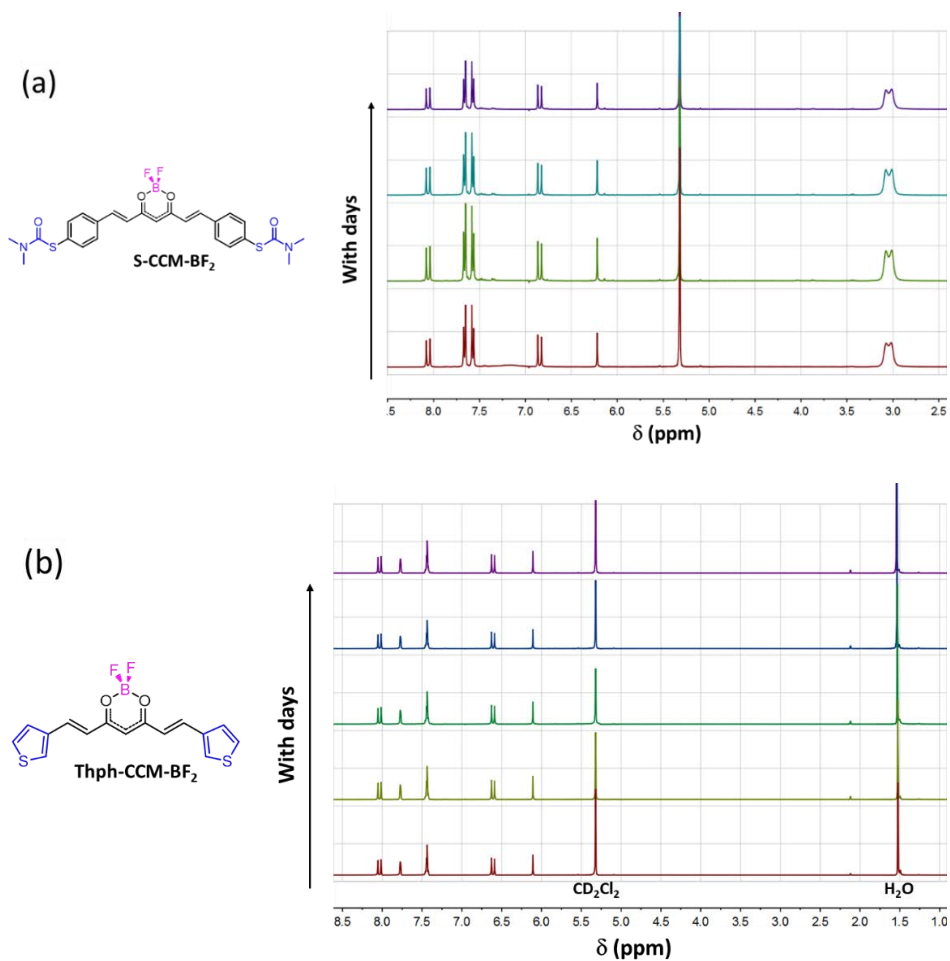


Figure A7.4 ¹H NMR spectra of the (a)S-CCM-BF₂ and (b) Thph-CCM-BF₂ in CD₂Cl₂ at room temperature for several days.

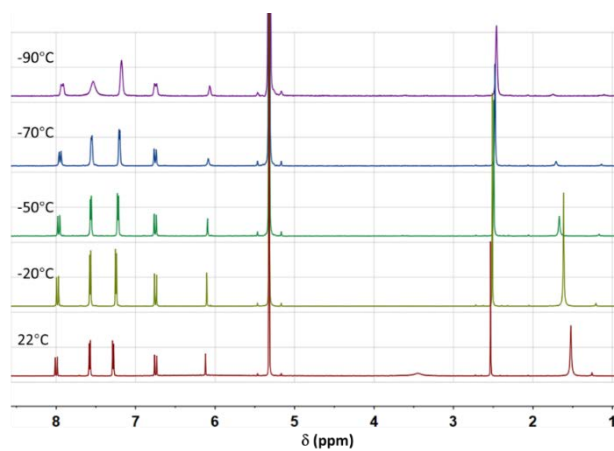


Figure A7.5. ¹H NMR spectra of the MeS-CCM-BF₂ in CD₂Cl₂ at different temperatures.

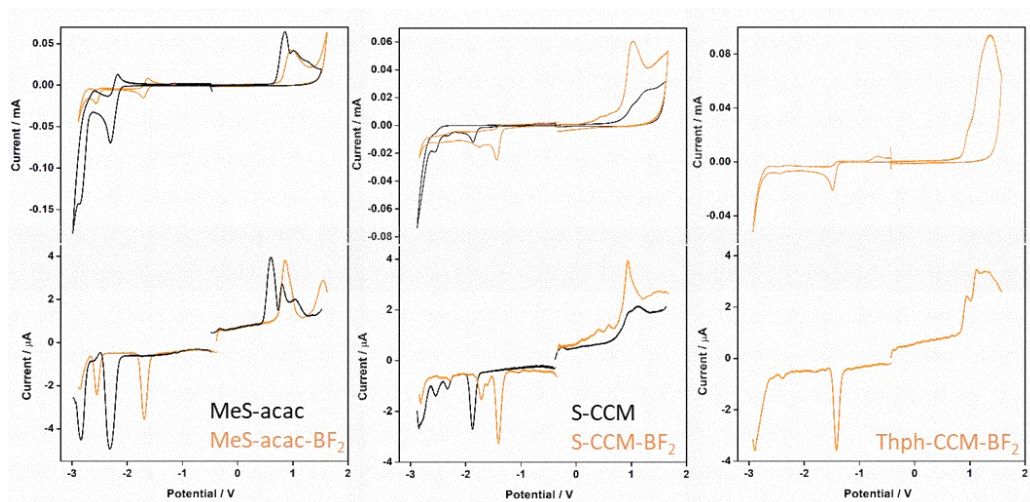


Figure A7.6. Cyclic voltammograms (CV) and differential pulse voltammograms (DPV) of curcuminoids with thiocarbamate and thiophene groups. Potentials vs. Fc/Fc^+ .

Table A7.1. Determination of the HOMO, LUMO and band-gap from electrochemistry measurements.

	MeS-CCM	MeS-CCM- BF_2	MeS-CCM-Cu	S-CCM	S-CCM- BF_2	Thph-CCM- BF_2	MeS-pry-CCM	MeS-isox-CCM	MeS-acac	MeS-acac- BF_2
E_{HOMO} (eV)	-5.11	-5.25	-5.06	-5.54	-5.61	-5.64	-5.48	-5.18	-5.27	-5.53
E_{LUMO} (eV)	-2.95	-3.37	-3.65	-3.03	-3.50	-3.47		-2.34	-2.65	-3.23
E_{g}^{ec} (eV)	2.16	1.88	1.41	2.51	2.11	2.17		2.84	2.62	2.30

References:

- (1) Qin, H.; Li, L.; Guo, F.; Su, S.; Peng, J.; Cao, Y.; Peng, X. *Energy & Environmental Science* **2014**, *7*, 1397.
- (2) Roth, K. M.; Yasserli, A. A.; Liu, Z.; Dabke, R. B.; Malinovskii, V.; Schweikart, K.-H.; Yu, L.; Tiznado, H.; Zaera, F.; Lindsey, J. S. *Journal of the American Chemical Society* **2003**, *125*, 505.
- (3) Chen, F.; He, J.; Nuckolls, C.; Roberts, T.; Klare, J. E.; Lindsay, S. *Nano Letters* **2005**, *5*, 503.
- (4) Leonat, L.; Sbârcea, G.; Branzoi, I. V. *UPB Sci Bull Ser B* **2013**, *75*, 111.
- (5) Pommerehne, J.; Vestweber, H.; Guss, W.; Mahrt, R. F.; Bässler, H.; Porsch, M.; Daub, J. *Advanced Materials* **1995**, *7*, 551.
- (6) Etcheverry - Berríos, A.; Olavarría, I.; Perrin, M. L.; Díaz - Torres, R.; Jullian, D.; Ponce, I.; Zagal, J. H.; Pavez, J.; Vásquez, S. O.; van der Zant, H. S. *Chemistry-A European Journal* **2016**, *22*, 12808.
- (7) Shafiee, A.; Salleh, M. M.; Yahaya, M. *Sains Malaysiana* **2011**, *40*, 173.

